Stony Brook University

Modified Ambient Template-Directed Synthesis, Characterization and Applications of One-Dimensional Nanomaterials

A Dissertation Presented

By

Fen Zhang

to

The Graduate School

in Partial Fulfillment of the

Requirements

for the Degree of

Doctor of Philosophy

in

Chemistry

Stony Brook University

December 2009

The Graduate School

Fen Zhang

We, the dissertation committee for the above candidate for the

Doctor of Philosophy degree, hereby recommend

acceptance of this dissertation.

Stanislaus S. Wong – Dissertation Advisor
Associate Professor, Department of Chemistry

Clare P. Grey – Chairperson of Defense
Professor, Department of Chemistry

Benjamin S. Hsiao – Third Member
Professor and Chair, Department of Chemistry

Laszlo Mihaly – Outside Member
Professor and Chair, Department of Physics

This dissertation is accepted by the Graduate School

Lawrence Martin

Dean of the Graduate School

Abstract of the Dissertation

Modified Ambient Template-Directed Synthesis, Characterization and Applications of One-Dimensional Nanomaterials

by

Fen Zhang

Doctor of Philosophy

in

Chemistry

Stony Brook University

2009

Nanomaterials have attracted considerable attention due to their unique physical properties and potential applications as building blocks in nanoscale devices. In particular, the intrinsic anisotropy inherent in one-dimensional (1D) nanomaterials renders them the smallest dimension structures that can be utilized for the efficient transport of electron and optical excitation. The template-directed synthesis technique represents the most straightforward and versatile route for achieving 1D growth. However, there are still challenges including (1) the development of an environmentally-friendly synthetic method, (2) a deep understanding of the relationship between size, composition, and physical properties in 1D nanostructures, (3) the design of 1D nanomaterials with novel properties, and (4) the application of 1D nanostructures in various fields, such as energy, catalysis, and biotechnology. Hence, the synthesis and characterization of 1D nanostructures, as well as the complementary study of the novel properties and potential applications of the resulting nanomaterials have been the focal points of my graduate study. Specifically, a modified template-directed technique has been developed, using a double-diffusion setup via a biomimetic crystallization process, which has enabled the successful preparation of various single-crystalline 1D nanostructures, including fluorides, tungstates, sulfides, and phosphates, under ambient, room-temperature conditions, without using either very harmful precursors or solvents, and without generating

particularly toxic byproducts. The family of alkaline-earth metal binary and perovskite ternary fluoride nanowires, doped with rare-earth ions, has displayed unique luminescence properties, with applications in optical devices. In addition, the generation of tungstate solid solution 1D nanostructures provides for a fundamental understanding of composition-modulated luminescence properties, leading to key structure-property correlations. A class of multifunctional 1D nanostructures has also been created by merging the favorable luminescent and magnetic properties via incorporating Mn ions into tungstate matrix. Moreover, the validity of this method has been demonstrated for the fabrication of semiconducting metal sulfide nanowires, which show higher photocatalytic degradation activity than their bulk counterparts. Finally, the technique has been extended to the large-scale synthesis of high aspect-ratio phosphate nanowires, which have been tested for their potential applicability as fluorescent labels in molecular imaging. The synthetic approach developed is quite generalized and flexible, and can be applied to the creation of other classes of nanomaterials.

Dedicated to:

My family, with love

Table of Contents

List of Abbreviations

0D	zero-dimensional
1D	one-dimensional
2D	two-dimensional
Å	angstrom
AAO	anodized aluminum oxide
AFM	atomic force microscopy
CNTs	carbon nanotubes
CVD	chemical vapor deposition
EDS	energy dispersive X-ray spectroscopy
eV	electron voltage
FC	field cooled
FE-SEM	field emission scanning electron microscopy
FETs	field-effect transistors
FTIR	Fourier Transform Infrared
h	hour
HRTEM	high-resolution transmission electron microscopy
JCPDS	Joint Committee on Powder Diffraction Standards
K	Kelvin
LEDs	light-emitting diodes

M	molar
min	minute
ml	milliliter
nm	nanometer
°C	degree Celsius
OTS	octadecyltetrachlorosilane
PC	polycarbonate
PDMS	polydimethylsiloxane
PL	photoluminescence
s	second
SAED	selected area electron diffraction
SAMs	self assembled monolayers
SQUID	superconducting quantum interference device
SPR	surface Plasmon resonance
STM	scanning tunneling microscopy
T	temperature
T_C	Curie temperature
TEM	transmission electron microscopy
T_N	Néel temperature
UV	ultraviolet
UV-vis	ultraviolet-visible

VLS	vapor-liquid-solid
XPS	X-ray photoelectron spectroscopy
XRD	X-ray powder diffraction
ZFC	zero field cooled
μm	micrometer
μs	microsecond
χ	magnetic susceptibility

List of Figures

List of Tables

Acknowledgements

First of all, I would like to express my sincere gratitude to my advisor Professor Stanislaus S. Wong for his continuous support of my Ph.D research, and for his guidance, advice, and encouragement at all times. His scientific enthusiasm and intuition have been an inspiration to me. I am also immensely grateful to my committee: Professor Clare Grey and Professor Benjamin Hsiao, for their insightful comments and discussions on my work. I would also like to thank Professor Laszlo Mihaly for serving on my committee as an outside member.

Special thanks to Dr. Jim Quinn and Dr. Yuanbing Mao, for their valuable help and advice, especially at the early stage of my research. And many thanks go to the members of the Wong group: Mandakini, Jingyi, Tirandai, T.-J., Hongjun, Xiaohui, Jon, Alex, Amanda, Chris, and all the undergraduates, for their thoughtful discussions and understanding, as well as sharing a wonderful time together as a family.

I gratefully acknowledge the support and assistance given to me by faculty and staff from Department of Chemistry (Stony Brook University) as well as Condensed Matter Physics and Materials Science Department (Brookhaven National Laboratory). In particular, I would like to thank Dr. Susan van Horn (CMIC, SBU) and Dr. Dezhi Wang (Physics, Boston College) for their help with electron microscopy. I acknowledge the technical service by Dr. Guowei Tian for confocal microscopy. I am grateful to Professor M. C. Aronson and Dr. Yuen Yiu (Physics, SBU), Dr. Arnold R. Moodenbaugh, Dr. Qiang Li and Mr. Qin Jie (CMPMS, BNL) for their assistant with SQUID measurements. I appreciate the support of Dr. Matthew Sfeir (CFN, BNL), Professor Erwin London, Professor Daniel Raleigh, and Ms. Fanling Meng with PL analyses. I also thank Dr. Rebecca Rowehl and Ms. Manisha Das for their help with cell culture at the Cell Culture and Hybridoma facility at SBU. Moreover, Sigma Xi is acknowledged for travel support.

I am greatly grateful to all of my friends in both U.S. and China, for their support and motivation. I treasure every moment of the times we spend together. Last but not least, I thank my Chinese family (the Zhangs), American family (the Silvermans), and Japanese family (Taiko Tides) for their endless love and support.

List of Publications

1. **F. Zhang**, S. S. Wong, "Ambient Large-Scale Template-Mediated Synthesis of High-Aspect Ratio Single-Crystalline, Chemically Doped Rare-Earth Phosphate Nanowires for Bioimaging", *ACS Nano*, submitted.
2. M. Feygenson, A. Kou, L. E. Kreno, A. L. Tiano, J. M. Patete, **F. Zhang**, M. S. Kim, V. Solovyov, S. S. Wong, and M. C. Aronson, "Properties of Highly Crystalline NiO and Ni Nanoparticles Prepared by High Temperature Oxidation and Reduction", *Phys. Rev. B*, submitted.
3. **F. Zhang**, S. S. Wong, "Controlled Synthesis of Semiconducting Metal Sulfide Nanowires", *Chem. Mater*. **2009**, 21, 4541.
4. A. Santulli, W. Xu, J. B. Parise, L. Wu, M. C. Aronson, **F. Zhang**, C. –Y. Nam, C. T. Black, A. L. Tiano, and S. S. Wong, "Synthesis and Characterization of V_2O_3 Nanorods", *Phys. Chem. Chem. Phys.* **2009**, *17*, 3718.
5. **F. Zhang**, Y. Yiu, M. C. Aronson, and S. S. Wong, "Exploring the Room-Temperature Synthesis and Properties of Multifunctional Doped Tungstate Nanorods", *J. Phys. Chem. C*, **2008**, *112*, 14816.
6. **F. Zhang**, M. Y. Sfeir, J. A. Misewich, and S. S. Wong, "Room-Temperature Preparation, Characterization, and Photoluminescence Measurements of Solid Solutions of Various Compositionally-Defined Single-Crystalline Alkaline-Earth-Metal Tungstate Nanorods", *Chem. Mater.*, **2008**, *20*, 5500.
7. **F. Zhang**, Y. Mao, T. –J. Park, and S. S. Wong, "Green Synthesis and Property Characterization of Single-Crystalline Perovskite Fluoride Nanorods", *Adv. Funct. Mater*. (cover) **2008**, *18*, 103.
8. Y. Mao, T. –J. Park, **F. Zhang**, H. Zhou, and S. S. Wong, "Environmentally Friendly Methodologies of Nanostructure Synthesis", *Small* (invited review) **2007**, *3***,** 1122.

9. Y. Mao†, **F. Zhang**† (equal contribution), and S. S. Wong, “Ambient Template-Directed Synthesis of Single-Crystalline Alkaline Earth Metal Fluoride Nanowires”, *Adv. Mater*. **2006**, *18*, 1895.
10. B. Liu, L. Li, Q. Zhang, **F. Zhang**, K. Jiang, S. –H. Yu, “Morphology Control of Stolzite Microcrystals with High Hierarchy in Solution”, *Angew. Chem. Int. Ed.* **2004**, *43*, 4745.
11. B. Liu, **F. Zhang**, L. Li, Q. Zhang, L. Ren, K. Jiang, S. –H. Yu, “Ring-Like Nanosheets Standing on Spindle-Like Rods: Unusual ZnO Superstructures Synthesized From A Flakelike Precursor $Zn_5(OH)_8Cl_2{\cdot}H_2O$”, *J. Phys. Chem. B* **2004**, *108*, 4338.
12. B. Liu, L. Li, **F. Zhang**, Q. Zhang, M. Yoshimura, P. Shen, S. –H. Yu, “Nanorod-Direct Oriented Attachment Growth and Promoted Crystallization Processes Evidenced in Case of $ZnWO_4$”, *J. Phys. Chem. B* **2004**, *108*, 2788.

Chapter I Background on Synthesis and Properties of 1D Nanomaterials

1.1 Nanoscience and Nanotechnology

"There's Plenty of Room at the Bottom" is the title of a famous lecture given by Richard Feynman in 1959. Feynman considered the possibility of direct manipulation of individual atoms as a more powerful form of synthetic chemistry than those used at the time. Since the discovery of carbon nanotubes by Sumio Ijima in 1991,[1] the term "nano" has become widely used as a ubiquitous prefix in science and technology. Moreover, it is becoming widely recognized by the general public.[2] "Nano" in the SI system of units denotes a factor of 10^{-9}. For example, one nanometer is equal to one-billionth of a meter. To provide a clear perspective of the nanometer scale, Figure 1.1 shows length scales in context.[3] Atoms are below a nanometer scale, whereas many molecules, including a number of proteins, range from a nanometer and upwards.

Nanoscience is the study of phenomena and manipulation of materials at atomic, molecular and macromolecular scales, where properties differ significantly from those at a large scale.[4] Nanoscience is associated with the intimate understanding and control of matter at dimensions of roughly 1 to 100 nm and is intrinsically important because of the genuine expectation that the properties of materials at this scale will differ significantly from those of their bulk counterparts.[5] The field is highly interdisciplinary, encompassing aspects of physics, chemistry, biology, materials science and engineering, and medicine. Owing to widespread interest and investment, nanoscience is growing and progressing at an unprecedented rate. However, nanoscience is still largely in the "discovery phase" wherein new materials are being synthesized on small scales for testing specific physical properties.

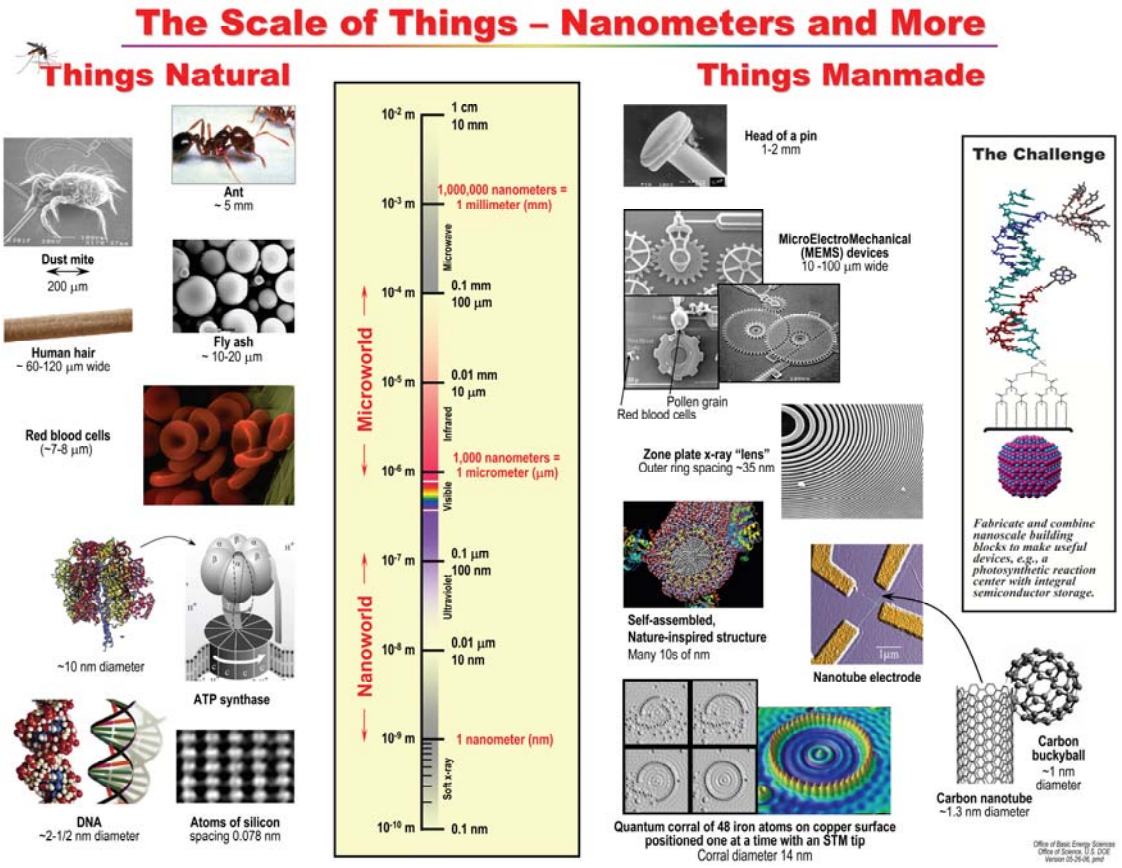

Figure 1.1 Length scale showing the nanometer in context. Natural as well as man-made things are highlighted at a nanometer length scale and a micrometer length scale for comparison. Reproduced from the DOE website.[3]

Nanotechnology refers to the design, characterization, production and application of structures, devices and systems by controlling their shape and size at nanometer scale.[4] It is the science of designing and manipulating materials through atom by atom engineering. There are four critical challenges in the development of nano-scale science and technology: (1) materials synthesis with controlled structure and precision at the atomic/molecular scale, (2) property characterization of the structurally well understood components, (3) nanodevice fabrication, and (4) system manipulation and integration.[6] In the emerging field of nanotechnology, a goal is to make nanostructures with special properties with respect to those of bulk or single particle species.

Nanostructures, which are defined as having at least one dimension between 1 and 100 nm, have received steadily growing interest as a result of their novel properties and applications superior to their bulk counterparts. The ability to generate such minuscule structures is essential to nanoscience and nanotechnology. In fact, examples of nanoscience and nanotechnology can be easily found in Nature, from the liposomes in cells that manufacture proteins atom-by-atom, to the chloroplasts of plants that turn sunlight, carbon dioxide, and water into copies of themselves.[7] Moreover, gold and silver nanoparticles have been used as pigments in ceramics and stained glasses since the 10th century AD.[8] During the past decade, scientists have developed techniques for synthesizing and characterizing many new nanostructures. Still, the design and synthesis of nanoscale materials with controlled properties is a significant and ongoing challenge within nanoscience and nanotechnology.

There are a large number of opportunities that might be realized by making new types of nanostructures, or simply by down-sizing existing microstructures into the nanoscale regime. The most successful example is provided by microelectronics, where "smaller" has meant greater performance ever since the invention of integrated circuits: more components per chip, faster operation, lower cost and less power consumption.[9] Miniaturization also brings numerous interesting phenomena such as the well-established size-dependent excitation and emission, as well as new techniques associated with nanostructures, including the invention of the scanning tunneling microscope (STM) in 1982 and the atomic force microscope (AFM) in 1986.[10]

Nanoscience and nanotechnology have created great excitement and expectation in the last few years, and have prompted collaboration between researchers in disparate disciplines, from chemistry and physics to biology, engineering and medicine, in order to share knowledge and techniques. Evolutionary developments in each of these fields towards investigating materials at increasingly smaller size scales have now come to be known as "nanoscience" and "nanotechnologies".[11]

1.2 Categorization of Nanomaterials

Nanomaterials, as we discussed in section 1.1, either as nanoscale building blocks or nanostructures, are defined as possessing at least one dimension between 1 and 100 nm, and are the fundamental focal points of nanoscience and nanotechnology. Nanomaterials are usually categorized as zero-dimensional (0D), one-dimensional (1D), and two-dimensional (2D) nanostructures, based on their number of dimensions at the nanoscale.

0D nanostructures includes materials that are nanoscale in three dimensions, such as quantum dots, fullerenes, colloids, and cubes.[12] With quantum dots as a model system, a rich number of interesting chemistry and physics has been studied by learning the evolution of their fundamental size-dependent properties. Quantum effects come into play when semiconducting particles are made small enough, limiting the energies at which electrons and holes can co-exist in particles. Since wavelength is related to energy, the optical properties of the particle can be finely tuned depending on its size.[13] As a result, quantum dots can be made to emit or absorb specific wavelengths of light, merely by controlling their size. Using quantum dots as active components, various types of nanoscale devices have been fabricated, such as light-emitting diodes (LEDs),[14] single-electron transistors,[15] optical detectors,[16] sensors,[17] and quantum-dot lasers.[18] For most of its applications, it is believed that the dimension of an individual quantum dot may represent the ultimate limit to the miniaturization of currently existing functional devices.

2D nanostructures are materials that have one of the three dimensions existing in the nanoscale, and these properties are extended in the other two dimensions, including layered structures such as thin films or surface coatings. In particular, thin films have been extensively studied for decades in the semiconducting and electronic device

manufacturing industries.[19] For example, in the silicon integrated-circuit industry, most of the electronic devices predominantly rely on thin films for their operation.[20] The fabrication and properties of the ultrathin layers are critical in the applications of thin film solar cells.[21] Advances have been made to control the composition and smoothness of surfaces, as well as the growth of thin films.

1D nanostructures represent materials of which two of the three dimensions are at the nanoscale (and extended in one dimension), including wires, rods, belts, and tubes, which are the focus of the present work. It is generally accepted that 1D nanostructures provide a good system in order to investigate the dependence of electrical and thermal transport as well as mechanical properties on dimensionality and size reduction (or quantum confinement). They are also expected to play an important role as both interconnects and functional units in fabricating electronic, optoelectronic, electrochemical, and electromechanical devices at the nanoscale.[22] As compared with 0D and 2D nanostructures, the advancement of 1D nanostructures has been slow until recently, as hindered by difficulties in their synthesis with controllable dimensions, morphology, phase purity, and chemical composition. The fabrication of 1D nanostructures with predictive, rational strategies is a major focal point of research for many groups worldwide.

Carbon nanotubes, for example, have been investigated intensely since Iijima's discovery.[1] Their large length and small diameter result in extremely high aspect ratios. Due to their novel chemical and physical properties, carbon nanotubes exhibit a wide range of applications, including in catalysis, energy storage, molecular electronics, drug delivery, and nanosensors.[23-27]

Inorganic 1D nanostructures are currently a major topic in nanoscale research owing to their unique applications in mesoscopic physics and fabrication of nanoscale devices.[28] They can be made from a number of materials, including metals, oxides, fluorides, chalcogenides, carbides, and nitrides. It has been reported that semiconducting nanowires made of silicon and gallium nitride demonstrate remarkable optical and electronic properties.[29] Multisegmented nanorods have recently been developed as well, as opposed to single-component 1D nanostructures. Scientists working at the nanoscale

hope to design multicomponent nanostructures and exploit their inherent multiple functionalities for use in many novel applications.[30]

1.3 Novel Properties of Nanomaterials

Nanomaterials are fundamentally interesting not only because they are small but also because they possess fascinating size-dependent optical, electronic, thermal, mechanical, chemical and catalytic properties, which are potentially distinctive from their bulk counterparts as well as from the atomic or molecular precursors from whence they were derived. This unique chemical and physical behavior of nanomaterials can in general be ascribed to the following attributes:

(1) Increased relative surface area: As a particle decreases in size, more atoms are localized at the surface as compared with that inside the core of particle. For example, a palladium cluster measuring 7 nm in size possess 35% of its atoms on its surface, at 5 nm 45% of its atoms, and at 1.2 nm 76% of its atoms. Figure 1.2 shows the percentage of surface atoms as a function of cluster diameter, where the surface atoms increase as the particle size decreases.[31] Surface atoms are chemically more active (in other words, less stable) as compared with interior atoms because they usually have fewer adjacent coordinated atoms as well as possess more unsaturated or dangling bonds. It has generally been accepted that the property of a material depends strongly on the nature of surface atoms. For example, as catalytic chemical reactions occur at surfaces, metallic nanostructures demonstrate a much higher reactivity than their bulk counterparts. Moreover, they have been widely used as catalysts, fuel cells, and batteries with higher efficiency.[32]

(2) Quantum effects or spatial confinement: A particle behaves as if it were free when the confining dimension is large as compared with the wavelength of the particle. In addition, the band gap remains at its original energy due to its continuous energy state. As the dimension dramatically decreases down to a certain limit, typically at the nanoscale, the energy levels become discrete. As a result, the band gap becomes size-dependent. This can significantly affect the optical, electric and magnetic properties of

nanomaterials. For example, different sized quantum dots emit different colored light due to quantum confinement.[33]

(3) Reduced imperfections: A self-purification process is involved in nanomaterials in that the impurities and defects tend to move to near the surface of nanostructures. The imperfection of the particle surface induces additional electronic states in the band gap, which act as electron or hole trap centers. With a high density of surface defects, for example, a decrease in the observed transition energy and a red-shifted emission can be observed due to defect band formation.[34] However, the chemical stability and mechanical property may be enhanced due to increased perfection inside nanostructures. For instance, carbon nanotubes have been reported to possess a Young's modulus much higher than that of high strength steel.[35]

1.4 Properties and Applications of 1D Nanomaterials

Applications of nanomaterials can be traced back for centuries. Specifically, colloidal gold and silver nanoparticles have been used as pigments in stained glass church windows. As compared with bulk materials, low-dimensional nanoscale materials, with their large surface areas and possible quantum confinement effects, exhibit novel physical, optical, thermal, electronic, magnetic, and mechanical properties. In many cases, 1D nanomaterials are superior to their counterparts with larger dimensions. For example, cyclic voltammetric detection limits for electroactive species located at an array of cylindrical gold nanoelectrodes could be three orders of magnitude lower than those observed using a conventional disk microelectrode made of bulk gold.[36] It is obvious that 1D nanostructures with well-controlled dimensions, composition, and crystallinity represent a new class of intriguing systems for investigating structure-property relationships and related applications.

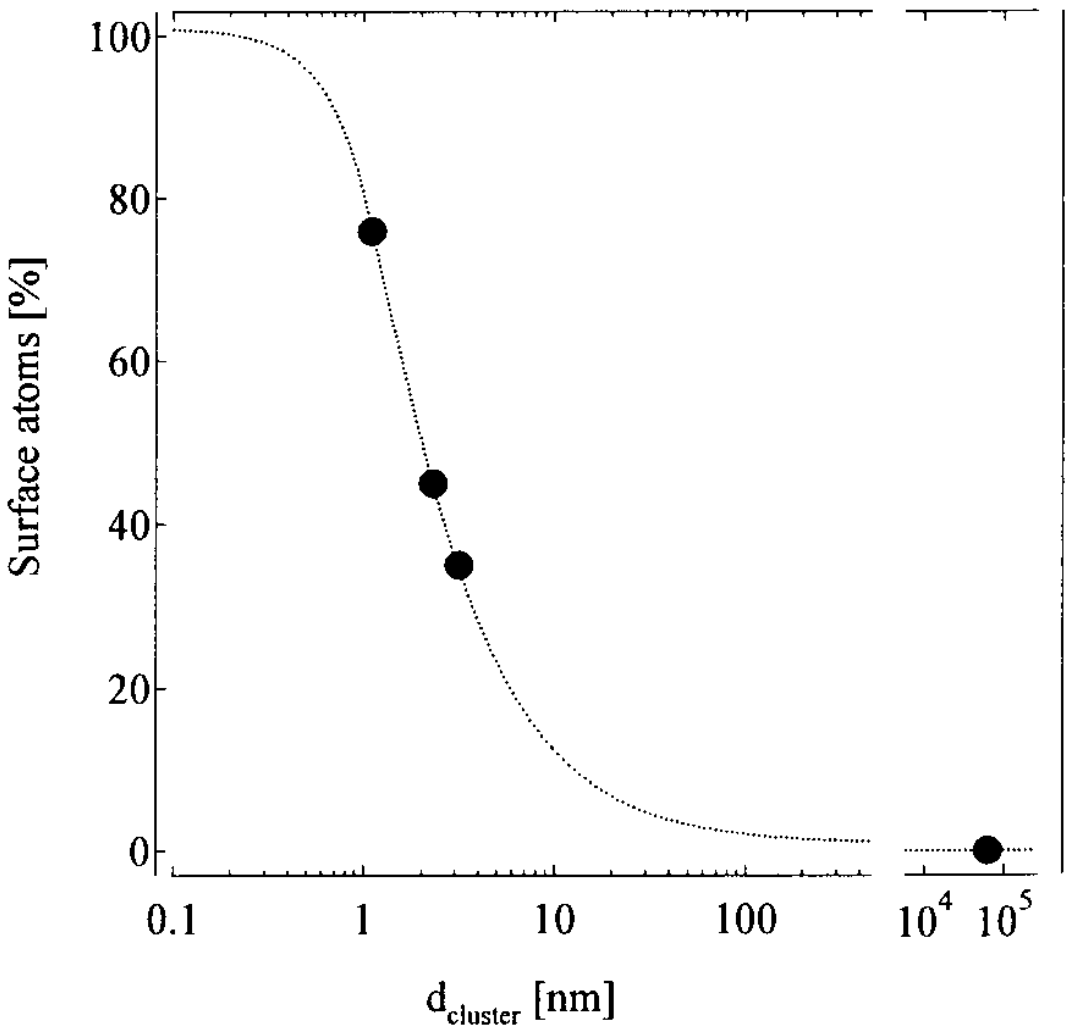

Figure 1.2 The percentage of surface atoms changes with the palladium cluster diameter. The samples used in this study are marked by black dots.[31]

1.4.1 Thermal Stability

The thermal stability of 1D nanostructures is of critical importance for their implementation as building blocks in nanoscale devices. It has been reported that the melting point of a solid material will be greatly reduced when it is processed into nanostructures.[37] For example, a Ge nanowire of 55 nm in diameter and 1 μm in length started to melt from both ends at about 650 °C, while the melting point of bulk Ge is 930 °C.[38] The remarkable reduction in melting point associated with 1D nanostructures has several important implications. First of all, the annealing temperature necessary for the synthesis of defect-free nanowires might only be a small fraction of the annealing temperature required for the bulk materials. Therefore, the purification of nanowires can be performed at modest temperatures. Secondly, a reduction in melting point enables one to cut, interconnect, and weld nanowires at relatively low temperatures, thereby providing a new tool to integrate 1D nanostructures into functional devices. Thirdly, as the diameters of 1D nanostructures can be reduced to sufficiently thin dimensions, their stabilities become extremely sensitive to environmental changes. Nanowires may spontaneously break up into shorter segments so as to reduce the high free energy associated with 1D nanostructures.[39]

1.4.2 Electron Transport Properties

As the critical dimension of an individual device becomes smaller and smaller, the electron transport properties of their components become an important issue to study. Miniaturization in electronics is expected to increase computing speed. Single-walled carbon nanotubes have recently been explored for nanoelectronic devices, such as single-electron transitors, field-effect transistors (FETs), sensors, and circuits.[40-43] Their electrical conductivity depends on their diameter and the inherent helicity of their graphen sheet. In addition, it has been shown that some metallic nanowires may undergo a transition to become semiconducting as their diameters are reduced below certain values.[44] As a result of quantum confinement, it was proposed that the external conduction sub-band and valence sub-band moved in opposite directions so as to open up a bandgap.

Another issue related to the electronic applications of 1D nanostructures is the assembly of these building blocks into various devices. To this end, a number of groups have demonstrated methods capable of directing the assembly of 1D nanostructures into a variety of electronic devices. It is worth noting that the Lieber group has been able to assemble semiconductor nanowires into cross-bar p-n junctions and junction arrays with controllable electrical characteristics with yields as high as 95%.[45] This "bottom-up" approach to nanoelectronics not only leads to a high density of devices on a chip, but also provides greater flexibility to generate tailored materials for a desired device functionality.

1.4.3 Optical Properties

Similar to quantum dots, size confinement also plays an important role in determining the energy levels of 1D nanostructures once their diameters are reduced below a critical value (Bohr radius). It has been reported that the absorption edge of Si nanowires was significantly blue-shifted as compared with the indirect bandgap of bulk silicon.[46] Sharp, discrete features in the absorption spectra and relatively strong "band-edge" photoluminescence were also observed in the system. These optical features most likely originated from quantum confinement effects, although surface states might also add additional contributions. As compared with quantum dots, light emitted from nanowires is highly polarized along their longitudinal axes. For example, the anisotropy in the PL intensities in the direction parallel to and perpendicular to the long axis of an individual, isolated InP nanowire can be used to fabricate polarization sensitive nanoscale photodetectors, which may find applicability in optical switches, near-field imaging, and high resolution detection.[47]

Semiconductor nanorods have also been used to enhance the processibility and efficiency of solar cells. The Alivisatos group has fabricated thin-film photovoltaic devices by combining CdSe nanorods with polythiophenes so as to obtain hybrid materials.[48] The performance of this device could be tuned by controlling the aspect ratios of the nanorods. In addition, the nanorods highlighted superior capability to quantum dots, because they could provide a direct path for electrical transport at much lower loadings.

Moreover, the surface plasmon resonance (SPR) properties of 1D nanostructures made of noble metals, such as Au and Ag, have been extensively studied. There exist two SPR modes in 1D nanostructures, corresponding to the transverse and longitudinal excitations. The latter one can be easily tuned to span across the spectral region from visible to near-infrared by controlling their aspect ratios.[49] Coupled with biological inertness, Au and Ag nanorods are ideal candidates for applications as contrast enhancing reagents and biological labels for *in vivo* optical imaging.

1.4.4 Field-Emission Properties

It is well known that 1D nanostructures with sharp tips can be used as cold cathode in the field emission of electrons. Apart from carbon nanotubes, Si, SiC and ZnO nanorods have also exhibited well-behaved and robust field emission.[50, 51] These nanorods exhibited a particularly high electron field emission, as well as good stability. Considering their ease of preparation, they have found wide applicability as active components in field-emission display devices.

1.4.5 Sensing Applications

Another major application for 1D nanostructures is related to the sensing of molecules, ranging from medical, environmental, to security-checking purposes.[22] The extremely high surface-to-volume ratios associated with 1D nanostructures make them extremely sensitive to species adsorbed on surfaces. For example, semiconductor nanowires have been modified and implemented as highly sensitive, real-time sensors for pH and biological species.[52] This mechanism can be explained in terms of the change in surface charge induced by protonation and deprotonation. The small dimensions and high sensitivities associated with these sensors suggest that they are good candidates for array-based screening and *in vivo* diagnostics.

1.4.6 Mechanical Properties

Single crystalline 1D nanostructures are supposed to be significantly stronger than their bulk counterparts, due to a reduction in the number of defects per unit length. Atomic force microscopy (AFM) has been used to determine the mechanical properties of individual nanorods, including elasticity, strength, and toughness.[53] The large Young's modulus associated with SiC nanorods implies that these 1D nanostructures are a class of

promising candidates that will generate strong composites, with ceramic, metal or polymer serving as the matrix.

1.4.7 Catalytic Properties

In general, nanomaterials with higher surface area provide for higher catalytic activity, which also depend on crystal shape, including faces, edges, corners, and defects. Catalytic activity often takes place at defects on the surfaces, steps, and kinks of 1D nanostructures. They allow for special bonding situations which are favorable for the breaking and making of bonds.[54] In addition, atoms near the surfaces of nanosturctures are much more flexible to move around than in the bulk. Therefore, surface reconstruction is much easier. Moreover, crystalline 1D nanostructures allow for more uniformity in the size and chemical structure of the catalyst, which therefore lead to greater catalytic activity and the production of fewer byproducts. It is also possible for specific or selective catalytic activity.[55]

1.5 Synthesis of 1D Nanomaterials

Both top-down and bottom-up approaches have been developed for the synthesis of nanomaterials. Top-down approaches are usually referred to as conventional manufacturing, which create nanomaterials by using larger, externally controlled components to direct their assembly, including milling, lithography, repeat quenching, and ink-jet printing. By contrast, bottom-up methods create complex assemblies from smaller components, such as molecules and atoms, using an atom-by-atom or molecule-by-molecule approach, which can produce nanomaterials or nanoscale devices in parallel.[56]

In general, top-down approaches offer reliability and device complexity, but they are more expensive, energy inefficient, and more wasteful as compared with bottom-up approaches. In the electronics industry, top-down methods dominate in the production of computer chips. However, the bottom-up strategy relies on the controlled growth of nanomaterials, pursued within the disciplines of materials science and chemistry.[2] Specifically, the goal of the present work is to control with atomic precision the

morphology, structure, composition, and size of nanomaterials, since these will define and enable our control over the physical properties of the resulting materials.

1.5.1 General Synthetic Approaches

The essence of 1D nanostructure formation is about crystallization, a process that has already been investigated for centuries. The evolution of a solid from a vapor, liquid, or solid phase involves two fundamental steps, namely nucleation and growth.[58] As the concentration of the building blocks, such as atoms, ions, or molecules, become sufficiently high, they aggregate into small clusters, which are known as nuclei, through homogeneous nucleation. With a continuous supply of the building blocks, these nuclei can serve as seeds for further growth so as to form larger structures. The process is schematically illustrated in Figure 1.3. Although it has been studied for decades, very little is quantitatively known about this process. It is still a significant challenge to achieve complete control over the whole process.

When developing a synthetic method for generating 1D nanostructures, the most important issue is the simultaneous control over dimensions, morphology, and monodispersity. In the past several years, a variety of chemical methods have been demonstrated as the bottom-up approach for achieving 1D growth, including the *chimie douce* solution method,[59, 60] the vapor-liquid-solid (VLS) method,[28, 61] the use of template-inspired method,[62, 63] the kinetic control of growth using appropriate capping reagents,[64, 65] the utilization of hydrothermal and solvothermal methods,[66, 67] a sol-gel processing method,[68] the use of microemulsions,[69] and biomimetic methods.[70] Figure 1.4 schematically illustrates some of these synthetic strategies that include: (A) use of an intrinsically anisotropic crystallographic structure of a solid to accomplish 1D growth; (B) introduction of a liquid-solid interface to reduce the symmetry of a seed; (C) use of various templates with 1D morphologies so as to direct the formation of 1D nanostructures; (D) use of appropriate capping reagents to kinetically control the growth rates of various facets of a seed; (E) self-assembly of 0D nanostructures; and (F) size reduction of 1D micron-scale structures.

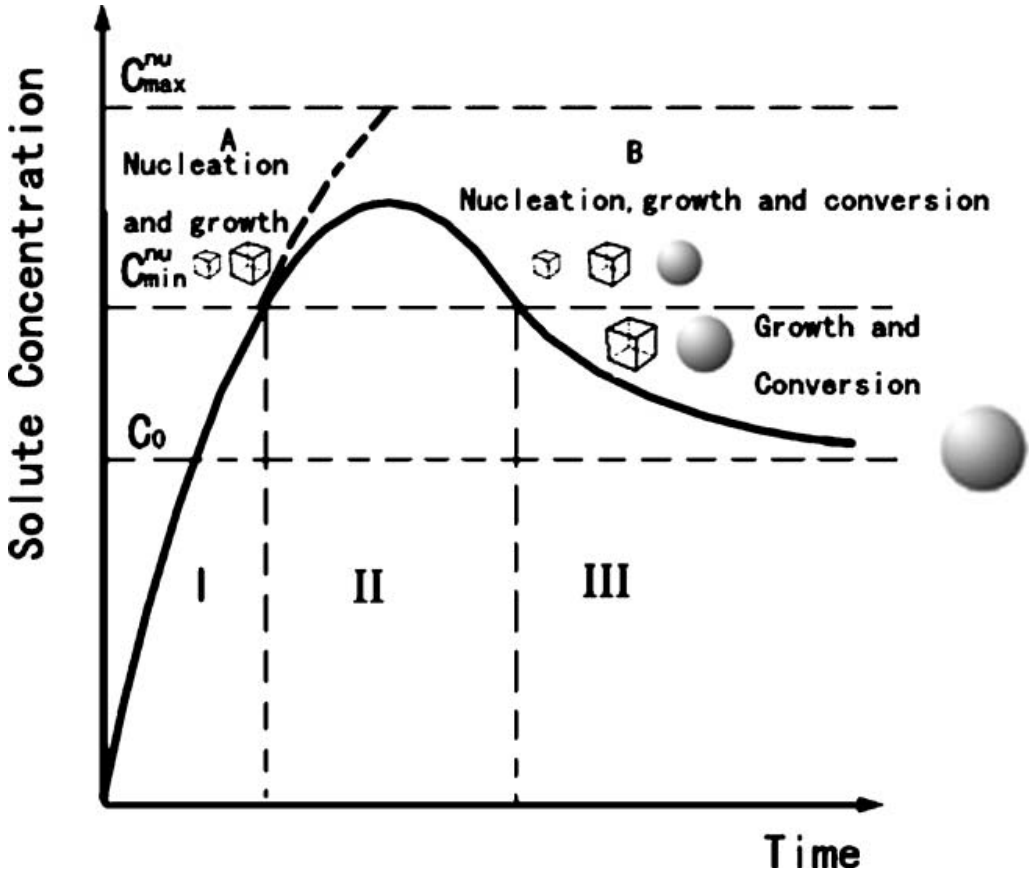

Figure 1.3 Schematic illustrating the processes of nucleation and subsequent growth.[57]

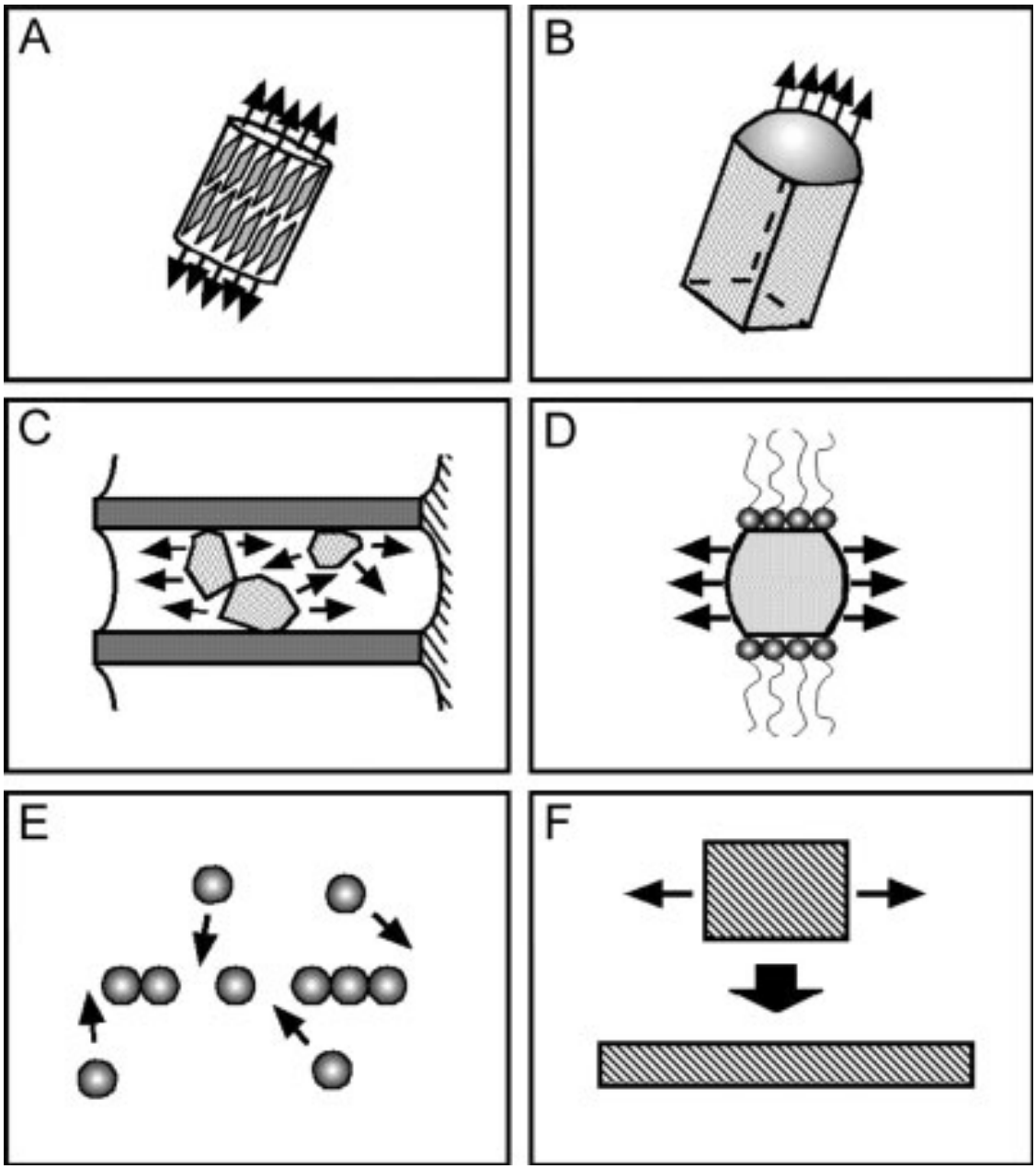

Figure 1.4 Schematic illustrations of six different strategies that have been demonstrated for achieving 1D growth: A) dictation by the anisotropic crystallographic structure of a solid; B) confinement by a liquid droplet as in the vapor-liquid-solid process; C) direction of growth through the use of a template; D) kinetic control provided by a capping reagent; E) self-assembly of 0D nanostructures; F) size reduction of a 1D micron-scale structure.[22]

Among the above methods, for example, in sol-gel process, because of the involvement of high temperature annealing, the resulting products are normally aggregates of nanoparticles. Furthermore, it is very difficult to control the shape of the products. Advantages of using microemulsion method include the preparation of very small particles and the ability to control particle size, while disadvantages include low product yields and the need to use large amount of liquids, so as related to the biomimetic process. Hydrothermal and solvothermal approaches generate a relative large number of products. However, they suffer from long reaction times and high reaction temperatures, as well as toxic byproducts associated with certain systems.

1.5.2 Template-Directed Synthesis

The template-directed synthesis technique represents a conceptually straightforward and versatile way to prepare 1D nanostructures. This method involves the synthesis of desired materials within the pores of template membranes. The template serves as a central confining structure, within which a different material is formed in situ and shaped into a nanostructure with its morphology based on that of the underlying template. The chemical and physical properties of these template membranes (i.e., pore geometry and monodisperse diameters) enable a high degree of control over the dimensions of the resulting 1D nanostructures. Another useful feature of this technique is that it is extremely generalized with respect to the types of materials that can be prepared. Indeed, nanotubes and nanofibrils of conductive polymers, metals, semiconductors, carbon, and other types of materials have been prepared within the confines of cylindrical pores of membranes.[71-75] Moreover, these tubular or fibrillar nanostructures can be assembled into a wide variety of different architectures. For instance, if a nanostructure-containing membrane were to be attached to a substrate and the membrane were to be subsequently removed, an ordered assembly, e.g. a vertical array of micro- or nanostructures protruding out from the surface of the substrate, can in principle be obtained.

Many different types of template membranes have been successfully used by various research groups worldwide, and it is generally agreed that templated syntheses are relatively simple, reasonably high-throughput, and cost-effective procedures, all of

which are conducive to their generalized applicability and hence, environmental acceptability. There are two general types of templates used, namely "soft" templates and "hard" templates. Naturally occurring gels, micelles, and chitin scaffolds are often considered as soft templates for the precipitation of single crystals of calcium carbonate and of calcium phosphate.[76-78] Other soft templates include DNA strands, polymer matrices, and reverse micelles. Hard templates tend to be associated with materials such as anodic alumina membranes and track-etched polycarbonate membranes, many of which are commercially available.[79] As a major drawback, nanostructures synthesized using template-directed methods are often polycrystalline, and the quantity of nanomaterials that can be produced in each synthesis run is relatively limited.

Herein, we focus on the class of templates with channels in porous membranes for the use in the synthesis of 1D nanostructures. This conventional template-directed method was pioneered and popularized by Martin's group.[74, 80, 81] Two types of porous membranes are commonly used: alumina films containing anodically etched pores and polymer films containing track-etched channels. Porous alumina membranes are often prepared using anodization of aluminum foils in an acidic medium, and they usually possess a high pore density (ranging as high as 10^{11} pores per cm^2), parallel and straight channels, a distribution of cylindrical pores of highly uniform diameter arranged in a hexagonal array, and size tunability of ~5 to 300 nm. Moreover, these templates are thermally and mechanically stable.[73-75] However, there is a need to selectively remove these templates without destroying the products, by using chemical post-synthesis treatments, such as the etching reagent NaOH, in order to collect the desired nanostructures. For track-etching, a polymer film is irradiated with heavy ions (from nuclear fission) so as to generate damaged spots in the surface of this film. These spots are then amplified through chemical etching to generate uniform, cylindrical pores penetrating the membrane film. The pores fabricated using this method are often randomly scattered across the membrane surface, and their orientation may also be tilted by as much as 34° with respect to the surface.[82] Polymer membranes can be removed through simple dissolution with a noninterfering, organic solvent such as dichloromethane.

A variety of materials have been examined for use with this class of templates, as diverse as semiconductors,[83] metals,[84] ceramics,[85] and organic polymers.[86] The precursors can be loaded into the pores using a method based on ultra vapor-phase sputtering, liquid-phase injection, or solution-phase chemical or electrochemical deposition. It is worth mentioning that the precursors might be preferentially deposited as uniform layers on the walls of these pores in order to form tubular 1D nanostructures, instead of solid rods, as indicated in Figure 1.5. In both cases, the resulting 1D nanostructures can exist as well-aligned arrays within the membranes, or they can be released from the templates and collected as ensembles in free-standing form.[87]

The major advantage associated with template-directed synthesis is that both the dimensions and compositions of 1D nanostructures can be easily controlled by varying experimental conditions. However, most nanomaterials produced by conventional templating procedures are polycrystalline, despite the variety of different deposition strategies used, including electrochemical deposition, electroless deposition, polymerization, sol-gel deposition, and layer-by-layer deposition in nanoporous templates. The reason for the observed polycrystallinity is that many of these methods require additional annealing steps at high temperatures.[74, 75, 88, 89]

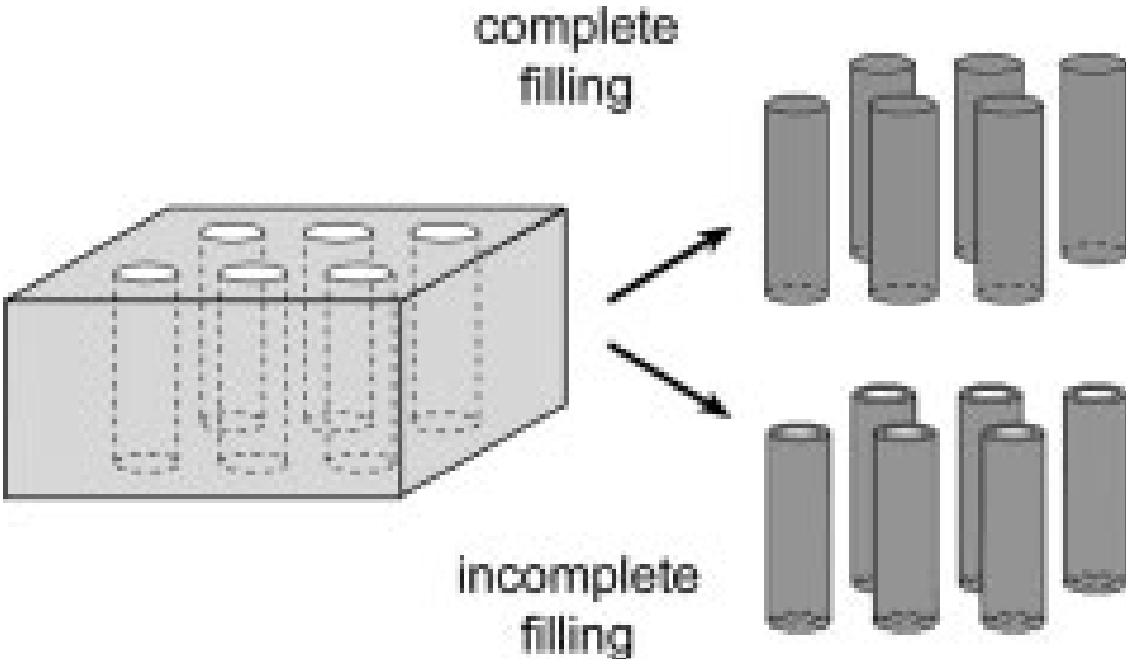

Figure 1.5 Schematic drawing illustrating the formation of nanowires and nanotubes by filling and partial filling of the pores within a porous membrane with desired precursor materials.[87]

1.6 Objectives of Present Work

On the basis of the previous discussion, various nanomaterials have drawn continuous research attention because of their unique electrical, optical and magnetic properties that are different from those of the bulk, as well as their potential applications in mesoscopic research and in nanoscale devices. In particular, the intrinsic anisotropy inherent in 1D nanostructures renders them the smallest dimensional structures that can be utilized for the efficient transport of electrons and optical excitations. Thus, nanowires, nanorods, nanobelts, and nanotubes are often used as functional building blocks for the assembly of electronic, optoelectronic, and sensing devices.

Over the past decade, a tremendous amount of work has been accomplished in the synthesis of 1D nanostructures, especially via the template-directed method. However, there are still challenges that we intend to address in the thesis:

(1) Development of an environmentally-friendly synthetic method (e.g. use of cost-effective, nontoxic precursors, room temperature, if at all possible.

(2) Understanding of the relationship between size, composition and physical properties in nanomaterials.

(3) Design of 1D nanostructures with novel properties.

(4) Application of as-prepared nanomaterials in various fields, including in energy, catalysis and biotechnology.

Hence, the synthesis and characterization of 1D nanostructures, as well as the study of the novel properties and potential applications of the resulting nanomaterials have been focal points of my study. The main research results we have achieved can be summarized as follows.

1.6.1 Single-crystalline alkaline-earth metal Binary fluoride nanowires and perovskite ternary fluoride nanorods

Fluorides possess wide applicability in optics, biological labels, and lenses, as well as components of insulators, gate dielectrics, wide-gap insulating overlayers, and

buffer layers in semiconductor-on-insulator structures. In addition, fluorides, doped with rare-earth ions such as Eu^{+3}, Nd^{+3}, and Ho^{+3}, have also been reported to display unique luminescence properties with correspondingly useful applications in diagnostics, lasing, solid-state light emitters, light amplification, optical telecommunication, and upconversion. It is reasonable to expect that nanoscale fluorides will play an important role in technological applications, including as high-density optical storage devices, nanosensors, and color displays. To the best of our knowledge, there have not been any reported syntheses of 1D nanostructures of either binary fluorides (CaF_2, SrF_2, and BaF_2) or ternary fluorides ($KMnF_3$ and NH_4MnF_3). In our work, we address the issue by applying a modified template-directed method so as to prepare single-crystalline alkaline-earth metal binary fluoride nanowires and perovskite ternary fluoride nanorods. (Figure 1.6 and 1.7)

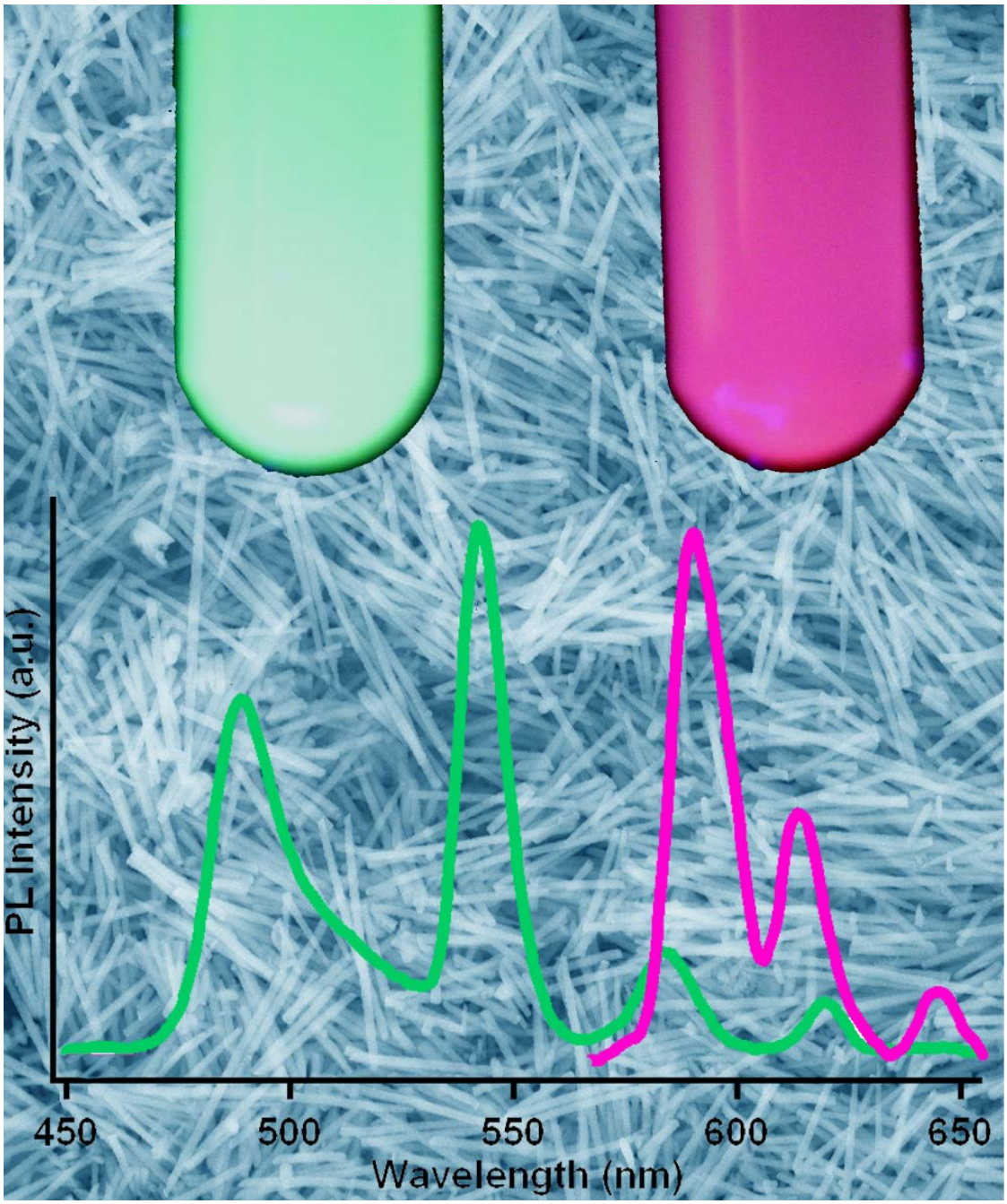

Figure 1.6 SEM image of as-prepared CaF_2 nanowires, and the PL spectra of rare-earth ion-doped CaF_2 nanowires, as well as the corresponding optical image.

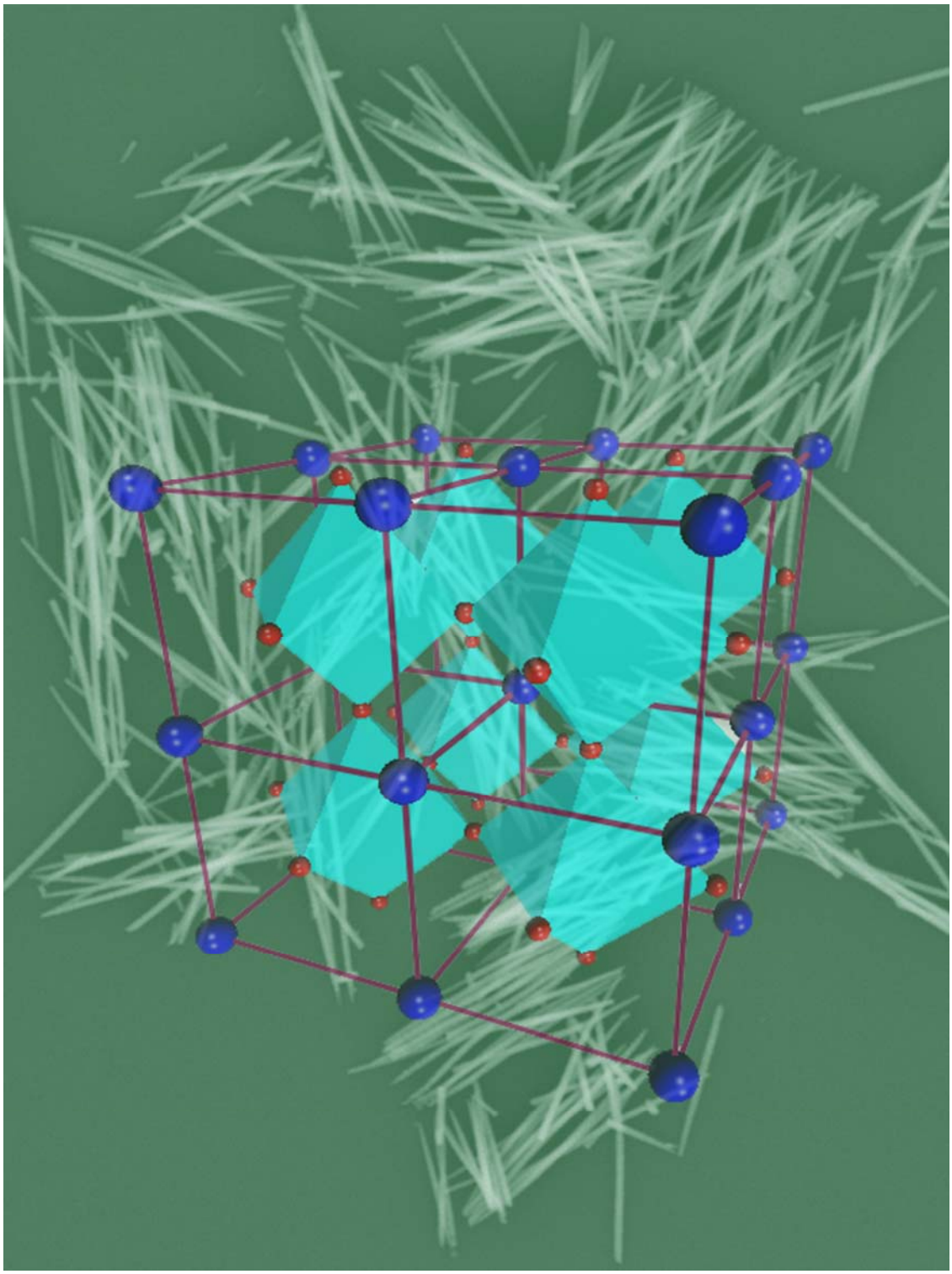

Figure 1.7 SEM image of as-prepared $KMnF_3$ nanorods and the corresponding perovskite atomic structure.

1.6.2 Solid solutions of various compositionally-defined single-crystalline alkaline-earth metal tungstate nanorods

Alkaline-earth-metal tungstates AWO_4 (Ca, Sr, Ba) represent an important family of inorganic, electrooptic materials with their distinctive scheelite structure and associated highly interesting physical properties such as excitonic luminescence, thermoluminescence, and stimulated Raman scattering (SRS). In fact, they are keenly sought as host materials for a wide range of technologically significant applications, including as phosphors, gas sensors, laser media, and optical fibers as well as components of electrochromic devices, amplifiers, diagnostic medical equipment, microwave systems, and the next generation of scintillator detectors. In this work, we seek to gain a fundamental understanding of how slight but controlled variations in the chemical composition of these scheelite materials may lead to favorable structure-property correlations in these systems. (Figure 1.8)

1.6.3 Multifunctional Doped Tungstate Nanorods

There is a high interest in developing versatile and flexible nanomaterials that are multifunctional, multicomponent, and multifaceted in their properties and, hence, potential applications. The idea is to create robust "smart" nanomaterials that can intrinsically and effectively respond to multiple, often disparate sets of external stimuli. In this work, we seek for the first time to merge the favorable properties of both classes of tungstates by incorporating Mn ions into the alkaline-earth metal tungstate scheelite matrix, thereby generating a separate family of novel materials endowed with both desirable luminescent as well as magnetic properties that mutually coexist within one structure without any evident property dilution. (Figure 1.9)

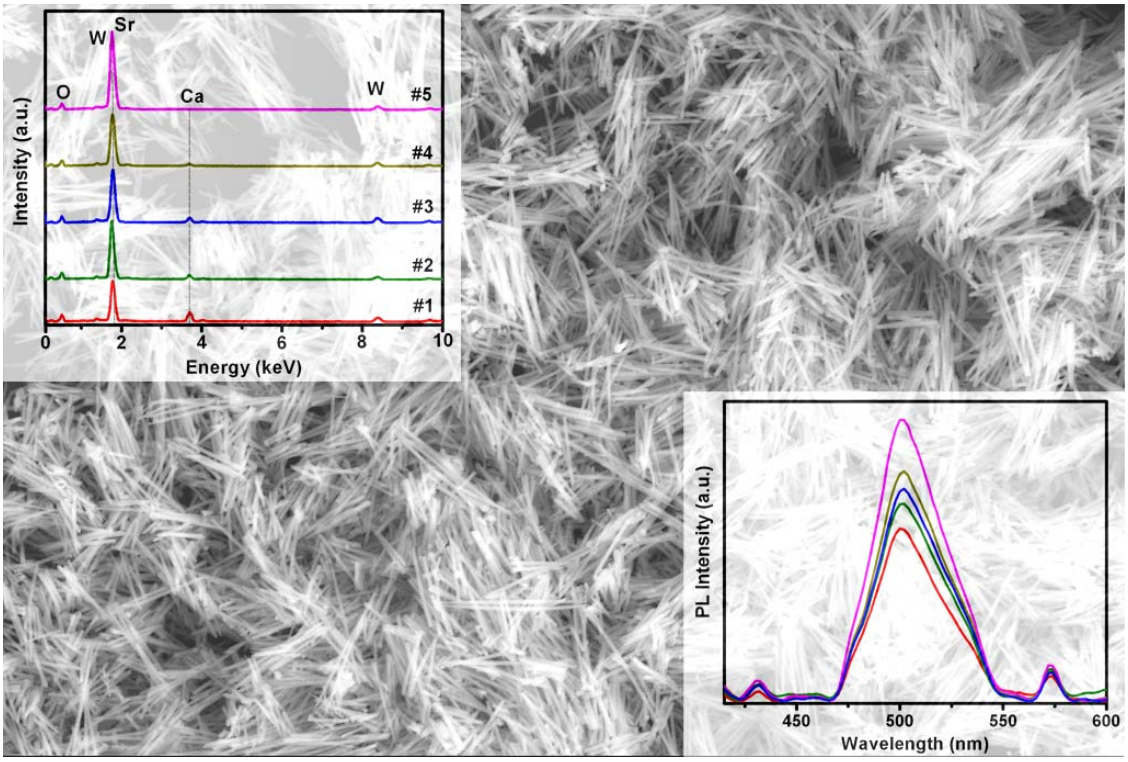

Figure 1.8 SEM image of as-prepared $CaWO_4$ nanorods, XRD patterns and PL spectra of solid solution $Sr_{1-x}Ca_xWO_4$ nanorod samples.

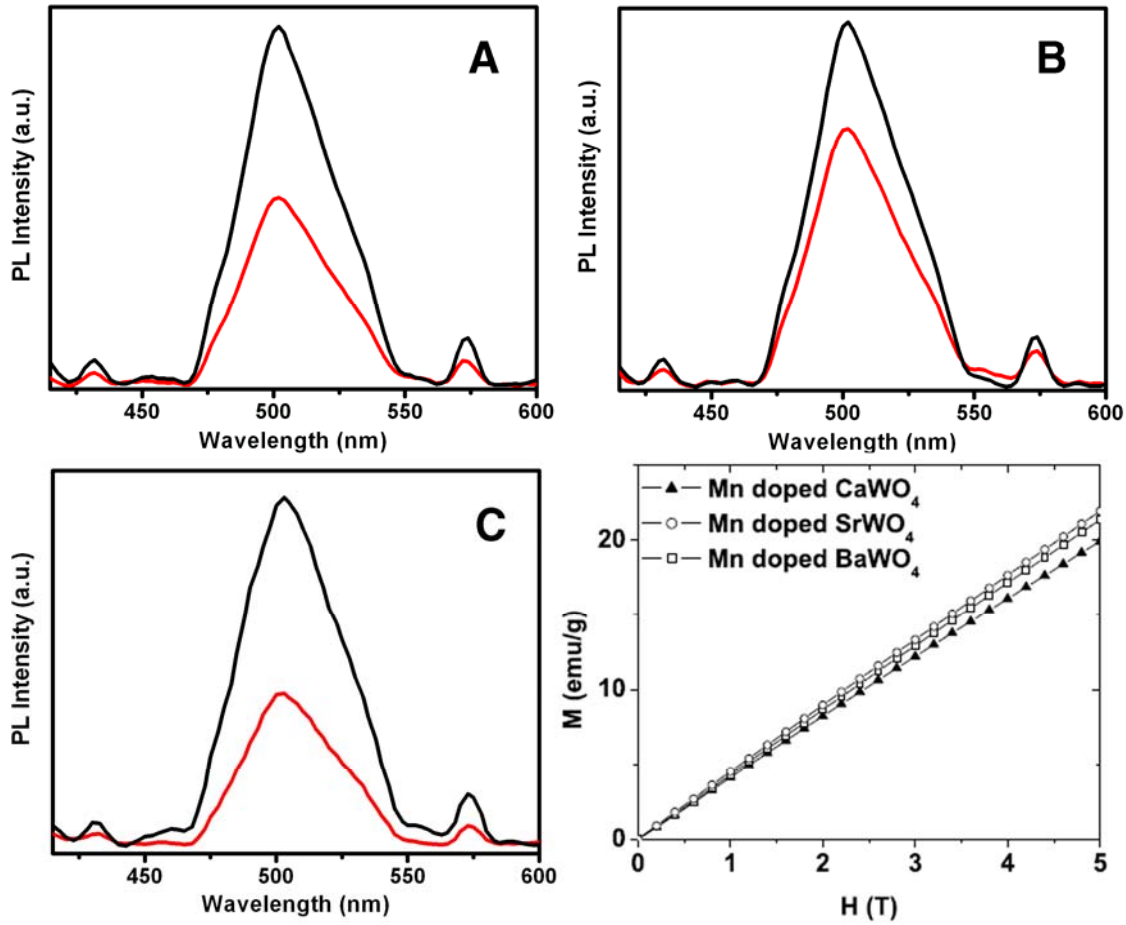

Figure 1.9 Photoluminescence spectra and SQUID data of Mn-doped alkaline-earth metal tungstate nanowires.

1.6.4 Semiconducting metal sulfide nanowires and their photocatalytic application

Semiconducting metal sulfide nanowires have been used as building blocks for a number of nanoscale energy conversion, photonic, and electro-optical devices (including field-effect transistors, light emitting diodes, logic gates, lasers, waveguides and solar cells), as well as electronic circuits. It would be desirable to develop a protocol that allows for a green, cost-effective methodology of metal sulfide 1D nanoscale synthesis without the need to sacrifice on sample quality, crystallinity, monodispersity, and purity. In this work, we have successfully demonstrated the validity of the template-directed method for the fabrication of CuS, PbS and CdS 1D nanostructures. (Figure 1.10)

1.6.5 Large-scale growth of high aspect ratio single-crystalline rare-earth phosphate nanowires and application for bioimaging

Rare-earth orthophosphate ($LnPO_4$) has played an important role as a biological label and probe. Phosphates show excellent chemical stability, long lifetime, high quantum yield, and low toxicity. Lanthanide probes also possess many distinctions, such as a sharp emission band and large Stokes shifts, so that the fluorescent signal can be detected far from the excitation wavelength with zero absorption, thereby improving sensitivity. Herein, we report the first demonstration of a room-temperature fabrication of ultrathin Tb-doped $CePO_4$ nanowires on a large scale, and their use as fluorescent labels for in vivo bioimaging. (Figure 1.11)

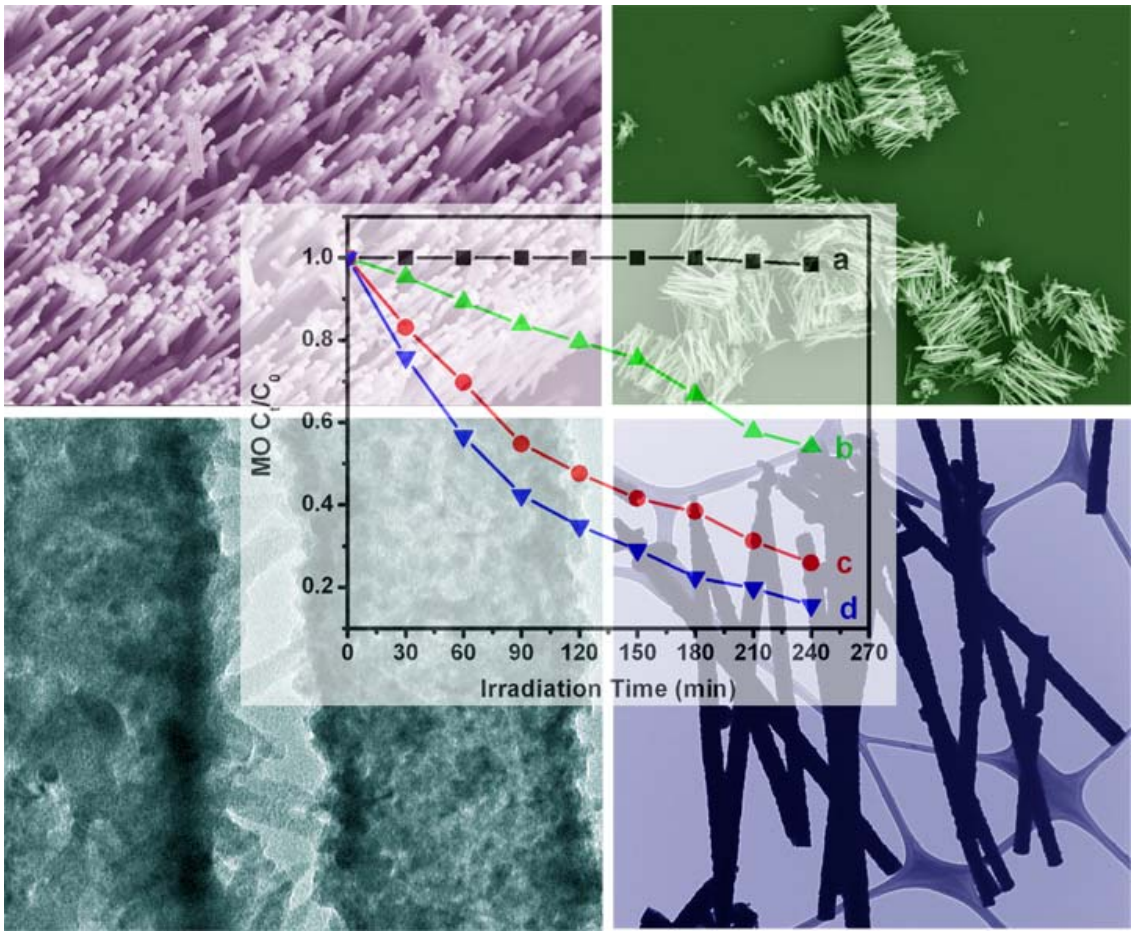

Figure 1.10 SEM and TEM images of semiconducting metal sulfide (CuS, PbS, and CdS) nanowires, as well as novel CdS cactus-like nanostructures. The center plot demonstrates the photocatalytic activity of CdS different morphologies.

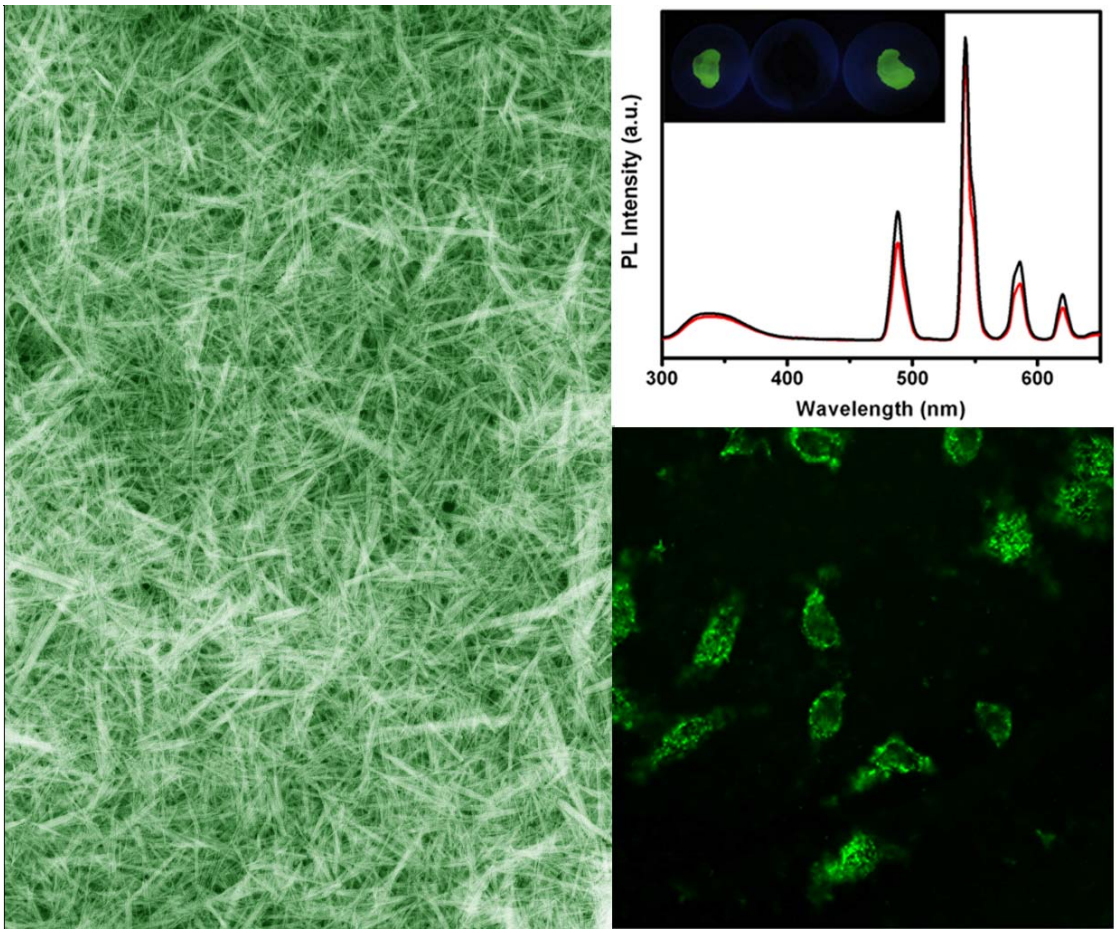

Figure 1.11 SEM image of as-prepared single-crystalline Tb-doped $CePO_4$ nanowires of high aspect ratio, PL spectra of the nanowires prior to (black) and after (red) redox cycles, as well as confocal fluorescence microscopy images of HeLa cells after incubation with fluorescent nanowires.

1.7 Nanomaterial Characterization Methods

After synthesis of the various systems of nanomaterials, a number of different characterization techniques have been applied to study their morphology, crystallinity, purity, phase and physical properties.

1.7.1 X-ray powder diffraction (XRD)

Crystallographic information on the resulting nanomaterials was obtained on a Scintag diffractometer, operating in the Bragg configuration using Cu Kα radiation (λ = 1.54 Å). XRD samples were generated by thorough grinding in ethanol using a mortar and pestle, followed by loading onto glass slides and subsequent drying in air. Diffraction patterns were collected between 10 and 80° (2-theta) at a scanning rate of 2° per minute with a step size of 0.02°. The range of 2-theta used was specific to certain samples. Parameters used for slit widths and accelerating voltage were identical for all samples.

1.7.2 X-ray photoelectron spectroscopy (XPS)

Pressed sample wafers were attached to stainless-steel holders using conductive double-sided tape and placed in the vacuum chamber of a Model DS800 XPS surface analysis system (Kratos Analytical Plc., Manchester, UK). The chamber was evacuated to a base pressure of ~5×10-9 torr (1 torr ~1.33 Pa). A hemispherical energy analyzer was used for electron detection. XPS spectra were first collected using a Mg Kα X-ray source at 80 eV pass energy and in 0.75 eV steps for each sample survey spectrum. As-obtained spectra were plotted and used to generate estimates of the atomic and weight concentrations of the elements indicated by the peaks present in the spectral data. High-resolution spectra were collected for the major elements detected to study their chemical bonding structures and were obtained at a pass energy of 40 eV and in 0.1 eV increments in order to correct for differential charging effects noted during data collection. High-resolution data were then peak fitted, plotted and tabulated to highlight the chemical species present for each major element detected.

1.7.3 Electron Microscopy

Scanning electron microscopy (SEM). The particle size and morphology of the resulting nanomaterials were initially characterized using a field emission SEM (Leo 1550) at accelerating voltages of 15 kV. This instrument was equipped with energy

dispersive X-ray spectroscopy (EDS). Specifically, the resulting nanomaterials were deposited onto Si wafers, which were then attached onto the surface of SEM brass stubs using a Cu tape. Samples were then conductively coated with gold by sputtering them for 10 seconds twice to minimize charging effects under standard SEM imaging conditions.

Transmission electron microscopy (TEM). Specimens for TEM and high-resolution TEM (HRTEM) were obtained by drying the resulting nanomaterial droplets from an ethanol dispersion onto a 300 mesh Cu grid coated with a lacey carbon film. TEM images were taken at an accelerating voltage of 120 kV on a Philip CM12 instrument. High resolution images were obtained on a JEOL 2010F HRTEM at an accelerating voltage of 200 kV. This instrument was equipped with an Oxford INCA EDS system with the potential of performing selected area electron diffraction (SAED) in order to further characterize individual nanomaterials.

1.7.4 Superconducting quantum interference device (SQUID)

Magnetization measurements were obtained using a magnetic property measurement system (MPMS) magnetometer. Powder samples of the resulting nanomaterials were pressed lightly, then loaded into a gel cap, and covered with silica wool. This was held within a uniform drinking straw, which was attached to the sample rod of the MPMS apparatus. Signals generated by measurements of an empty sample holder demonstrated that the holder assembly contributed <1% to the overall magnetic signal.

1.7.5 Optical Spectroscopy

UV-visible spectroscopy. UV-vis spectra were obtained at high resolution on a Thermospectronics UV1 spectrometer using quartz cells with a 10-mm path length. Specimens were sonicated in distilled water so as to yield homogenous dispersions. UV-vis absorption spectra were recorded using distilled water as a blank.

Photoluminescence (PL) spectroscopy. Samples for PL spectra were dispersed in deionized water and sonicated for a few minutes. Fluorescence data were obtained at room temperature on a Jobin Yvon Spex FluoroMax-4 instrument with a 10 s integration time. PL spectra for different nanostructures were measured at corresponding excitation wavelengths respectively.

Fourier transform infrared (FTIR) spectroscopy. FTIR spectra were obtained on a Nexus 670 (ThermoNicolet) equipped with a single-reflectance ZnSe ATR accessory, a KBr beam splitter, and a DTGS KBr detector. As-prepared solid powder samples were placed onto a ZnSe crystal, where data were taken with a reproducible pressure. A background correction was performed using the ZnSe crystal in the spectral range studied.

Raman spectroscopy. Specimens were prepared by depositing a droplet of the resulting nanomaterials from an ethanol dispersion onto a Si wafer. The spectra were acquired with a Raman micro spectrometer (Renishaw 1000, Drexel University Central Characterization Facility) using an Ar ion laser (514.5 nm) in back-scattering geometry. A 50x objective and low laser power density were chosen for irradiation of the sample and signal collection. The laser power was kept low enough to avoid heating of the samples by optical filtering and/or defocusing the laser beam at the samples surface. Spectra were collected in the range of 1000 to 100 cm^{-1} with a resolution of 1 cm^{-1}.

1.8 References

1. Iijima, S., *Nature* **1991,** *354*, 56.
2. Lieber, C. M., *MRS Bulletin* **2003,** *28*, 486.
3. http://www.science.doe.gov/bes/scale_of_things.html.
4. *Nanoscience, and Nanotechnology: Opportunities and Uncertainties. The Royal Society* **2004**.
5. *A special issue on nanoscale materials, Acc. Chem. Res.* **1999,** *32*.
6. Wang, Z. L., *Adv. Mater.* **2000,** *12*, 1295.
7. Huczko, A., *Appl. Phys. A* **2000,** *70*, 365.
8. Erhardt, D., *Nat. Mater.* **2003,** *2*, 509.
9. *Future Trends in Microelectronics: The Nano Millennium* **2002**.
10. Binning, G.; Rohrer, H.; Gerber, C.; Weibel, E., *Phys. Rev. Lett.* **1982,** *49*, 57.
11. Whitesides, G. M., *Nat. Biotech.* **2003,** *21*, 1161.
12. Rao, C. N. R.; Cheetham, A. K., *J. Mater. Chem.* **2001,** *11*, 2887.
13. Nirmal, M.; Brus, L., *Acc. Chem. Res.* **1999,** *32*, 407.
14. Colvin, V. L.; Schlamp, M. C.; Alivisatos, A. P., *Nature* **1994,** *370*, 354.

15. Klein, D. L.; Roth, R.; Lim, A. K. L.; Alivisatos, A. P.; McEuen, P. L., *Nature* **1997,** *389*, 699.

16. Phillips, J., *J. Appl. Phys.* **2002,** *91*, 4590.

17. Shipway, A. N.; Katz, E.; Willner, I., *ChemPhysChem* **2000,** *1*, 18.

18. Klimov, V. I.; Mikhailovsky, A. A.; Xu, S.; Malko, A.; Hollingsworth, J. A.; Leatherdale, C. A.; Eisler, H. J.; Bawendi, M. G., *Science* **2000,** *314*, 290.

19. Gates, S. M., *Chem. Rev.* **1996,** *96*, 1519.

20. Kaiser, N., *Appl. Optics* **2002,** *41*, 3053.

21. Poortmans, J.; Arkhipov, V., *Thin film solar cells: fabrication, characterization and applications. Wiley* **2006**.

22. Xia, Y.; Yang, P.; Sun, Y.; Wu, Y.; Mayers, B.; Gates, B.; Yin, Y.; Kim, F.; Yan, H., *Adv. Mater.* **2003,** *15*, 353.

23. Ghosh, S.; Sood, A. K.; Kumar, N., *Science* **2003,** *299*, 1042.

24. Chen, J.; Chen, S.; Zhao, X.; Kuznetsova, L. V.; Wong, S. S.; Ojima, I., *J. Am. Chem. Soc.* **2008,** *130*, 16778.

25. Collins, P. G.; Zettl, A.; Bando, H.; Thess, A.; Smalley, R. E., *Science* **1997,** *278*, 100.

26. Gadd, G. E., *Science* **1997,** *277*, 933.

27. Dillon, A. C., *Nature* **1997,** *386*, 377.

28. Hu, J.; Odom, T. W.; Lieber, C. M., *Acc. Chem. Res.* **1999,** *32*, 435.

29. Wang, J.; Gudiksen, M. S.; Duan, X.; Cui, Y.; Lieber, C. M., *Science* **2001,** *293*, 1455.

30. Hurst, S. J.; Payne, E. K.; Qin, L.; Mirkin, C. A., *Angew. Chem. Int. Ed.* **2006,** *45*, 2672.

31. Nutzenadel, C.; Zuttel, A.; Chartouni, D.; Schmid, G.; Schlapbach, L., *Eur. Phys. J. D* **2000,** *8*, 245.

32. Schwarz, J. A.; Contescu, C.; Contescu, A., *Chem. Rev.* **1995,** *95*, 477.

33. Rossetti, R.; Nakahara, S.; Brus, L., *J. Chem. Phys.* **1983,** *79*, 1086.

34. Alivisatos, A. P., *Science* **1996,** *271*, 933.

35. Robertson, D. H.; Brenner, D. W.; Mintmire, J. W., *Phys. Rev. B* **1992,** *45*, 12592.

36. Menon, V. P.; Matin, C. R., *Anal. Chem.* **1995,** *67*, 1920.

37. Buffat, P.; Borel, J.-P., *Phys. Rev.* **1976,** *13*, 2287.

38. Wu, Y.; Yang, P., *Adv. Mater.* **2001,** *13*, 520.

39. Quere, D.; Meglio, J.-M. D.; Brochard-Wyart, F., *Science* **1990,** *249*, 1256.

40. Postma, H. W. C.; Peepen, T.; Yao, Z.; Grifoni, M.; Dekker, C., *Science* **2001,** *293*, 76.

41. Kong, J.; Franklin, N. R.; Zhou, C.; Chapline, M. G.; Peng, S.; Cho, K.; Dai, H., *Science* **2000,** *287*, 622.

42. Liu, X.; Lee, C.; Zhou, C.; Han, J., *Appl. Phys. Lett.* **2001,** *79*, 3329.

43. Collins, P. G.; Arnold, M. S.; Avouris, P., *Science* **2001,** *292*, 706.

44. Zhang, Z.; Sun, X.; Dresselhaus, M. S.; Ying, J. Y., *Phys. Rev. B* **2000,** *61*, 4850.

45. Huang, Y.; Duan, X.; Wei, Q.; Lieber, C. M., *Science* **2001,** *291*, 630.

46. Lu, X.; Hanrath, T.; Johnston, K. P.; Korgel, B. A., *Nano Lett.* **2003,** *3*, 93.

47. Wang, J. F.; Gudiksen, M. S.; Duan, X.; Cui, Y.; Lieber, C. M., *Science* **2001,** *293*, 1455.

48. Huynh, W. U.; Dittmer, J. J.; Alivisatos, A. P., *Science* **2002,** *295*, 2425.

49. El-Sayed, M. A., *Acc. Chem. Res.* **2001,** *34*, 257.

50. Zhou, X. T.; Lai, H. L.; Peng, H. Y.; Au, F. C. K.; Liao, L. S.; Wang, N.; Bello, I.; Lee, C. S.; Lee, S. T., *Chem. Phys. Lett.* **2000,** *318*, 58.

51. Lee, C. J.; Lee, T. J.; Lyu, S. C.; Zhang, Y.; Ruh, H.; Lee, H. J., *Appl. Phys. Lett.* **2002,** *81*, 3648.

52. Cui, Y.; Wei, Q.; Park, H.; Lieber, C. M., *Science* **2001,** *293*, 1289.

53. Wong, E. W.; Sheehan, P. E.; Lieber, C. M., *Science* **1997,** *277*, 1971.

54. Burda, C.; X., C.; Narayanan, R.; El-Sayed, M. A., *Chem. Rev.* **2005,** *105*, 1025.

55. Hashmi, A. S. K.; Hutchings, G. J., *Angew. Chem. Int. Ed.* **2006,** *45*, 7896.

56. Xia, Y.; Rogers, J. A.; Paul, K. E.; Whitesides, G. M., *Chem. Rev.* **1999,** *99*, 1823.

57. Haruta, M.; Delmon, B., *J. Chim. Phys. Phys.-Chim. Biol.* **1986,** *83*, 859.

58. Givargizov, E. I., *Highly Anisotropic Crystals. Reidel, Dordrecht, The Netherlands* **1987**.

59. Song, J. H.; Messer, B.; Wu, Y.; Kind, H.; Yang, P., *J. Am. Chem. Soc.* **2001,** *123*, 9714.

60. Tong, H.; Zhu, Y.-J.; Yang, L.-X.; Li, L.; Zhang, L., *Angew. Chem. Int. Ed.* **2006,** *45*, 7739.

61. Pan, Z. W.; Dai, Z. R.; Wang, Z. L., *Science* **2001,** *291*, 1947.

62. Parthasarathy, R. V.; Martin, C. R., *Nature* **1992,** *369*, 298.

63. Zhang, G.; Lu, X.; Zhang, T.; Qu, J.; Wang, W.; Li, X.; Yu, S., *Nanotech.* **2006,** *17*, 4252.

64. Puntes, V. F.; Krishnan, K. M.; Alivisatos, A. P., *Science* **2001,** *291*, 2115.

65. Park, K. H.; Jang, K.; Kim, S.; Son, S. U., *J. Am. Chem. Soc.* **2006,** *128*, 14780.

66. Wang, X.; Li, Y., *J. Am. Chem. Soc.* **2002,** *124*, 2880.

67. Heath, J. R.; Legoues, F. K., *Chem. Phys. Lett.* **1993,** *208*, 263.

68. Hench, L. L.; West, J. K., *Chem. Rev.* **1990,** *90*, 33.

69. Schwuger, M.; Stickdom, K.; Schomacker, R., *Chem. Rev.* **1995,** *95*, 849.

70. Yu, S.-H., *Handbook of nanostructured biomaterials and thier applications in nanobiotechnology* **2005**.

71. Kovtyukhova, N. I.; Kelly, B. K.; Mallouk, T. E., *J. Am. Chem. Soc.* **2004,** *126*, 12738.

72. Kovtyukhova, N. I.; Mallouk, T. E.; Mayer, T. S., *Adv. Mater.* **2003,** *15*, 780.

73. Mallouk, T. E., *Science* **2001,** *291*, 443.

74. Hulteen, J. C.; Martin, C. R., *J. Mater. Chem.* **1997,** *7*, 1075.

75. Schmid, G., *J. Mater. Chem.* **2002,** *12*, 1231.

76. Becker, A.; Becker, W.; Marxen, J. C.; Epple, M., *Z. Anorg. Allg. Chem.* **2003,** *629*, 2305.

77. Schwarz, K.; Epple, M., *Chem. Eur. J.* **1998,** *4*, 1898.

78. Grassmann, O.; Lobmann, P., *Biomaterials* **2004,** *25*, 277.

79. Lu, Q.; Gao, F.; Komarneni, S.; Mallouk, T. E., *J. Am. Chem. Soc.* **2004,** *126*, 8650.

80. Martin, C. R., *Science* **1994,** *266*, 1961.

81. Martin, C. R., *Chem. Mater.* **1996,** *8*, 1739.

82. Fleisher, R. L.; Price, P. B.; Walker, R. M., *Nuclear tracks in solids. University of California Press, Berkeley, CA* **1975**.

83. Cao, H.; Xu, Y.; Hong, J.; Liu, H.; Yin, G.; Li, B.; Tie, C.; Xu, Z., *Adv. Mater.* **2001,** *13*, 1393.

84. Gao, T.; Meng, G.; Zhang, J.; Sun, S.; Zhang, L., *Appl. Phys. A* **2002,** *74*, 403.

85. Lei, Y.; Zhang, L. D.; Meng, G. W.; Li, G. H.; Zhang, X. Y.; Liang, C. H.; Chen, W.; Wang, S. X., *Appl. Phys. Lett.* **2001,** *78*, 1125.

86. Sapp, S. A.; Mitchell, D. T.; Martin, C. R., *Chem. Mater.* **1999,** *26*, 3264.

87. Martin, C. R., *Acc. Chem. Res.* **1995,** *28*, 61.

88. Lakshmi, B. B.; Dorhout, P. K.; Martin, C. R., *Chem. Mater.* **1997,** *9*, 857.

89. Limmer, S. J.; Seraji, S.; Wu, Y.; Chou, T. P.; Nguyen, C.; Cao, G. Z., *Adv. Funct. Mater.* **2002,** *12*, 59.

Chapter II Single-Crystalline Alkaline-Earth Metal Binary Fluoride Nanowires and Perovskite Ternary Fluoride Nanorods

2.1 Introduction

As a class of materials, solid inorganic fluorides possess a number of interesting properties such as electron-acceptor behavior, a large optical transmission domain, high resistivity, and anionic conductivity.[1] Not surprisingly, fluorides have found wide applicability as components of high-density optical devices, lenses, biological labels, sensors, and insulators.[2-5] In addition, fluorides doped with rare-earth ions such as Eu^{+3}, Nd^{+3}, and Ho^{+3}, have also been reported to display unique luminescence properties with correspondingly useful applications in diagnostics, lasing, solid-state light emitters, light amplification, optical telecommunication, and upconversion.[6-8] It is reasonable to expect that with the rapid shrinkage in the size of electronic and optical devices, nanoscale fluorides may play an important role in a variety of technological applications.[9-11]

In general, the preparation of novel nanomaterials with control of size, shape, and morphology continues to be actively pursued because of fundamental scientific considerations. At the same time, the potentially broad applicability and high technological promise of these nanomaterials arises from their intrinsically intriguing physicochemical properties which are expected to be enhanced as compared with those of the bulk. Specifically, the study of 1D nanostructures, including nanowires, nanobelts, nanorods, and nanotubes, is of fundamental interest because of their singular properties associated with quantum confinement and low dimensionality. In particular, anisotropic 1D systems represent the smallest dimension structures that can be used for the efficient transport of electrons and optical excitations. As such, they have potential applications as building blocks for the assembly of nanoscale electronic, optoelectronic, and sensing devices.[12] Hence, the problem of devising convenient synthesis methods to produce chemically well-defined, monodisperse, single-crystalline nanostructures, with

controllable size, shape, and morphology using environmentally friendly protocols remains a vital challenge in nanoscale chemistry.

Whereas prior efforts have generally focused on carbon nanotubes, quantum dots, metallic nanoparticles, as well as metal oxide nanostructures, the preparation of low-dimensional nanoscale alkaline-earth metal fluorides, including barium fluoride, strontium fluoride, and calcium fluoride, is at a nascent stage. To the best of our knowledge, there have not been any reported syntheses of CaF_2 and SrF_2 1D nanostructures, except for their 0D nanoparticulate formulations.[13-15] Similarly, literature on nanoscale barium fluoride has focused almost exclusively on nanoparticulate motifs;[2, 3, 5] high aspect ratio (> 1000) BaF_2 whiskers have been synthesized using a microemulsion- mediated hydrothermal method.[10] Therefore, the development of facile, mild, and effective approaches for generating size-controllable 1D fluoride nanostructures remains a significant challenge.

What is less known is that ternary metal fluorides, possessing cubic perovskite structures with a chemical formula of $AMnF_3$ (A = K, NH_4, Rb, Tl, Cs), are antiferromagnetic and that these materials have generated considerable interest due to their exceptional magnetic, piezoelectric, and photoluminescent properties.[16-18] In fact, this family of cubic perovskites provides an excellent example of simple cubic Heisenberg antiferromagnets with spin S = 5/2.[19] A good deal of the research into magnetic nanostructures has been associtated with ferro- and ferrimagnetic materials. Antiferromagnetic compounds are also of great technological importance as they are responsible for the exchange-bias (EB) effect,[18] which is widely used in state-of-the-art magnetic storage devices. Their relevant applications include but are not limited to the field of giant magnetoresistant (GMR) materials.

Regarding previous work with these materials, to the best of our knowledge, whereas nanoscale motifs of $KMnF_3$ and NH_4MnF_3 have been produced, their one-dimensional (1D) nanostructured analogues have not as yet been fabricated.[20-23] In terms of NH_4MnF_3, nanocrystallites measuring 10 to 60 nm have been synthesized using a microemulsion technique with size control obtained by varying aqueous phase content, salt concentration, synthesis temperature, and mixing time of reagents.[20] In addition,

(100)-oriented NH_4MnF_3 perovskites with different morphologies have been synthesized in situ using an organic template.[21] $KMnF_3$ nanoparticles, measuring ~68 nm, have been generated using a reverse micelle technique and self-assembled into periodic arrays.[22] By contrast, comparatively little work, with the exception of a solvothermal synthesis of acicular $KMnF_3$ nanostructures at 160 °C,[23] has been performed on the fabrication and characterization of 1D structures of ternary metal fluoride nanorods.

As discussed in Chapter I, whereas conventional templating procedures typically generate polycrystalline products as a result of the necessity of additional annealing steps at high temperature, we have recently developed a modified template-synthesis technique, enabling us to prepare a family of single-crystalline nanorods. In this Chapter, we report on the successful generalization of this synthetic approach to the synthesis of nanowires of not only binary alkaline-earth metal fluorides but also more complex perovskite ternary fluorides.

2.2 Experimental Section

2.2.1 Materials Preparation

Commercially available polycarbonate membranes (Whatman Co., UK) used in this study contain pore sizes of 50, 100, and 200 nm diameter, respectively, with a thickness of ca. 6 μm. These polycarbonate filters contain track-etched channels. Pores were randomly distributed across the filter membranes, and pore densities were quoted as approaching 3×10^8 pores cm^{-2}. In order to avoid air-bubble formation on their surfaces, the membranes were prehydrated by immersion and sonication in a small volume of distilled, deionized water for a few minutes. Subsequently, the membrane was placed between the two arms of a U-shaped tube.

To limit unwanted particle formation and deposition onto the exterior of our polycarbonate templates, we sought to ensure that the nanowire products were being selectively fabricated within the inner pores only. To this end, we used microcontact printed octadecyltetrachlorosilane (OTS) self-assembled monolayers as passivation layers on the external surfaces of polycarbonate membranes.[24] Hence, prior to mounting of the polymeric membrane templates between the two halves of the U-shaped tube, both sides

of the polycarbonate membranes were gently pressed with a homemade polydimethylsiloxane stamp, which had been initially inked with a 10 mM hexane solution of OTS and subsequently dried with nitrogen.

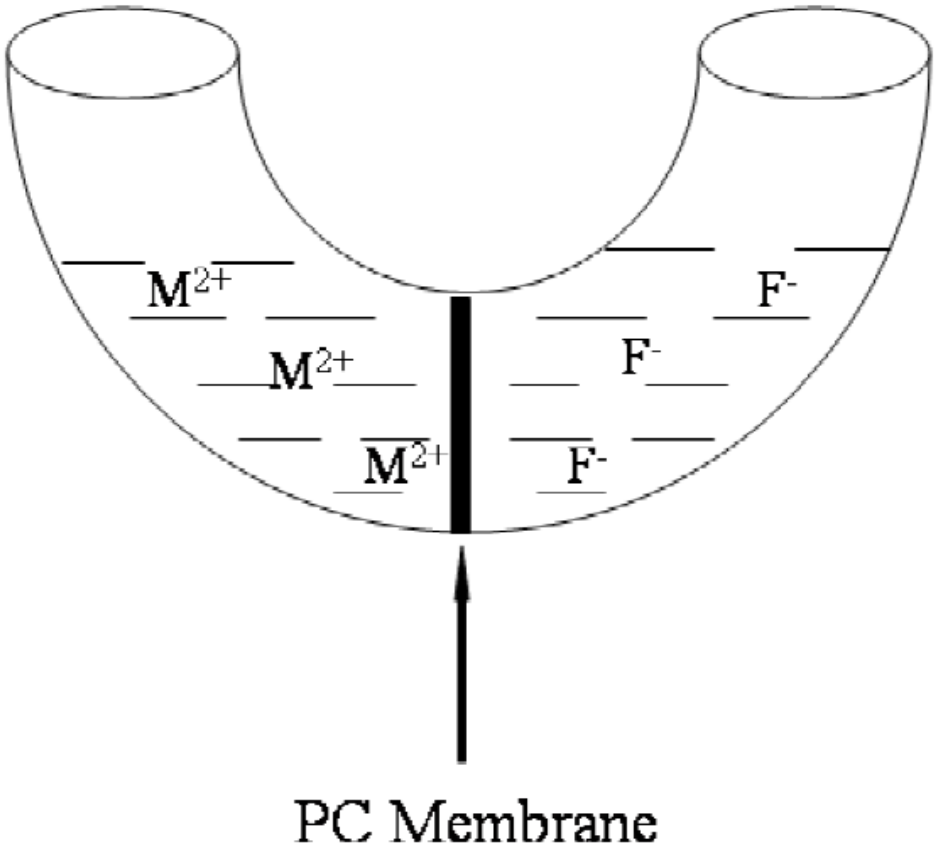

Figure 2.1 Schematic of the experimental setup used to synthesize alkaline earth metal fluoride nanowires. The polycarbonate membranes used in this work had pore diameters of 50, 100 and 200 nm, respectively.

In a typical synthesis of alkaline-earth metal binary fluoride nanowires, each half cell was filled with a solution of 0.25M NH_4F and either 0.125 M $CaCl_2$, $SrCl_2$, or $Ba(NO_3)_2$ solutions to generate calcium fluoride, strontium fluoride and barium fluoride nanowires, respectively (Figure 2.1). After immersion times of up to 12 h at room temperature, the polycarbonate membrane was detached and thoroughly washed with deionized water and subsequently dissolved in the presence of methylene chloride. Upon washing, alkaline-earth metal fluoride nanowires were collected using centrifugation.

Regarding the preparation of perovskite ternary fluoride nanorods, one of the two half cells was filled with $MnCl_2$ solution, and the other half cell contained a solution of either KF or NH_4F, so as to generate $KMnF_3$ and NH_4MnF_3 nanorods, respectively (Figure 2.2). The system was then left unperturbed for an incubation period of up to 3 days at room temperature. Pursuant to immersion, the polycarbonate membrane was detached, sonicated for ~2 min to remove unwanted particles on the surface, and thoroughly washed with distilled water, prior to dissolution with methylene chloride. As-prepared ternary metal fluoride nanorods were collected from solution by centrifugation after washing with aqueous solvents.

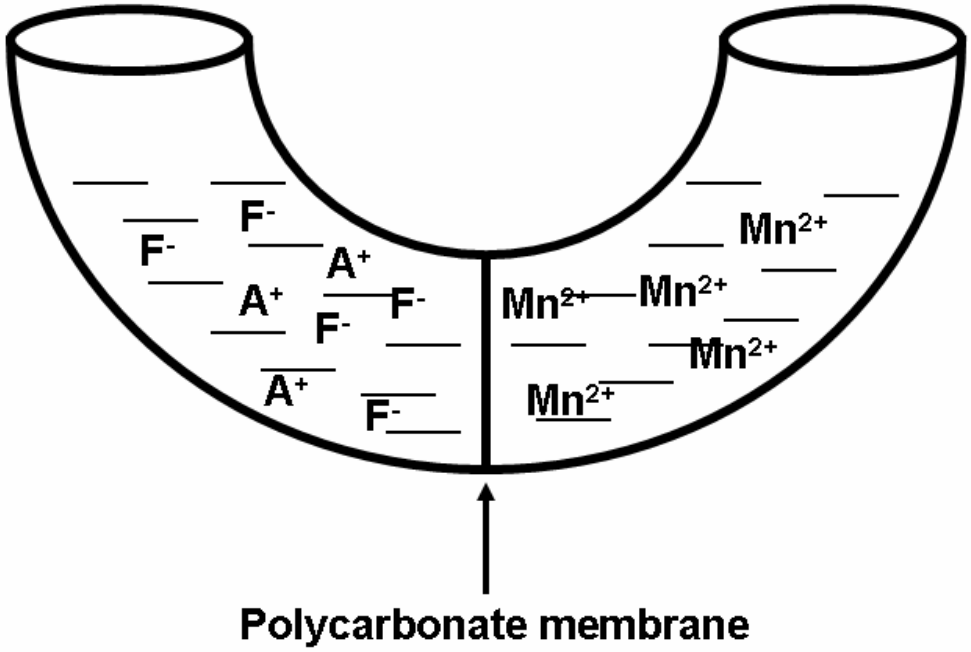

Figure 2.2 Schematic of the experimental setup used to synthesize complex fluoride nanorods. A^+ represents either K^+ or NH_4^+ ions, respectively. Polycarbonate membranes used in this work maintained pore diameters of 50, 100, or 200 nm.

2.2.2 Materials Characterization

X-ray Powder Diffraction See Section 1.7.1.

Electron Microscopy See Section 1.7.3.

Optical Spectroscopy See Section 1.7.5.

Magnetic Measurements See Section 1.7.4.

2.3 Results and Discussion

2.3.1 Alkaline-Earth Metal Binary Fluoride Nanowires

The purity and crystallinity of as-prepared alkaline-earth metal fluoride samples were characterized using powder X-ray diffraction (XRD). Figure 2.3 shows diffraction patterns collected from as-prepared samples of CaF_2, SrF_2, and BaF_2 in the 2θ range of 10 to 80 degrees. Very little if any impurity peaks are present. All of the diffraction peaks in Figure 1A can be readily indexed to a pure face-centered cubic phase [space group: Fm3m (225)] of CaF_2 with a calculated lattice constant a = 5.435 Å, which is in good agreement with the literature value of a = 5.4355 Å (Joint Committee on Powder Diffraction Standards (JCPDS) 77-2096). Similarly, diffraction peaks in Figure 1B can be ascribed to a pure face-centered cubic phase [space group: Fm3m (225)] of SrF_2 with an accompanying lattice constant a = 5.802 Å comparable to the corresponding literature value of a = 5.800 Å (JCPDS 06-0262). Finally, diffraction peaks in Figure 1C have been assigned to a face-centered cubic phase [space group: Fm3m (225)] of BaF_2 with a lattice constant a = 6.198 Å, a value consistent with the accepted value of a = 6.196 Å (JCPDS 85-1341) for this material.

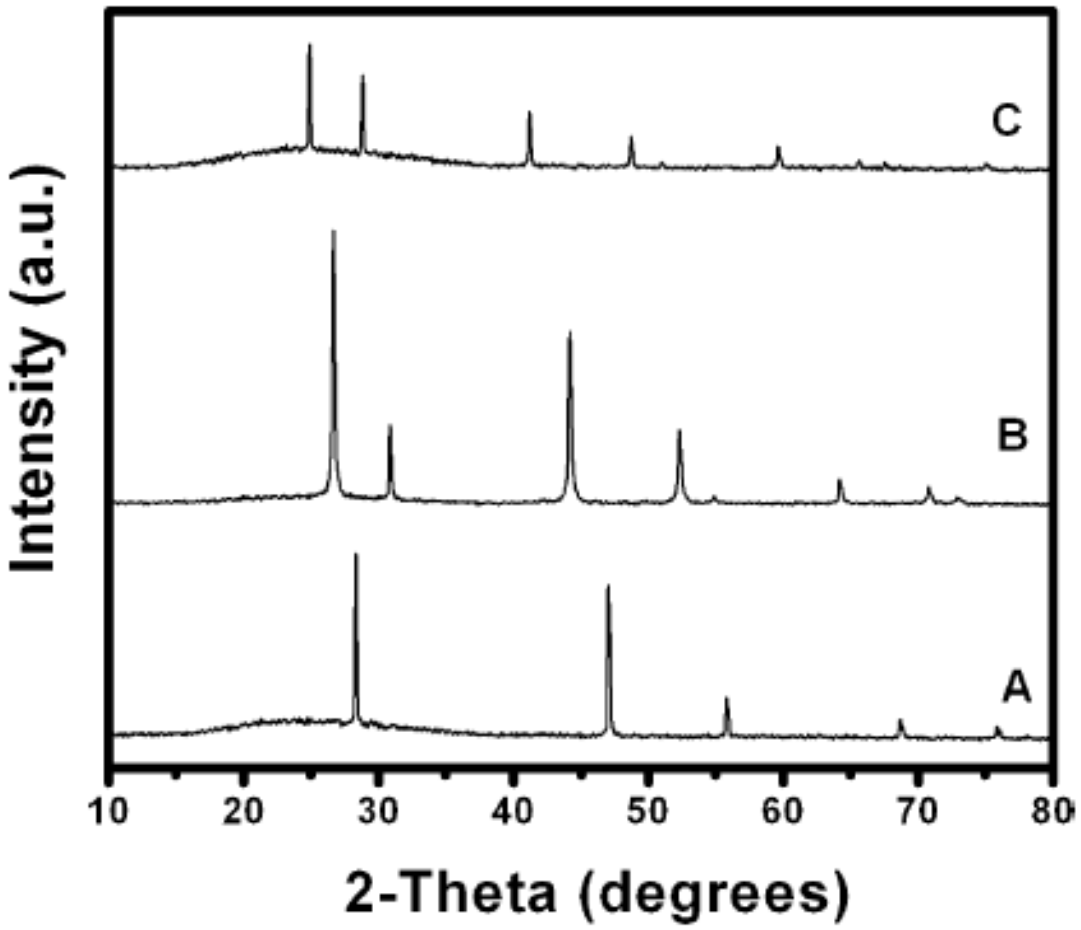

Figure 2.3 XRD patterns of as-prepared samples, prepared using polycarbonate membranes with pore sizes of 200 nm diameter: (A) CaF_2, (B) SrF_2, and (C) BaF_2 nanowires.

The size and morphology of as-synthesized alkaline-earth metal fluoride nanowires were initially examined using field-emission scanning electron microscopy (FE-SEM) and transmission electron microscopy (TEM). Typical SEM and TEM images, as shown in Figure 2.4A and B, respectively, reveal that as-prepared CaF_2 products, which were fabricated using polycarbonate membranes with pore sizes as small as 50 nm, consist of straight nanowires with a uniform, homogeneous size along their axis direction. The diameters of the CaF_2 nanowires obtained were in the range of 50 ± 5 nm, based on the 50 nm pore sizes of the polycarbonate membranes used. Measured lengths of CaF_2 nanowires varied from one to several micrometers. Figure 2.4C and D shows representative SEM and TEM images of SrF_2 nanowires, respectively, derived from the 100 nm pore size of the polycarbonate membranes used as templates. These images suggest the reproducible synthesis of straight and crystalline SrF_2 nanowires with a diameter range of 80 to 110 nm and a length range of 2 to 3 μm. Representative SEM and TEM images of BaF_2 nanowires, grown in polycarbonate membranes with 200 nm pore sizes, are depicted in Figure 2.4E and F, respectively. The microscopic images show the presence of dispersed individual nanowires as well as of bundled, aggregated species. As-prepared nanowires possess diameters ranging from 175 to 200 nm and lengths of 2 to 3.5 μm. These nanowires maintain a uniform diameter around 200 nm throughout their entire length; surfaces of these structures are smooth over much of their lengths, with the presence of relatively few if any extraneous particulate debris.

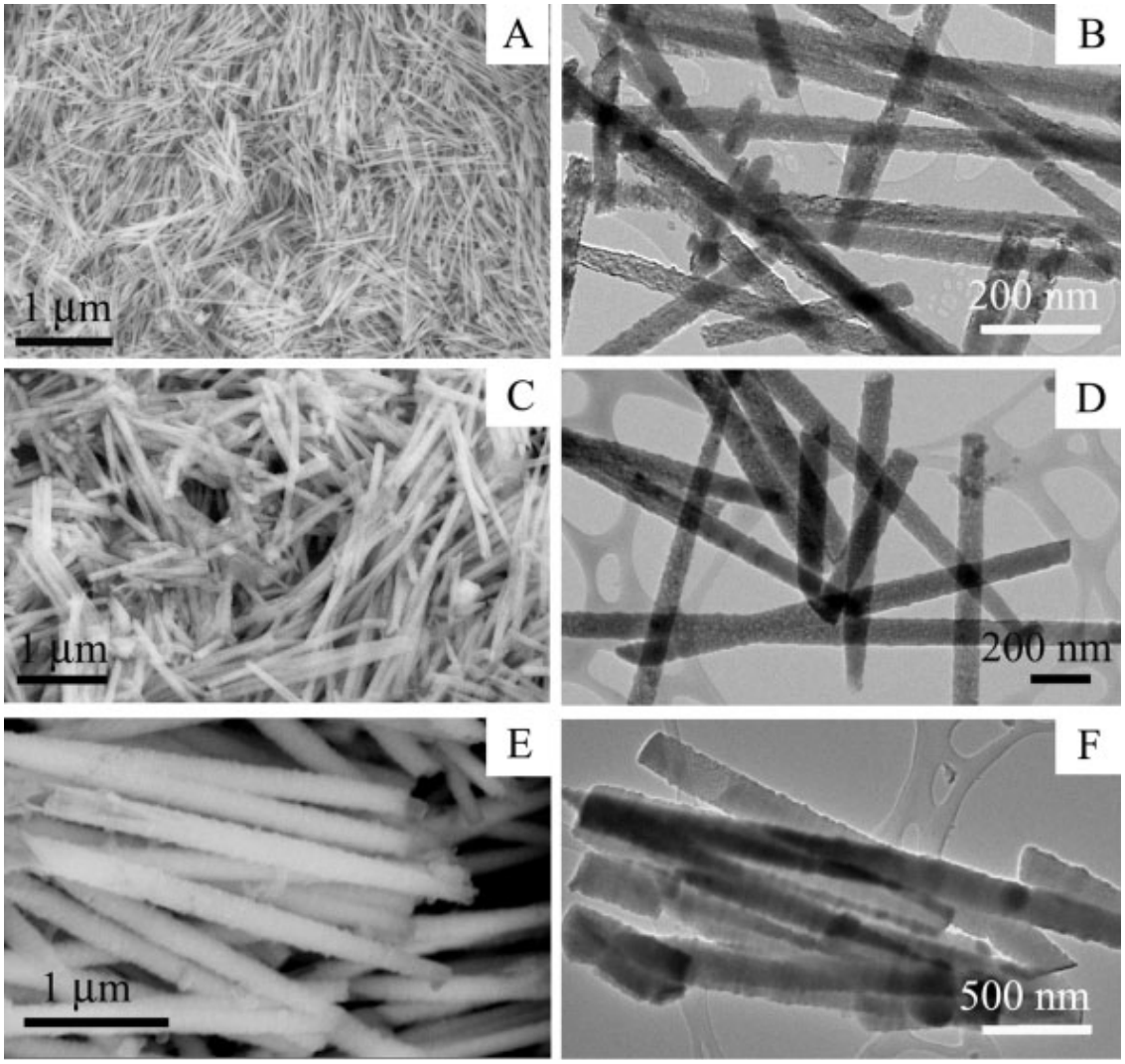

Figure 2.4 (A, B) Typical SEM and TEM images, respectively, of CaF_2 nanowires prepared using polycarbonate membranes with 50 nm pore sizes. (C, D) Representative SEM and TEM images, respectively, of SrF_2 nanowires prepared using polycarbonate membranes with 100 nm pore diameters. (E, F) Typical SEM and TEM images, respectively, of BaF_2 nanowires generated using polycarbonate membranes with pore diameters measuring 200 nm.

It is noteworthy that SEM and TEM images were obtained from randomly selected areas of the sample, and as such, are representative of the overall sizes and shapes of our as-generated alkaline-earth metal fluoride nanowires. Moreover, energy-dispersive X-ray spectroscopy (EDS) data, taken during SEM analysis, revealed signals associated with either Ca, Sr, or Ba, as well as F, that is, elemental signatures (Figure 2.5) expected of CaF_2, SrF_2, and BaF_2, respectively.

All of the data presented suggest that as-prepared alkaline earth metal fluoride nanowires are monodisperse with controllable morphology. In other words, the ambient synthesis of straight, crystalline wirelike structures is possible using a modified template-directed method without the need for sophisticated experimental setups. Moreover, the shapes and sizes of these fluoride nanowires accurately replicated the interior pore structure as well as the pore lengths and diameters of the polycarbonate templates from whence they were generated. Whereas nanowires with expected lengths of several micrometers were routinely noted, shorter fluoride nanowires were also observed from TEM images; the latter could be attributed to localized fracturing, occurring during the sonication step employed prior to the preparation of the TEM samples.

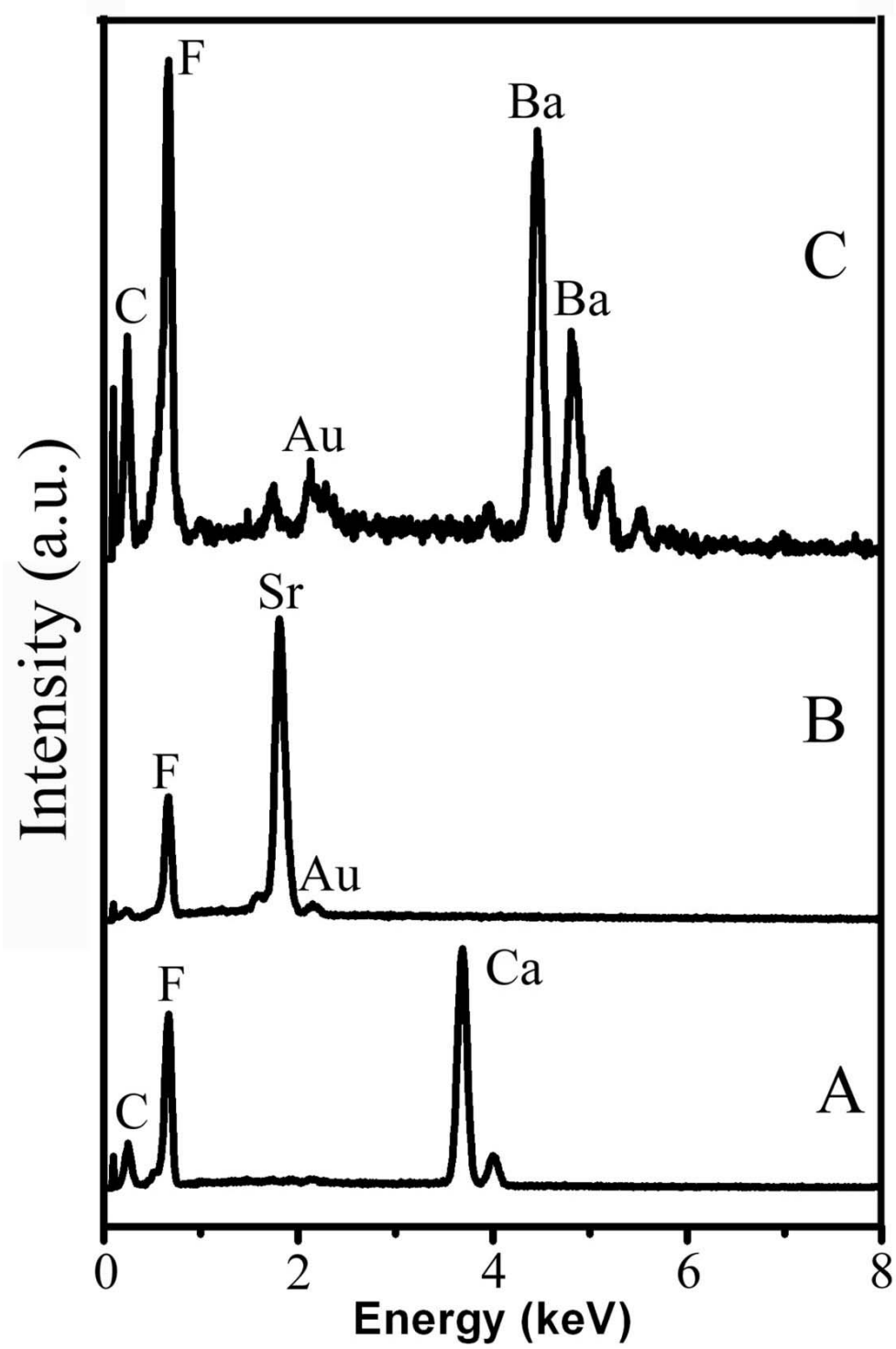

Figure 2.5 EDS data of as-synthesized alkaline earth metal fluoride nanowires, corresponding to SEM images shown in Figure 2A, 2C, and 2E, respectively. (A) CaF_2, (B) SrF_2 and (C) BaF_2. The C and Au peaks originate from the conductive carbon tape and gold coating, respectively.

To provide additional details about the crystallographic structure and chemical composition of as-prepared fluoride nanostructures, individual fluoride nanowires were investigated using high-resolution TEM (HRTEM), selected area electron diffraction (SAED), as well as EDS. Figure 2.6A shows a randomly chosen individual CaF_2 nanowire generated from polycarbonate membranes with a 50 nm pore size. Localized chemical composition analysis by EDS from a number of selected regions along the nanowires (Figure 2.6B) confirms that the chemical signatures associated with the product are essentially identical within experimental accuracy and that the nanowires are composed of the elements Ca and F. The Cu signal arises from the TEM grid. Figure 2.6C shows the SAED pattern taken from a portion of a single CaF_2 nanowire shown in Figure 2.6A. The presence of sharp diffraction spots, as opposed to an amorphous ring, strongly supports the formation of single-crystalline CaF_2 nanowires. The pattern has been indexed to the reflection of a face-centered cubic CaF_2 structure, in good agreement with the XRD results presented above. Moreover, SAED patterns obtained from different positions along the same nanowire structure have been found to be essentially identical. In Figure 2.6D, a representative HRTEM image of a part of an individual CaF_2 nanowire, initially outlined in Figure 2.6A, is displayed. These data further confirm that the CaF_2 nanowire is single crystalline, without any obvious defects or dislocations. The 2D lattice fringes reveal that the nanowire is structurally uniform with interplanar spacings of about 3.06 Å and 2.01 Å, corresponding to the (111) and (220) planes, respectively, of bulk crystalline CaF_2. These findings are consistent with observations from the XRD pattern data.

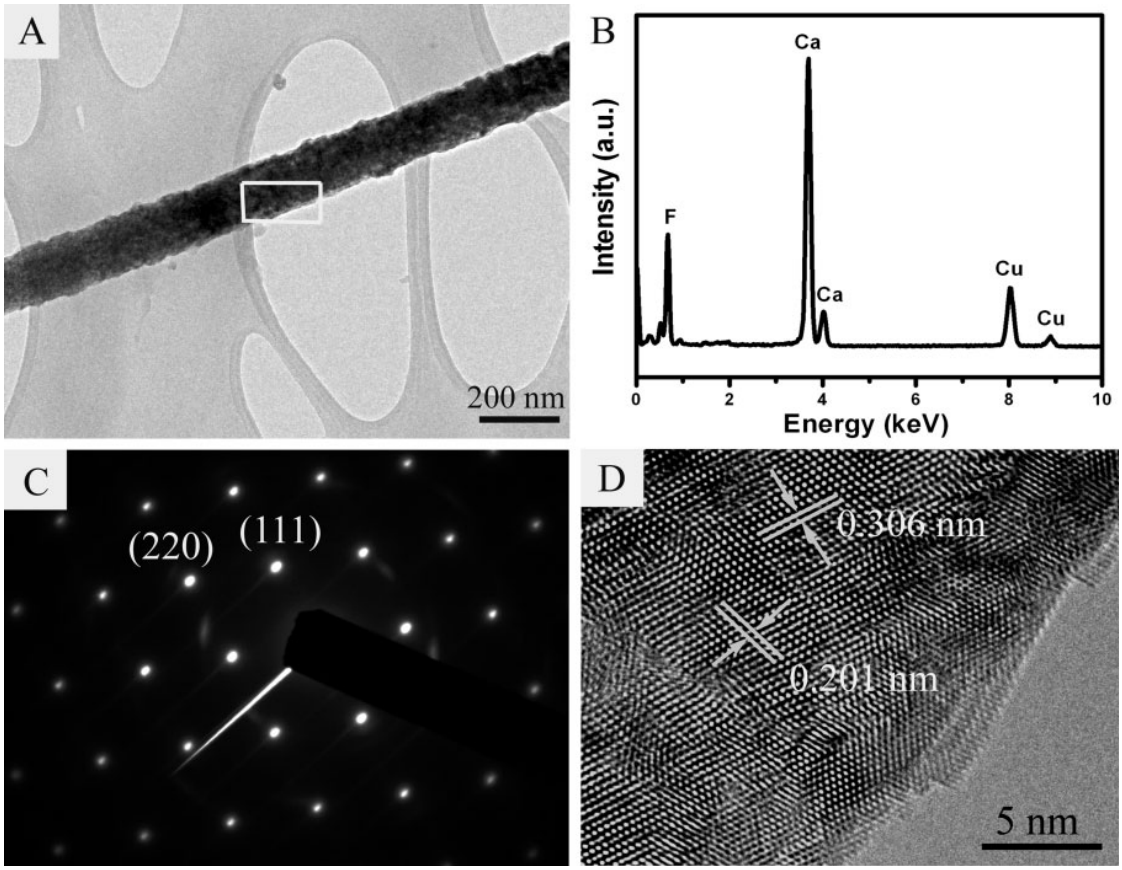

Figure 2.6 (A) TEM image of a single CaF_2 nanowire. (B) EDS spectrum of as-prepared CaF_2 nanowires. The Cu peaks originate from the TEM grid. (C, D) SAED pattern and HRTEM image of a representative section of a CaF_2 nanowire, as defined by the white rectangle in (A).

The corresponding structural and chemical analyses from HRTEM data of as-prepared SrF_2 and BaF_2 nanowires are shown in Figures 2.7 and 2.8, respectively. The slight surface roughness, as determined from HRTEM images, of our as-prepared fluoride nanowires likely reflects local differences in smoothness of the inner surfaces of polycarbonate.

The key to our fabrication technique (Figure 2.1) is the placement of membranes within a double-diffusion setup, which enables the continuous flow of precursor ions into spatially confined membrane pores. We propose that single crystals of nanoscale fluoride materials are derived from isolated, disparate, and multiple nucleation sites (consisting of MF_2 nuclei generated via the reaction between M^{2+} and F^-), which then grow by extension through the porous network. Continued growth then occurs at the particle surface at a rate limited by ion availability, until the crystal impinges on the polycarbonate template surface, which ultimately limits further growth. Hence, due to the spatially constrained volume defined by the presence of the template itself, nanowires instead of nanoparticles are formed owing to the growth environment conducive to these 1D structures. In effect, the growth of our nanowires within the confinement of polymeric membranes is analogous to the precipitation of single crystals of calcium carbonate and calcium phosphate within the geometric confinement of gels, micelles, chitin scaffolds, and collagen matrices.

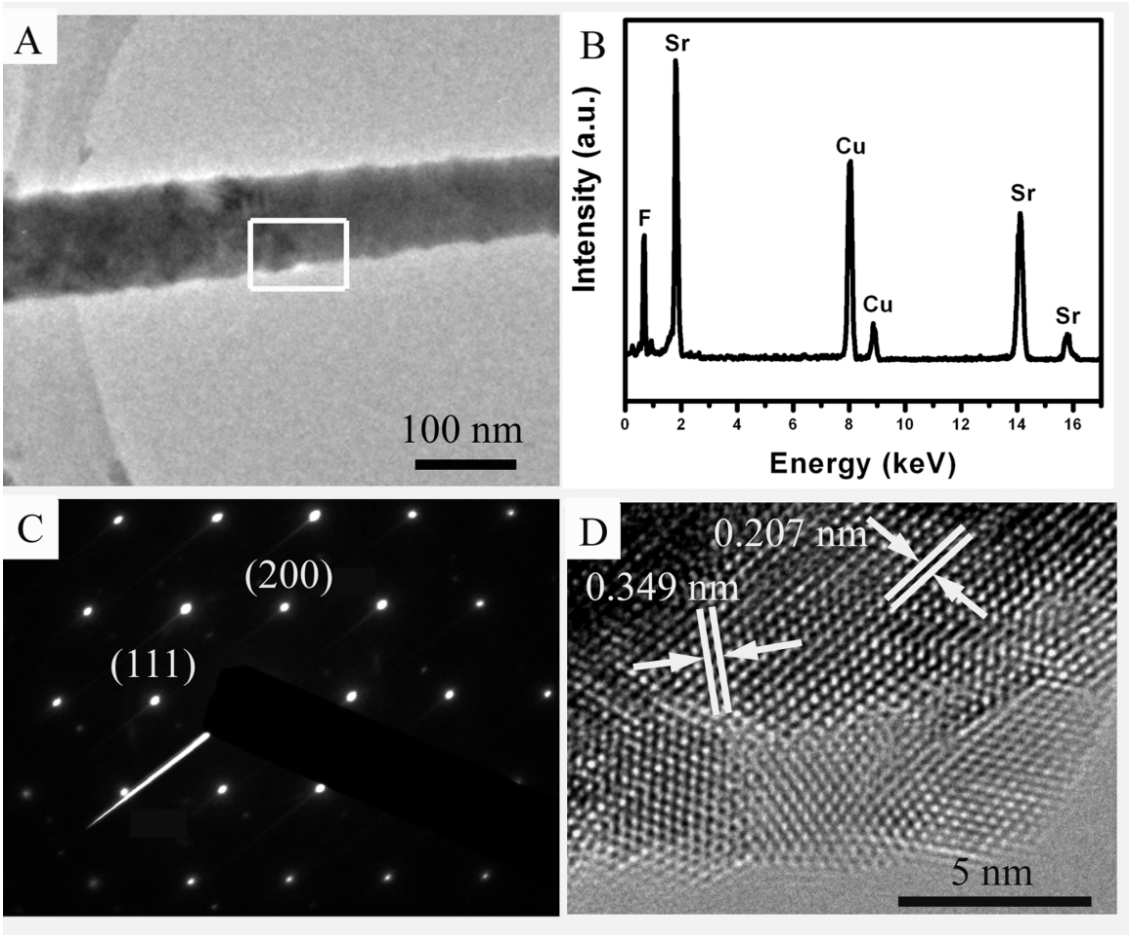

Figure 2.7 (A) TEM image of a single SrF_2 nanowire. (B) EDS spectrum of as-prepared SrF_2 nanowires. The Cu peaks originate from the TEM grid. (C) and (D) SAED pattern and HRTEM image of a representative part of a SrF_2 nanowire, as defined by the white square in (A).

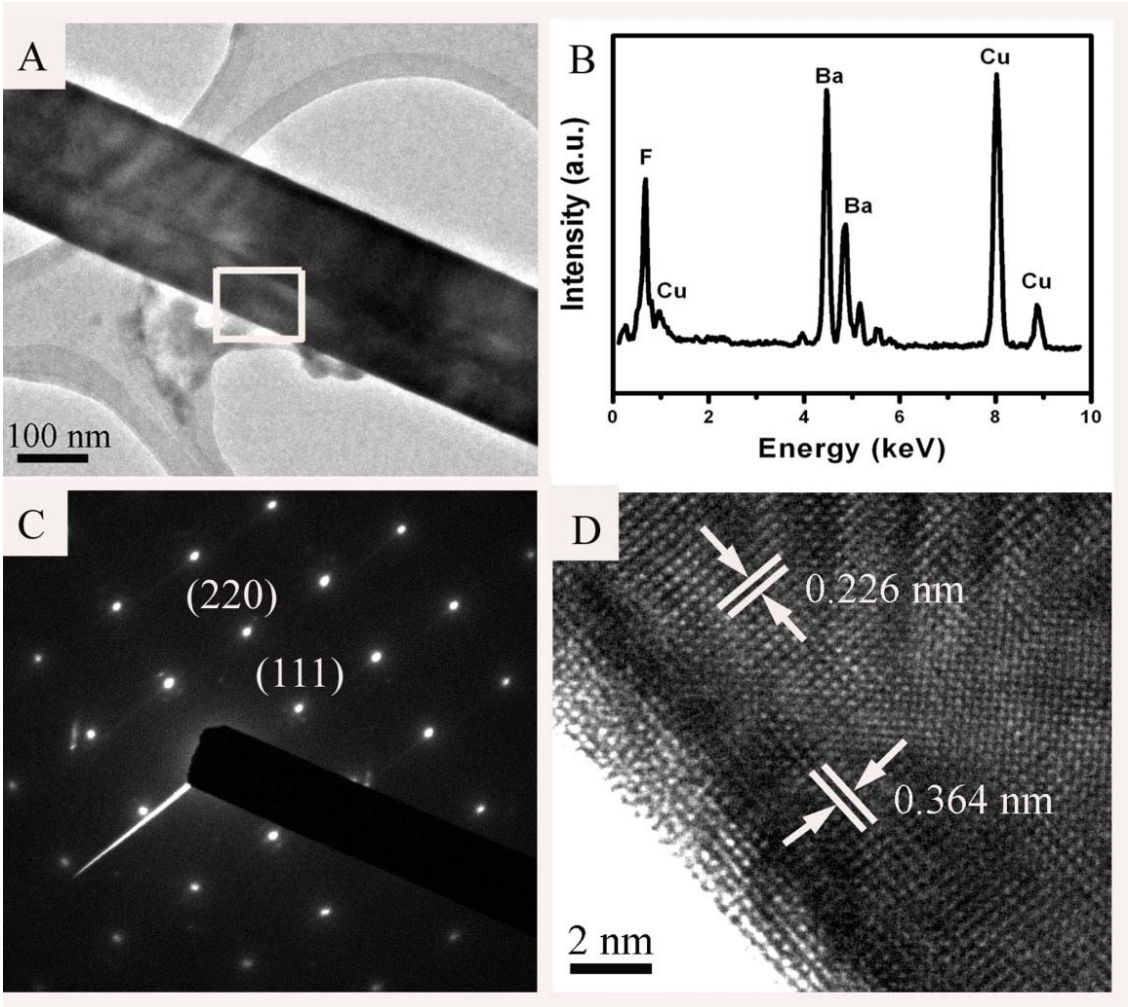

Figure 2.8 (A) TEM image of a single BaF_2 nanowire. (B) EDS of as-prepared BaF_2 nanowires. The Cu peaks originate from the TEM grid. (C) and (D) SAED pattern and HRTEM image of a representative part of a BaF_2 nanowire, as defined by the white square in (A).

As previously mentioned, bulk alkaline-earth metal fluoride crystals doped with rare-earth metal ions display unique luminescence properties. As a demonstration of principle, as-prepared alkaline-earth metal fluoride nanowire samples, doped with either Eu^{3+} and Tb^{3+}, displayed either pink or green luminescence, respectively, under UV lamp excitation (Figure 2.9). Figures 2.10 and 2.11 show the corresponding photoluminescence (PL) spectra of lanthanide-doped alkaline-earth metal fluoride nanowires. The major peak at 591 nm in Eu-doped alkaline-earth metal fluoride nanowires has been attributed to the $^5D_0 \rightarrow {}^7F_1$ emission peak, characteristic of Eu^{3+} ions surrounded by fluoride ions; the peak at 614 nm can be plausibly ascribed to a $^5D_0 \rightarrow {}^7F_2$ electric-dipole transition, which is similarly sensitive to small changes in the chemical environment as well as to symmetry considerations surrounding the Eu^{3+}ions.[25, 26] By analogy, the four well-resolved peaks, positioned at 489, 542, 584, and 620 nm, which have been observed for Tb-doped alkaline- earth metal fluoride nanowires, likely correspond to ligand- sensitized emission of the Tb^{3+} ions, specifically electronic transitions corresponding to $^5D_4 \rightarrow {}^7F_J$ (J = 6, 5, 4, 3).[27, 28] Results on our nanowires agreed favorably with comparable measurements taken on analogous bulk samples (Figure 2.11).

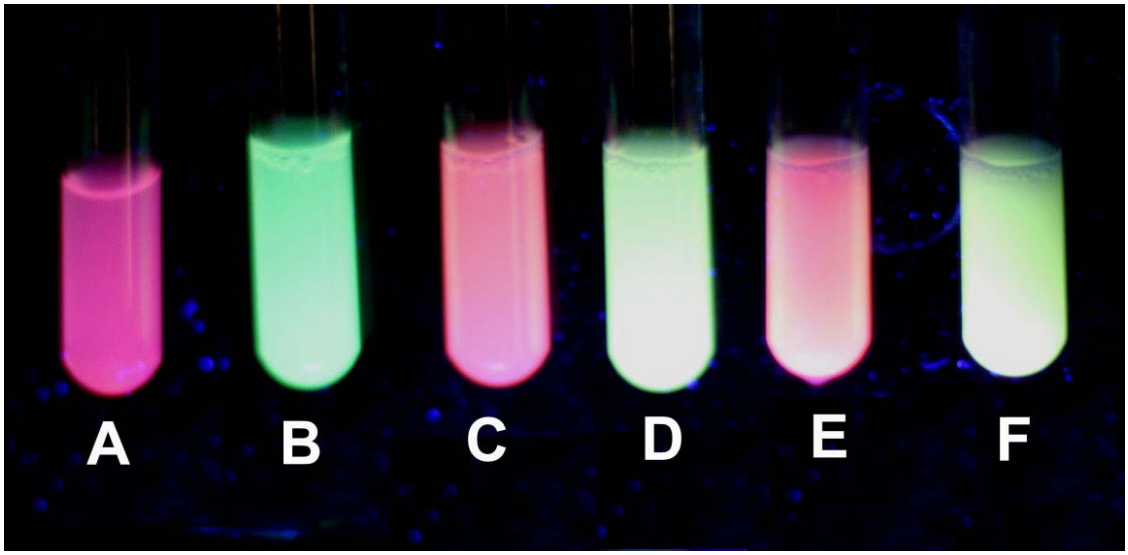

Figure 2.9 Photographs of dispersions of nanowires of (A) CaF_2 doped with Eu^{3+}; (B) CaF_2 doped with Tb^{3+}; (C) SrF_2 doped with Eu^{3+}; (D) SrF_2 doped with Tb^{3+}; (E) BaF_2 doped with Eu^{3+}; (F) BaF_2 doped with Tb^{3+} taken in dilute ethanol solution, while under irradiation using a 366 nm UV lamp.

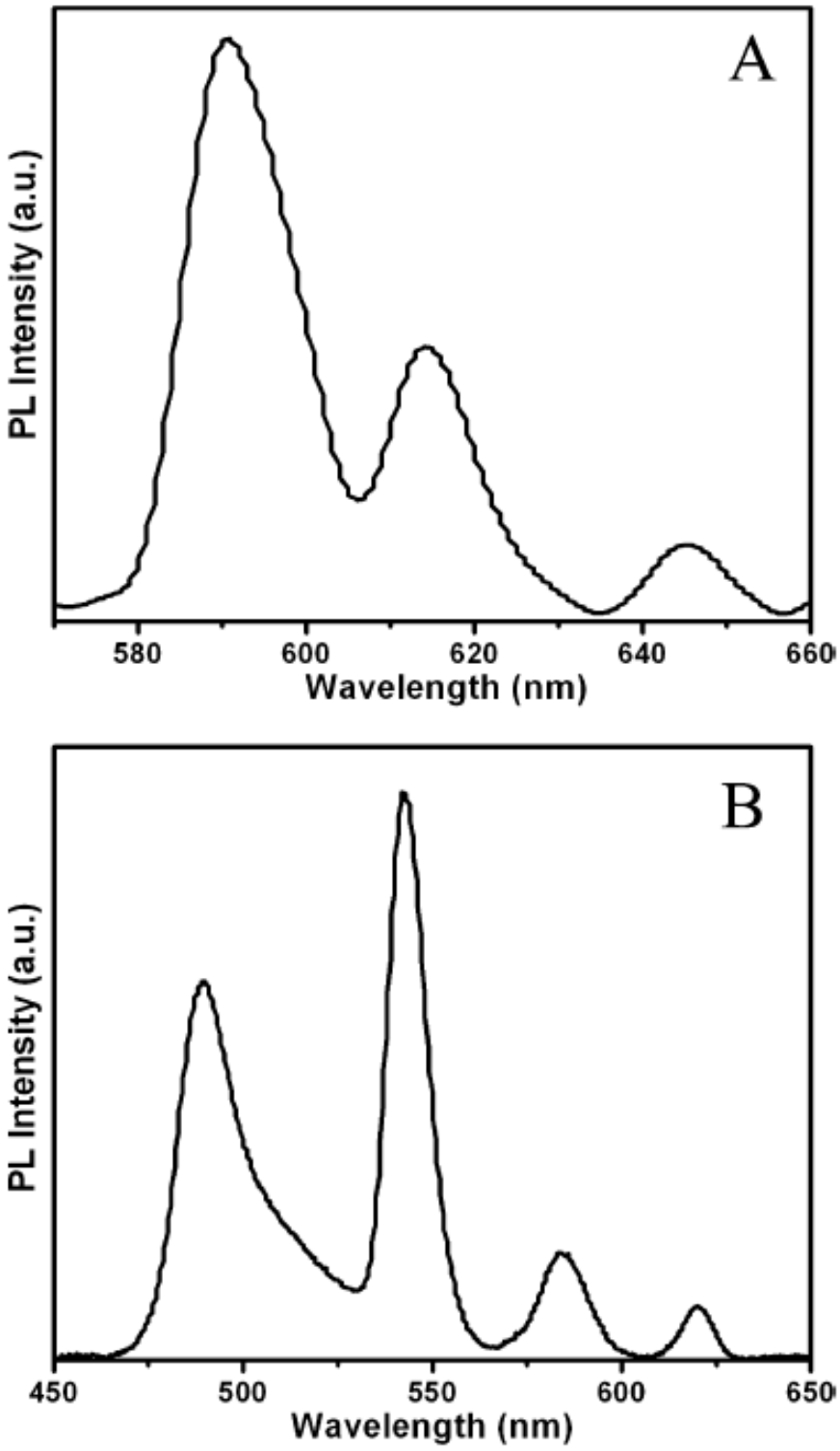

Figure 2.10 PL spectra of as-prepared CaF_2 nanowires doped with: (A) Eu^{3+} and (B) Tb^{3+}.

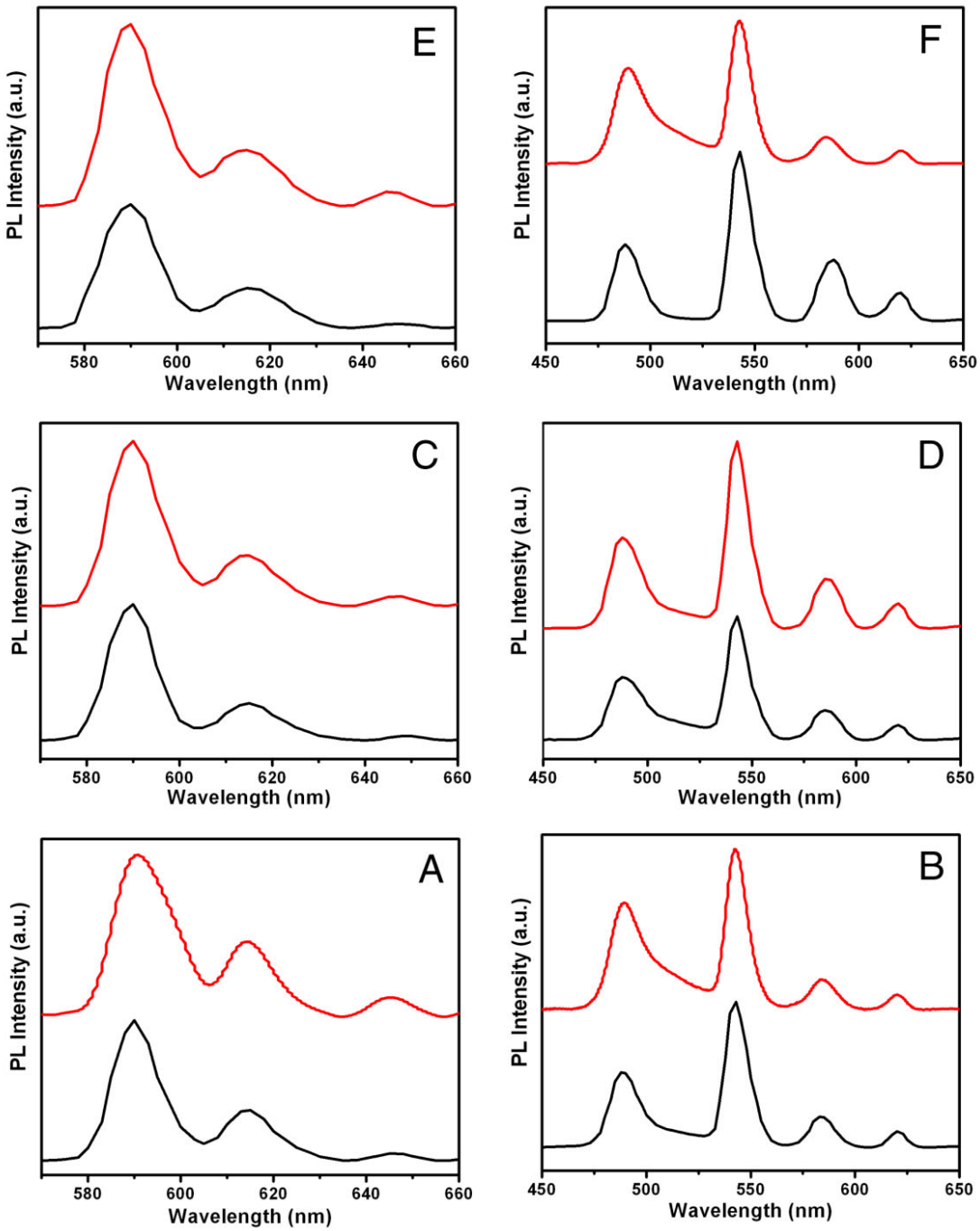

Figure 2.11 Photoluminescence spectra of as-prepared alkaline earth metal fluoride nanowires (red curves) as well as of bulk samples generated from direct mixing of commercially available precursor solutions (black curves). All samples were doped with Eu^{3+} and Tb^{3+}, respectively, in independent runs. (A) CaF_2 doped with Eu^{3+}; (B) CaF_2 doped with Tb^{3+}; (C) SrF_2 doped with Eu^{3+}; (D) SrF_2 doped with Tb^{3+}; (E) BaF_2 doped with Eu^{3+}; (F) BaF_2 doped with Tb^{3+}.

2.3.2 Perovskite Ternary Fluoride Nanorods

All of the diffraction peaks observed in Figure 2.12 can be readily indexed to a pure cubic phase [space group: P*m*3*m* (221)] of the perovskite, $KMnF_3$, with a calculated lattice constant, a = 4.186 Å, which is in good agreement with the reported database value of 4.184 Å (Figure 2.12B, JCPDS File No. 82-1334). Similarly, diffraction peaks in Figure 2.12C can be ascribed to a pure cubic phase [space group: P*m*3*m* (221)] of the perovskite, NH_4MnF_3, with an accompanying lattice constant, a = 4.237 Å, which is numerically close to the reported value (4.236 Å) of the corresponding bulk materials (Figure 2.12D, JCPDS File No. 83-0178).

Typical SEM and TEM images of $KMnF_3$ nanorods, which had been fabricated using polycarbonate membranes with pore sizes as small as 100 nm, are depicted in Figures 2.13A and 2.14A, respectively. On the basis of these data, it can be observed that straight and smooth $KMnF_3$ nanorods with uniform, homogeneous size could be routinely produced. Diameters of the wire-like $KMnF_3$ nanorods obtained were in the range of 85 to 115 nm, as expected, based on the corresponding 100-nm pore sizes of the polycarbonate membranes used in the synthesis. It is reasonable to conclude that the shapes of these nanorods accurately replicated the internal pore structure (and accompanying substructure) of the originating polycarbonate templates. Measured lengths of as-obtained $KMnF_3$ nanorods varied from one to several microns. Representative EDS analysis (Figure 2.13B) confirms that the chemical signatures taken within different parts of the sample are identical within experimental accuracy and that the nanorods are essentially composed of the elements K, Mn, and F. The extraneous C signal arises from the conductive carbon tape and atmospheric contamination. Corresponding SEM and TEM images of smaller $KMnF_3$ nanorods, synthesized from polycarbonate templates maintaining pore sizes of 50 nm, are shown in Figure 2.16A and 2.16B.

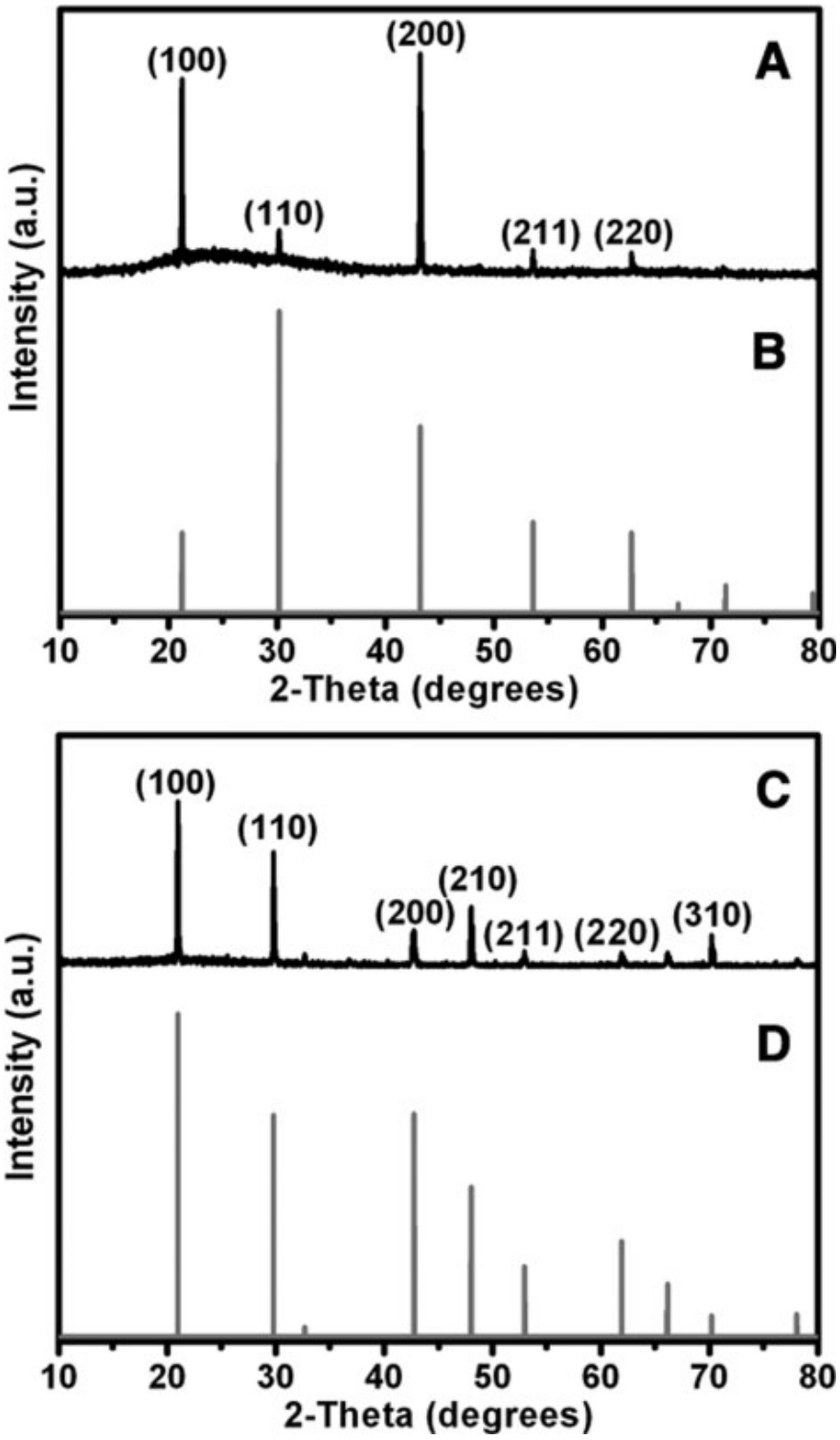

Figure 2.12 XRD patterns obtained from: (A) as-prepared $KMnF_3$ nanorods; (B) JCPDS no. 82-1334 database standard for $KMnF_3$; (C) as-prepared NH_4MnF_3 nanorods; and (D) JCPDS no. 83-0178 database standard for NH_4MnF_3.

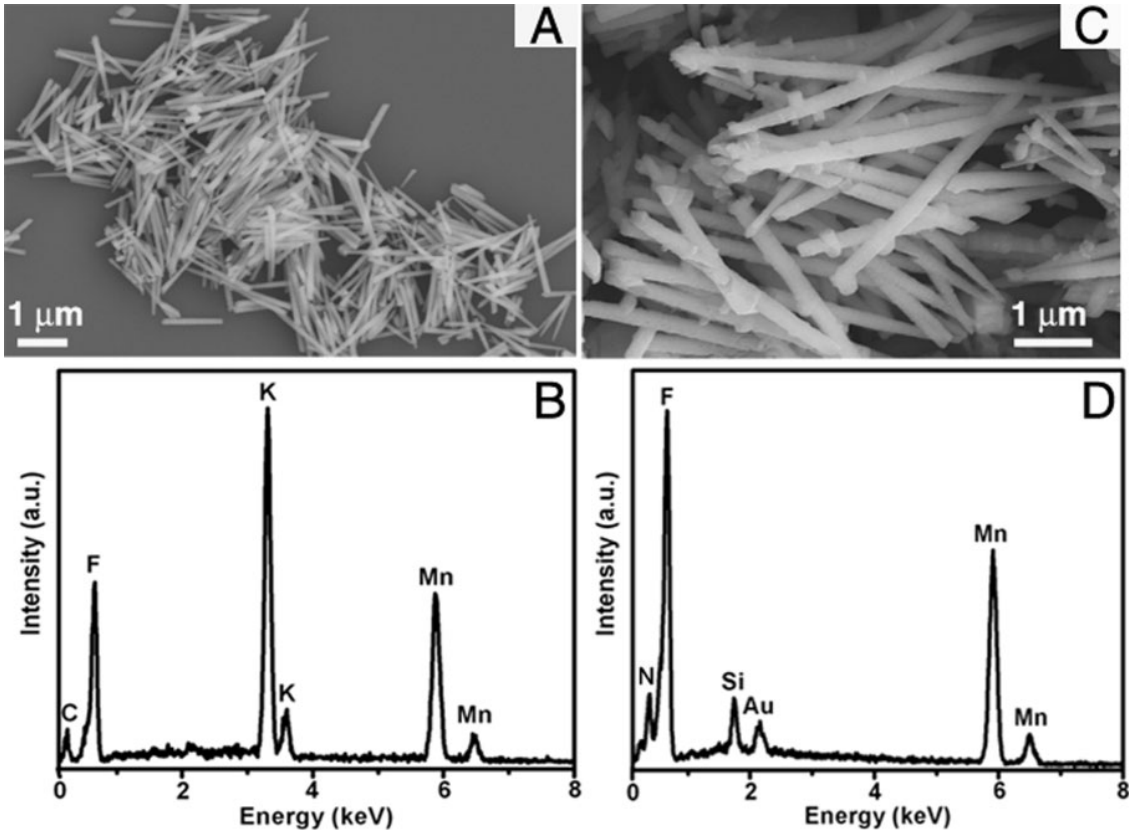

Figure 2.13 (A) Typical SEM image of as-prepared $KMnF_3$ nanorods, prepared using polycarbonate membranes composed of 100-nm pore sizes. (B) EDS spectrum of as-prepared $KMnF_3$ nanorods. The C peak originates from the conductive carbon tape. (C) Representative SEM image of NH_4MnF_3 nanorods, generated using polycarbonate membranes possessing 200-nm pore sizes. (D) EDS spectrum of as-prepared NH_4MnF_3 nanorods. The observed Si and Au peaks originate from the silicon wafer and gold coating, respectively.

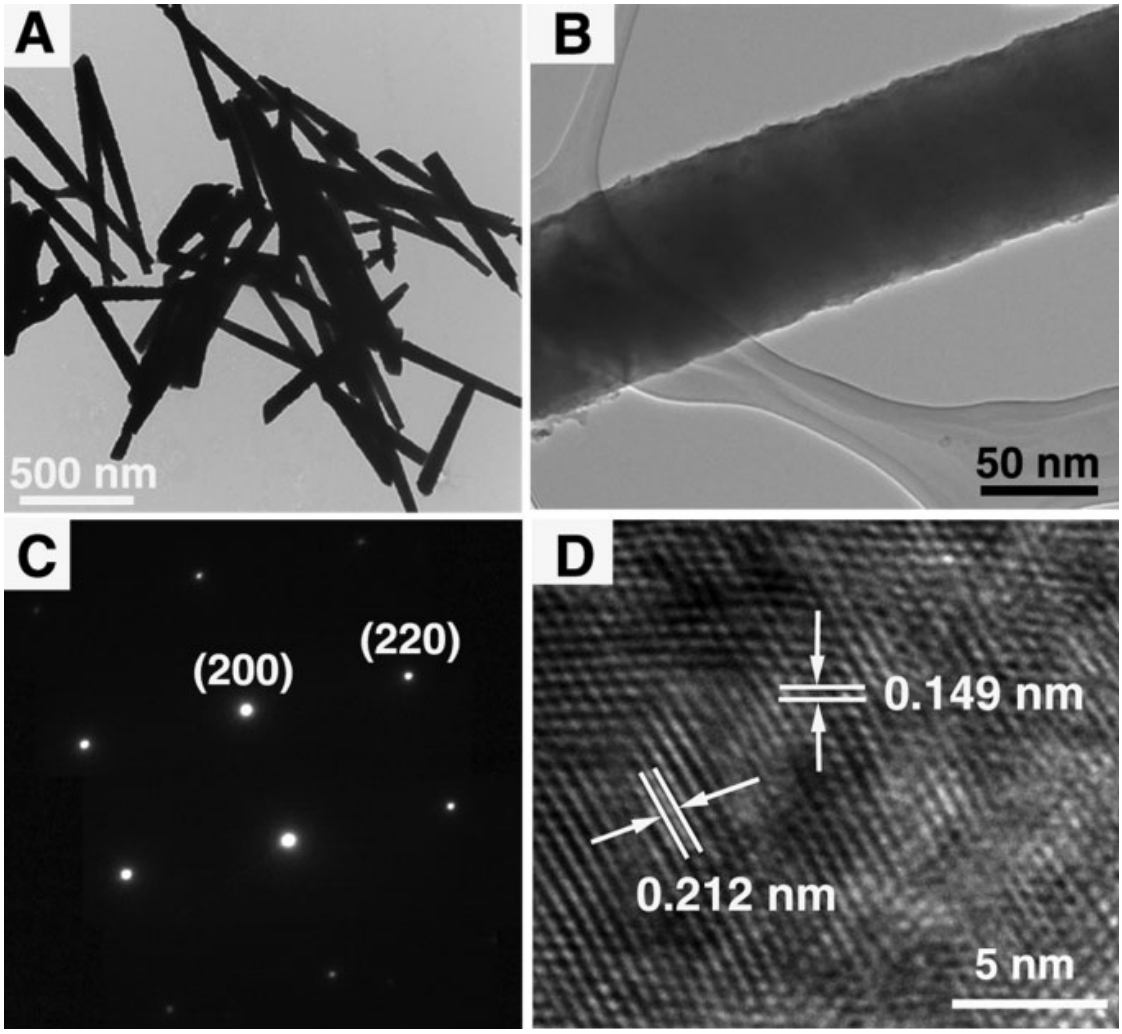

Figure 2.14 (A) Typical TEM image of as-prepared $KMnF_3$ nanorods, generated using polycarbonate membranes composed of 100-nm pore sizes. (B) TEM image of a single $KMnF_3$ nanorod from a different sample area. (C) SAED pattern and (D) HRTEM image of a representative portion of an individual $KMnF_3$ nanorod shown in (B).

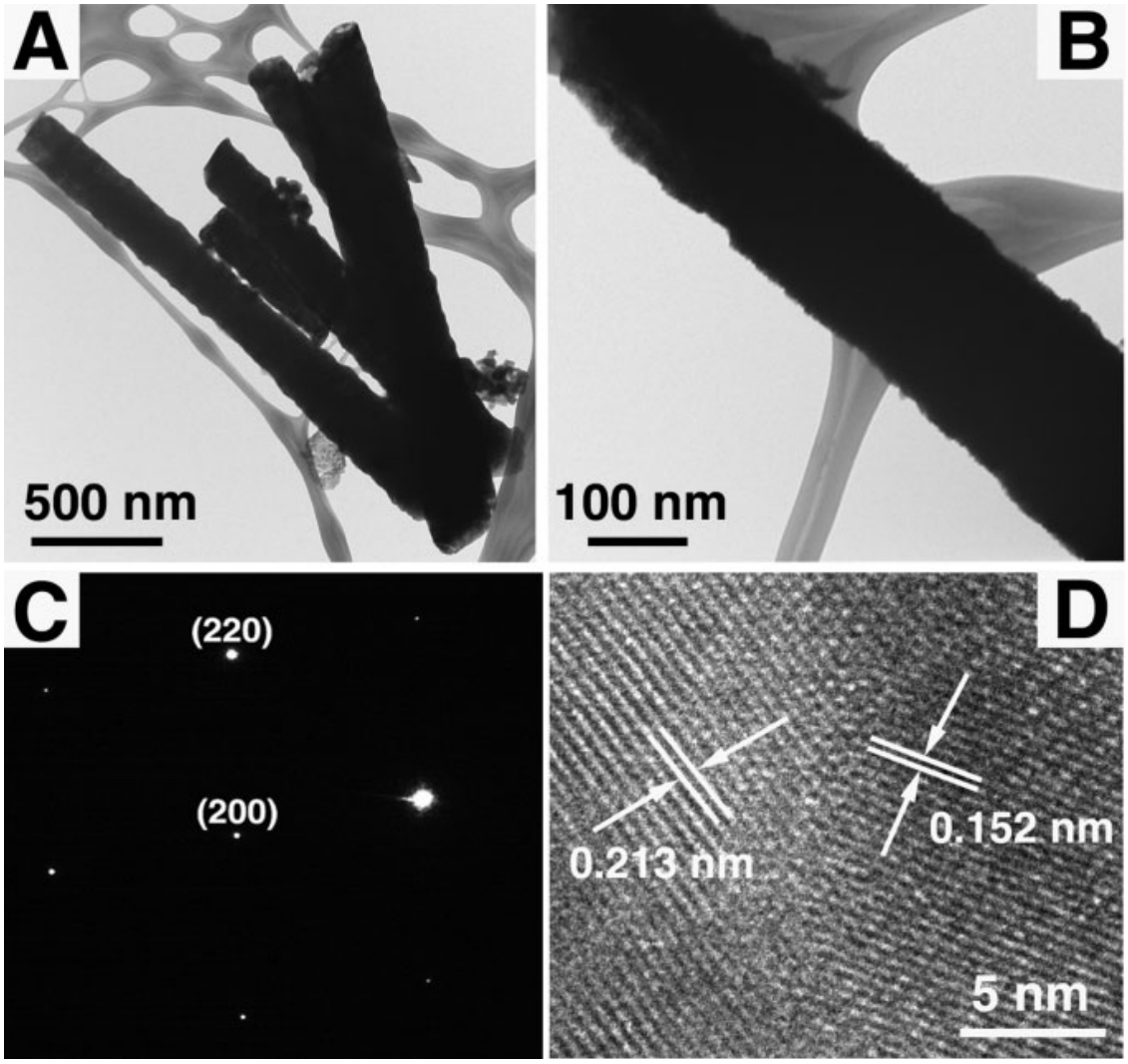

Figure 2.15 (A) Typical TEM image of as-prepared NH_4MnF_3 nanorods, generated using polycarbonate membranes possessing 200-nm pore sizes. (B) TEM image of a single NH_4MnF_3 nanorod from a different sample area. (C) SAED pattern and D) HRTEM image of a representative section of an individual NH_4MnF_3 nanorod shown in (B).

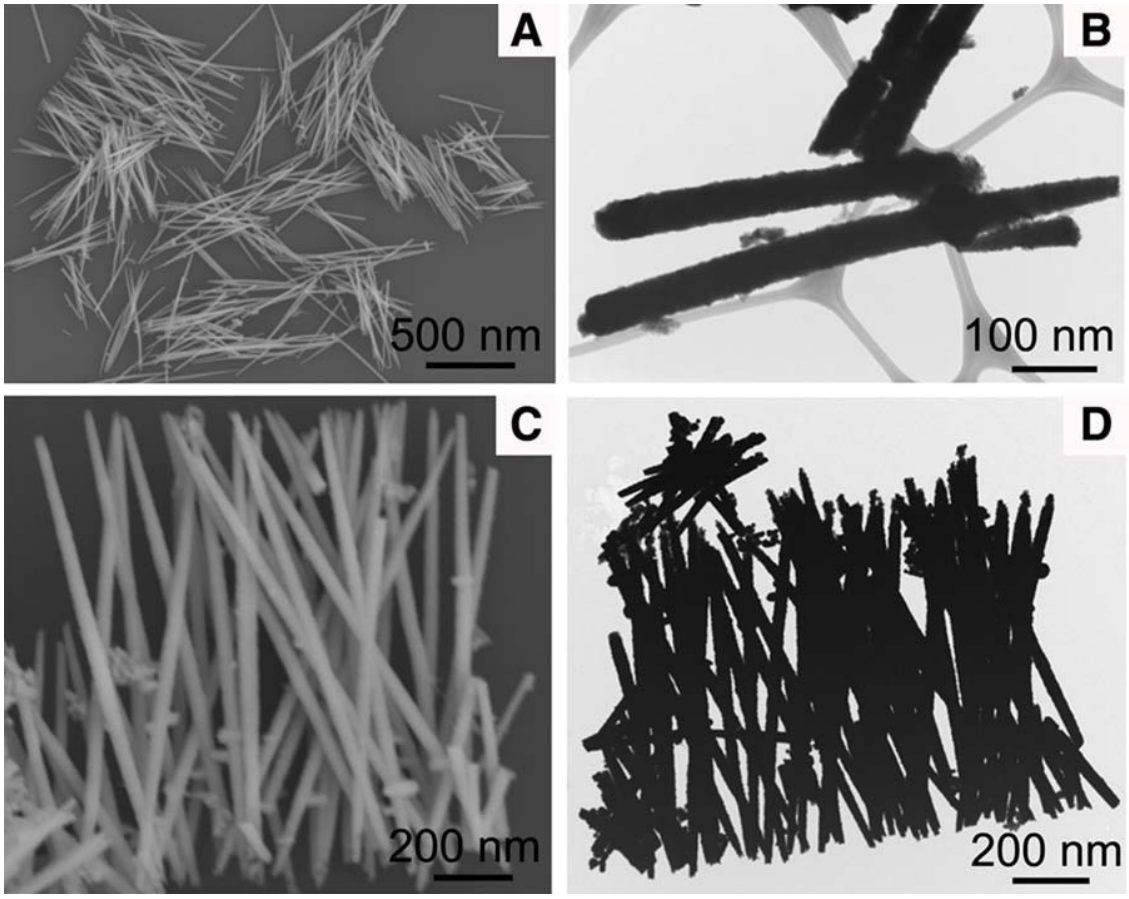

Figure 2.16 (A, B) Typical SEM and TEM images of as-prepared $KMnF_3$ nanorods, generated using polycarbonate membranes possessing 50-nm diameter pore sizes. Measured nanorod diameters are in the range of 42 to 53 nm. (C, D) Representative SEM and TEM images of as-prepared NH_4MnF_3 nanorods, produced using polycarbonate membranes composed of 50-nm diameter pore sizes. Measured nanorod diameters range from 45 to 52 nm.

Figures 2.13C and 2.15A show representative SEM and TEM images of NH_4MnF_3 nanorods, respectively, which had been generated from the 200-nm pore sizes of the polycarbonate membranes utilized as templates. The presence of dispersed individual nanorods as well as of bundled, aggregated species is evident from these images. All of the straight and crystalline NH_4MnF_3 nanorods possessed diameters ranging from 180 to 200 nm and lengths of 1.5 to 4 μm, suggestive of their reproducible synthesis, as mediated by the presence of templates. Surfaces of these 1-D structures were smooth over much of their lengths, though they were periodically roughened by the presence of inhomogeneities and protrusions, which likely originated from intrinsic surface incongruities and defects of the inner template pores from whence these nanorods were initially formed. EDS elemental analysis data (Figure 2.12D) clearly indicate that the nanorods are composed of N, Mn, and F, as predicted, with the presence of Si and Au peaks attributable to the silicon wafer and gold coating, respectively. Analogous SEM and TEM images of smaller NH_4MnF_3 nanorods, synthesized from polycarbonate templates possessing pore sizes of 50 nm, are shown in Figure 2.16C and D.

It should be noted that all of the data presented herein were obtained from randomly selected regions of as-prepared samples, and as such, are representative of the structures obtained. Our results therefore are consistent with the controllable production of ternary metal fluoride nanorods, which are relatively monodisperse in size and shape. Whereas the majority of as- generated $KMnF_3$ and NH_4MnF_3 nanorods possessed lengths of up to several microns as predicted from the membrane thickness, shorter rods were also observed, which could be attributed to the sonication step, associated with the preparation of the microscopy samples.

To obtain further insight into the crystallographic structure and chemical composition of as-prepared $KMnF_3$ and NH_4MnF_3 nanorods, individual nanorods were analyzed using HRTEM, as well as SAED. Figure 2.14B illustrates an individual $KMnF_3$ nanorod generated from polycarbonate membranes, possessing 100-nm pore sizes. SAED patterns taken along a number of selected regions along the same nanorod were effectively indistinguishable from each other within experimental accuracy. A representative pattern is shown in Figure 3C. The presence of sharp diffraction spots

rather than amorphous rings strongly supports the formation of single-crystalline $KMnF_3$ nanorods. The pattern can be indexed to the reflection of a cubic $KMnF_3$ structure, consistent with the XRD results presented above. Figure 2.14D displays a typical HRTEM image of the central region of the individual nanorod shown in Figure 2.14B. The 2D lattice fringes further confirm that the nanorod is single crystalline. In fact, the data reveal that the $KMnF_3$ nanorod is structurally uniform with interplanar spacings of approximately 2.12 Å and 1.49 Å, corresponding to the (200) and (220) planes, respectively.

The corresponding HRTEM data of an individual NH_4MnF_3 nanorod, shown in Figure 2.15, confirm the preparation of single –crystalline NH_4MnF_3 with the presence of expected elemental compositions, as well as with lattice spacing data, consistent with complementary observations from XRD data. Figure 2.15B highlights a single NH_4MnF_3 nanorod. Whereas template methods typically generate polycrystalline nanostructures, the SAED pattern taken from an individual NH_4MnF_3 nanorod (Figure 2.15C) clearly shows sharp diffraction spots, as opposed to the presence of an amorphous ring; this observation is suggestive of the presence of single-crystalline NH_4MnF_3 nanorods in our sample. Indeed, the electron diffraction pattern, indexed in Figure 2.15C, is consistent with the formation of pure NH_4MnF_3 crystals, possessing a cubic perovskite structure. In Figure 2.15D, a representative HRTEM image of a portion of an individual nanorod, illustrated in Figure 2.15B, is displayed. This image corroborates the single-crystalline nature of the as-prepared NH_4MnF_3 nanorod, which possesses lattice fringe spacings of ~2.13 Å and 1.52 Å. These two values can be ascribed to the (200) and (220) planes, respectively, in good agreement with prior observations noted from the XRD pattern.

Magnetic properties of as-prepared ternary metal fluoride nanorods were investigated with a superconducting quantum interference device (SQUID) magnetometer in the temperature range of 5–300 K at an applied magnetic field of 100 Oe. Figure 2.17A shows the temperature dependence of the magnetic susceptibility of $KMnF_3$ nanorods after analysis of the sample at zero field cooling (ZFC) as well as with field cooling (FC). The two curves display antiferromagnetic behavior, as previously detected in $KMnF_3$ nanoparticles.[22, 29] The ZFC and FC plots diverge from each other at around 87 K,

corresponding to the reported Néel temperature of T_N = 88 K.[30] Above T_N, the two curves are coincident, and moreover obey the Curie-Weiss law, $\chi = C / (T - \theta)$, with a calculated paramagnetic Curie temperature of T_C = –192.6 K, which is comparable with the previously reported value of –191.7 K for this system.[22] A detailed plot of the inverse magnetic susceptibility ($1/\chi$) *vs*. temperature (K) used to calculate T_C is shown in Figure 2.17B. Below T_N, an abrupt increase in χ (T) is observed. Since no macroscopic structural change is obviously apparent at this temperature, it is possible that the ordered state implied corresponds to a more complicated spin structure as compared to the simple picture of a two-sublattice antiferromagnet.[19] In fact, the most probable explanation for the observed peak at around T_N is the occurrence of some canting between the magnetization axes of the two sublattices, giving rise to a weak ferromagnetism which is symptomatic of a structural distortion, albeit small. That is, the weak moment appears to result from a distortion of the magnetic sublattices, because of differences in the sublattice anisotropy and fundamentally from differences in lattice parameters; the process has been called a first order transition of the Jahn-Teller type.[31] Though the exact mechanism giving rise to a magnetic moment in antiferromagnetic particles is still not totally resolved, the magnitude of the peak around T_N appears to be a function of particle size as well as of orientation.[19]

A similar trend has been observed in the magnetic susceptibility behavior of as-synthesized NH_4MnF_3 nanorods measured as a function of temperature, as shown in Figure 2.18A. The ZFC and FC plots diverge from each other, yielding a measured Néel temperature of T_N = 82 K, which is consistent with the reported literature data of 84 K for the analogous coarse grained material.[32] A similar jump measured around 74 K in the susceptibility curves below T_N was also observed, as with $KMnF_3$, and can be ascribed to the presence of a spontaneous weak ferromagnet moment, resulting from a localized distortion/magnetization event.[19] Figure 7B shows a detailed plot of the behavior of the inverse magnetic susceptibility ($1/\chi$) *vs*. temperature (K). Hence, the Curie-Weiss law above T_N provides for a value of the paramagnetic temperature for NH_4MnF_3 nanorods; in this case, the straight-line fit above T_N yields a Curie temperature (T_C) of –163.6 K.

To examine a possible size dependence of our magnetic data, we also collected magnetic measurements on fluoride nanorods samples, prepared using templates with pores measuring 50 nm in diameter. These data (Figure 2.19) show Néel temperatures of 88 K and 82 K for $KMnF_3$ and NH_4MnF_3, respectively, which are consistent with our values on larger-sized samples (e.g. those measuring ~100 and ~200 nm in diameter). Qualitatively, features of the magnetic susceptibility curves (Figure 2.19, including ZFC and FC) behave in a very similar fashion to what we have observed and discussed previously for our other samples.

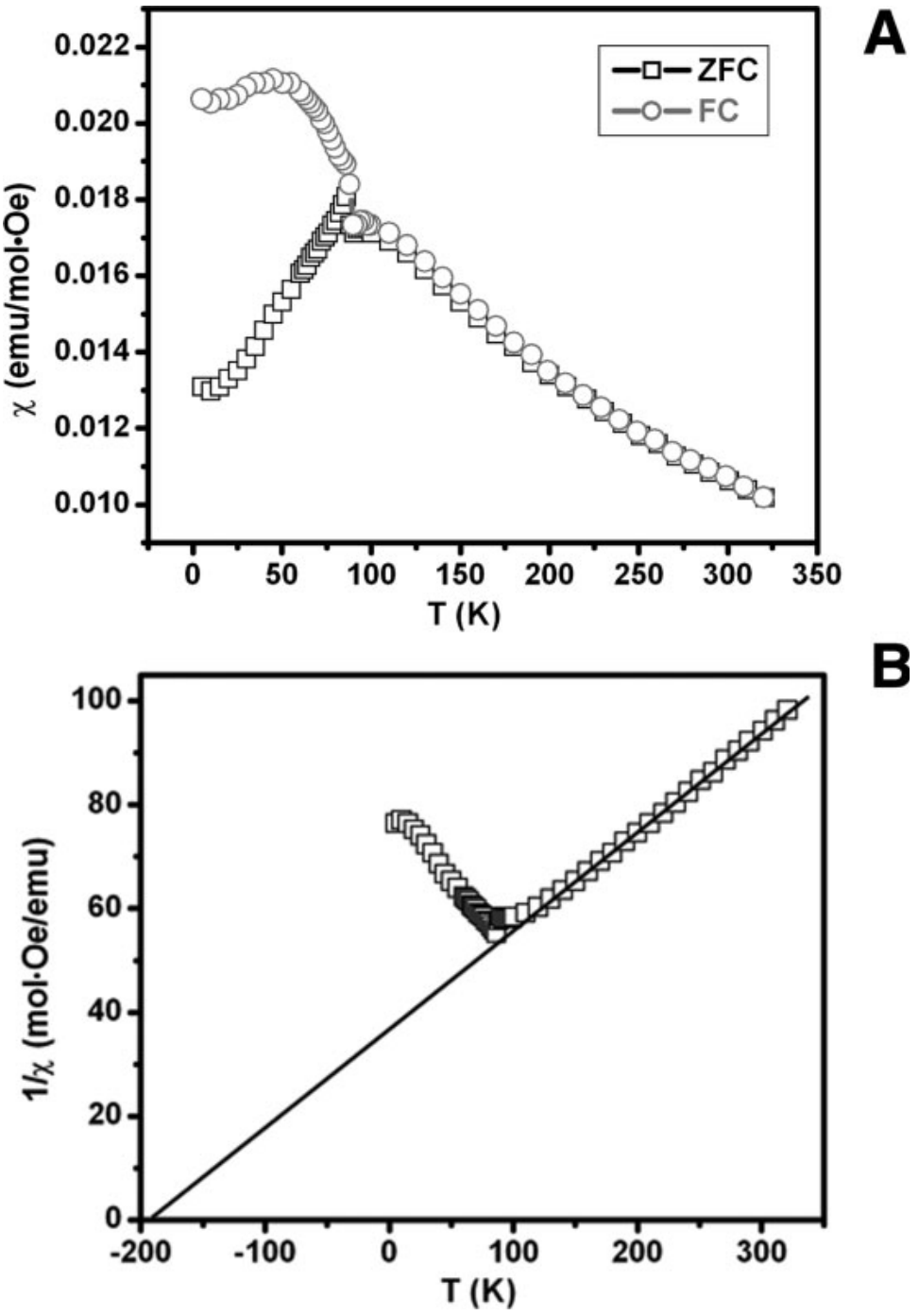

Figure 2.17 (A) Temperature dependence of the magnetic susceptibility of as-prepared $KMnF_3$ nanorods (measuring ~100 nm in diameter), showing zero field cooling (ZFC, black cubes) and field cooling (FC, black circles) curves at an applied magnetic field of 100 Oe. (B) The inverse magnetic susceptibility (represented as open cubes) and the corresponding fit of the Curie-Weiss law above T_N to as-obtained experimental data for $KMnF_3$ nanorods.

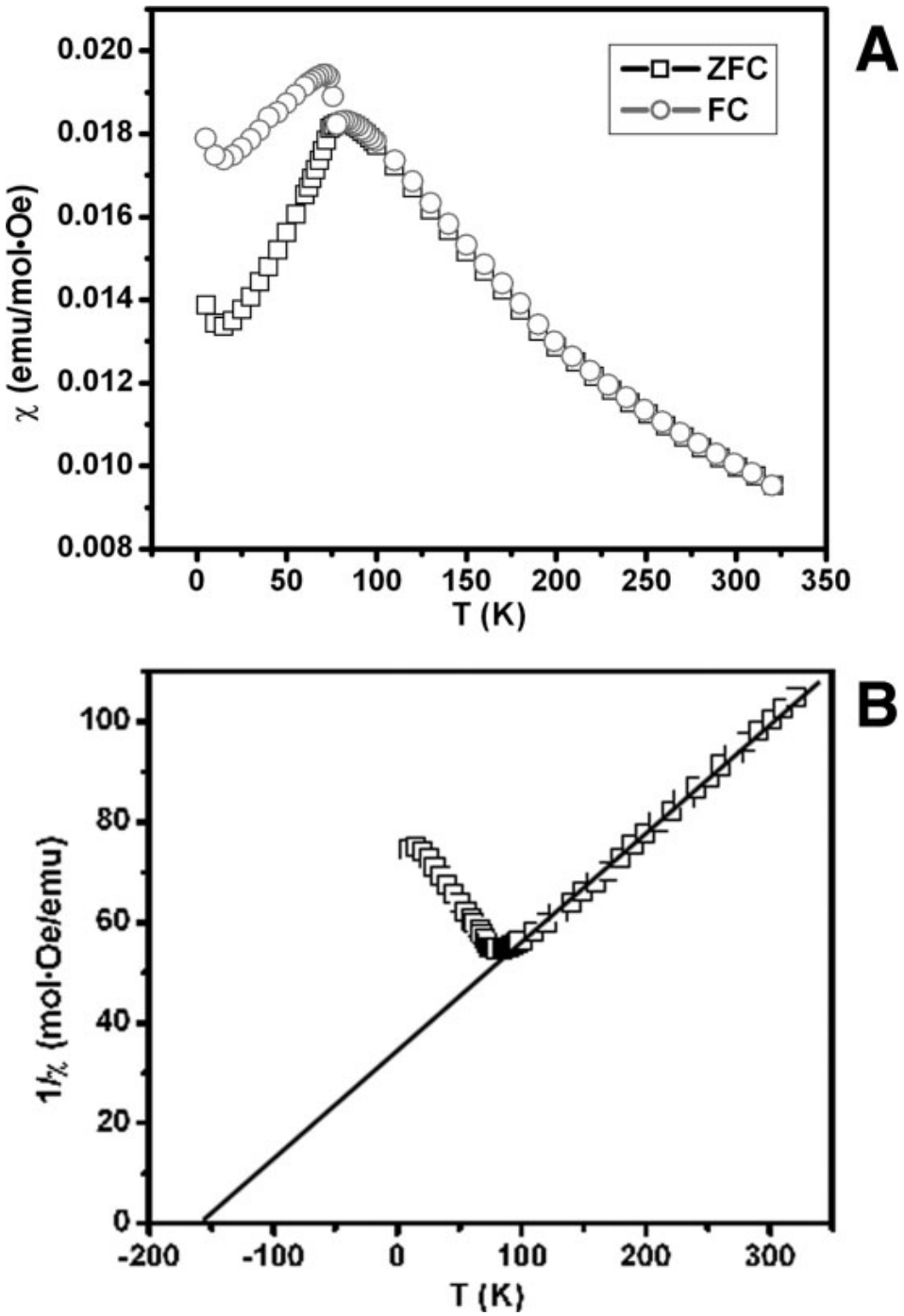

Figure 2.18 (A) Temperature dependence of the magnetic susceptibility of as-prepared NH_4MnF_3 nanorods (measuring ~200 nm in diameter), showing zero field cooling (ZFC, black cubes) and field cooling (FC, black circles) curves at an applied magnetic field of 100 Oe. (B) The inverse magnetic susceptibility (represented as open cubes) and corresponding fit of the Curie-Weiss law above T_N to as-obtained experimental data for NH_4MnF_3 nanorods.

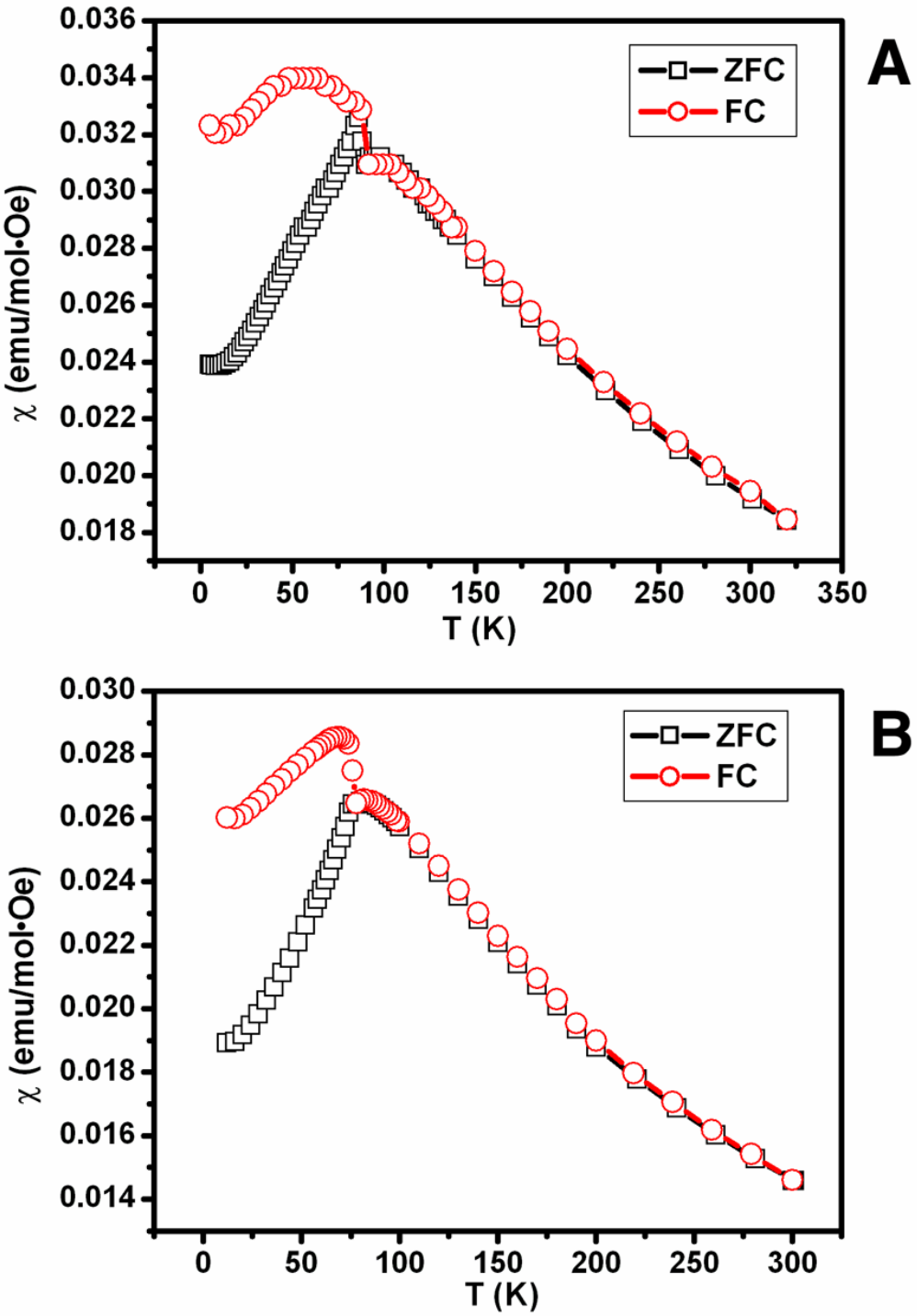

Figure 2.19 Temperature dependence of the magnetic susceptibility of as-prepared (A) $KMnF_3$ and (B) NH_4MnF_3 nanorods, measuring ~50 nm in diameter, showing zero field cooling (ZFC, black cubes) and field cooling (FC, red circles) curves at an applied magnetic field of 100 Oe.

As previously mentioned, fluorides doped with rare-earth metal ions have been reported to display unique luminescence properties with correspondingly useful optical applications.[33] Figure 2.20 shows the PL spectra of as-prepared ternary metal fluoride nanorods, doped with either Eu^{3+} or Tb^{3+} ions. Both $KMnF_3$ and NH_4MnF_3 nanorods evince similar curves as well as peak positions, when used as host materials for trivalent rare-earth metal ions. The major peak localized at around 598 nm in Eu-doped ternary metal fluoride nanorods (Figure 2.19A and C) can be ascribed to a $^5D_0 \rightarrow {}^7F_1$ electric-dipole transition. The other two peaks observed at 614 nm and 646 nm can be plausibly attributed to $^5D_0 \rightarrow {}^7F_2$ and $^5D_0 \rightarrow {}^7F_3$ emission peaks, respectively. By analogy, the PL bands for Tb-doped ternary metal fluoride nanorods obtained at room temperature were deconvoluted into four individual components, resulting in four Gaussian curves with their maxima localized at 495, 531, 578 and 620 nm, respectively, as shown in Figure 2.20B and D. The four peaks can be reasonably assigned to ligand-sensitized emission of the Tb^{3+} ions, and specifically to $^5D_4 \rightarrow {}^7F_J$ (J = 6, 5, 4, 3) electronic transitions. Specific lanthanide transitions in the as-doped ternary metal fluoride nanorods observed in these PL spectra are consistent with literature reports, where it is expected that the lanthanide ions occupy the Mn^{2+} sites.[28, 33] Data for smaller doped $KMnF_3$ and NH_4MnF_3 nanorods, prepared from templates containing 50 nm pore sizes, are shown in Figure 2.21. The peak positions observed for the rare earth ion transitions in those doped nanoscale fluoride samples are essentially indistinguishable from that depicted in Figure 2.20.

The corresponding chemical compositions and morphologies of the as-doped ternary metal fluoride nanorods can be extracted from the EDS and SEM data, respectively, as shown in Figure 2.22. The data reveal that the doping process is non-destructive to the intrinsic nanorod morphology, derived from the templating process, and moreover, actual dopant levels are somewhat lower than expected (data shown in Figure caption), based on the initial concentrations (～10%) of lanthanide ions used.

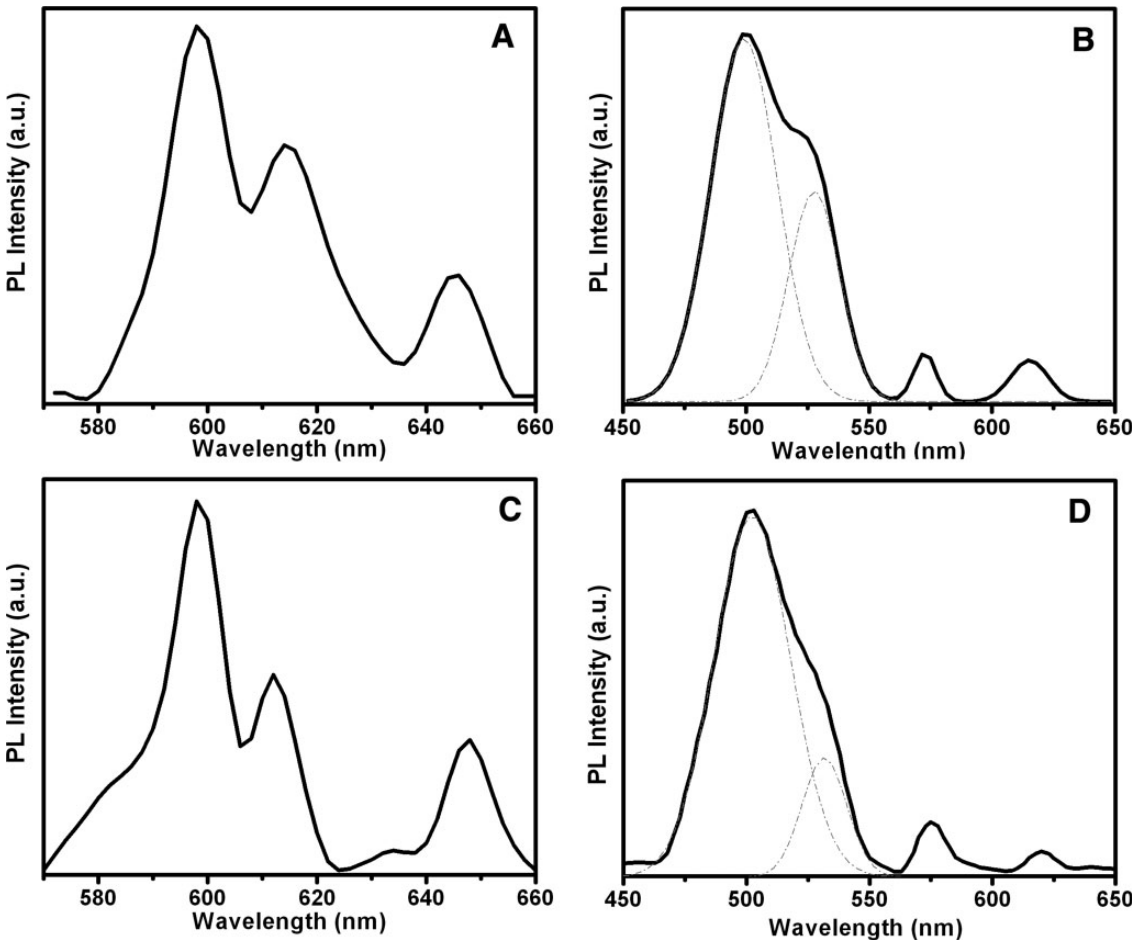

Figure 2.20 Photoluminescence spectra of as-prepared ternary metal fluoride nanorods doped with rare-earth metal ions. (A, B) $KMnF_3$ nanorods doped with Eu^{3+} and Tb^{3+}, respectively; (C,D) NH_4MnF_3 nanorods doped with Eu^{3+} and Tb^{3+}, respectively. The dotted lines correspond to Gaussian curves, representing a deconvolution of the as-obtained spectra into their relevant emission transitions.

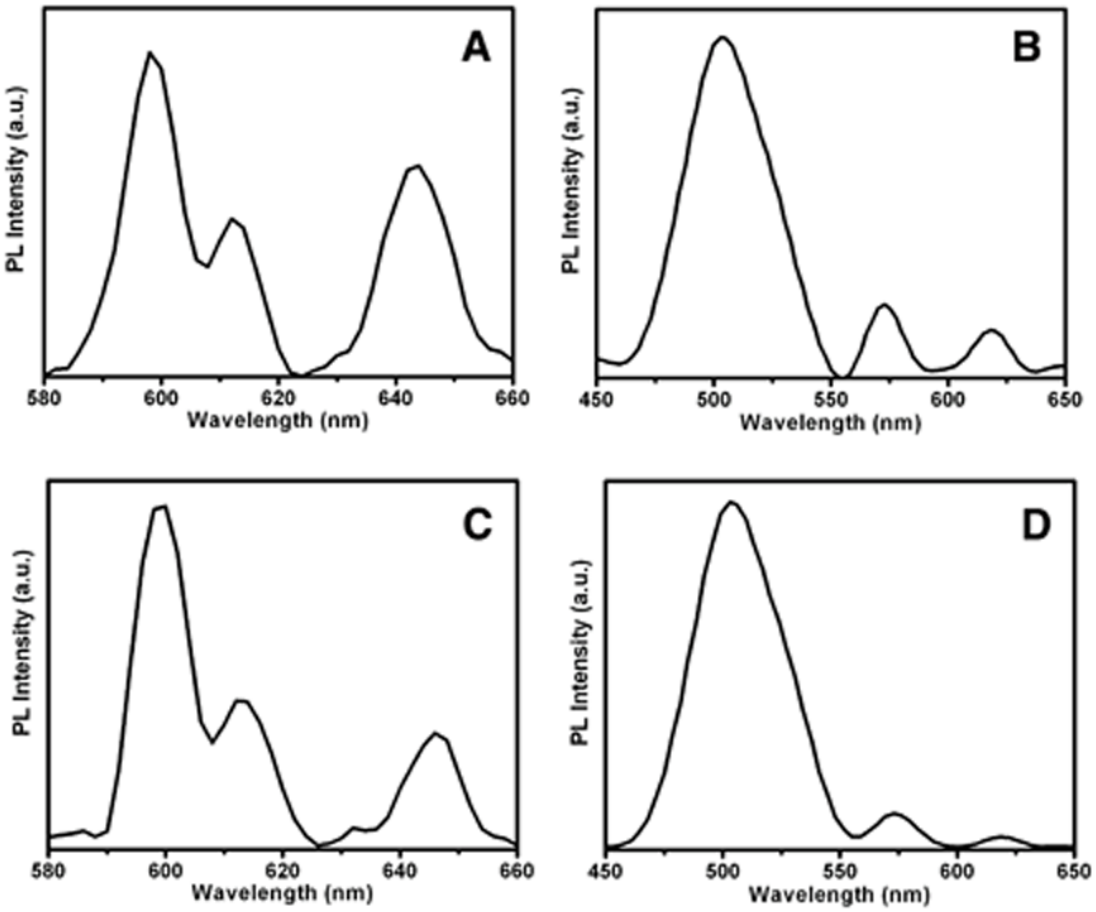

Figure 2.21 Photoluminescence spectra of ternary metal fluoride nanorods doped with rare-earth metal ions, prepared using polycarbonate membranes possessing 50-nm pore sizes. (A, B) $KMnF_3$ nanorods doped with Eu^{3+} and Tb^{3+}, respectively. (C, D) NH_4MnF_3 nanorods doped with Eu^{3+} and Tb^{3+}, respectively.

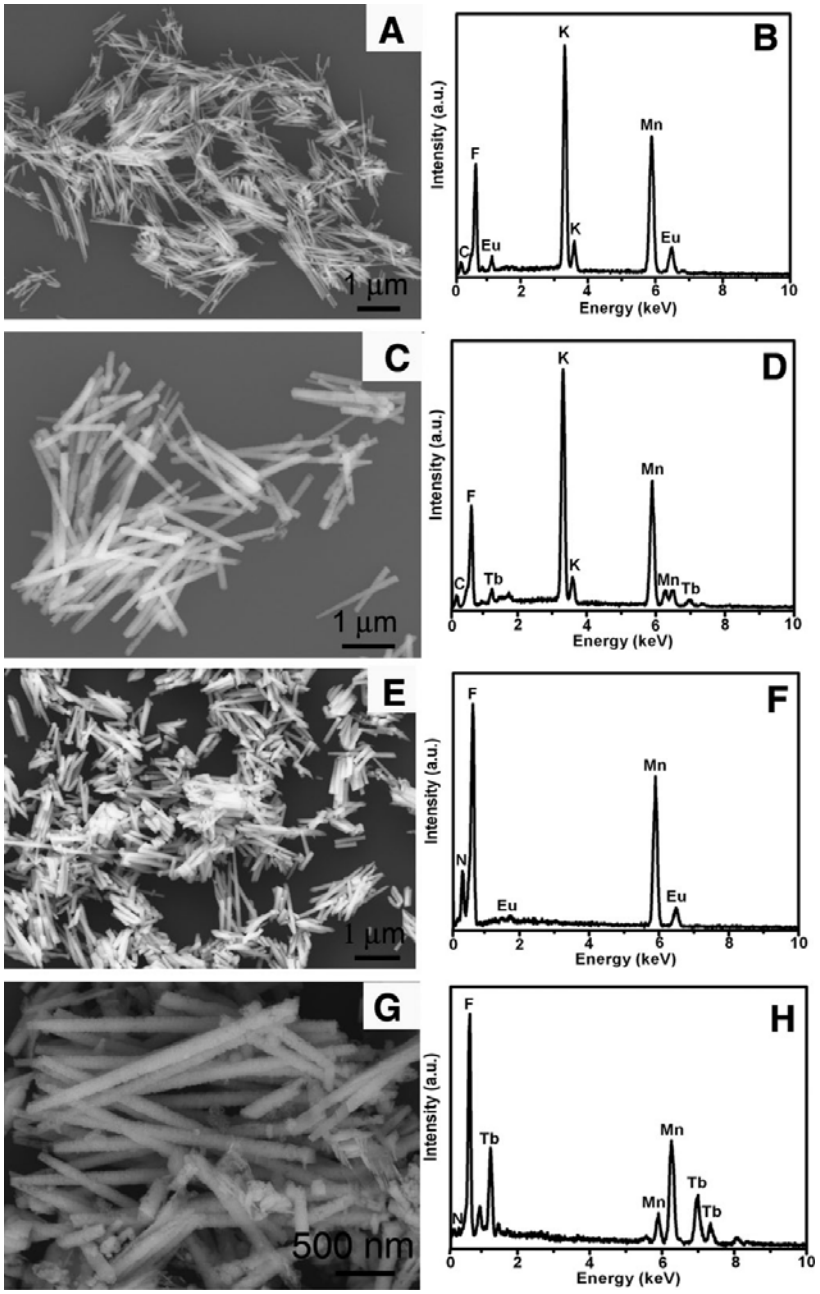

Figure 2.22 (A, B) SEM image and EDS spectrum of as-prepared ~100 nm $KMnF_3$ nanorods, doped with Eu^{3+} ions (concentration spectrally estimated to be ~1.08%). (C, D) SEM image and EDS spectrum of as-prepared ~100 nm $KMnF_3$ nanorods, doped with Tb^{3+} ions (concentration spectrally estimated to be ~1.17%). (E, F) SEM image and EDS spectrum of as-prepared ~200 nm NH_4MnF_3 nanorods, doped with Eu^{3+} ions (concentration spectrally estimated to be ~0.45%). (G, H) SEM image and EDS spectrum of as-prepared ~200 nm NH_4MnF_3 nanorods, doped with Tb^{3+} ions (concentration spectrally estimated to be ~1.85%). Carbon signals in (B) and (D) emanate from the conductive carbon tape used.

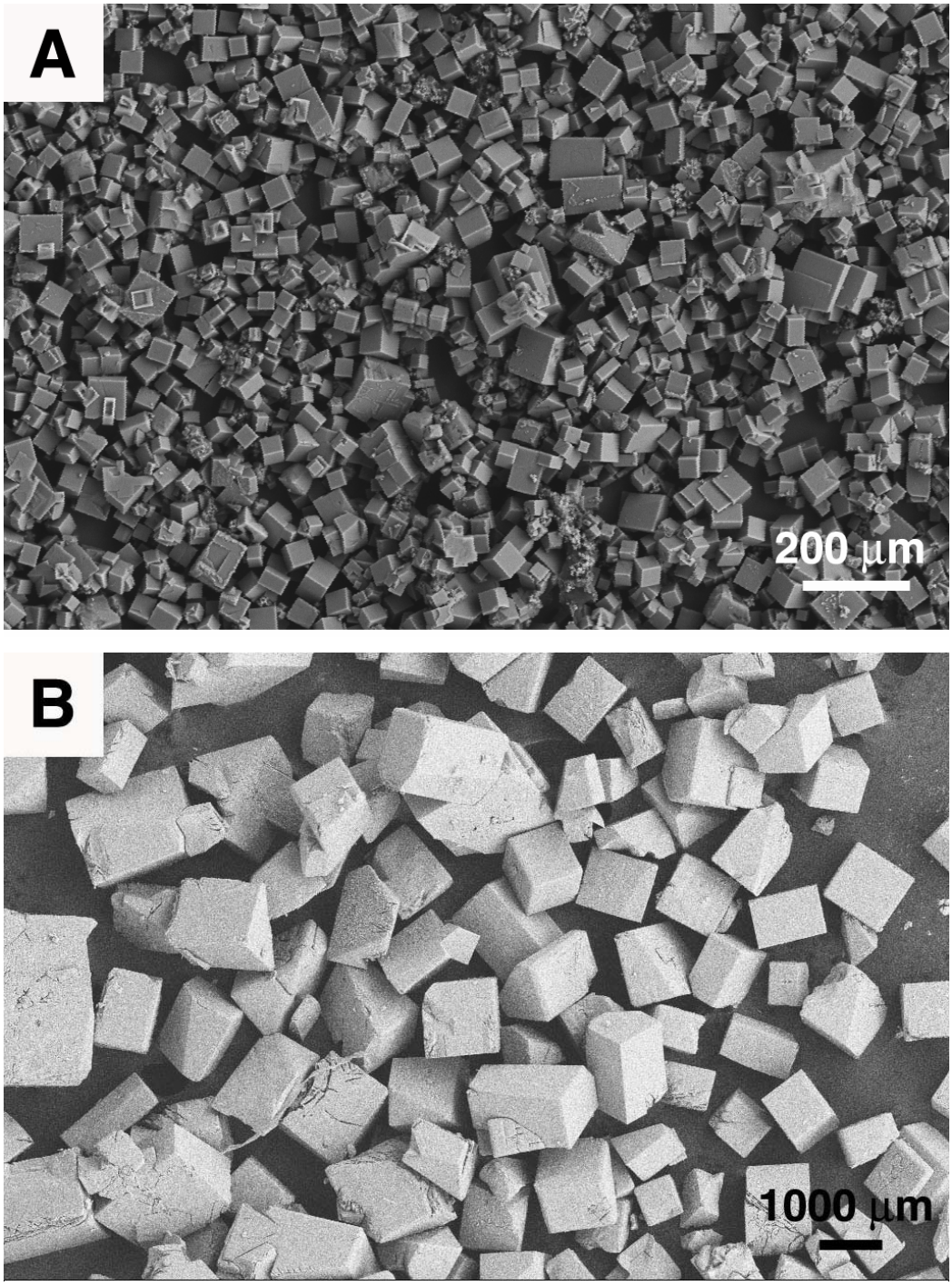

Figure 2.23 SEM images of (A) $KMnF_3$ and of (B) NH_4MnF_3 bulk particles, formed by direct mixing of two different precursor solutions at room temperature, respectively, in the absence of a template.

2.4 Conclusions

Our key advance in this ambient, room-temperature technique was the use of polycarbonate membranes in the double diffusion setup to spatially direct the crystal growth observed; these membranes were reasonably chemically inert towards both the reactants and the products as well as intervening reagents. That is, in order for single-crystalline fluoride structures to form, these nanorods must have originated from isolated single nucleation sites, which subsequently grew by extension through the porous network. Crystal growth in localized regions of the membrane was typically slow, and limited by the availability of ions from the two adjoining reservoirs of precursor solutions, separated by the polycarbonate membranes. Thus, the membranes not only enabled a continuous flow of precursor ions through the membrane pores but also slowed down precursor diffusion and mixing as well as product crystallization rates. Therefore, this spatial confinement effect allowed for the generation of single-crystalline ternary metal fluoride one-dimensional nanorods as opposed to either 0D nanoparticles or bulk aggregates, the latter of which could be formed in a template-less fashion merely by direct mixing of the two different precursor solutions (Figure 2.23).

It is noted that we are not forming hollow nanotubes because the interactions between the reagent molecules are likely stronger than those between the reagent molecules and the pore walls. In the case of polymeric microtubules formed in templates, nascent polymer chains initially adsorb to the pore walls yielding a thin polymer "skin", that becomes thicker with time until quenching with water.[34] We do not believe this accurately reflects the growth mechanism of our system, which is effectively similar to biomineralization.

The current chapter describes the synthesis of a family of single-crystalline alkaline-earth metal binary fluoride nanowires and more complex perovskite ternary fluoride nanorods, in addition to their rare-earth ion-doped analogues, of varying controllable sizes using a modified template-directed methodology. It is noteworthy that single-crystalline, alkaline-earth metal fluoride nanowires can be produced very readily using this modified, room-temperature, template-assisted method, without the use of either sophisticated experimental setups or high-temperature annealing. Moreover, the

diameters of the as-fabricated nanowires could be controlled by choosing polycarbonate membranes with predictable pore sizes. Resulting nanowires have been extensively characterized using microscopy, spectroscopy and magnetic techniques. Because of the simplicity and versatility of the synthetic approach used, it is anticipated that this particular technique can be generalized to the preparation of other types of nanomaterials with controllable size and shape. In addition, the antiferromagnetic properties of as-prepared ternary metal fluoride nanorods as well as the luminescence properties of their as-doped counterparts suggest the possibility of their incorporation into functional nanoscale devices, with various potential applications in a number of diverse fields.

2.5 References

1. Gao, P.; Xie, Y.; Li, Z., *eur. J. Inorg. Chem.* **2006**, 3261.
2. Bender, C. M.; Burlitch, J. M.; Barber, D.; Pollock, C., *Chem. Mater.* **2000,** *12*, 1969.
3. Lian, H.; Liu, J.; Ye, Z.; Shi, C., *Chem. Phys. Lett.* **2004,** *386*, 291.
4. Singh, R.; Sinha, S.; Chou, P.; Hsu, N. J.; Radpour, F., *J. Appl. Phys.* **1989,** *66*, 6179.
5. Hua, R.; Zang, C.; Shao, C.; Xie, D.; Shi, C., *Nanotechnology* **2003,** *14*, 588.
6. Johnson, L. F.; Guggenheim, H. J., *Appl. Phys. Lett.* **1971,** *19*, 44.
7. Zhang, X. X.; Hong, P.; Bass, M.; Chai, B. H. T., *Phys. Rev. B* **1995,** *51*, 9298.
8. Xie, P.; Rand, S. C., *Opt. Lett.* **1992,** *17*, 1198.
9. Cao, M.; Hu, C.; Wang, E., *J. Am. Chem. Soc.* **2003,** *125*, 11196.
10. Cao, M.; Wang, Y.; Qi, Y.; Guo, C.; Hu, C., *J. Solid State Chem.* **2004,** *177*, 2205.
11. De, G.; Qin, W.; Zhang, J.; Zhao, D.; Zhang, J., *Chem. Lett.* **2005,** *34*, 914.
12. Xia, Y.; Yang, P.; Sun, Y.; Wu, Y.; Mayers, B.; Gates, B.; Yin, Y.; Kim, F.; Yan, H., *Adv. Mater.* **2003,** *15*, 353.
13. Sun, X.; Li, Y., *Chem. Commun.* **2003**, 1768.
14. Grass, R. N.; Stark, W. J., *Chem. Commun.* **2005**, 1767.
15. Wang, F.; Fan, X.; Pi, D.; Wang, M., *Solid State Commun* **2005,** *133*, 775.

16. Laguna, M. A.; Sanuan, M. L.; Orera, V. M.; Rubin, J.; Palacios, E.; Pique, M. C.; Bartolome, J.; Berar, J. F., *J. Phys.: Condens. Matter.* **1993,** *5*, 283.

17. Pilla, O.; Freire, P. T. C.; Lemos, V., *Phys. Rev. B* **1995,** *52*, 177.

18. Zhao, C.; Feng, S.; Xu, R.; Shi, C.; Ni, J., *Chem. Commun.* **1997**, 945.

19. Bartolome, J.; Burriel, R.; Palacio, F.; Gonzalez, D.; Navarro, R.; Rojo, J. A.; De Jongh, J., *Physica B* **1983,** *115*, 190.

20. Roth, M.; Hempelmann, R., *Chem. Mater.* **1998,** *10*, 78.

21. Lu, L.; Wang, H.; Zhang, H.; Xi, S., *Chem. Commun.* **2001**, 1342.

22. Agnoli, F.; Zhou, W. L.; O'Connor, C. J., *Adv. Mater.* **2001,** *13*, 1697.

23. Tang, Q.; Shen, J.; Zhou, W.; Liu, J.; Liu, Z.; Qian, Y., *Inorg. Chem. Commun.* **2004,** *7*, 283.

24. Kumar, A.; Whitesides, G. M., *Appl. Phys. Lett.* **1993,** *63*, 2002.

25. Pi, D.; Wang, F.; Fan, X.; Wang, M.; Zhang, Y., *Spectrochim. Acta Part A* **2005,** *61*, 2455.

26. Cannas, C.; Casu, M.; Mainas, M.; Musinu, A.; Piccaluga, G.; Polizzi, S.; Speghini, A.; Bettinelli, M., *J. Mater. Chem.* **2003,** *13*, 3079.

27. Pivin, J. C.; Gaponenko, N. V.; Molchan, I.; Kudrawiec, R.; Misiewicz, J.; Bryja, L.; Thompson, G. E.; Skeldon, P., *J. Alloys Compd.* **2002,** *341*, 272.

28. Liu, P.; Liang, D.; Tong, Z.; Liu, X., *Macromolecules* **2002,** *35*, 1487.

29. O'Connor, C. J.; Kolesnichenko, V.; Carpenter, E.; Sangregorio, C.; Zhou, W.; Kumbhar, A.; Sims, J.; Agnoli, F., *Synth. Met.* **2001,** *122*, 547.

30. Hirakawa, K.; Hashimoto, T., *J. Phys. Soc. Jpn.* **1960,** *15*, 2063.

31. Heeger, A. J.; Beckman, O.; Portis, A. M., *Phys. Rev.* **1961,** *123*, 1652.

32. Pickart, S. J.; Alperin, H. A.; Nathans, R., *J. Phys.* **1964,** *25*, 565.

33. Shionoya, S.; Hirano, M., *Phys. Lett.* **1968,** *26A*, 533.

34. Martin, C. R.; Van Dyke, L. S.; Cai, Z.; Liang, W., *J. Am. Chem. Soc.* **1990,** *112*, 8976.

Chapter III Solid Solutions of Various Compositionally-Defined Single-Crystalline Alkaline-Earth Metal Tungstate Nanorods

3.1 Introduction

Alkaline-earth-metal tungstates AWO_4 (A = Ca, Sr, Ba) represent an important family of inorganic, electrooptic materials[1-3] with their distinctive scheelite structure and associated highly interesting physical properties such as excitonic luminescence, thermoluminescence, and stimulated Raman scattering (SRS). In fact, they are keenly sought as host materials for a wide range of technologically significant applications,[4-17] including as phosphors, gas sensors, laser media, and optical fibers as well as components of electrochromic devices, amplifiers, diagnostic medical equipment, microwave systems, and the next generation of scintillator detectors. As compared with the wolframite (wolframite = (Fe, Mn) WO_4) structure, tungstates of relatively large bivalent cations (ionic radius > 0.99 Å: Ca, Sr, Ba, Pb) exist in so-called scheelite (scheelite = $CaWO_4$) structure, wherein tungsten ions adopt a tetrahedral coordination within oxygen-ion cages and are isolated from each other, while cations are surrounded by eight oxygen ions (Figure 3.1).[18, 19] Meanwhile, scheelite-type tungstates of the same divalent metal are reciprocally soluble in the entire compositional range,[20, 21] which can result in a rich family of solid-state solution compounds, showing high interest in the field of electrooptics.

One key point is that all of the as-mentioned applications, which render scheelites as appropriately attractive materials, are evidently and intimately coupled with their lattice dimension, crystallographic symmetry, as well as band structure. Hence, in this Chapter, we seek to gain a fundamental understanding of how slight but controlled variations in the chemical composition of these scheelite materials may lead to favorable structure-property correlations in these systems.

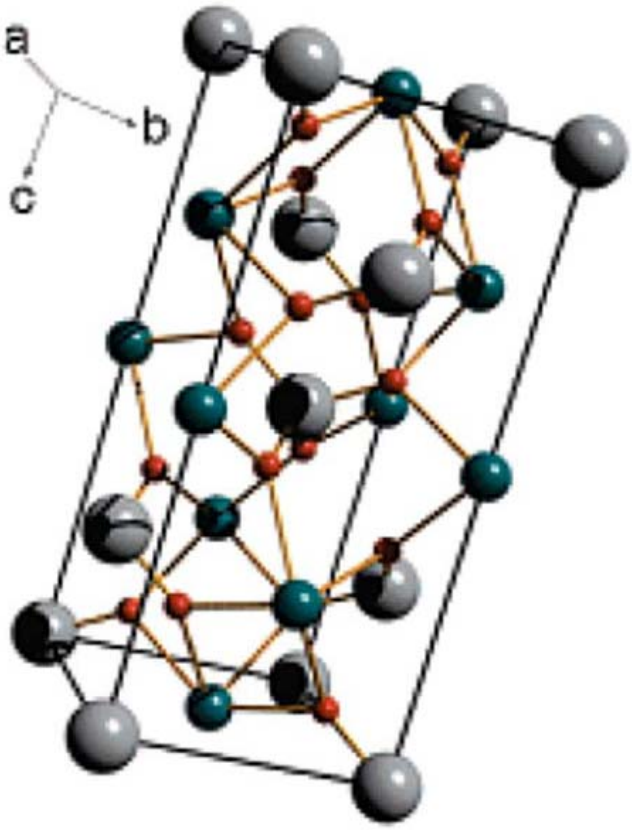

Figure 3.1 Schematic view of alkaline-earth metal tungstate scheelite structure. Gray, green, and red spheres designate Ca, W, and O atoms, respectively.[19]

One viable and legitimate experimental strategy for approaching this problem lies in the reproducible and reliable generation of stoichiometrically controlled, homogeneous, single-phase solid solutions of such materials. For example, by rationally altering the precursor compositions of ZnS and $AgInS_2$, the energy gap of highly luminescent $(AgIn)_xZn_{(1-x)}S_2$ solid solution nanoparticles could be modulated through a wide range of visible light, thereby enabling tuning of the emission color of these materials from green to red, depending on their chemical composition; this nanoscale chemical manipulation had implications for the photocatalytic behavior of these systems.[22-24] In another case, the degree of ferromagnetism, magnetoresistance, and transport behavior of epitaxial $Cr_xTi_{1-x}N$ thin films grown using pulsed laser deposition were found to depend very strongly on the magnitude of x.[25] Moreover, the conductivity and dielectric properties of $Ba_{5x/2}Bi_{(1-x)5/3}Nb_5O_{15}$[26] and $YBa_{1-x}Sr_xCo_2O_{5+\delta}$,[27] respectively, were observed to vary with chemical composition, degree of oxygen ordering, as well as the nature of the cation substitution. In addition, it has been demonstrated that solid solutions of $Zn_xTi_{1-x}O_{2-x}$ evince significant photocatalytic activity in the photodegradation of phenols.[28] Theoretically, it has been shown that the hardness parameter as well as elastic constants associated with multicomponent solid solutions of nitride spinels, titanium nitrogen carbides (e.g., $TiN_{1-x}C_x$), transition-metal nitrides (e.g., TiN_{1-x}), and B-doped semiconductors (e.g., $Si_{1-x}B_x$) as well as of $U_xLa_{1-x}S$ systematically depend on predictive adjustment of 'x'.[29, 30] Of particular pertinence to this work, it has been demonstrated that unlike for scheelite-powellite solid solutions,[31] the family of pure scheelite-type metal tungstates allows for isomorphic replacement of the divalent metal cation, thereby creating a highly miscible solid solution over vast compositional ranges.[21, 32, 33]

The second key point, i.e., the equally important, motivating factor for this project, resides in the development of low-dimensional nanomaterials with controllable size, shape, and morphology for the realization of novel functional devices at the nanoscale.[34-36] In particular, one-dimensional (1D) nanostructures, including nanowires, nanorods, nanobelts, and nanotubes, are the focus of intensive research owing to their unique, shape-dependent properties, allowing for their use as building blocks in the assembly of a range of electronic, optoelectronic, and sensing devices.[37-39] Part of the challenge in this

area has been the rational and precise tuning of the chemical composition of these 1D structures so as to systematically optimize their optical, mechanical, and electronic properties.

In terms of previous work with nanoscale alkaline-earth-metal tungstates, the vast majority of prior results have focused on the generation of either nanoparticles or nanoparticles aggregates,[7, 8, 40-42] synthesized using either hydrothermal, solvothermal, or molten salt methodologies. Nonetheless, work on creating one-dimensional nanostructures of these scheelite materials does exist. For example, $CaWO_4$ nanorods, with widths of about 20 nm and lengths of 100-250 nm, have been fabricated using a solvothermal technique in the presence of PEG-200 at 180 °C and at pH 9 for 14 h;[43] slightly longer nanorods with average diameters of 20-30 nm and mean lengths of 600-1000 nm were controllably generated using a microemulsion-mediated hydrothermal procedure.[44] With respect to $SrWO_4$, nanorods measuring 100 nm in diameter and 500-1500 nm in length were synthesized using a solvothermal-mediated microemulsion technique involving water, organic solvent, and surfactant.[19] For $BaWO_4$ nanorods, their 2-dimensional organization at the water-air interface was accomplished using a Langmuir- Blodgett technique.[45, 46] Recently, uniform, high-aspect-ratio, single-crystalline $BaWO_4$ nanorods with diameters as small as 3.5 nm and lengths up to more than 50 μm have been synthesized using a catanionic reversed micelle templating protocol;[47, 48] bundles of these nanorods could be generated in combination with a solvothermal methodology.[49] With the further use of double-hydrophilic block copolymers as effective crystal growth modifiers, morphological variants, namely penniform $BaWO_4$ nanostructures, could be prepared using this generalized reverse micellar technique.[50]

Nonetheless, development of facile, mild (i.e., under ambient conditions), and effective approaches for creating size-controlled, chemically precise, and crystalline 1D alkaline-earth- metal tungstate nanostructures as well as their associated array architectures remains a significant scientific challenge, especially because control of chemical composition in these systems would lead to a correspondingly high degree of predictability in the photoluminescence properties of these systems.[32, 51] Resolving this

issue is the convergence point of the two key interests outlined in this project. That is, we performed the synthesis and optical characterization of a series of stoichiometrically controlled, homogeneous, single-phase solid solutions of 1D nanomaterials in order to deduce systematic nanoscale structure-property correlations. Specifically, the interactions between the calcium, strontium, and barium ions and the emission centers in discrete solid solutions of these oxide nanomaterials may contribute differentially to their observed optical spectra.

To accomplish this overall goal, whereas conventional templating procedures typically generate polycrystalline products as a result of the necessity of additional annealing steps at high temperature,[37] we recently developed a modified template-directed technique. This protocol has allowed us to previously prepare pure single-crystalline metal oxide and fluoride nanorods under ambient conditions while utilizing reasonably stable and nontoxic precursors in aqueous solution and without generating large quantities of harmful byproducts. Specifically, in this article, we report on the successful generalization of this synthetic protocol to the preparation of not only 1D nanostructures of an entire family of alkaline-earth-metal tungstate scheelite structures but also their single-crystalline, stoichiometrically defined solid-solution analogues with controllable size and chemical composition. Experimentally, a commercially available, track-etched polycarbonate membrane of varying pore size was mounted between two halves of a U-shaped reaction tube, each of which contained aqueous precursor solutions, so as to control the growth of the corresponding 1D nanostructures. As a rigorous and logical extension of our previous work on $BaWO_4$ nanorods,[52] herein we not only decreased the diameters of as-prepared barium tungstate nanostructures to 50 nm but also extended this generalizable methodology to the preparation of calcium tungstate and strontium tungstate analogues. Moreover, we systematically characterized the luminescence properties of several series of samples prepared within a wide range of tunable, achievable chemical compositions and found a linear correlation between optical behavior and tungstate stoichiometry. In addition, we measured lifetimes and quantum yields associated with our systems.

3.2 Experimental Section

3.2.1 Materials Preparation

Polycarbonate (PC) track-etch membranes of ca. 6 μm thickness, containing pore sizes of 50, 100, and 200 nm diameter, were purchased from Whatman Co., U.K. The membranes were initially hydrated by immersion and sonication in a small volume of distilled, deionized water for a few minutes so as to limit air bubble formation either within their interior pore structures or on their external surfaces.

Subsequently, the polymer membrane was mounted between two half arms of a U-shaped tube cell. In a typical synthesis, one of the two half cells was filled with Na_2WO_4 solution and the other half cell contained a solution of either $CaCl_2$, $SrCl_2$, or $Ba(NO_3)_2$ to correspondingly generate $CaWO_4$, $SrWO_4$, or $BaWO_4$ nanorods, respectively. Solid-solution $Sr_{1-x}Ca_xWO_4$ and $Ba_{1-x}Sr_xWO_4$ nanorods, respectively, were prepared by mixing relevant molar ratios of either $CaCl_2$ and $SrCl_2$ or $SrCl_2$ and $Ba(NO)_3$ solutions, respectively, depending on the desired nanostructure, into the appropriate U-tube half cell containing the metal ions. The system was then left unperturbed for an incubation period of up to 1 day at room temperature. Subsequent to immersion, the polycarbonate membrane was detached, sonicated for about 2 min to remove unwanted particles on the surface, and thoroughly washed with distilled water prior to being dissolved in methylene chloride solution. As-prepared tungstate nanorods were collected from solution by centrifugation after washing.

As a typical protocol for functionalizing nanorods with capping ligands, 5 mg of as-prepared $CaWO_4$ nanorods were dispersed in 10 mL of distilled, deionized water and subsequently stirred with 0.5 g/L of either poly(acrylic acid) (PAA) or sodium oleate for 1 day. Isolated nanorod precipitates were cleaned by washing multiple times with distilled, deionized water.

3.2.2 **Materials Characterization**

X-ray Powder Diffraction See Section 1.7.1.

X-ray Photoelectron Spectroscopy See Section 1.7.2.

Electron Microscopy See Section 1.7.3.

Optical Spectroscopy See Section 1.7.5.

Time-resolved emission spectra were measured at room temperature using a Varian Cary-Eclipse fluorescence spectrometer. The excitation wavelength used for our lifetime measurements was 190 nm as it yielded the strongest luminescence signals. Spectra were measured at 502 nm with a 2 μs gate time.

3.3 Results and Discussion

3.3.1 X-ray Diffraction

The purity and crystallinity of the two series of as-prepared $Sr_{1-x}Ca_xWO_4$ and $Ba_{1-x}Sr_xWO_4$ ($0 \leq x \leq 1$) nanorods were initially characterized using powder XRD. Figure 3.2A shows diffraction patterns collected from five $Sr_{1-x}Ca_xWO_4$ samples of varying compositions in the 2θ range of 10-80°. Very little if any elemental impurity peaks were noted. All of the diffraction peaks for Sample 1 in Figure 3.2A can be readily indexed to the pure body-centered tetragonal phase [space group $I4_1/a$] of $CaWO_4$, with calculated lattice constants of a = 5.240 $\pm$ 0.011 Å and c = 11.371 $\pm$ 0.016 Å, which are in good agreement with the literature values of their corresponding bulk counterpart (a = 5.242 Å, c = 11.372 Å, JCPDS File No. 07-0210). Similarly, diffraction peaks for Sample 5 in Figure 1A can be ascribed to a pure body-centered tetragonal phase [space group $I4_1/a$] of $SrWO_4$ with accompanying lattice constants of a = 5.414 $\pm$ 0.016 Å and c = 11.950 $\pm$ 0.015 Å, which are comparable in value with the corresponding reported data of a = 5.417 Å and c = 11.951 Å (JCPDS File No. 08-0490) for the bulk.

When we more carefully analyzed all five XRD patterns in Figure 3.2A simultaneously, we generally observed that each peak for $Sr_{1-x}Ca_xWO_4$ nanorods shifted to a lower 2θ value with increasing Sr concentration. For example, Figure 3.2B illustrates XRD peak behavior at 2θ values between 25° and 30° for all five samples. It can be clearly observed that the (112) peak initially corresponding to the tetragonal phase of $CaWO_4$ gradually shifts to lower 2θ positions as a function of composition, eventually transforming into the (112) peak of the tetragonal phase of $SrWO_4$. The exact (112) peak 2θ positions for the five samples were located at 28.80°, 28.38°, 28.08°, 27.96°, and 27.70°, corresponding to nanorod compositions of $CaWO_4$, $Sr_{0.3}Ca_{0.7}WO_4$, $Sr_{0.5}Ca_{0.5}WO_4$, $Sr_{0.7}Ca_{0.3}WO_4$, and $SrWO_4$, respectively. Calculated unit-cell lattice parameters, namely,

a and **c**, assuming tetragonal $Sr_{1-x}Ca_xWO_4$, varied effectively monotonically with composition change, as shown in Figure 3.3 and in agreement with Vegard's law, described as follows in eqs 1 and 2

$$\mathbf{a}(Sr_{1-x}Ca_xWO_4) = \mathbf{a}(CaWO_4)+(1-x)[\mathbf{a}(SrWO_4) - \mathbf{a}(CaWO_4)] \quad (1)$$

$$\mathbf{c}(Sr_{1-x}Ca_xWO_4) = \mathbf{c}(CaWO_4)+(1-x)[\mathbf{c}(SrWO_4) - \mathbf{c}(CaWO_4)] \quad (2)$$

Our results are consistent with a previously observed data sequence for a continuous compositional range of $Sr_{1-x}Ca_xWO_4$ films. It should be noted that neither an apparent phase separation nor a separate nucleation of either $CaWO_4$ or $SrWO_4$ was observed in the alloyed solid-state solutions.[32]

By analogy, X-ray diffraction patterns of $Ba_{1-x}Sr_xWO_4$ ($0 \leq x \leq 1$) nanorods are shown in Figure 3.2C. All of the diffraction peaks for each of the samples shifted to lower 2θ positions upon increasing the Ba concentration. Unit-cell parameters for $Ba_{1-x}Sr_xWO_4$ changed continuously from $a = 5.414 \pm 0.016$ Å and $c = 11.950 \pm 0.015$ Å for tetragonal $SrWO_4$ ($x = 1$) to $a = 5.610 \pm 0.021$ Å and $c = 12.716 \pm 0.018$ Å for tetragonal $BaWO_4$ ($x = 0$). These unit-cell values correlate well with reported database numbers for the corresponding pure tungstates (i.e., JCPDS File Nos. 08- 0490 and 08-0457), respectively. Figure 3.2D shows the behavior of the (112) peak, corresponding to the tetragonal phase of $Ba_{1-x}Sr_xWO_4$ in greater detail. When the value of 'x' changes systematically from 1 to 0, the peak positions shifted continuously from 27.70° to 26.48° with decreasing Sr concentration in each of the five samples. Calculated unit cell lattice parameters, assuming tetragonal $Ba_{1-x}Sr_xWO_4$, varied essentially monotonically with systematic composition change, as shown in Figure 3.4 and in agreement with Vegard's law, described as follows in eqs 3 and 4

$$\mathbf{a}(Ba_{1-x}Sr_xWO_4) = \mathbf{a}(SrWO_4)+(1-x)[\mathbf{a}(BaWO_4) - \mathbf{a}(SrWO_4)] \quad (3)$$

$$\mathbf{c}(Ba_{1-x}Sr_xWO_4) = \mathbf{c}(SrWO_4)+(1-x)[\mathbf{c}(BaWO_4) - \mathbf{c}(SrWO_4)] \quad (4)$$

Our results are consistent with a previously observed data sequence for a continuous compositional range of electrochemically prepared $Ba_{1-x}Sr_xWO_4$ solid-solution films.[33] By analogy, neither a noted phase separation nor a separate nucleation of either $BaWO_4$ or $SrWO_4$ was apparent for these alloyed solid-state solution samples.

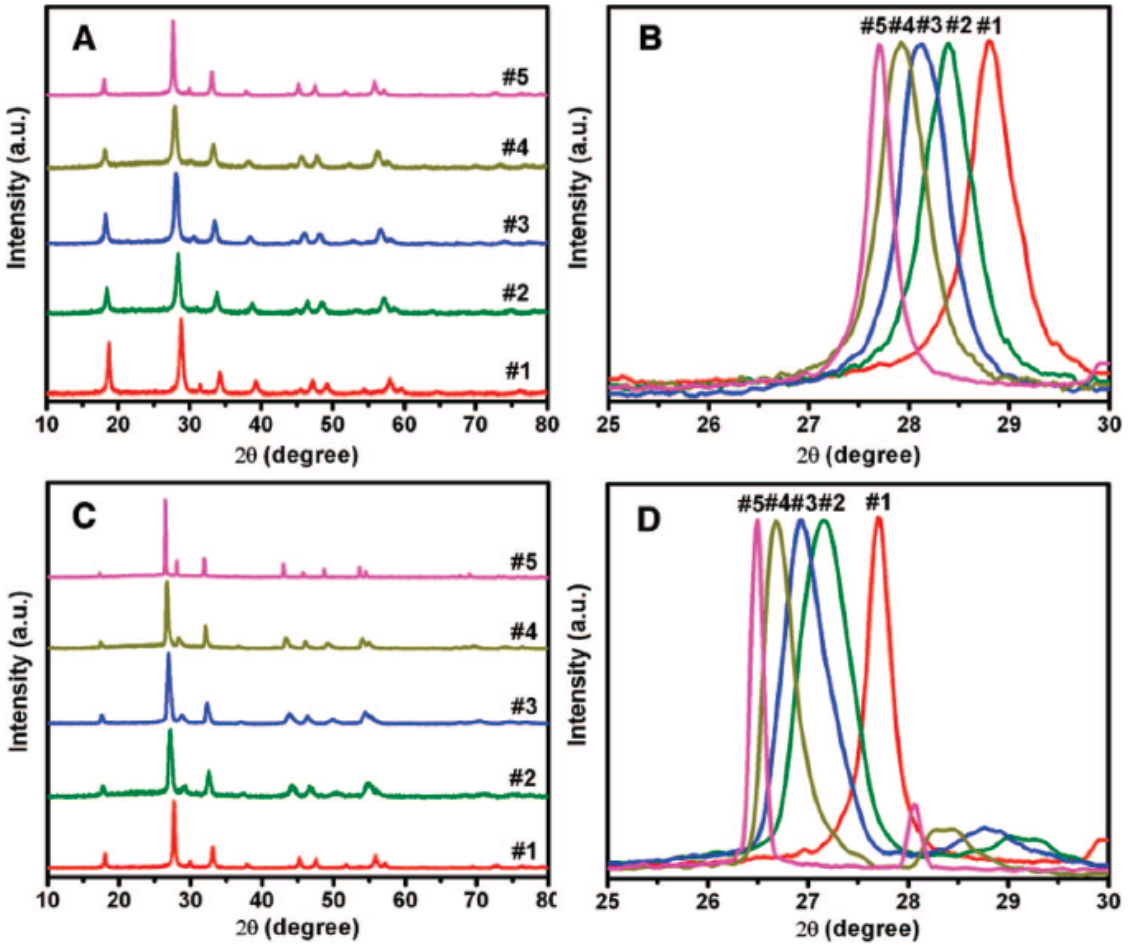

Figure 3.2 (A) XRD patterns of as-prepared $Sr_{1-x}Ca_xWO_4$ nanorod samples in the 2θ range of 10-80°: (1) $CaWO_4$, (2) $Sr_{0.3}Ca_{0.7}WO_4$, (3) $Sr_{0.5}Ca_{0.5}WO_4$, (4) $Sr_{0.7}Ca_{0.3}WO_4$, and (5) $SrWO_4$. Labels and colors are identical for B. (B) Expanded view of the 2θ diffraction peaks between 25° and 30° for all five of the $Sr_{1-x}Ca_xWO_4$ nanorod samples. (C) XRD patterns of as-prepared $Ba_{1-x}Sr_xWO_4$ nanorod samples in the 2θ range of 10-80°: (1) $SrWO_4$, (2) $Ba_{0.3}Sr_{0.7}WO_4$, (3) $Ba_{0.5}Sr_{0.5}WO_4$, (4) $Ba_{0.7}Sr_{0.3}WO_4$, and (5) $BaWO_4$. Labels and colors are identical for D. (D) Expanded view of the 2θ diffraction peaks between 25° and 30° for all five of the $Ba_{1-x}Sr_xWO_4$ nanorod samples.

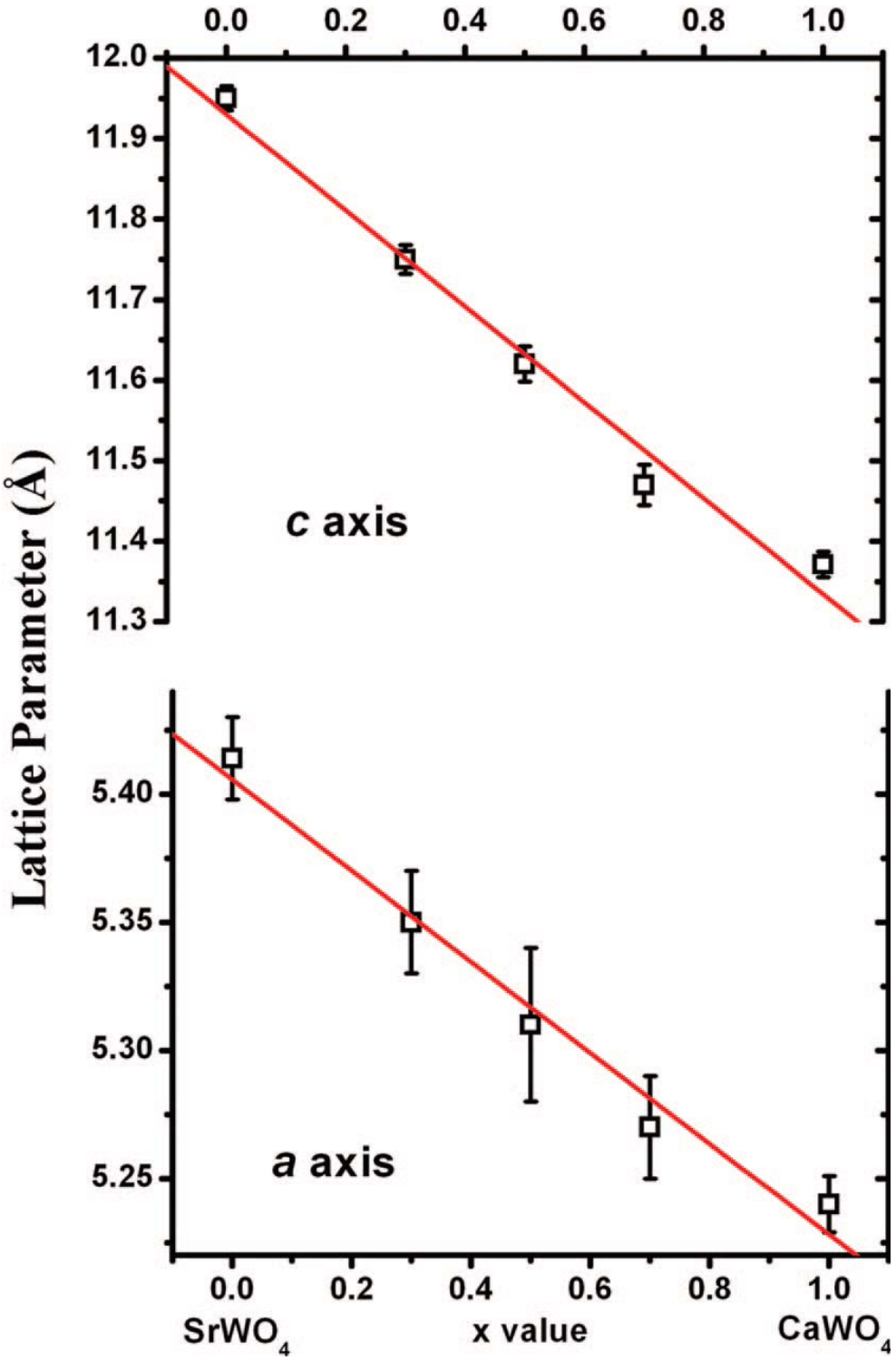

Figure 3.3 Systematic variation of the lattice parameters associated with $Sr_{1-x}Ca_xWO_4$ nanorods as a function of solid-solution composition.

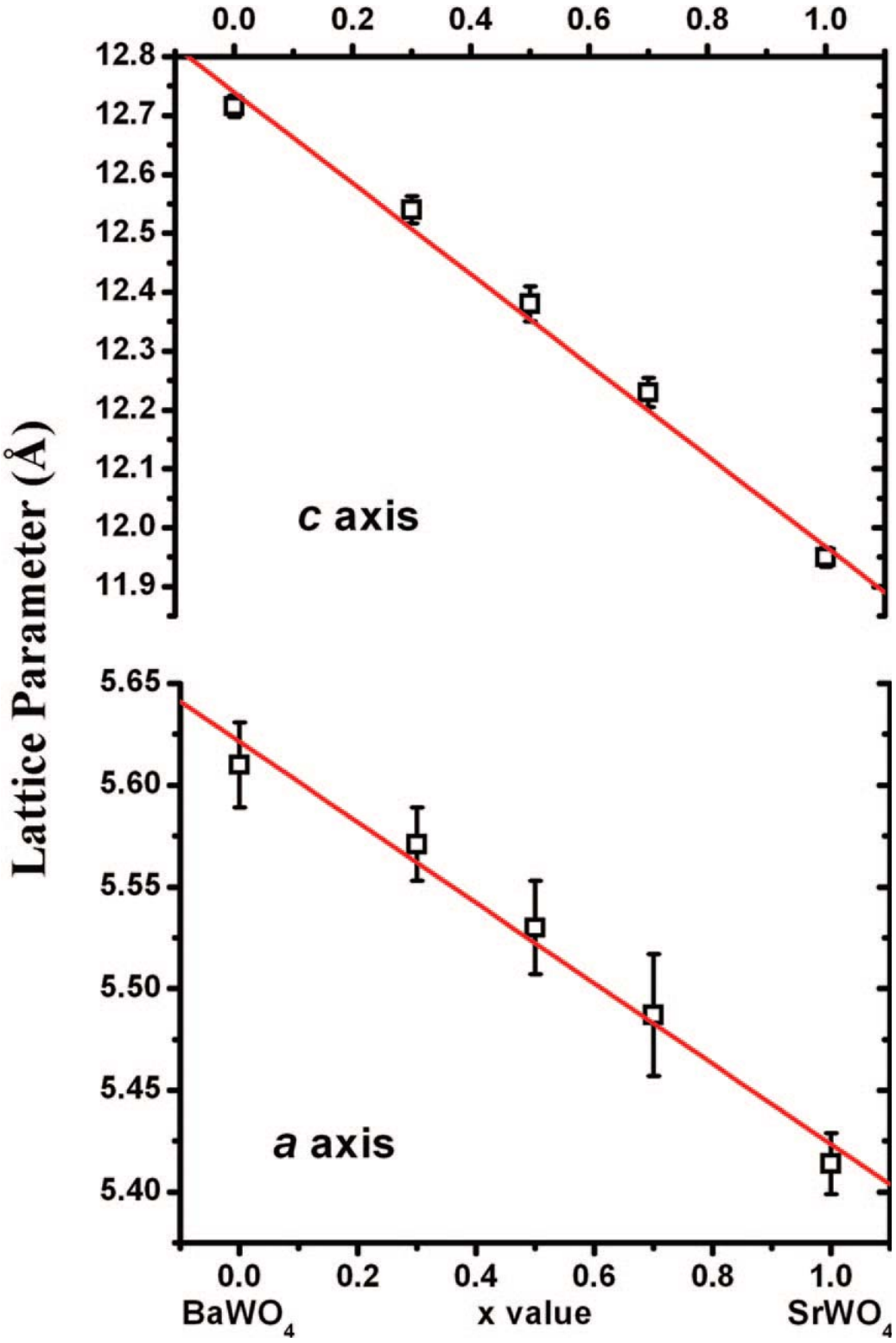

Figure 3.4 Systematic variation of the lattice parameters associated with $Ba_{1-x}Sr_xWO_4$ nanorods as a function of solid-solution composition.

3.3.2 X-ray Photoelectron Spectroscopy

The survey X-ray photoelectron spectroscopy (XPS) spectra collected on successive

$Sr_{1-x}Ca_xWO_4$ nanorod samples (where x = 0.7, 0.5, 0.3) are shown in Figure 3.5. Peak values localized at 34.8, 132.4, 530.1, and 346.9 eV can be readily assigned to the binding energies of W 4f, Sr 3d, O 1s, and Ca 2p, respectively. It is evident that the amount of Sr gradually decreases while that of Ca systematically increases with increasing x values in this series of samples. By XPS, the atomic ratio of Ca:Sr content was found to vary from 2.5:1, 1.1:1, and finally to 0.46:1 as the molar value of 'x' was systematically altered from 0.7, 0.5, to 0.3 in the precursor solutions. These experimental data are in acceptable agreement with the calculated atomic ratios of Ca:Sr, which theoretically ought to have altered from 2.3:1, 1:1, and ultimately to 0.43:1 with the corresponding variation in solid-solution composition.

Figure 3.6 shows typical high-resolution XPS spectra of as-prepared $Sr_{0.3}Ca_{0.7}WO_4$ nanorod samples. The Ca 2p peaks and Sr 3d peak (Figure 3.6A and 3.6B) are consistent with the oxidation states of Ca and Sr, as both being +2, respectively, which also supports the notion that Ca ions can be randomly substituted by Sr ions within the scheelite structure.[32] Moreover, the W 4f and O 1s spectra (Figure 3.6C and 3.6D) are consistent with oxidation states of W^{6+} and $O^{2-,}$ respectively, which would be expected from the anticipated formation of WO_4^{2-} groups in these nanoscale samples.[53] Similar high-resolution XPS spectra have been obtained for as-prepared $Sr_{0.5}Ca_{0.5}WO_4$ and $Sr_{0.7}Ca_{0.3}WO_4$ nanorod samples (Figure 3.7 and 3.8).

Survey XPS spectra collected on $Ba_{0.3}Sr_{0.7}WO_4$ and $Ba_{0.5}Sr_{0.5}WO_4$ nanorod samples (Figure 3.9) also highlight the systematic variation of Sr and Ba content with corresponding changes in the magnitude of 'x' values. By XPS, the atomic ratio of Sr: Ba content was found to vary from 2.7:1 and 1.3:1 for $Ba_{0.3}Sr_{0.7}WO_4$ and $Ba_{0.5}Sr_{0.5}WO_4$ nanorod solid solutions, respectively. These experimental data are in reasonable agreement with the calculated atomic ratios of Sr:Ba, which theoretically ought to have altered from 2.3:1 to 1:1 with the corresponding variation in solid solution composition. Moreover, detailed information on the intrinsic nature of the chemical bonding in these

systems was collected using high-resolution XPS spectra, as shown in Figures 3.10 and 3.11. The Sr 3d and Ba 3d peaks (Figure 3.10A and 3.10B), located at 132.4 and 779.5 eV for $Ba_{0.3}Sr_{0.7}WO_4$ nanorods, are consistent with the oxidation states of Ba and Sr, as both being +2, respectively, which also supports the notion that Ba ions can be randomly substituted by Sr ions within the scheelite structure.[54] Figure 3.10C and 3.10D further confirm the existence of WO_4^{2-} groups in these nanorod samples.

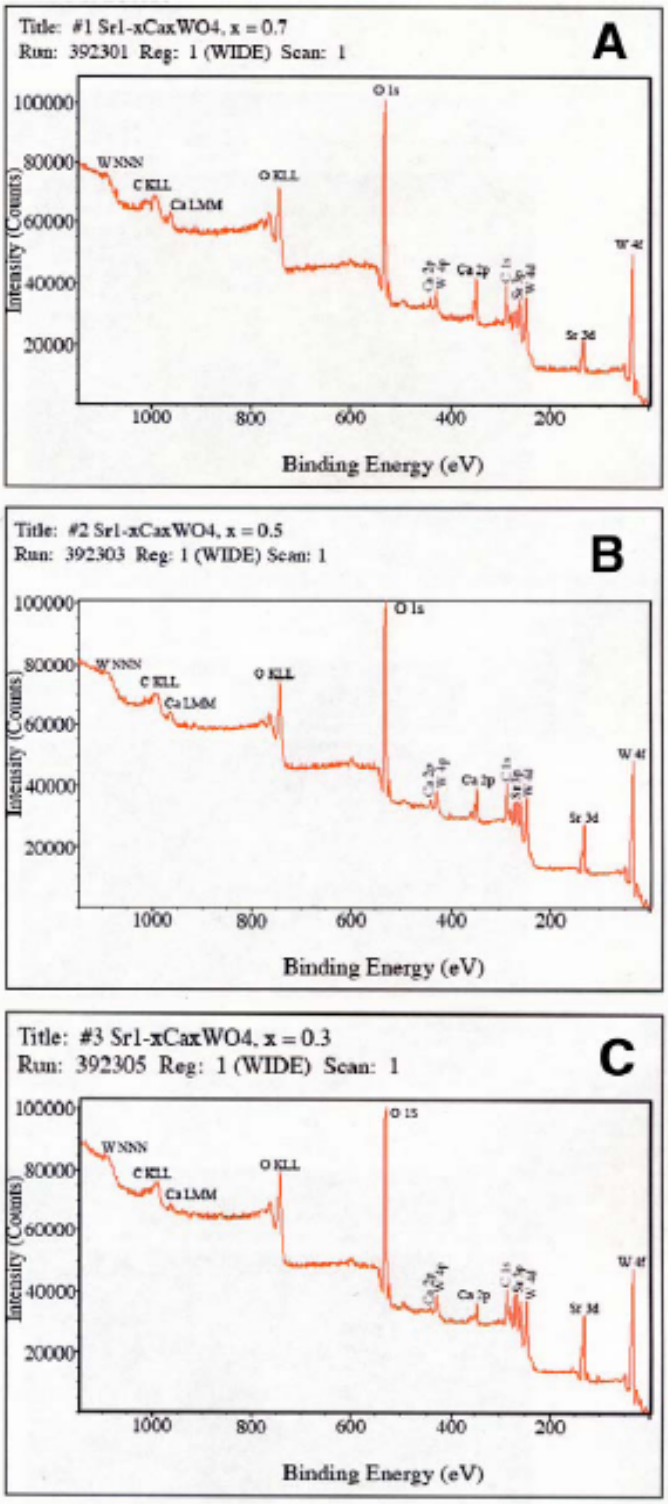

Figure 3.5 Survey XPS spectra of as-prepared $Sr_{1-x}Ca_xWO_4$ nanorod samples: (A) $Sr_{0.3}Ca_{0.7}WO_4$, (B) $Sr_{0.5}Ca_{0.5}WO_4$, and (C) $Sr_{0.7}Ca_{0.3}WO_4$.

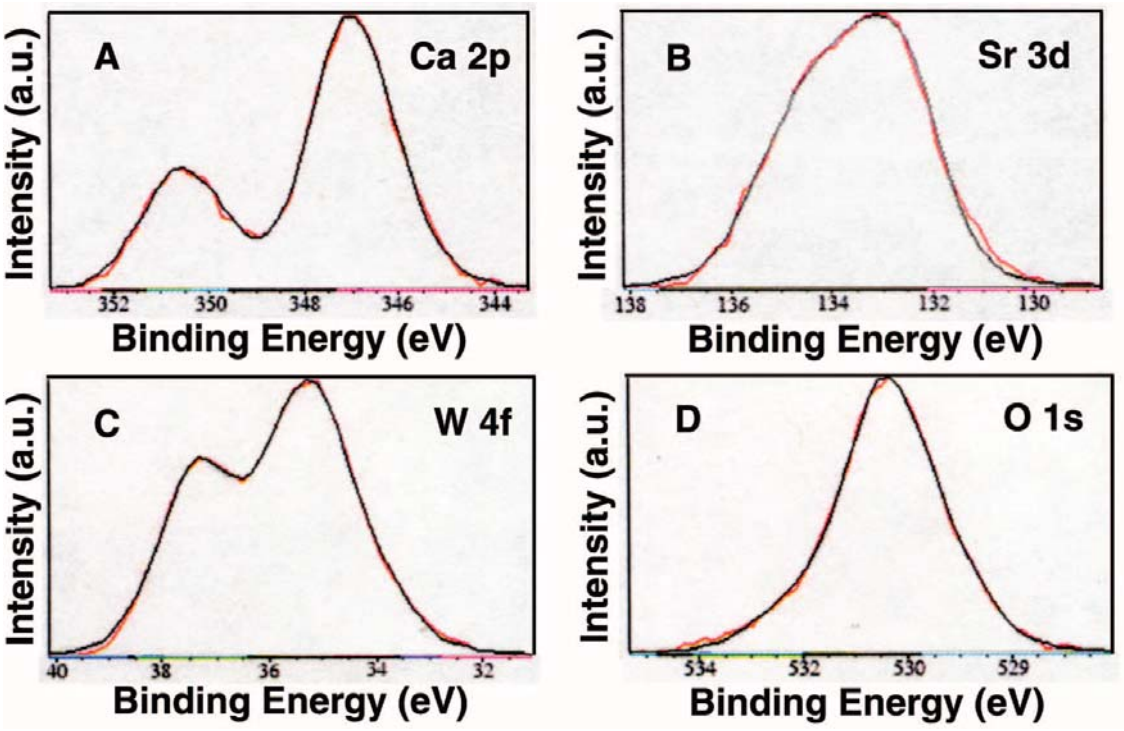

Figure 3.6 XPS spectra of as-prepared $Sr_{0.3}Ca_{0.7}WO_4$ nanorod samples: (A) Ca 2p spectrum, (B) Sr 3d spectrum, (C) W 4f spectrum, and (D) O 1s spectrum.

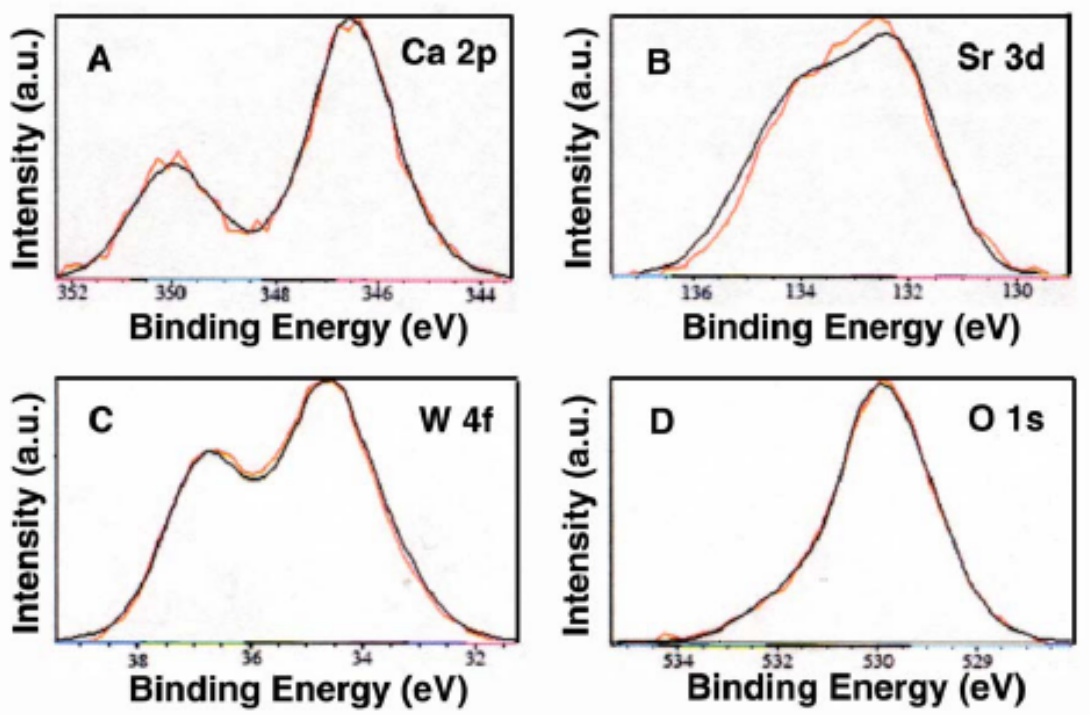

Figure 3.7 High-resolution XPS spectra of as-prepared $Sr_{0.5}Ca_{0.5}WO_4$ nanorod samples. (A) Sr 3d spectrum, (B) Ba 3d spectrum, (C) W 4f spectrum, and (D) O 1s spectrum.

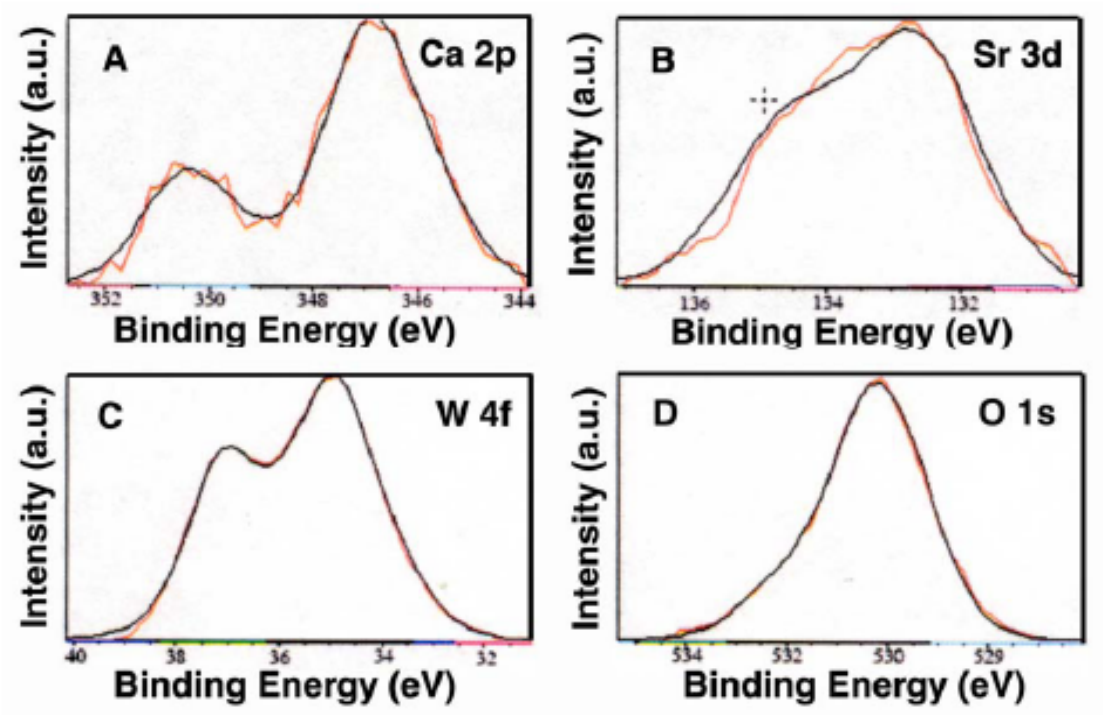

Figure 3.8 High-resolution XPS spectra of as-prepared $Sr_{0.7}Ca_{0.3}WO_4$ nanorod samples. (A) Sr 3d spectrum, (B) Ba 3d spectrum, (C) W 4f spectrum, and (D) O 1s spectrum.

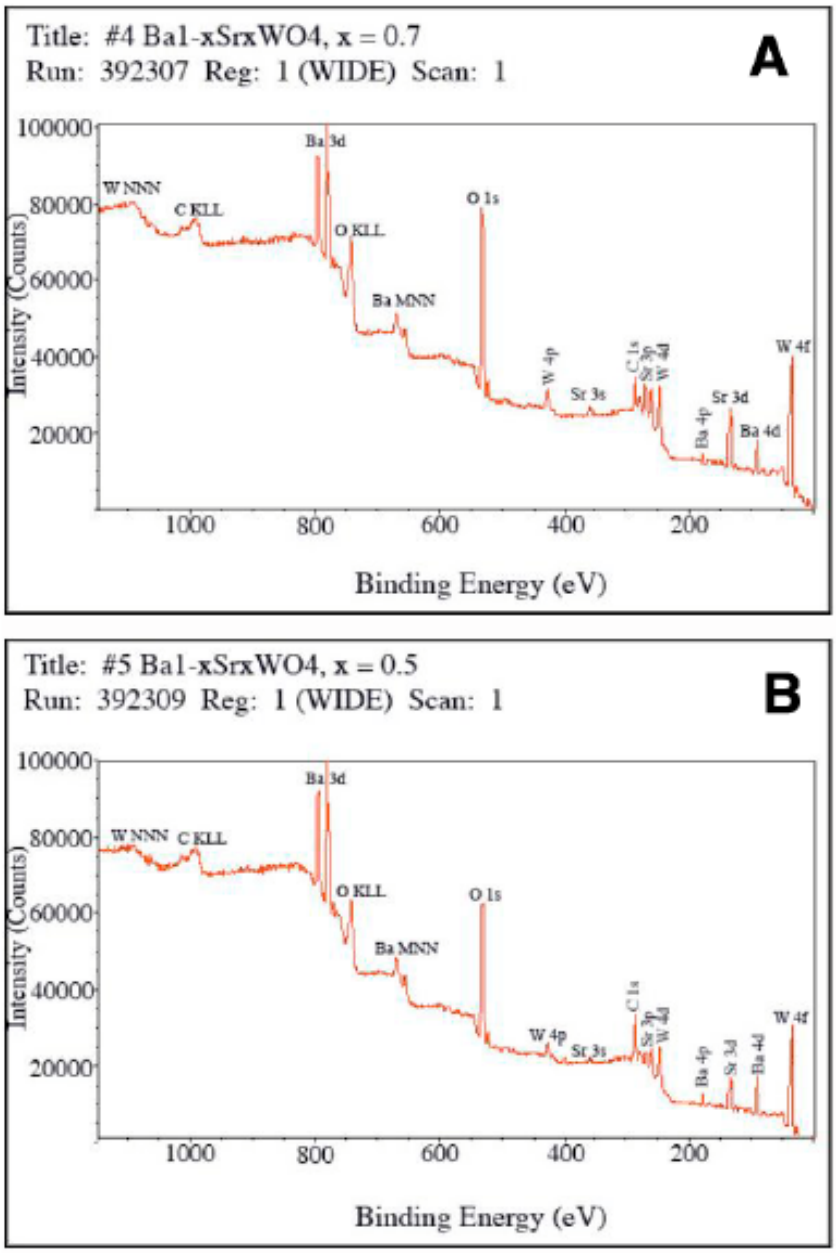

Figure 3.9 Survey XPS spectra of the as-prepared $Ba_{1-x}Sr_xWO_4$ nanorod samples: (A) $Ba_{0.3}Sr_{0.7}WO_4$, and (B) $Ba_{0.5}Sr_{0.5}WO_4$.

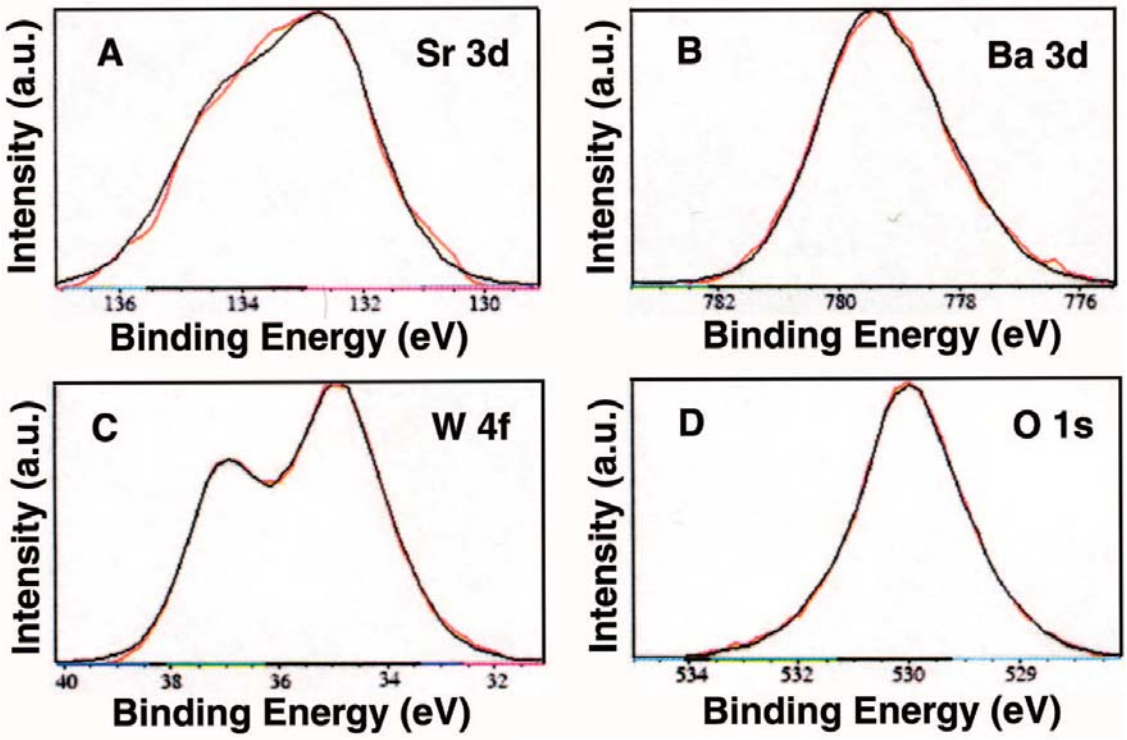

Figure 3.10 XPS spectra of as-prepared $Ba_{0.3}Sr_{0.7}WO_4$ nanorod samples: (A) Sr 3d spectrum, (B) Ba 3d spectrum, (C) W 4f spectrum, and (D) O 1s spectrum.

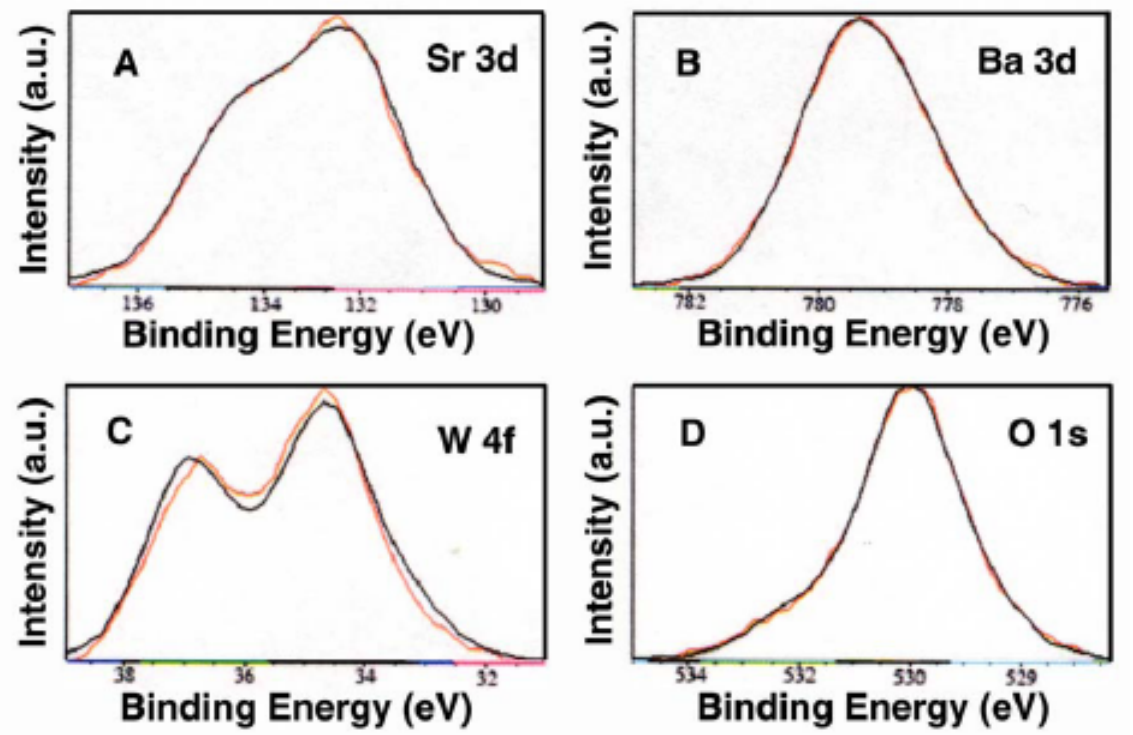

Figure 3.11 High-resolution XPS spectra of as-prepared $Ba_{0.5}Sr_{0.5}WO_4$ nanorod samples. (A) Sr 3d spectrum, (B) Ba 3d spectrum, (C) W 4f spectrum, and (D) O 1s spectrum.

3.3.3 Electron Microscopy

Figure 3.12 shows SEM images and the corresponding EDS data of all five as-prepared $Sr_{1-x}Ca_xWO_4$ (where x = 1, 0.7, 0.5, 0.3, and 0) nanorod samples, which were fabricated using polycarbonate membranes with pore sizes as small as 50 nm. It can be observed that all the products of (A) $CaWO_4$, (B) $Sr_{0.7}Ca_{0.3}WO_4$, (C) $Sr_{0.5}Ca_{0.5}WO_4$, (D) $Sr_{0.3}Ca_{0.7}WO_4$, and (E) $SrWO_4$ mainly consist of straight and smooth nanorods with uniform, homogeneous size along their axis direction. By analyzing magnified SEM images of these five samples, as shown in the insets of Figure 3.12A-E, diameters of the wire-like nanorods obtained were noted to be in the range of 50 $\pm$ 5 nm, based on the corresponding as-reported 50 nm pore sizes of the commercial templates used in the synthesis. Measured lengths of the five $Sr_{1-x}Ca_xWO_4$ nanorods varied from one to several micrometers with an average value of 2.8 μm, somewhat shorter than the entire thickness of the membrane, which measures about 6 μm. One possible explanation is that longitudinal nanorod growth is limited to some extent by the availability and accessibility of precursor ions. That is, this parameter is determined not only by the overall reaction time but also by the growth rate of the nanorod diameter across the width of the template pores; at a certain point, the increasing nanorod diameter may become sufficiently large to physically block access to ion diffusion through the membrane. In addition, we should note that the sonication step involved in SEM sample preparation may also have physically shortened some of the nanorods. It is noteworthy that the SEM images were obtained from randomly selected areas of all of the five samples and as such are representative of the overall sizes and shapes of as-prepared $Sr_{1-x}Ca_xWO_4$ nanorods. It is reasonable to conclude that the ultimate morphology of each product accurately replicated the internal pore structure and morphology of the originating polycarbonate membranes and that this factor was independent of the chemical composition of the corresponding $Sr_{1-x}Ca_xWO_4$ solid solutions.

Moreover, in every $Sr_{1-x}Ca_xWO_4$ nanorod sample analyzed by EDS (Figure 3.12F), chemical signatures taken within different parts of each of the samples were noted to be identical within experimental accuracy, and all of the as- prepared nanorods were essentially composed of elements such as Ca and/or Sr, W, and O, as expected. The Sr

signals overlapped with W signals in the energy scale at around 1.9 keV. In the normalized data, the intensities of the Ca signals gradually decrease with either increasing Sr content or decreasing values of x in the $Sr_{1-x}Ca_xWO_4$ system. The actual overall atomic content of Ca for each sample varied from 16.7%, 11.5%, 9.1%, 5.5%, to 0%, corresponding to molar values of 'x' = 1, 0.7, 0.5, 0.3, and 0. On the basis of calculation, the theoretical content of Ca in the corresponding sample systems would have been expected to alter from 16.7%, 11.7%, 8.3%, 5.0%, to 0%, respectively, which is in reasonable agreement with experiment. Moreover, this result is consistent with our previously described XPS spectral observations, reinforcing the notion that the chemical compositions of the product $Sr_{1-x}Ca_xWO_4$ nanorod solid solutions are primarily dictated by the initial chemical concentrations of the precursor solutions.

Analogous SEM and EDS data for as-synthesized $Ba_{1-x}Sr_xWO_4$ system are shown in Figure 3.13. The microscopy images (Figure 3.13A–E) showed the presence of dispersed individual nanorods as well as of bundled, aggregated species. In particular, Figure 3.13E highlights $BaWO_4$ nanorod arrays, where the nanorods are roughly parallel to each other so as to form an aggregate of arrays. All of the straight and crystalline $Ba_{1-x}Sr_xWO_4$ nanorods in Figure 3.13A-E possessed diameters ranging from 90 to 112 nm and lengths spanning from 2.5 to 5 μm. These nanorods maintained a uniform diameter of around 100 nm throughout their entire length, corresponding to the as-reported 100 nm pore size of the commercial polycarbonate membranes used as templates. Surfaces of these one-dimensional nanostructures were found to be relatively smooth over most of their lengths. EDS spectra (Figure 3.13F) were taken at a number of selected positions along all five of the $Ba_{1-x}Sr_xWO_4$ samples. Elemental signatures obtained were found to be identical within experimental accuracy, and essentially only Sr and/or Ba, W, and O were detected, as expected. Moreover, it was determined from these data that the peak intensity, representing the atomic content of Ba, increased from 0%, 4.6%, 8.3%, 10.7%, to 15.2% as the value of 'x' decreased from 1, 0.7, 0.5, 0.3, to 0 in the $Ba_{1-x}Sr_xWO_4$ system. Our calculations show that Ba content should have altered from 0%, 5.0%, 8.3%, 11.7%, to 16.7% with a systematic decrease in 'x' over the same range of chemical composition in this solid-solution system, which agrees favorably with our actual results.

In addition, our data corroborate previously described XPS measurements, suggesting that the resultant chemical compositions of $Ba_{1-x}Sr_xWO_4$ nanorod solid solutions are mainly determined by the initial chemical concentrations of the precursor solutions.

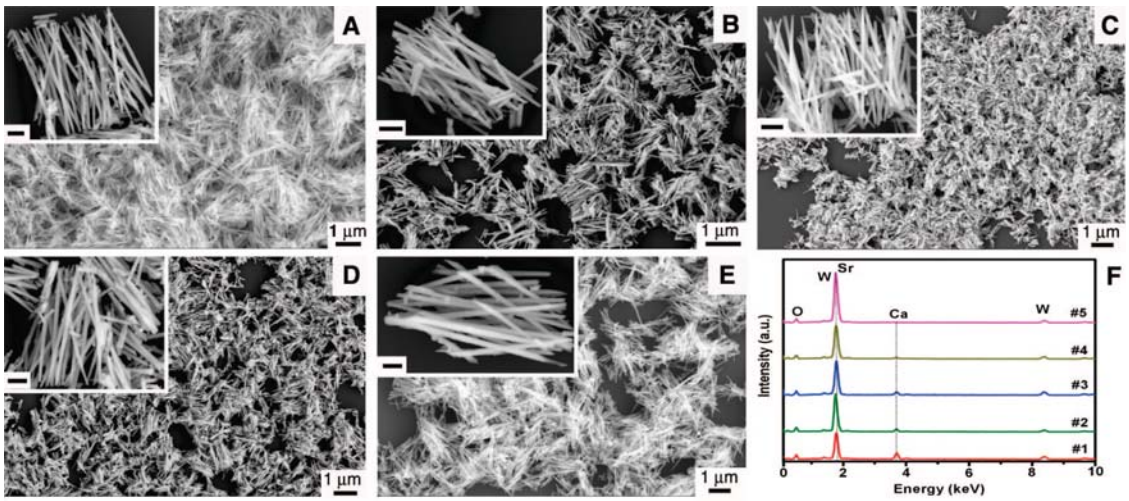

Figure 3.12 Representative SEM images of as-prepared $Sr_{1-x}Ca_xWO_4$ nanorod samples generated using polycarbonate membranes composed of 50-nm pore sizes: (A) $CaWO_4$, (B) $Sr_{0.3}Ca_{0.7}WO_4$, (C) $Sr_{0.5}Ca_{0.5}WO_4$, (D) $Sr_{0.7}Ca_{0.3}WO_4$, and (E) $SrWO_4$. Associated insets show corresponding magnified views of the as-generated products. Scale bars in the insets are 200 nm. (F) EDS spectra of all five of the $Sr_{1-x}Ca_xWO_4$ nanorods: (1) $CaWO_4$, (2) $Sr_{0.3}Ca_{0.7}WO_4$, (3) $Sr_{0.5}Ca_{0.5}WO_4$, (4) $Sr_{0.7}Ca_{0.3}WO_4$, and (5) $SrWO_4$. Intensities of the peaks for each of the samples have been normalized based on the intensity of the second W peak.

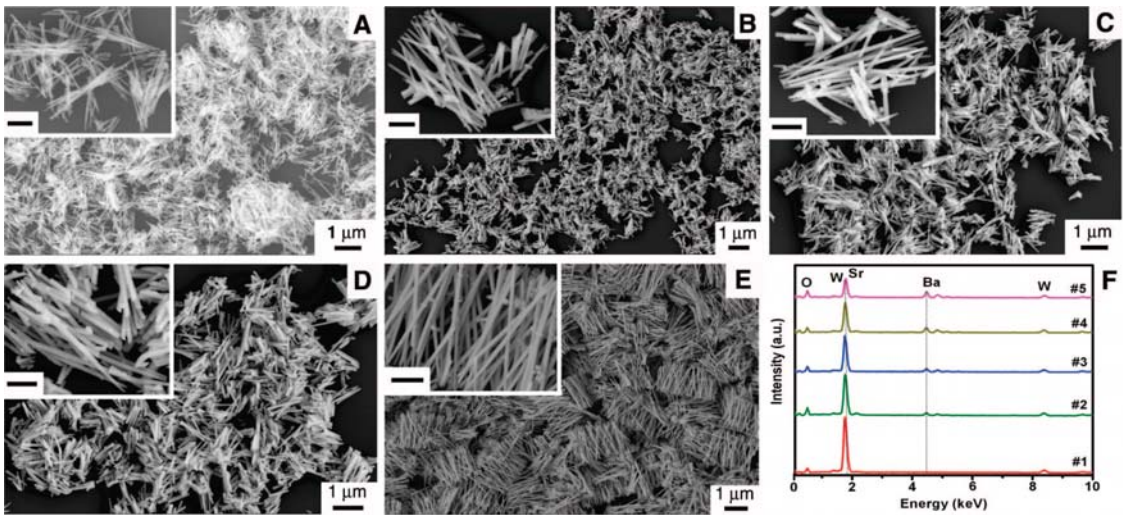

Figure 3.13 Typical SEM images of as-prepared $Ba_{1-x}Sr_xWO_4$ nanorod samples generated using polycarbonate membranes composed of 100-nm pore sizes: (A) $SrWO_4$, (B) $Ba_{0.3}Sr_{0.7}WO_4$, (C) $Ba_{0.5}Sr_{0.5}WO_4$, (D) $Ba_{0.7}Sr_{0.3}WO_4$, and (E) $BaWO_4$. Associated insets show corresponding magnified views of the as-generated products. Scale bars in the insets are 200 nm. (F) EDS spectra of all five of the $Ba_{1-x}Sr_xWO_4$ nanorods: (1) $SrWO_4$, (2) $Ba_{0.3}Sr_{0.7}WO_4$, (3) $Ba_{0.5}Sr_{0.5}WO_4$, (4) $Ba_{0.7}Sr_{0.3}WO_4$, and (5) $BaWO_4$. Intensities of the peaks for each of the samples have been normalized based on the intensity of the second W peak.

To provide additional details into the nature of the morphology and crystallographic structure of the $Sr_{1-x}Ca_xWO_4$ and $Ba_{1-x}Sr_xWO_4$ solid-solution systems, as-prepared metal oxide nanorod samples were further analyzed by both low- and high-magnification TEM as well as with SAED.

Figure 3.14 shows representative TEM, HRTEM, and SAED images of as-prepared $Sr_{1-x}Ca_xWO_4$ solid-solution nanorods. It can be observed that all the products, prepared using the 50 nm pore size of the polycarbonate membranes, mainly consist of discrete, one-dimensional wire-like nanostructures with smooth outer surfaces and that the as-measured diameters were essentially around 50 nm over much of their lengths. Though these nanorods tended to aggregate fairly easily, as can be seen from their SEM images (Figure 3.13), a further sonication step could readily resolve this problem and generate isolated nanostructures, as shown in the accompanying TEM images.

All of the HRTEM images and SAED patterns taken along a number of selected regions for each of the individual nanorods were effectively indistinguishable within experimental accuracy for every $Sr_{1-x}Ca_xWO_4$ solid-solution sample analyzed. A representative HRTEM image taken from a portion of a randomly chosen single $CaWO_4$ nanorod is shown in Figure 3.14B. The presence of visible, 2D lattice fringes clearly illustrate that the nanorod is single crystalline with little if any defects or dislocations. Interplanar spacings were computed to be about 3.12 and 4.75 Å, which corresponds to the (112) and (101) planes, respectively. The associated electron diffraction pattern shown in the inset can be indexed to the reflection of a pure body-centered tetragonal $CaWO_4$ scheelite structure. The presence of sharp diffraction spots, as opposed to an amorphous ring, further confirms formation of single-crystalline $CaWO_4$ nanorods, whereas conventional template methods typically yield polycrystalline nanostructures. The corresponding structural analyses from HRTEM data and SAED patterns of as-prepared $Sr_{0.3}Ca_{0.7}WO_4$ and $Sr_{0.7}Ca_{0.3}WO_4$ nanorods, measuring 50 nm in diameter, are presented in Figure 3.14D and F, respectively. By analogy, the presence of clearly visible 2D lattice fringes as well as sharp diffraction spots strongly supports generation of single-crystalline nanorods via our modified template-directed method at room temperature and under ambient conditions. In addition, the interplanar spacings, corresponding to the (112)

and (101) planes, respectively, are in good agreement with prior observations noted from the XRD patterns for these materials, corresponding to the tetragonal phase of the scheelite structure.

Similarly, the corresponding TEM images and SAED patterns of the as-prepared $Ba_{1-x}Sr_xWO_4$ solid-solution system, shown in Figure 3.15, confirm the preparation of single-crystalline $Ba_{1-x}Sr_xWO_4$ nanorods with lattice spacing data consistent with complementary observations generated from XRD data. Indeed, the interplanar spacings, which can be ascribed to the (112) and (101) planes, respectively, tended to increase with decreasing values of x or decreasing Sr content in the $Ba_{1-x}Sr_xWO_4$ system. As can be seen from Figure 3.15B, D and F, the lattice spacings, corresponding to the (112) and (101) planes, an increase from 3.24, 3.33, to 3.65 Å and also from 4.95, 5.07, to 5.18 Å, respectively, for the $SrWO_4$, $Ba_{0.5}Sr_{0.5}WO_4$, and $BaWO_4$ nanorod samples. These findings are consistent with the XRD peak behavior we previously detailed as a function of chemical composition. The same trend was also detected in the $Sr_{1-x}Ca_xWO_4$ solid-solution system in Figure 3.14, where lattice spacings appeared to increase with decreasing Ca content. Specifically, for the (112) and (101) planes, lattice spacings increased from 3.12, 3.15, to 3.20 Å as well as from 4.75, 4.83, to 4.87 Å for the $CaWO_4$, $Sr_{0.3}Ca_{0.7}WO_4$ and $Sr_{0.7}Ca_{0.3}WO_4$ nanorod samples, respectively. Overall, these results agreed well with the corresponding behavior for the relevant transitions in the associated XRD peaks.

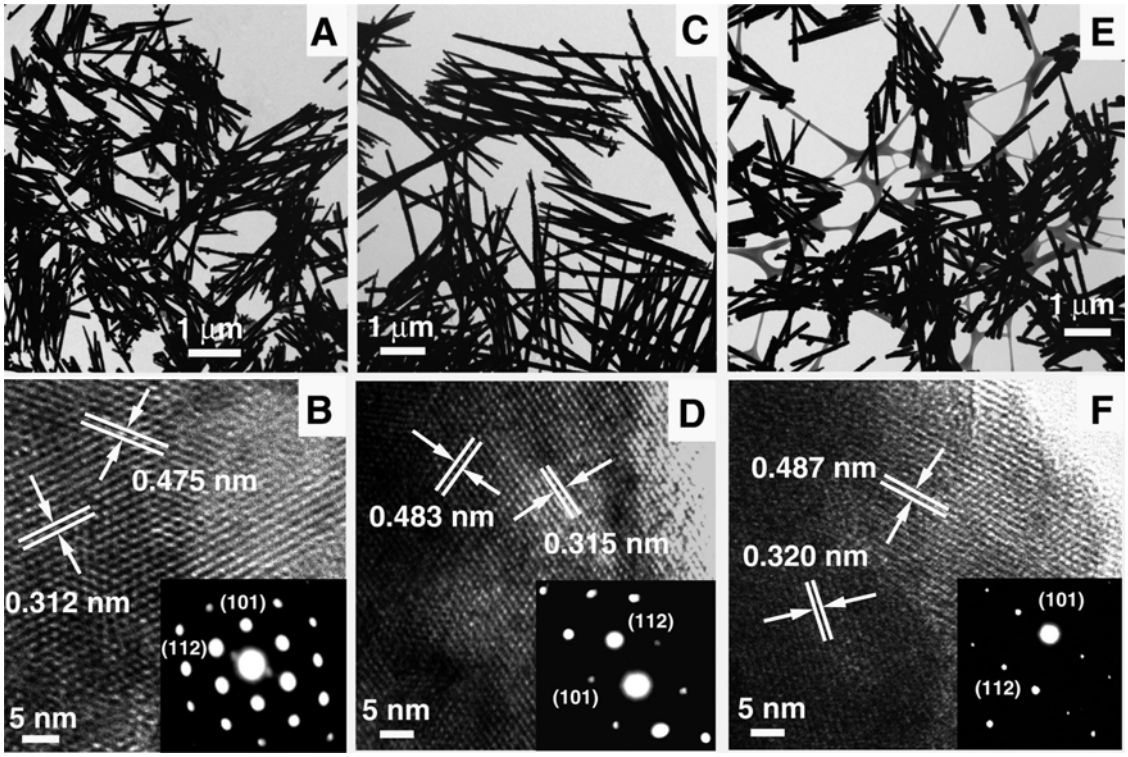

Figure 3.14 Typical TEM images of as-prepared $Sr_{1-x}Ca_xWO_4$ nanorods using polycarbonate membranes composed of 50-nm pore sizes. HRTEM images of representative portions of individual nanorods. Corresponding SAED patterns are shown in the insets: (A, B) $CaWO_4$; (C, D) $Sr_{0.3}Ca_{0.7}WO_4$; (E, F) $Sr_{0.7}Ca_{0.3}WO_4$.

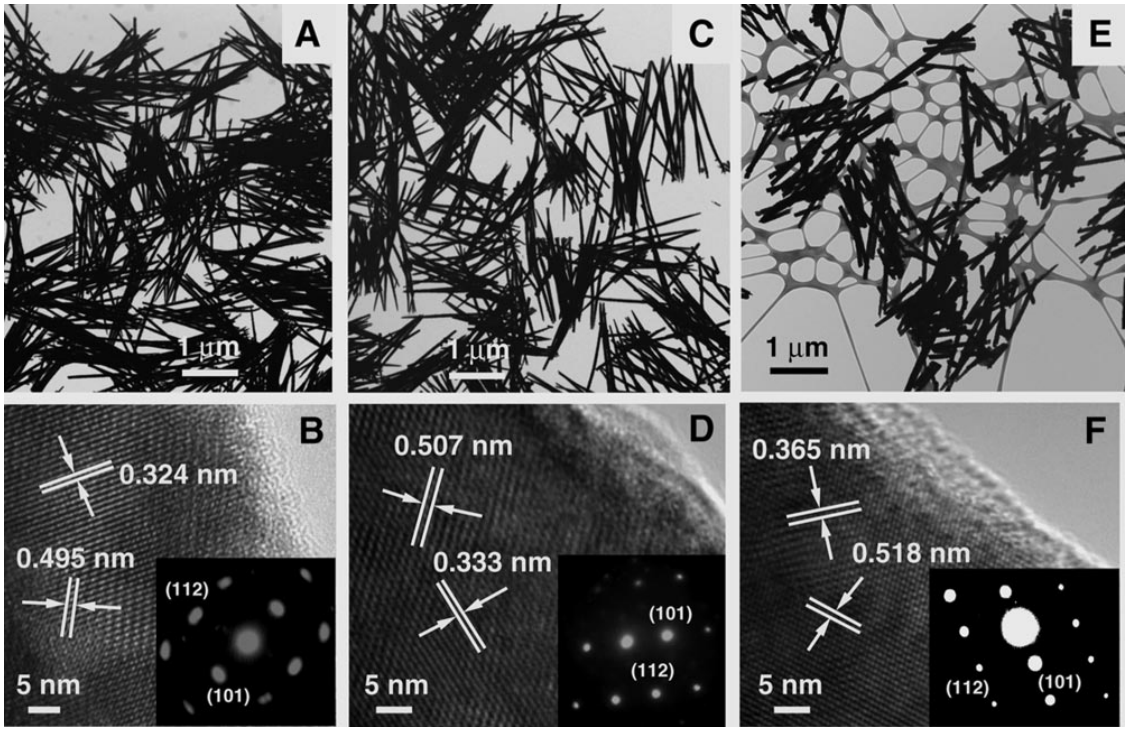

Figure 3.15 Typical TEM images of as-prepared $Ba_{1-x}Sr_xWO_4$ nanorods using polycarbonate membranes composed of 50-nm pore sizes. HRTEM images of representative portions of individual nanorods. Corresponding SAED patterns are shown in the insets: (A, B) $SrWO_4$; (C, D) $Ba_{0.5}Sr_{0.5}WO_4$; (E, F) $BaWO_4$.

3.3.4 Optical Spectroscopy

The optical properties of the as-prepared alkaline-earth-metal tungstate, AWO_4 (A = Ca, Sr, Ba), nanorods were investigated. Figure 3.16 shows the FTIR spectra of $CaWO_4$, $SrWO_4$, and $BaWO_4$ nanorods generated using the 50, 100, or 200 nm pore sizes of the polycarbonate membranes, respectively. The strong absorption band located around 800 cm^{-1} appears in Figure 3.16A of $CaWO_4$ nanorods and likely originates from the W-O antisymmetric stretching vibrational mode, corresponding to the internal ν_3 (B_g) mode in bulk AWO_4-type scheelite oxides.[20, 55, 56] The presence of similar characteristic absorption bands in Figure 3.16B and 3.16C further corroborates the identity of our other as-prepared nanorods as belonging to $SrWO_4$ and $BaWO_4$, respectively, as expected.

As previously mentioned, the emission spectra of scheelite tungstates exhibit a broad luminescence band in the blue spectral region. The as-observed excitonic luminescence can be attributed to a radiative transition within the undisturbed, anionic, tetrahedral WO_4^{2-} complex.[57-60] The photoluminescence behavior of as-prepared nanorods with different diameters (50, 100, or 200 nm) was noted to be similar, showing little discernible diameter dependence. In another series of experiments, we also found out that PL measurements are not dependent on the length distribution of the nanorods either. Specifically, we sonicated as-prepared nanorods for 1 h, yielding $CaWO_4$ and $Ba_{0.5}Sr_{0.5}WO_4$ nanostructures (Figures 3.17A and C) possessing length distributions of 0.83 ± 0.12 and 0.89 ± 0.27 μm, respectively, but were unable to clearly differentiate their optical behavior from that of untreated nanorods (Figures 3.17B and D). It has been previously reported that in some systems, such as ZnO and $PbCrO_4$, PL intensities are susceptible to and will actually increase with increasing nanorod length,[61, 62] presumably due to the lessening influence of defects as the nanorods become longer. We did not observe such an effect herein.

Moreover, we performed additional experiments, coating our nanorods with organic ligands, such as either PAA or oleic acid, to determine potential surface effects on optical behavior. Figure 3.18 shows IR spectroscopy data associated with functional groups present on the surfaces of functionalized $CaWO_4$ nanorods. In Figure 3.18A, for PAA-coated nanorods, the bands at 1230 and 1450 cm^{-1} can be assigned to the

antisymmetric and symmetric vibrational modes of the -COO- group. The band at 1700 cm^{-1} is associated with the stretching mode of the -COOH group. Additionally, the shoulder at 2920 cm^{-1} can be ascribed to the asymmetric stretching mode of $-CH_3$ groups. On the basis of these observations, one can conclude that PAA is bound to the surface of $CaWO_4$ nanorods. In oleic acid-coated nanorods, the band at 2916 cm^{-1} in Figure 3.18B is significantly enhanced, suggesting an increase in quantity of $-CH_3$ groups. All of the remaining bands also suggest adsorption of oleic acid onto the nanorod surface through formation of bidentate bonds.[63, 64] While our data showed that such surfactant capping could definitely yield a more stable dispersion of functionalized nanorods, on the order of days as compared with merely hours for as-prepared nanorods, in aqueous solvents, in agreement with a previous report,[65] PL behavior for our processed tungstate nanorods, though slightly different, was indistinguishable within the limits of experimental error from that of uncapped nanorods (Figure 3.19). By contrast, in general, the presence of capping agents such as either polymer or alkyl amines has been known to either enhance or quench photoluminescence relative to that of the corresponding, unmodified nanorods.[66-68]

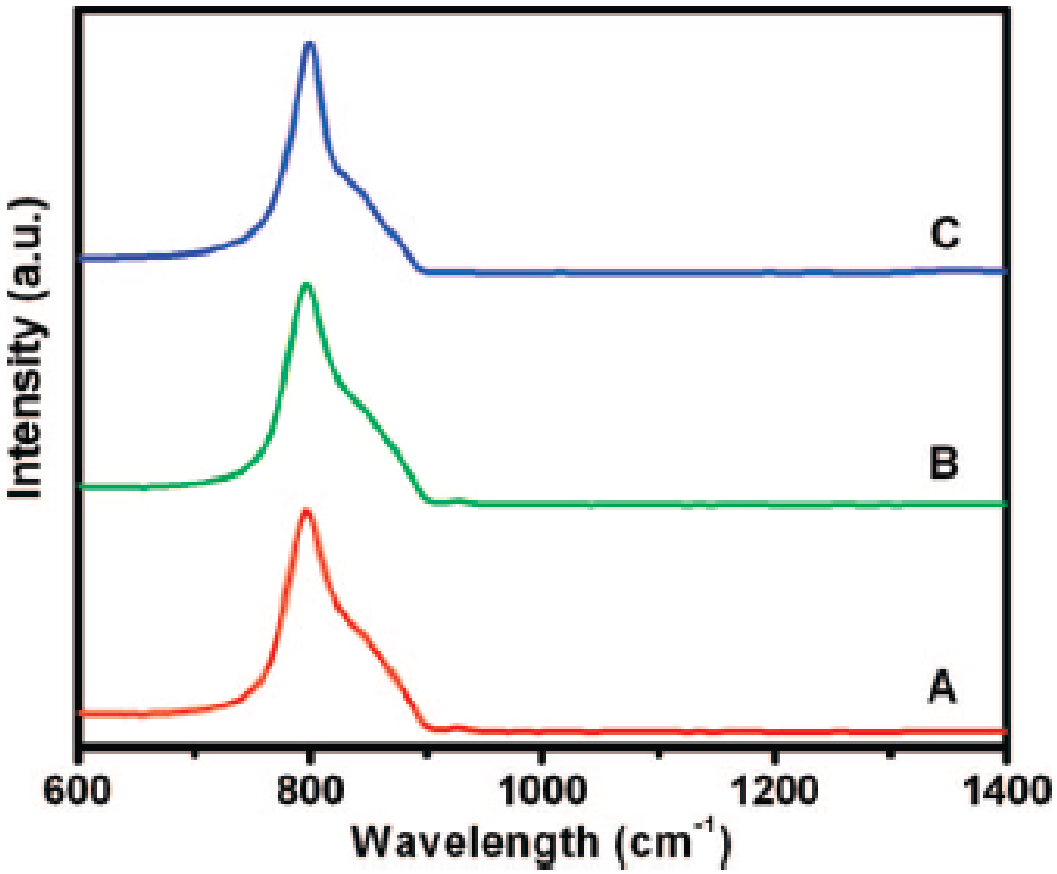

Figure 3.16 FT-IR spectra of as-prepared single-crystalline alkaline-earth-metal tungstate nanorods: (A) $CaWO_4$; (B) $SrWO_4$; (C) $BaWO_4$.

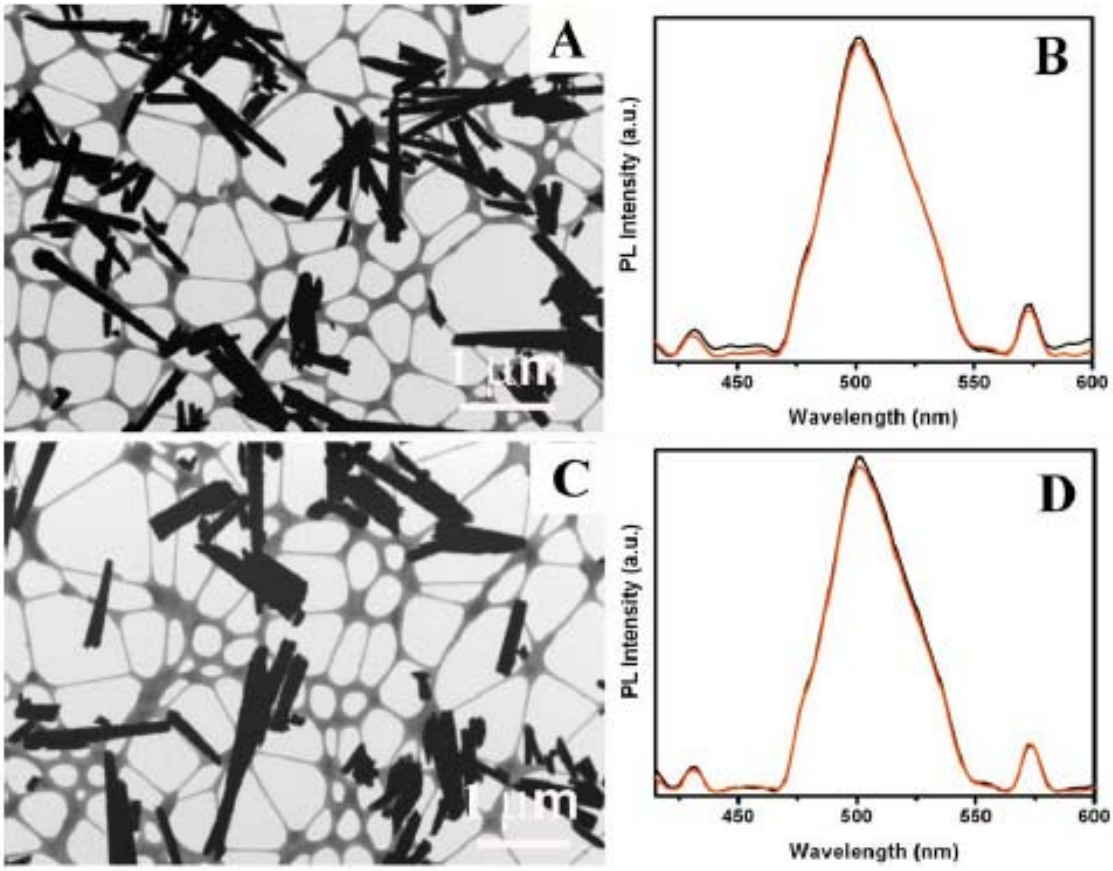

Figure 3.17 (A) TEM image of shortened $CaWO_4$ nanorods prepared from templates measuring 50-nm in diameter after 1 hour of sonication. (B) Corresponding PL spectra of shortened $CaWO_4$ nanorods before (black) and after (red) sonication. (C) TEM image of shortened $Ba_{0.5}Sr_{0.5}WO_4$ nanorods prepared from templates measuring 100-nm in diameter after 1 hour of sonication. (D) Corresponding PL spectra of shortened $Ba_{0.5}Sr_{0.5}WO_4$ nanorods before (black) and after (red) sonication.

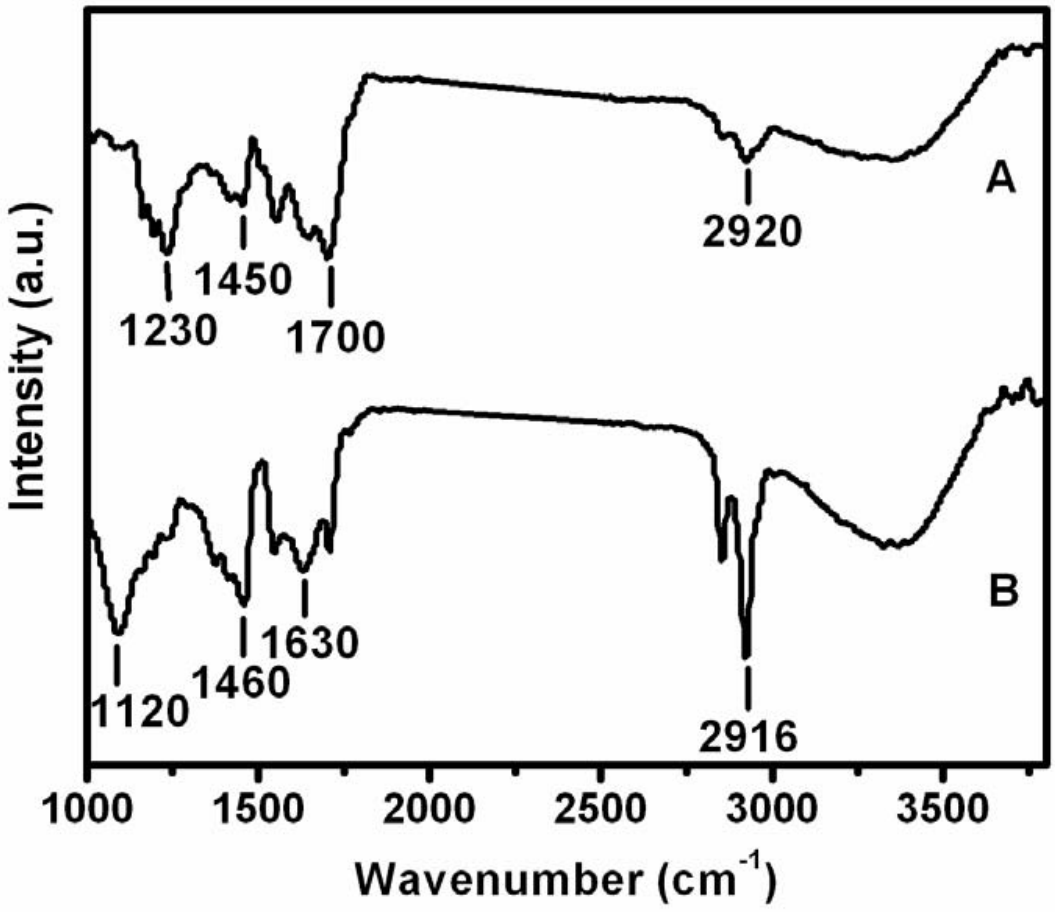

Figure 3.18 FT-IR spectra of $CaWO_4$ nanorods coated with organic ligands: (A) polyacrylic acid (PAA) and (B) oleic acid.

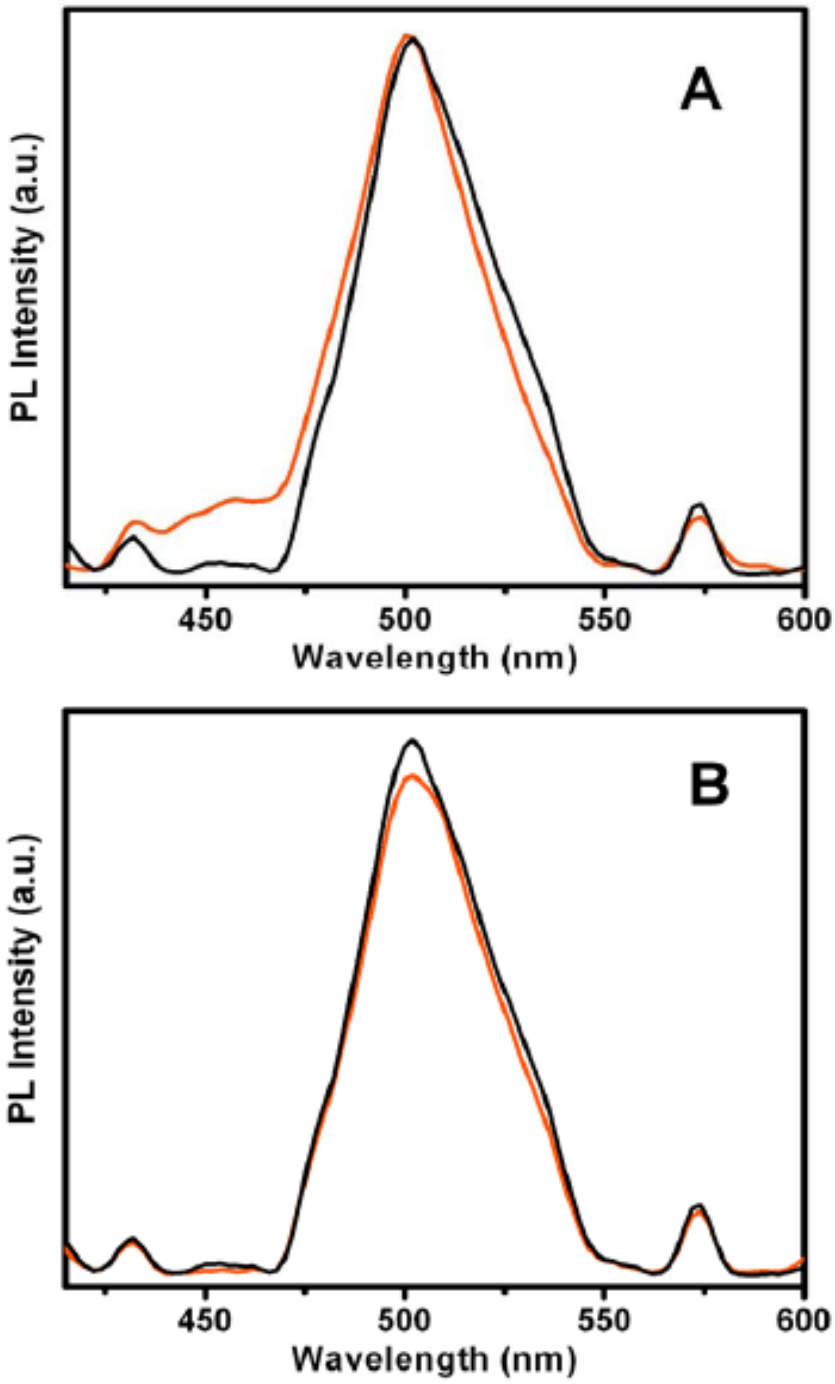

Figure 3.19 PL spectra of (A) $CaWO_4$ nanorods prior to (black) and after (red) functionalization with PAA; (B) $CaWO_4$ nanorods prior to (black) and after (red) functionalization with oleic acid.

Figure 3.20 illustrates typical PL spectra of $Sr_{1-x}Ca_xWO_4$ nanorods, where 'x' = 1, 0.7, 0.5, 0.3, and 0, with increasing Sr content from top to bottom. It can be observed that all five emission curves exhibit a broad luminescence in the blue wavelength range and possess a triple-peak, spread-eagle-shape structure wherein a relatively narrow central peak is surrounded by two shoulders.[57, 60, 69] Similar behavior was observed in the collective emission spectra of nanorods of the $Ba_{1-x}Sr_xWO_4$ system (Figure 3.20B). For all samples, all of the emission peak positions were not noticeably altered by the variation in chemical composition, implying that the energy gap related to the blue emission was not overly affected by changes in either Ca, Sr, or Ba content. As mentioned, the dominant blue emission band of the metal tungstates can be attributed to charge transfer transitions within the $[WO_4^{2-}]$ group between the last fully occupied t_1 orbital and the first empty 2e orbital.[70] That is, excitation from the ground state ($^1A_1$) of $[WO_4^{2-}]$ gives rise to four excited states, i.e., $^1T_2$, $^1T_1$, $^3T_2$, and $^3T_1$, from which only the transition between $^1A_1$ and $^1T_2$ is electric dipole allowed.[71] However, the WO_4^{2-} complexes in scheelite tungstates are slightly distorted from T_d to D_{2d} symmetry by the influence of the Jahn-Teller effect (through coupling of Jahn-Teller active vibrational modes of t_2 symmetry for instance) and electron phonon interactions in general.[69] Hence, the orbitally degenerate T state undergoes distortion and symmetry lowering to a D_{2d} symmetry state, which strongly enhances the number of transitions observed. Specifically, both $^1A_1$ to $^1T_2$, $^1T_1$ as well as $^1A_1$ to $^3T_2$, $^3T_1$ transitions become partially allowable, thereby rendering radiative transitions from low-lying triplet excited states to the $^1A_1$ ground state as clearly detectable emission peaks (i.e., at 437 nm) in the blue luminescent spectra. The resulting theoretical emission bands therefore possess a spread-eagle shape.[72] In addition, the presence of weak green and red emission bands in our nominally pure nanorods could be ascribed to the presence of radiative transitions within defect centers, such as Frenkel defects (i.e., oxygen ions shifted to intersite positions with a simultaneous creation of a vacancy) on the surfaces of our samples as well as the possibility of Schottky defects, i.e., WO_3.[57, 70, 71]

It is worth emphasizing that though emission peak positions were essentially unchanged across sample composition, variations in emission peak intensities were

observed. Photoluminescence is sensitive to local lattice symmetry and could be used as an intrinsic probe to map out variations in scheelite nanocrystals, characteristic of changes in chemical composition, such as in lattice dimension and symmetry which often accompany size reductions.[7] We indeed found this to be the case with our samples. In Figure 3.20A, Ca-rich nanorods showed a very strong luminescence, whereas Sr-rich nanorods evinced a much weaker emission. To account for the inefficiency of luminescence with increasing Sr content, it has been suggested that because Sr^{2+} ions (1.13 Å), surrounding the tungstate groups, are bigger than Ca^{2+} ions (0.99 Å), they do not effectively counteract the expansion of the WO_4^{2-} complexes upon excitation as well as Ca^{2+} ions do. As a result, there is a lower thermal quenching temperature of the blue luminescence with increasing Sr content and a correspondingly higher probability of radiationless transitions.[73] By contrast, in Figure 3.20B, Sr-rich nanorods yielded a comparatively stronger luminescence than their Ba-rich nanorod counterparts. An analogous argument could be made with respect to the size of the larger Ba^{2+} ions (1.35 Å) relative to Sr^{2+} ions (1.13 Å), rendering them less capable of counteracting the expansion of WO_4^{2-} groups upon excitation and thereby indirectly contributing to an increase in competing radiationless transitions.[33]

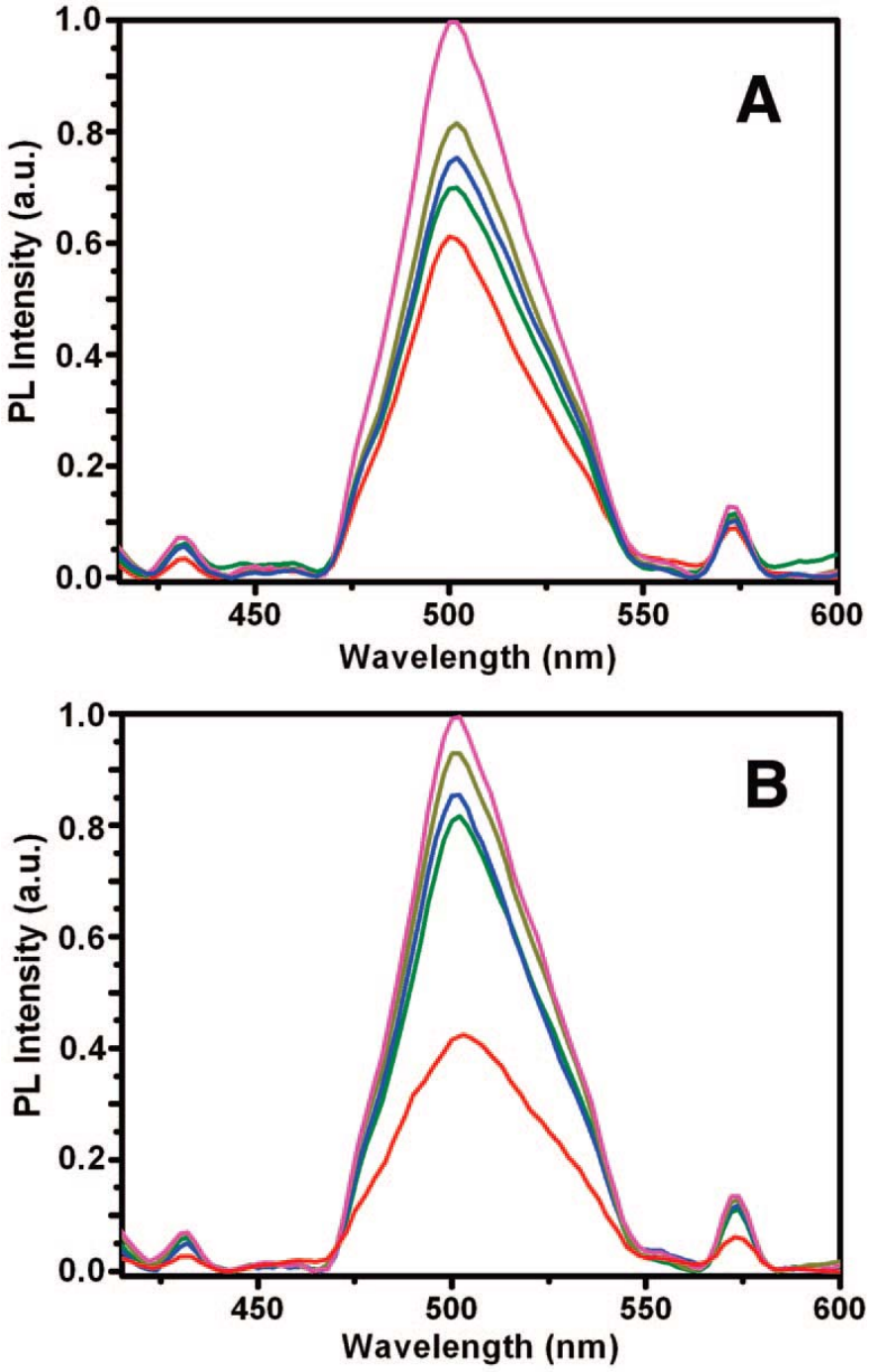

Figure 3.20 Photoluminescence spectra of as-prepared alkaline-earth-metal tungstate solid-solution nanorods collected at room temperature: (A) $Sr_{1-x}Ca_xWO_4$ nanorods. From top to bottom: $CaWO_4$ (pink), $Sr_{0.3}Ca_{0.7}WO_4$ (olive green), $Sr_{0.5}Ca_{0.5}WO_4$ (blue), $Sr_{0.7}Ca_{0.3}WO_4$ (dark green), and $SrWO_4$ (red), respectively. (B) $Ba_{1-x}Sr_xWO_4$ nanorods. From top to bottom: $SrWO_4$ (pink), $Ba_{0.3}Sr_{0.7}WO_4$ (olive green), $Ba_{0.5}Sr_{0.5}WO_4$ (blue), $Ba_{0.7}Sr_{0.3}WO_4$ (dark green), and $BaWO_4$ (red).

Importantly, it should be noted that with decreasing values of '*x*' and hence decreasing Ca content in the $Sr_{1-x}Ca_xWO_4$ system, the normalized intensities of the major emission peaks decreased in parallel in a systematic fashion, from 100%, 80%, 76%, 69%, and to 60%, associated with values of x = 1, 0.7, 0.5, 0.3, and 0. Figure 3.21A highlights a linear relationship between the solid-solution composition-dependent **x** values and the corresponding normalized PL intensities (**y**), as described by eq 5, with a slope of 0.38 (R^2 = 0.953).

$$\mathbf{y} = 0.38(\mathbf{x}) + 0.58 \qquad (5)$$

We found an analogous relationship between the normalized PL intensity and the chemical composition in the $Ba_{1-x}Sr_xWO_4$ system. That is, with decreasing values of '*x*' and hence vanishing Sr content, the normalized intensities of the major emission peaks similarly but predictably decreased from 100%, 92%, 85%, 81%, to 41%, associated with $SrWO_4$, $Ba_{0.3}Sr_{0.7}WO_4$, $Ba_{0.5}Sr_{0.5}WO_4$, $Ba_{0.7}Sr_{0.3}WO_4$, and $BaWO_4$, respectively. However, as others have observed the luminescence of pure $BaWO_4$ crystals and films to be anomalously weak and potentially less interpretable as compared with that of their $SrWO_4$ analogues,[59] we only considered data corresponding to '*x*' = 1, 0.7, 0.5, and 0.3 in the $Ba_{1-x}Sr_xWO_4$ system in our subsequent analysis. Figure 3.21B therefore illustrates a linear relationship between the solid-solution composition-dependent **x** values and the corresponding normalized PL intensities (**y**), as described by eq 6, with a slope of 0.28 (R^2 = 0.994).

$$\mathbf{y} = 0.28(\mathbf{x}) + 0.72 \qquad (6)$$

Apart from a controlled use of small percentages of dopants and guest ion intercalants, a clear dependence of photoluminescence intensity on chemical composition has rarely been convincingly demonstrated. Nonetheless, this effect, though, has been previously detected in $CuGaSe_2$ films.[74, 75] In addition, optical properties, including absorption and PL, have been systematically tuned in compositionally modulated $Zn_xCd_{1-x}S$ alloyed nanocrystals, $Zn_xCd_{1-x}Te$ alloyed nanocrystals, as well as binary and ternary mercury chalcogenide clusters.[76-78] Moreover, the photoluminescence quantum yield of CdTe quantum dots has been found to depend on the precise stoichiometric ratio of Cd to Te precursors used.[78] However, a clear correlation between the chemical composition of

robust nanoscale solid solutions and photoluminescent intensity, as established herein, has, to the best of our knowledge, never been observed in 1D metal oxide systems. As such, this finding reported herein is highly significant from the point of view of obtaining predictive structure-property relationships in 1D nanorods prepared from solid solutions. Specifically, in our case, using a quasi-standardization plot, we can readily compute the magnitude of expected PL intensities from a knowledge of the precise chemistry of well-defined alkaline-earth-metal tungstate solid solution samples, whereas, conversely, PL data can be reliably used to deduce the exact chemical compositions of these nanoscale materials.

Time-resolved luminescence measurements were carried out in order to further explore the photoluminescent properties of our solid-solution nanorod samples. Figure 3.22 shows a typical time-resolved luminescence decay curve of as-prepared $SrWO_4$ nanorods, which can be satisfactorily fitted into a single-exponential function with the decay lifetime, τ, equal to 1.62 $\pm$ 0.05 μs. Additional lifetime data with appropriate standard deviations for all of our samples are listed in Table 3.1. Within our experimental resolution, there does not seem to be an obvious trend with respect to photoluminescent lifetimes across samples of different cation stoichiometry (Ca, Sr, Ba). The average lifetime was calculated to be 1.6 $\pm$ 0.1 μs, which is comparable to the reported value of bulk $CaWO_4$ crystal which is on the order of microseconds.[79, 80] In addition, any real differences in the decay constants may be attributed to corresponding differences in excitation conditions.[81] The exponential tail of the decay curve reflects the lifetime of the exciton emission due to radiative recombination of photoinduced charge carriers.[82, 83] In general, the presence of surface defects (e.g., vacancy centers) as well as surface degradation and disorder may decrease observed lifetimes, whereas compositional disorder and exciton localization may have the opposite effect and increase lifetimes.[79, 84] The fact that essentially similar lifetimes were observed for all systems implies that the surface properties of our nanorods associated with these luminescence processes were effectively identical for each sample.

Table 3.1 Emission Lifetimes Measured at Room Temperature, Under Ambient Conditions, at 502 nm for As-Prepared Alkaline-Earth-Metal Tungstate Solid-Solution Nanorods.

sample	lifetime (μs)	standard deviation (μs)
$CaWO_4$	1.64	0.06
$Sr_{0.3}Ca_{0.7}WO_4$	1.67	0.07
$Sr_{0.5}Ca_{0.5}WO_4$	1.84	0.10
$Sr_{0.7}Ca_{0.3}WO_4$	1.47	0.04
$SrWO_4$	1.62	0.05
$Ba_{0.3}Sr_{0.7}WO_4$	1.71	0.07
$Ba_{0.5}Sr_{0.5}WO_4$	1.41	0.03
$Ba_{0.7}Sr_{0.3}WO_4$	1.54	0.06
$BaWO_4$	1.47	0.02

While we were not able to measure the quantum yield (QY) directly, we can estimate it by comparing our measured lifetimes to those reported in the literature using eq 7

$$QY_A = \frac{\frac{1}{\tau_r}}{\frac{1}{\tau_r} + \frac{1}{\tau_{nr}^A}}; \frac{QY_A}{QY_B} = \frac{\left(\frac{1}{\tau_r} + \frac{1}{\tau_{nr}^B}\right)}{\left(\frac{1}{\tau_r} + \frac{1}{\tau_{nr}^A}\right)} \qquad (7)$$

where A represents our nanorod systems and B is associated with the bulk reference. τ_r and τ_{nr} represent the radiative and nonradiative lifetimes, respectively.

For example, one study quotes a lifetime ranging from 5 to 6.7 μs at room temperature,93 which suggests a corresponding quantum efficiency value of ~24-32% relative to bulk calcium tungstate material. It should be noted that in that bulk study, the reported lifetime values were not representative of the true radiative lifetime of the material since the room-temperature efficiency was arbitrarily set to 1. As such, we should emphasize that the computed quantum yield of 24-32% for our nanorods cannot necessarily be considered as an absolute quantum yield. A further confirmation of this assertion can be found in another paper, reporting a low-temperature (75 K) decay time of >200 μs;[11] using 200 μs in our calculations would have reduced our quantum yield to less than 1%. On the basis of all of this data, it is reasonable to state that the quantum yield of our as-prepared alkaline-earth-metal tungstate nanorods is likely to be no worse than 25% as compared with their bulk counterparts at room temperature. We expect to continue with additional comprehensive photooptical studies on these as well as the analogous systems since there are few such studies in the literature that conclusively deal with these important issues.

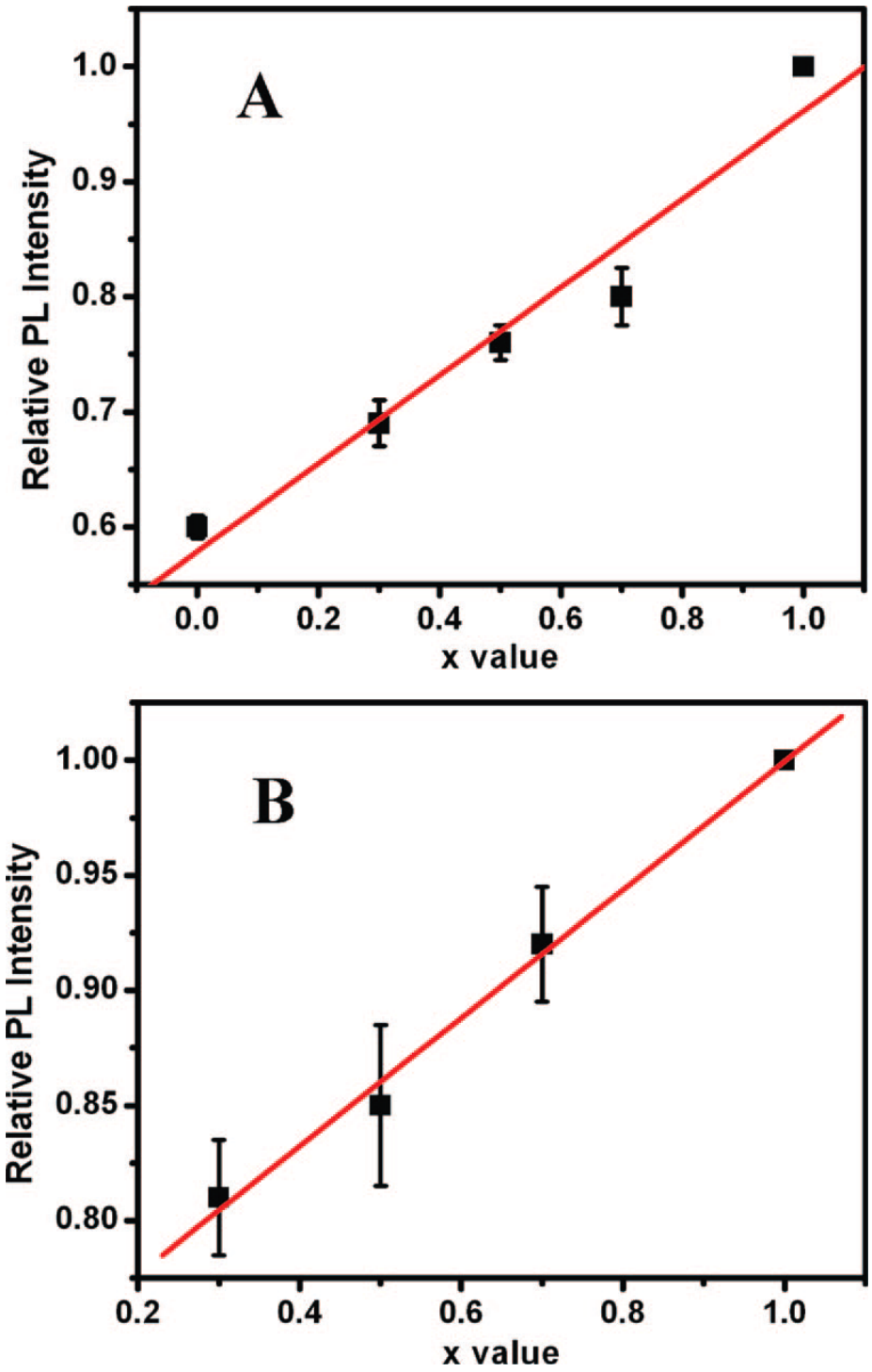

Figure 3.21 Dependence of normalized photoluminescence intensities on the rationally modulated chemical compositions of as-prepared (A) $Sr_{1-x}Ca_xWO_4$ and (B) $Ba_{1-x}Sr_xWO_4$ solid-solution nanorods.

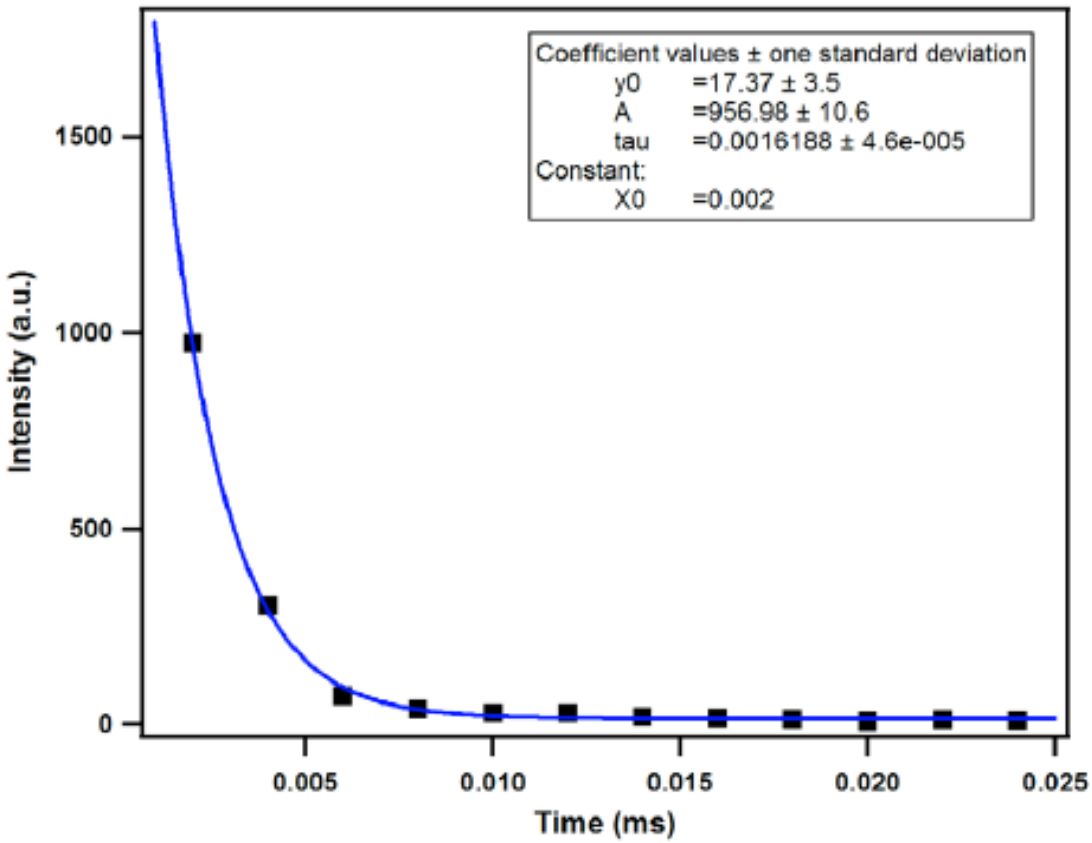

Figure 3.22 Typical time-resolved emission profile of as-prepared $SrWO_4$ nanorods measured at room temperature under ambient conditions. Parameters of the equation used to fit the decay curve are summarized in the inset.

3.4 Conclusions

The current chapter demonstrates the ambient, room-temperature synthesis using a modified template-directed methodology of single-crystalline alkaline-earth-metal tungstates AWO_4 (A = Ca, Sr, Ba) nanorods as well as the corresponding series of their crystalline solid-solution analogues, $Sr_{1-x}Ca_xWO_4$ and $Ba_{1-x}Sr_xWO_4$ ($0 < x < 1$), with varying controllable sizes. As-obtained photoluminescent lifetimes and quantum yields suggest that these nanoscale materials are comparable in optical behavior to those of bulk. The growth mechanism for these 1D nanostructures has been previously discussed. Generally, the fabrication of single crystals in solution is difficult because too many nuclei are produced as a result of a high degree of supersaturation, resulting in the formation of many particles. In order to obtain a low degree of supersaturation, it is therefore necessary to control the reaction rate. The point is that under controlled nucleation and growth conditions, single-crystalline alkaline-earth metal tungstates and their reciprocal solid-solution counterparts with one-dimensional rod-like morphologies were readily prepared within a constrained volume provided by polycarbonate membranes.

The resulting nanorods have been extensively characterized via microscopy and spectroscopy. Because of the simplicity and versatility of the approach used, it is anticipated that we can generalize this methodology to the preparation of other important classes of stoichiometrically precise nanomaterials with controllable size and shape. In addition, whereas much of the relevant literature in solid-solution synthesis has focused on generating 1D nanostructures of bimetallic materials, such as diluted magnetic, semiconducting (DMS) nanorods in particular,[85-88] the current work is focused on an important extension of this idea to trimetallic oxide systems. In fact, the relatively mild synthetic methodology we developed offers improved control over morphology, tunable chemical composition, and a reliable understanding of associated physical properties. Moreover, the composition-modulated luminescence properties over several distinctive series of as-prepared solid-solution nanorods of alkaline-earth-metal tungstates provide the fundamental basis for a more thorough investigation and understanding of their

optical and optoelectronic properties, which may eventually lead to the rational incorporation of these materials into functional nanoscale devices.

3.5 References

1. Saito, N.; Sonoyama, N.; Sakata, T., *Bull. Chem. Soc. Japan* **1996,** *69*, 2191.
2. Liao, H.-W.; Wang, Y.-F.; Liu, X.-M.; Li, Y.-D.; Qian, Y.-T., *Chem. Mater.* **2000,** *12*, 2819.
3. Kloprogge, J. T.; Weier, M. L.; Duong, L. V.; Frost, R. L., *Mater. Chem. Phys.* **2004,** *88*, 438.
4. Wang, H.; Medina, F. D.; Zhou, Y. D.; Zhang, Q. N., *Phys. Rev. B* **1992,** *45*, 10356.
5. Nagirnyi, V.; Feldbach, E.; Jönsson, L.; Kirm, M.; Lushchik, A.; Lushchik, C.; Nagornaya, L. L.; Ryzhikov, V. D.; Savikhin, F.; Svensson, G.; Tupitsina, I. A., *Radiat. Mes.* **1998,** *29*, 247.
6. Park, I.-H.; Kim, B.-S.; Kim, K.-Y.; Kim, B.-H., *Jpn. J. Appl. Phys.* **2001,** *40*, 4956.
7. Li, L.; Su, Y.; Li, G., *Appl. Phys. Lett.* **2007,** *90*, 054105.
8. Zhang, Q.; Yao, W.-T.; Chen, X.; Zhu, L.; Fu, Y.; Zhang, G.; Sheng, L.; Yu, S.-H., *Crystal Growth & Design* **2007,** *7*, 1423.
9. Nitsch, K.; Nikl, M.; Ganschow, S.; Reiche, P.; Uecker, R., *J. Cryst. Growth* **1996,** *165*, 163.
10. Kaminskii, A. A.; Eichler, H. J.; Ueda, K.-I.; Klassen, N. V.; Redkin, B. S.; Li, L. E.; Findeisen, J.; Jaque, D.; García-Sole, J.; Fernández, J.; Balda, R., *Appl. Optics* **1999,** *38*, 4533.
11. Treadaway, M. J.; Powell, R. C., *Phys. Rev. B* **1975,** *11*, 862.
12. Martini, M.; Meinardi, F.; Spinolo, G.; Vedda, A.; M., N.; Usuki, Y., *Phys. Rev. B* **1999,** *60*, 4653.
13. Cho, W.-S.; Yashima, M.; Kakihana, M.; Kudo, A.; Sakata, T.; Yoshimura, M., *Appl. Phys. Lett.* **1995,** *66*, 1027.

14. Yu, S.-H.; Liu, B.; Mo, M.-S.; Huang, J.-H.; Liu, X.-M.; Qian, Y.-T., *Adv. Funct. Mater.* **2003,** *13*, 639.

15. Pode, R. B.; Dhoble, S. J., *Phys. Stat. Sol. B* **1997,** *203*, 571.

16. Kobayashi, M.; Usukib, Y.; Ishiic, M.; Yazawac, T.; Harad, K.; Tanakad, M.; Nikle, M.; Nitsch, K., *Nucl. Instrum. Methods Phys. Res. A* **1997,** *399*, 261.

17. Murk, V.; Nikl, M.; Mihokova, E.; Nitsch, K., *J. Phys.: Condens. Matter* **1997,** *9*, 249.

18. Errandonea, D.; Somayazulu, M.; Häusermann, D., *Phys. Stat. Sol. B* **2003,** *235*, 162.

19. Sun, L.; Guo, Q.; Wu, X.; Luo, S.; Pan, W.; Huang, K.; Lu, J.; Ren, L.; Cao, M.; Hu, C., *J. Phys. Chem. C* **2007,** *111*, 532.

20. Tarte, P.; Liegeois-Duyckaerts, N., *Spectrochim. Acta Part A* **1972,** *28*, 2029.

21. Liegeois-Duyckaerts, N.; Tarte, P., *Spectrochim. Acta Part A* **1972,** *28*, 2037.

22. Tsuji, I.; Kato, H.; Kobayashi, H.; Kudo, A., *J. Am. Chem. Soc.* **2004,** *126*, 13406.

23. Torimoto, T.; Adachi, T.; Okazaki, K.; Sakuraoka, M.; Shibayama, T.; Ohtani, B.; Kudo, A.; Kuwabata, S., *J. Am. Chem. Soc.* **2007,** *129*, 12388.

24. Tsuji, I.; Kato, H.; Kudo, A., *Chem. Mater.* **2006,** *18*, 1969.

25. Inumaru, K.; Koyama, K.; Miyaki, Y.; Tanaka, K.; Yamanaka, S., *Appl. Phys. Lett.* **2007,** *91*, 152501.

26. Muktha, B.; Simon, A.; Darriet, J.; Guru Row, T. N., *Chem. Mater.* **2006,** *18*, 1240.

27. McKinlay, A.; Connor, P.; Irvine, J. T. S.; Zhou, W., *J. Phys. Chem. C.* **2007,** *111*, 19120.

28. Kolen'ko, Y. V.; Kovnir, K. A.; Gavrilov, A. I.; Garshev, A. V.; Meskin, P. E.; Churagulov, B. R.; Bouchard, M.; Colbeau-Justin, C.; Lebedev, O. I.; Van Tendeloo, G.; Yoshimura, M., *J. Phys. Chem. B* **2005,** *109*, 20303.

29. Hu, Q. M.; Kádas, K.; Hogmark, S.; Yang, R.; Johansson, B.; Vitos, L., *Appl. Phys. Lett.* **2007,** *91*, 121918.

30. Varshney, D.; Kaurav, N.; Kinge, R.; Singh, R. K., *J. Phys.: Condens. Matter* **2007,** *19*, 346212.

31. Fernandez-Gonzalez, A.; Andara, A. P., M., *Crystal Growth & Design* **2007,** *7*, 545.

32. Cho, W.-S.; Yashima, M.; Kakihana, M.; Kudo, A.; Sakata, T.; Yoshimura, M., *Appl. Phys. Lett.* **1996,** *68*, 137.

33. Cho, W.-S.; Yoshimura, M., *Jpn. J. Appl. Phys.* **1997,** *36*, 5658.

34. Wang, Z. L.; Song, J., *Science* **2006,** *312*, 242.

35. Ge, J.; Hu, Y.; Yin, Y., *Angew. Chem. Int. Ed.* **2007,** *46*, 7428.

36. Kovalenko, M. V.; Bodnarchuk, M. I.; Lechner, R. T.; Hesser, G.; Schäffler, F.; Heiss, W., *J. Am. Chem. Soc.* **2007,** *129*, 6352.

37. Xia, Y.; Yang, P.; Sun, Y.; Wu, Y.; Mayers, B.; Gates, B.; Yin, Y.; Kim, F.; Yan, H., *Adv. Mater.* **2003,** *15*, 353.

38. Rutherglen, C.; Burke, P., *Nano. Lett.* **2007,** *7*, 3296.

39. Ma, R.-M.; Dai, L.; Huo, H.-B.; Xu, W.-J.; Qin, G. G., *Nano. Lett.* **2007,** *7*, 3300.

40. Su, Y.; Li, G.; Xue, Y.; Li, L., *J. Phys. Chem. C* **2007,** *111*, 6684.

41. Wang, Y.; Ma, J.; Tao, J.; Zhu, X.; Zhou, J.; Zhao, Z.; Xie, L.; Tian, H., *Mater. Lett.* **2006,** *60*, 291.

42. Li, D.; Wu, H.; Li, Z.; Cong, X.; Sun, J.; Ren, Z.; Liu, L.; Li, Y.; Fan, D.; Hao, J., *Colloids Surf., A* **2006,** *274*, 18.

43. Chen, S.-J.; Li, J.; Chen, X.-T.; Hong, J.-M.; Xue, Z.; You, X.-Z., *J. Cryst. Growth* **2003,** *253*, 361.

44. Sun, L.; Cao, M.; Wang, Y.; Sun, G.; Hu, C., *J. Cryst. Growth* **2006,** *289*, 231.

45. Kwan, S.; Kim, F.; Akana, J.; Yang, P., *Chem. Commun.* **2001**, 447.

46. Kim, F.; Kwan, S.; Akana, J.; Yang, P., *J. Am. Chem. Soc.* **2001,** *123*, 4360.

47. Shi, H.; Qi, L.; Ma, J.; Cheng, H., *Chem. Commun.* **2002**, 1704.

48. Shi, H.; Qi, L.; Ma, J.; Cheng, H.; Zhu, B., *Adv. Mater.* **2003,** *15*, 1647.

49. Zhang, C.; Shen, E.; Wang, E.; Kang, Z.; Gao, L.; Hu, C.; Xu, L., *Mater. Chem. Phys.* **2006,** *96*, 240.

50. Shi, H.; Qi, L.; Ma, J.; Cheng, H., *J. Am. Chem. Soc.* **2003,** *125*, 3450.

51. Cho, W.-S.; Yoshimura, M., *J. Am. Ceram. Soc.* **1996,** *79*, 2783.

52. Mao, Y.; Wong, S. S., *J. Am. Chem. Soc.* **2004,** *126*, 15245.

53. Atuchin, V. V.; Kesler, V. G.; Maklakova, N. Y.; Pokrovsky, L. D.; Sheglov, D. V., *Eur. Phys. J. B* **2006,** *51*, 293.

54. Itoh, M.; Fujita, N.; Inabe, Y., *J. Phys. Soc. Jpn.* **2006,** *75*, 084705.

55. Ling, Z. C.; Xia, H. R.; Ran, D. G.; Liu, F. Q.; Sun, S. Q.; Fan, J. D.; Zhang, H. J.; Wang, J. Y.; Yu, L. L., *Chem. Phys. Lett.* **2006,** *426*, 85.

56. Zhang, G.; Jia, R.; Wu, Q., *Mater. Sci. Eng. B* **2006,** *128*, 254.

57. Ryu, J. H.; Yoon, J.-W.; Shim, K. B., *Electrochem. Solid-State. Lett.* **2005,** *8*, D15.

58. Orhan, E.; Anicete-Santos, M.; Maurera, M. A. M. A.; Pontes, F. M.; Paiva-Santos, C. O.; Souza, A. G.; Varela, J. A.; Pizani, P. S.; Longo, E., *Chem. Phys.* **2005,** *312*, 1.

59. Oaki, Y.; Imai, H., *Adv. Mater.* **2006,** *18*, 1807.

60. Nikl, M.; Bohacek, P.; Mihokova, E.; Kobayashi, M.; Ishii, M.; Usuki, Y.; Babin, V.; Stolovich, A.; Zazubovich, S.; Bacci, M., *J. Lumin.* **2000,** *87-89*, 1136.

61. Al-Suleiman, M.; Che Mofor, A.; El-Shaer, A.; Bakin, A.; Wehmann, H.-H.; Waag, A., *Appl. Phys. Lett.* **2006,** *89*, 231911.

62. Cheng, B.; Guo, H.; Yu, J.; Zhao, X., *J. Alloys Compd.* **2007,** *431*, L4.

63. Willis, A. L.; Turro, N. J.; O'Brien, S., *Chem. Mater.* **2005,** *17*, 5970.

64. Zhang, T.; Ge, J.; Hu, Y.; Yin, Y., *Nano Lett.* **2007,** *7*, 3203.

65. Wang, L.; Li, Y., *Nano Lett.* **2006,** *6*, 1645.

66. Zhang, Q.; Russell, T. P.; Emrick, T., *Chem. Mater.* **2007,** *19*, 3712.

67. Zhang, Y.; Guo, J.; White, T.; Tan, T. T. Y.; Xu, R., *J. Phys. Chem. C* **2007,** *111*, 7893.

68. Lu, S. W.; Lee, B. I.; Wang, Z. L.; Tong, W.; Wagner, B. K.; Park, W.; Summers, C. J., *J. Lumin.* **2001,** *92*, 73.

69. Polak, K.; Nikl, M.; Nitsch, K.; Kobayashi, M.; Ishii, M.; Usuki, Y.; Jarolimek, O., *J. Lumin.* **1997,** *72-74*, 781.

70. Grasser, R.; Scharmann, A., *J. Lumin.* **1976,** *12/13*, 473.

71. Grasser, R.; Scharmann, A.; Strack, K.-R., *J. Lumin.* **1982,** *27*, 263.

72. Toyozawa, Y.; Inoue, M., *J. Phys. Soc. Jpn.* **1966,** *21*, 1663.

73. Cho, W.-S.; Yoshimura, M., *J. Appl. Phys.* **1998,** *83*, 518.

74. Siebentritt, S.; Schuler, S., *J. Phys. Chem. Solids* **2003,** *64*, 1621.

75. Xue, C.; Papadimitriou, D.; Esser, N., *J. PHys. D: Appl. Phys.* **2004,** *37*, 2267.

76. Kuno, M.; Higginson, K. A.; Qadri, S. B.; Yousuf, M.; Lee, S. H.; Davis, B. L.; Mattoussi, H., *J. Phys. Chem. B* **2003,** *107*, 5758.

77. Wang, Y.; Hou, Y.; Tang, A.; Feng, B.; Li, Y.; Liu, J.; Teng, F., *J. Cryst. Growth* **2007,** *308*, 19.

78. Zhao, K.; Li, J.; Wang, H.; Zhuang, J.; Yang, W., *J. Phys. Chem. C* **2007,** *111*, 5618.

79. Beard, G. B.; Kelly, W. H.; Mallory, M. L., *J. Appl. Phys.* **1962,** *33*, 144.

80. Born, G.; Hofstaetter, A.; Scharmann, A.; Schwarz, G., *J. Lumin.* **1970,** *1/2*, 641.

81. Mikhailik, V. B.; Kraus, H.; Wahl, D.; Itoh, M.; Koike, M.; Bailiff, I. K., *Phys. Rev. B* **2004,** *69*, 205110.

82. de Mello Donegá, C.; Hickey, S. G.; Wuister, S. F.; Vanmaekelbergh, D.; Meijerink, A., *J. Phys. Chem. B* **2003,** *107*, 489.

83. Lee, H.; Holloway, P. H.; Yang, H.; Hardison, L.; Kleiman, V. D., *J. Chem. Phys.* **2006,** *125*, 164711.

84. Wehrenberg, B. L.; Wang, C.; Guyot-Sionnest, P., *J. Phys. Chem. B* **2002,** *106*, 10634.

85. Zhang, X. L.; Qiao, R.; Qiu, R.; Li, Y.; Kang, Y. S., *J. Phys. Chem. A* **2007,** *111*, 4195.

86. Jun, Y.-W.; Jung, Y.-Y.; Cheon, J., *J. Am. Chem. Soc.* **2002,** *124*, 615.

87. Na, C. W.; Han, D. S.; Kim, D. S.; Kang, Y. J.; Lee, J. Y.; Park, J.; Oh, D. K.; Kim, K. S.; Kim, D., *J. Phys. Chem. B* **2006,** *110*, 6699.

88. Ando, K., *Science* **2006,** *312*, 1883.

Chapter IV Multifunctional Doped Tungstate Nanorods

4.1 Introduction

There is a high interest in developing versatile and flexible nanomaterials that are multifunctional, multicomponent, and multifaceted in their properties and, hence, potential applications. The idea is to create multifunctional nanomaterials, which are responsive to multiple external stimuli, have recently become an attractive research field for their potential applications as building blocks in novel nanoscale devices. For example, multifunctional nanoparticles with interesting magnetic and luminescent properties have been used as effective platforms for biomedical imaging, drug delivery, protein separation, cell sorting, and MRI contrast imaging.[1-6] In addition, incorporation of carbon nanotubes into a polymer matrix provides the composites with enhanced flexibility, transparency, conductivity, and mechanical strength.[7-10] The above mentioned multifunctional nanomaterials mostly depend on mixing more than two different functional composites into one hybrid to achieve the goal, as opposed to one discrete homogeneous structure, which is the focus of our studies herein.

To that effect, our current work, unique to the family of ternary metal oxides, is analogous to another class of multifunctional materials, namely, diluted magnetic semiconductors (DMSs) such as $Cd_{1-x}Mn_xS$ ($x \leq 0.3$), in which host cations are randomly substituted by magnetic ions. DMS materials have attracted significant attention for their potential use as key materials in magnetooptical and electronic devices.[11-14] All these investigations clearly show the possibilities of incorporating multifunctional nanomaterials into devices with multiple applications in various fields.

Alkaline-earth metal tungstates AWO_4 (A = Ca, Sr, Ba) with their scheelite-like structures represent an important family of inorganic materials, with their interesting structural properties and distinct physical properties such as excitonic luminescence, thermoluminescence and stimulated Raman scattering (SRS) properties, which have

found a wide range of applications.[15-20] In fact, their optical characteristics are keenly sought for a wide range of technologically significant applications,[21-24] including as phosphors, laser media, and optical fibers. On the other hand, $MnWO_4$, otherwise known as hübnerite, is described by a wolframite structure and is a multiferroic material, meaning that it can undergo simultaneous ferromagnetic ordering (or any other kind of magnetic) and ferroelectric ordering and possesses spontaneous electric polarization manifested in a spiral magnetically ordered state.[25-29] Pure $MnWO_4$ displays interesting antiferromagnetic behavior with potential applications as components of giant magnetoresistant (GMR) materials and intrinsically bistable ferromagnetic films in magnetic storage devices.[30-32]

In this project, we seek for the first time to merge the favorable properties of both classes of tungstates by incorporating Mn ions into the alkaline-earth metal tungstate scheelite matrix, thereby generating a separate family of novel materials endowed with both desirable luminescent as well as magnetic properties that mutually coexist within one structure without any evident property dilution. That is, we have created reasonably homogeneously doped tungstates, which are truly multifunctional. Hence, our samples stand in contrast with previously reported tungstate systems, doped with uranium, neodymium, europium, ytterbium, or samarium, which had been created with the important but distinctly different intention of highlighting and strengthening the existing luminescence and lasing properties intrinsic to scheelites.[33-36] The key point of this Chapter is to incorporate Mn ions into the alkaline-earth metal tungstate matrix, endowing these well-known optical materials with magnetic properties. The blending of magnetic properties with characteristic luminescent materials promises a new type of multifunctional nanomaterials.

In particular, we have created multifunctional 1D nanostructures with controllable size, shape, and morphology. In general, 1D nanostructures with their inherent anisotropy are the smallest dimension structures that can be used for the efficient transport of electrons and optical excitations. As such, they are applicable as building blocks for the realization of novel functional devices at the nanoscale.[37-40] Specifically, we mounted commercially available, track-etched polycarbonate membrane of varying pore sizes

between the two halves of a U-shaped tube, containing aqueous precursor solutions, so as to spatially control the growth of our crystalline 1D nanostructures of Mn-doped alkaline-earth metal tungstates nanorods at room temperature. We found that our as-prepared nanostructures reproducibly and simultaneously displayed both luminescent and antiferromagnetic properties, suggesting the possibility of their future incorporation into multifunctional nanoscale devices.

4.2 Experimental Section

4.2.1 Materials Preparation

Polycarbonate (PC) track-etched membranes of ca. 6 μm in thickness, containing pore sizes of 50, 100, and 200 nm diameter, respectively, were purchased from Whatman Co., UK. The membranes were initially hydrated by immersion and sonication in a small volume of distilled, deionized water for a few minutes, so as to limit the formation of air bubbles either within their interior pore structures or on their surfaces.

Subsequently, the membrane was mounted between the two half-arms of a U-shaped tube cell apparatus. In a typical ambient synthesis, one of the two half-cells was filled with Na_2WO_4 solution, and the other half-cell contained a mixed solution containing either $CaCl_2$, $SrCl_2$, or $Ba(NO_3)_2$, together with $MnCl_2$ at a concentration of up to 10.0 mol %, so as to generate Mn-doped $CaWO_4$, $SrWO_4$, and $BaWO_4$ nanorods, respectively. Pure, undoped alkaline-earth metal tungstate nanorods were prepared under identical conditions, with the exception that $MnCl_2$ was not added to the half-cell filled with either $CaCl_2$, $SrCl_2$, or $Ba(NO_3)_2$ solutions. Pure manganese tungstate nanorods were synthesized using solutions of $MnCl_2$ and $NaWO_4$ as precursors. The system was then left unperturbed for an incubation period of up to 1 day at room temperature. To isolate the product, the polycarbonate membrane was detached, sonicated for about 2 min to remove the unwanted particles on the surface, and thoroughly washed with distilled water before being completely dissolved by immersion in ~5 mL of methylene chloride. As-prepared Mn-doped tungstate nanorods were collected from solution by centrifugation upon washing.

4.2.2 Materials Characterization

X-ray Powder Diffraction See Section 1.7.1.

Electron Microscopy See Section 1.7.3.

Optical Spectroscopy See Section 1.7.5.

Magnetic Measurements See Section 1.7.4.

4.3 Results and Discussion

4.3.1 X-ray Diffraction

The purity and crystallinity of as-prepared Mn-doped tungstate nanorod samples were initially characterized using XRD. All of the diffraction peaks observed from as-prepared Mn-doped $CaWO_4$ nanorods in Figure 4.1A (top, black curve) can be readily ascribed to a pure body-centered tetragonal phase [space group: $I4_1/a$] of pristine $CaWO_4$ (bottom, red curve), with lattice constants of a = 5.231 Å and c = 11.358Å, which are comparable to reported database values of a = 5.242 Å and c = 11.372 Å for pure $CaWO_4$ bulk materials (JCPDS File No.07-0210). Likewise, Figure 4.1B presents a diffraction pattern collected from as-prepared Mn-doped $SrWO_4$ nanorods (top, black curve) in the 2θ range of 10 to 80°; this is very similar to what would be expected of its pure $SrWO_4$ bulk counterpart (bottom, red curve) possessing a body-centered tetragonal phase [space group: $I4_1/a$]. The calculated lattice constants of a = 5.404 Å and c = 11.932 Å are numerically close to the corresponding database values of a = 5.417 Å and c = 11.951 Å (JCPDS File No. 08-0490). Finally, the diffraction peaks (top, black curve) in Figure 4.1C can be assigned to a pure body-centered tetragonal phase [space group: $I4_1/a$] of pristine $BaWO_4$ (bottom, red curve), with lattice constants of a = 5.597 Å and c = 12.703 Å, which are consistent with the reported values of a = 5.613 Å and c = 12.720 Å expected for pure $BaWO_4$ (JCPDS File No.08-0457).

The presence of dopant likely did not affect the structure of the AWO_4 scheelite materials we were studying. In fact, neither secondary phases nor diffraction peaks due to either Mn or Mn-containing derivatives, such as manganese oxides, were detected. We also did not observe any peaks that could be unambiguously ascribed to $MnWO_4$. All of these results suggest a reasonably homogeneous dispersion of Mn within the underlying

alkaline-earth metal tungstate AWO_4 (A = Ca, Sr, Ba) matrix.[41, 42] On the basis of a statistical analysis of our data, doping with Mn ions produces no real, quantifiable shift in lattice parameters, and apparent alterations in unit cell dimensions are actually coupled with peak width effects.[43]

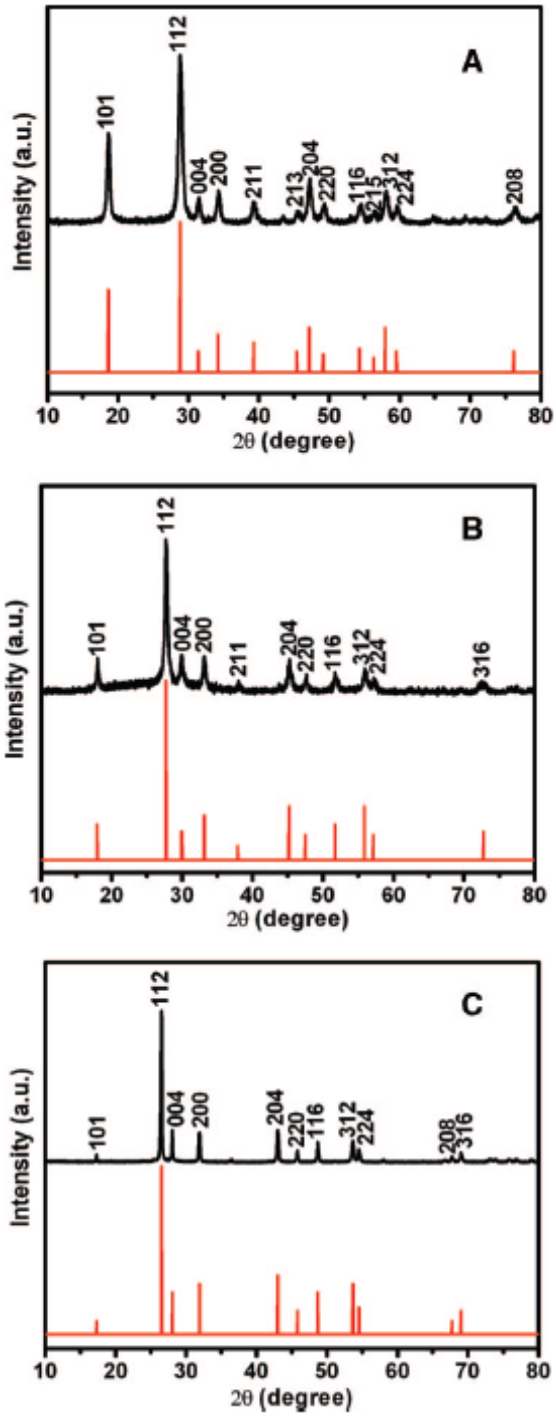

Figure 4.1 XRD patterns obtained from (A) as-prepared Mn-doped $CaWO_4$ nanorods (top, black) and JCPDS No. 07-0210 database standard for $CaWO_4$ (bottom, red); (B) as-prepared Mn-doped $SrWO_4$ nanorods (top, black) and JCPDS No. 08-0490 database standard for $SrWO_4$ (bottom, red); (C) as-prepared Mn-doped $BaWO_4$ nanorods (top, black) and JCPDS No. 08-0457 database standard for $BaWO_4$ (bottom, red).

4.3.2 Electron Microscopy

TEM images of pure, undoped alkaline-earth metal tungstate nanorods are shown in Figure 4.2. By analogy, the size and morphology of as-synthesized Mn-doped tungstate nanorod samples were examined using FE-SEM and TEM. Figure 4.3A and C, show typical SEM and

TEM images of Mn-doped $CaWO_4$ nanorods, respectively, which had been fabricated using polycarbonate membranes with pore sizes as small as 200 nm in diameter. The presence of dispersed individual nanorods as well as of bundled, aggregated species is evident from these images. All of the straight and smooth nanorods possess uniform, homogeneous size along their axis direction, in the diameter range of 183 to 209 nm. Lengths measured from 25 different nanorods varied from 1.6 to 3.8 μm. EDS elemental analysis data (Figure 4.3B) clearly indicate that the nanorods are composed of Ca, W, O, and Mn, as expected, with the presence of the C peak attributable to the underlying conductive carbon tape. The molar ratio of Mn was spectrally estimated to be 5.92%, slightly lower than the initial starting concentration (10%) and which can be justified based on incomplete incorporation into the matrix. Additional details on the crystallographic structure of as-prepared Mn-doped tungstate nanorods were investigated using high-resolution TEM (HRTEM). Figure 4.3D shows a typical HRTEM image taken from a randomly chosen individual nanorod from Figure 4.3C, with an interplanar spacing of ~3.08 Å, corresponding to the (112) plane of bulk crystalline $CaWO_4$. The findings are consistent with observations from the XRD pattern shown in Figure 4.1A.

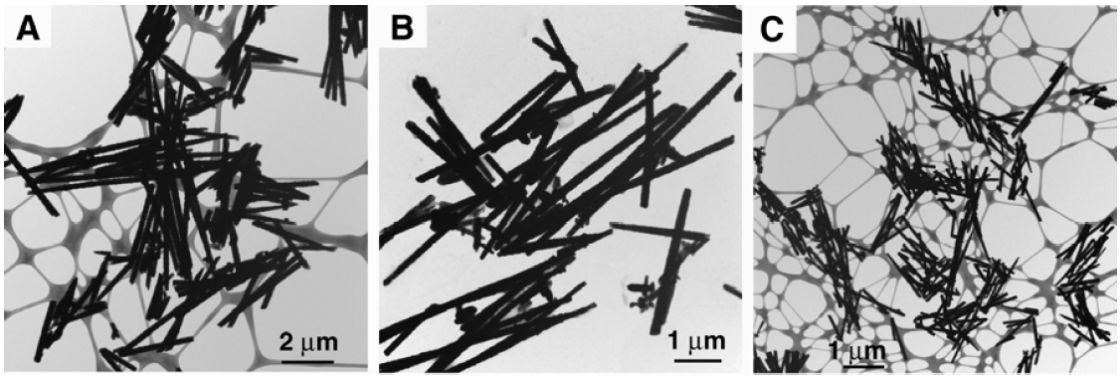

Figure 4.2 TEM images of as-prepared pure alkaline-earth metal tungstate nanorods. (A) $CaWO_4$ nanorods, prepared using polycarbonate membranes with 200-nm pore diameters; (B) $SrWO_4$ nanorods, prepared using polycarbonate membranes with 100-nm pore diameters. (C) $BaWO_4$ nanorods, prepared using polycarbonate membranes with 50-nm pore diameters.

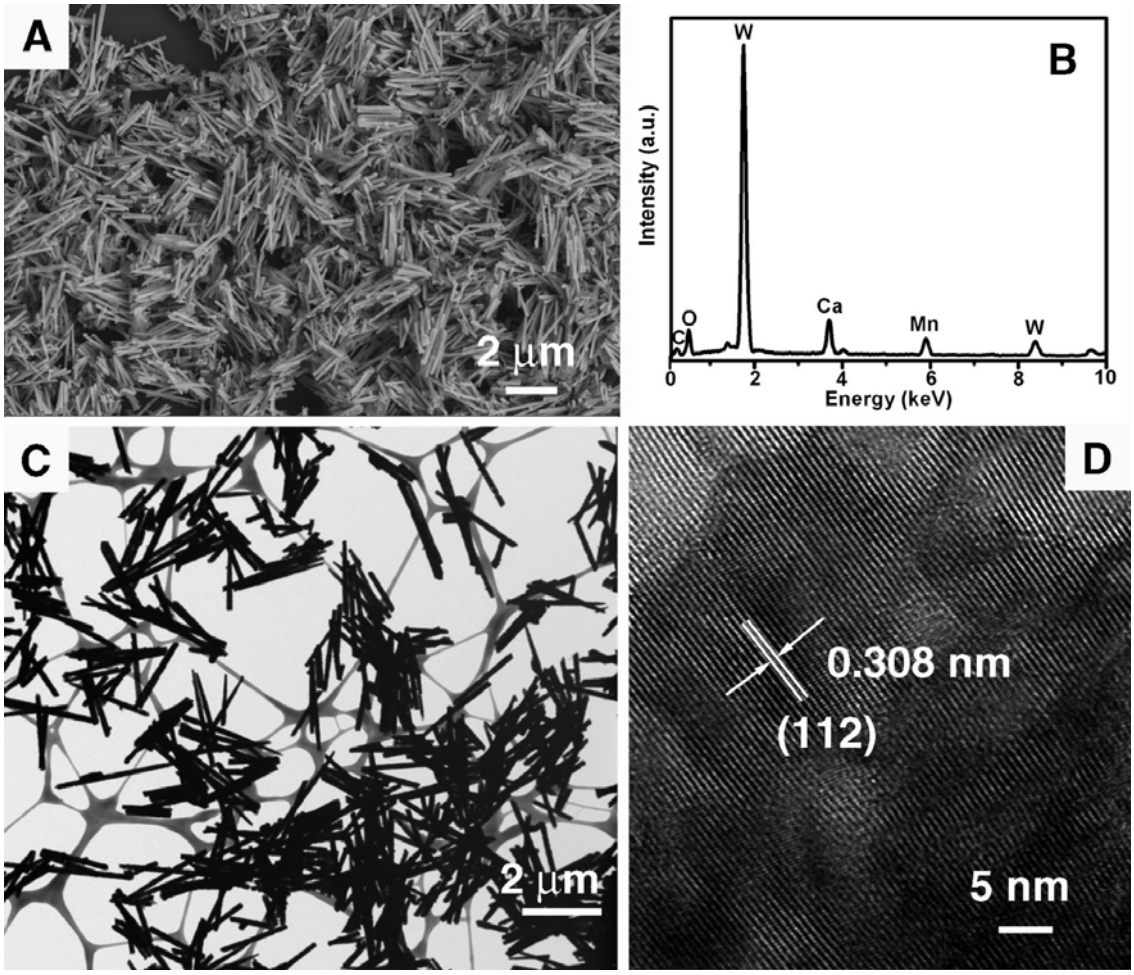

Figure 4.3 (A, C) Typical SEM and TEM images of as-prepared Mn-doped $CaWO_4$ nanorods, prepared using polycarbonate membranes with 200-nm pore diameters. (B) EDS spectrum of as-prepared Mn-doped $CaWO_4$ nanorods. The C peak originates from the conductive carbon tape. (D) HRTEM image of a representative portion of an individual Mn-doped $CaWO_4$ nanorod shown in (C).

Similarly, representative SEM and TEM images, as highlighted in panels A and C of Figure 4.4, respectively, reveal that as-prepared Mn-doped $SrWO_4$ samples, generated using poly carbonate membranes with 100 nm pore sizes, consist of straight, wire-like nanorods with a uniform diameter in the range of 100 $\pm$ 12 nm throughout their entire length of approximately 2.5-4 μm. EDS spectra (Figure 4.4B) reveal signals associated with Sr, W, O, as well as a molar concentration of Mn of up to 7.03%. The Sr signals overlap with W signals in the energy scale of around 1.9 keV. Corresponding HRTEM data of a single Mn-doped $SrWO_4$ nanorod, shown in Figure 4.4D, suggest a lattice spacing of 3.20 Å, which can be indexed as the (112) plane of a body-centered tetragonal phase of a bulk $SrWO_4$ crystal (JCPDS File No. 08-0490).

Panels A and C of Figure 4.5 present typical SEM and TEM images of as-prepared Mn-doped $BaWO_4$ nanorod samples, respectively. It can be observed that straight and smooth nanorods with uniform and homogeneous size could be routinely synthesized. The measured nanorods possess diameters ranging from 47 to 52 nm, based on the corresponding 50 nm pore sizes of the polycarbonate membranes used, and a length range of 4 to 6 μm, reaching an aspect ratio of up to 100. The chemical signatures obtained from EDS spectra (Figure 4.5B) are identical within experimental accuracy, and only Ba, W, O, and Mn elements are observed, as expected. The C signal arises from the underlying conductive carbon tape. The actual Mn dopant level was determined to be 5.81%, a somewhat lower value than expected based on the starting dopant concentration, but nevertheless in agreement with its incomplete incorporation into the underlying tungstate matrix. A representative HRTEM image, shown in Figure 4.5D, illustrates the crystalline nature of as-doped nanorods with an interplanar spacing of about 3.28 Å, corresponding to the (112) plane of pure $BaWO_4$, which agrees with XRD results initially described with Figure 4.1C.

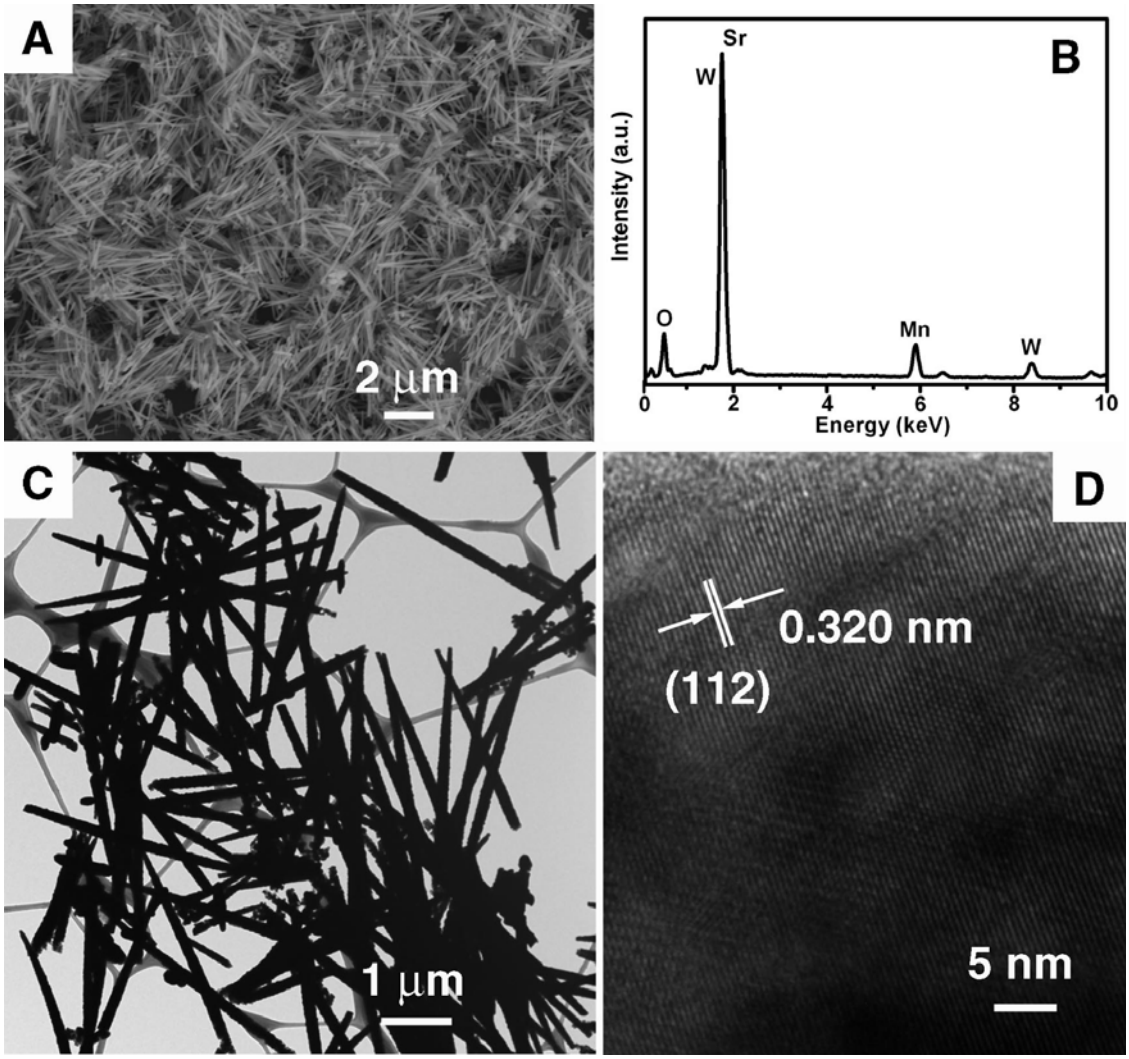

Figure 4.4 (A, C) Typical SEM and TEM images of as-prepared Mn-doped $SrWO_4$ nanorods, prepared using polycarbonate membranes with 100-nm pore diameters. (B) EDS spectrum of as-prepared Mn-doped $SrWO_4$ nanorods. (D) HRTEM image of a representative portion of an individual Mn-doped $SrWO_4$ nanorod shown in panel C.

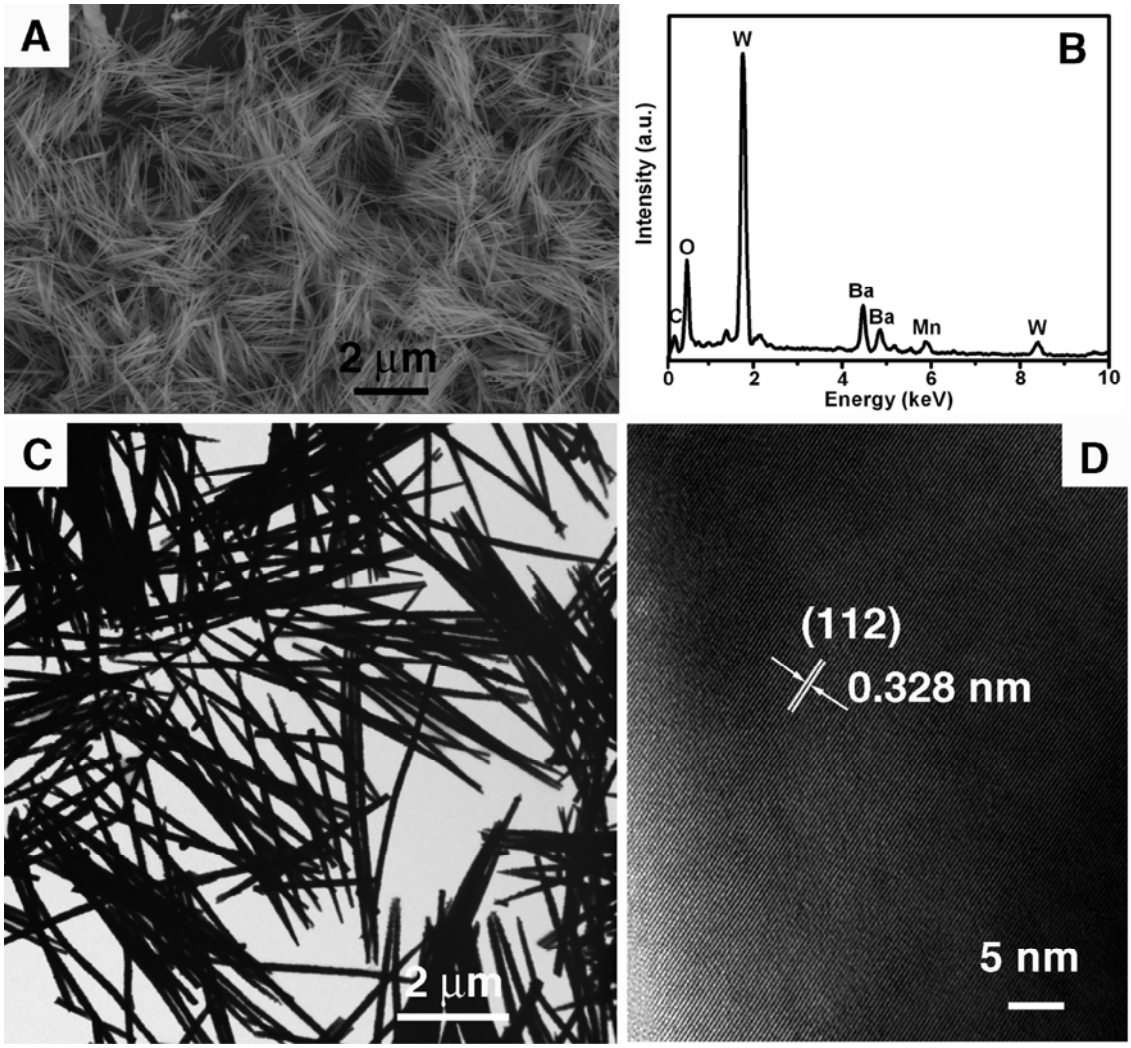

Figure 4.5 (A, C) Typical SEM and TEM images of as-prepared Mn-doped $BaWO_4$ nanorods prepared using polycarbonate membranes with 50-nm pore sizes. (B) EDX spectrum of as-prepared Mn-doped $BaWO_4$ nanorods. The C peak originates from the conductive carbon tape. (D) HRTEM image of a representative portion of an individual Mn-doped $BaWO_4$ nanorod shown in panel C.

It should be mentioned that even though the electron microscopy data for all of the as-prepared Mn-doped tungstate nanorods suggest that these nanomaterials are definitely crystalline, it is also evident that the nanorods are actually polycrystalline in nature and are composed of multiple adjacent, discrete, nanosized but misoriented single-crystalline domain regions. We attribute this observation to incorporation of the Mn dopant into the tungstate lattice, which corroborates other data, specifically photoluminescence data, we have collected. As with XRD, our electron microscopy data did not obviously yield evidence for the formation of isolated $MnWO_4$ domains.

In addition, we actually simulated each of the EDS spectra (Figure 4.6) containing a ratio of alkaline-earth metal (Ca, Sr, or Ba) to W to be 1:1 and in each case, these closely resembled our experimental results. Hence, as shown in Figures 4.3B, 4.4B, and 4.5B, if we integrate peak areas, we can state the following: the Ca peak arises from a K transition, the Sr peak originates from an L transition, the Ba peak is derived from an L transition, the Mn peak can be attributed to a K transition, and the W peaks can be ascribed to M and L transitions. The relatively strong W signal arises from its particularly sensitive M transitions. Moreover, the signal for W overlaps to a certain extent with the contribution of the underlying Si wafer.

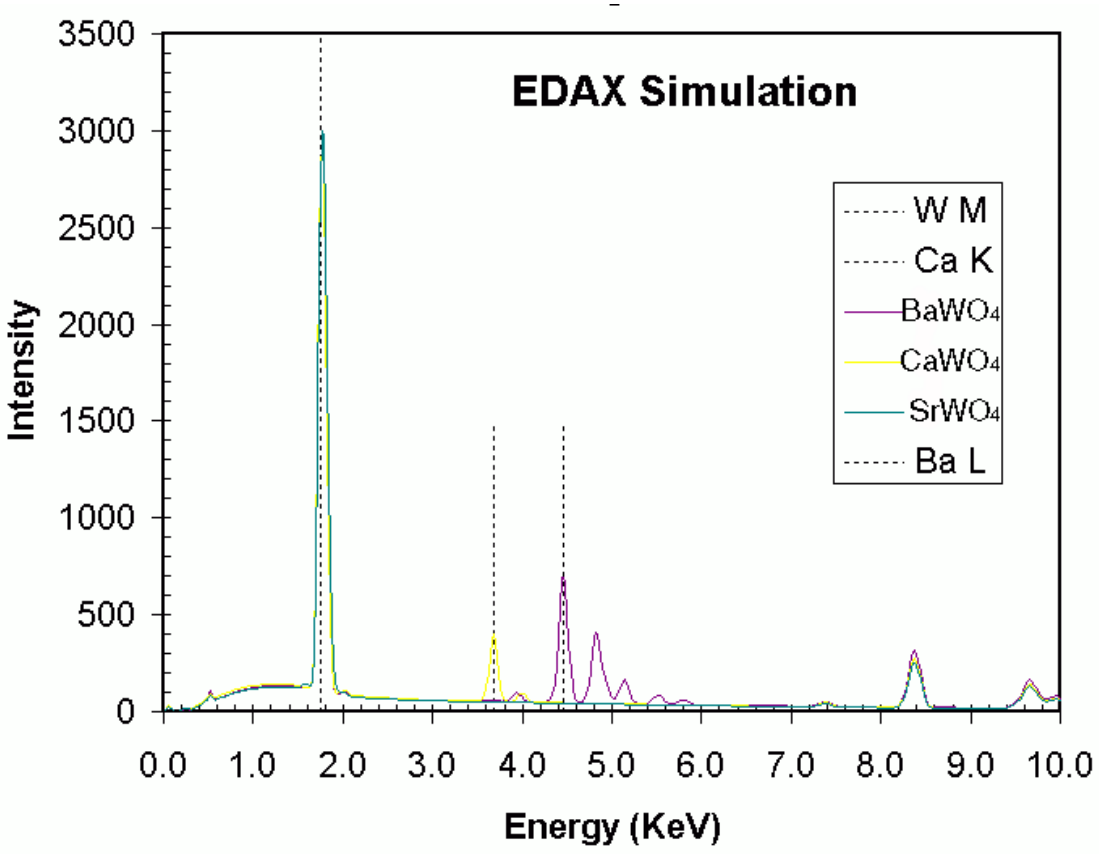

Figure 4.6 Simulated EDS spectra of alkaline earth tungstate materials.

4.3.3 Optical Spectroscopy

The optical properties of multifunctional nanorods were investigated. Figure 4.7 highlights UV-visible absorption spectra of as-prepared Mn-doped tungstate nanorods, collected at room temperature. It is evident that, for all three of the samples, there is a broadband absorption in the range from 350 to 450 nm, corresponding to the $^6A_1$ - $^4T_1$ transition associated with the 3d states of Mn^{2+} ions.[44-46] We show the corresponding UV-visible spectrum of $MnCl_2$ in Figure 4.8A, which is clearly distinctive. We also analyzed the UV-visible spectrum for $MnWO_4$ nanorods (Figure 4.8B). As well, we collected the corresponding UV-visible spectra for undoped $CaWO_4$, $SrWO_4$, and $BaWO_4$, in addition to data for all of these nanomaterials subsequently mixed physically with $MnWO_4$ itself (Figure 4.9). In each of these control samples, the data were essentially featureless in the 350-450 nm region of interest. All of these points should hopefully eliminate the possibility that the signals arose from free Mn^{2+} ions in solution and support the notion that the absorption curves originated from Mn^{2+} ions incorporated within the nanorod structures themselves.

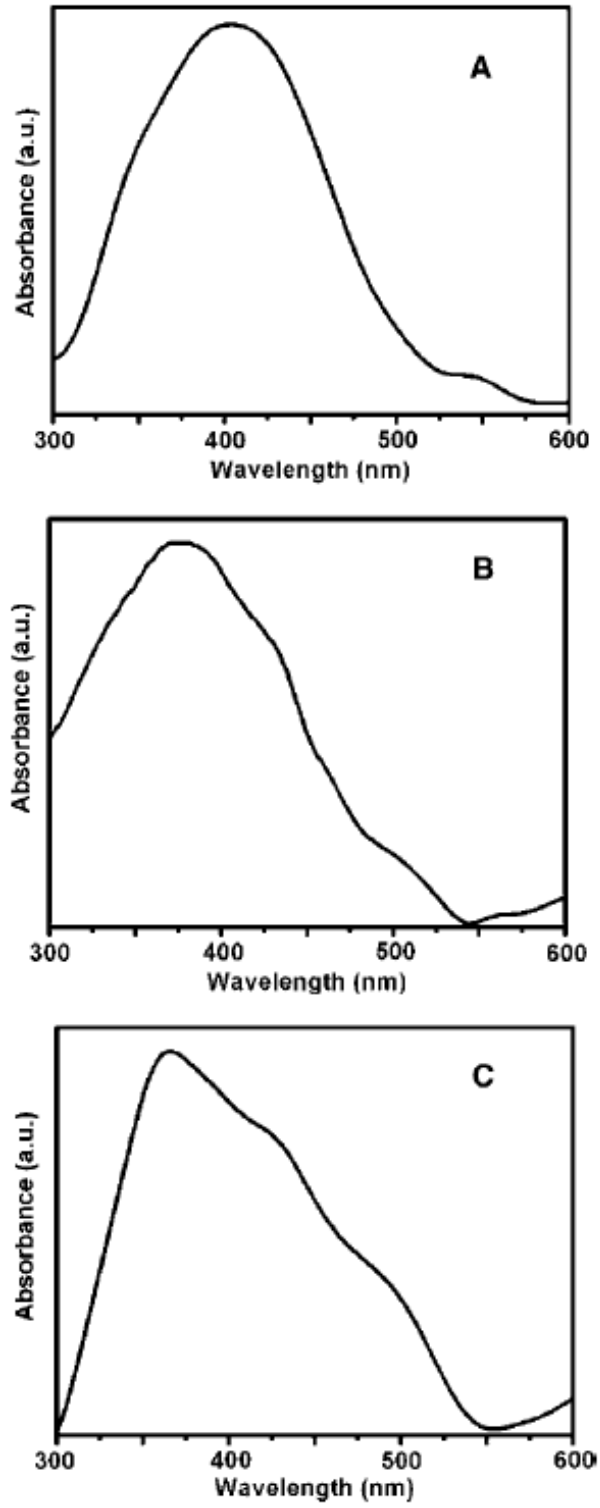

Figure 4.7 UV-visible spectra of as-prepared (A) Mn-doped $CaWO_4$ nanorods, (B) Mn-doped $SrWO_4$ nanorods, and (C) Mn-doped $BaWO_4$ nanorods.

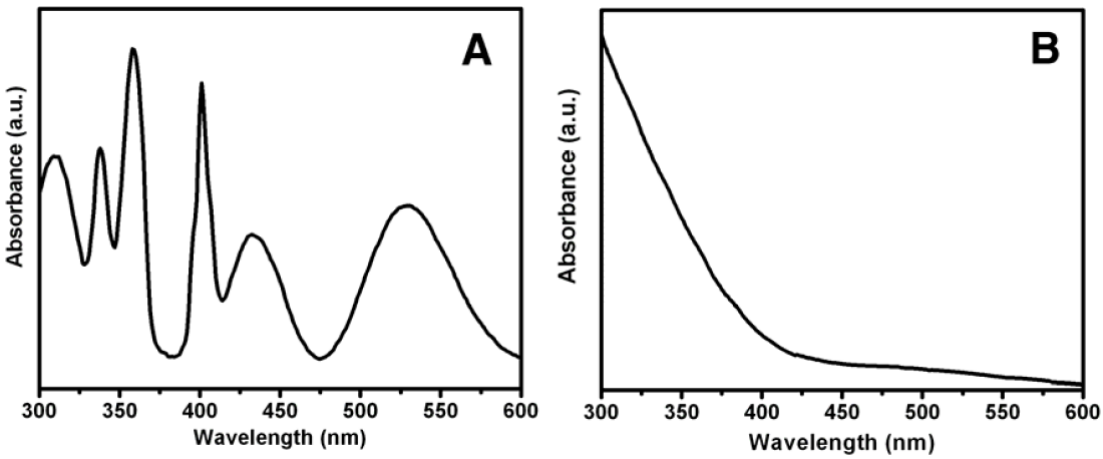

Figure 4.8 UV-visible spectra of (A) $MnCl_2$ solution and (B) $MnWO_4$.

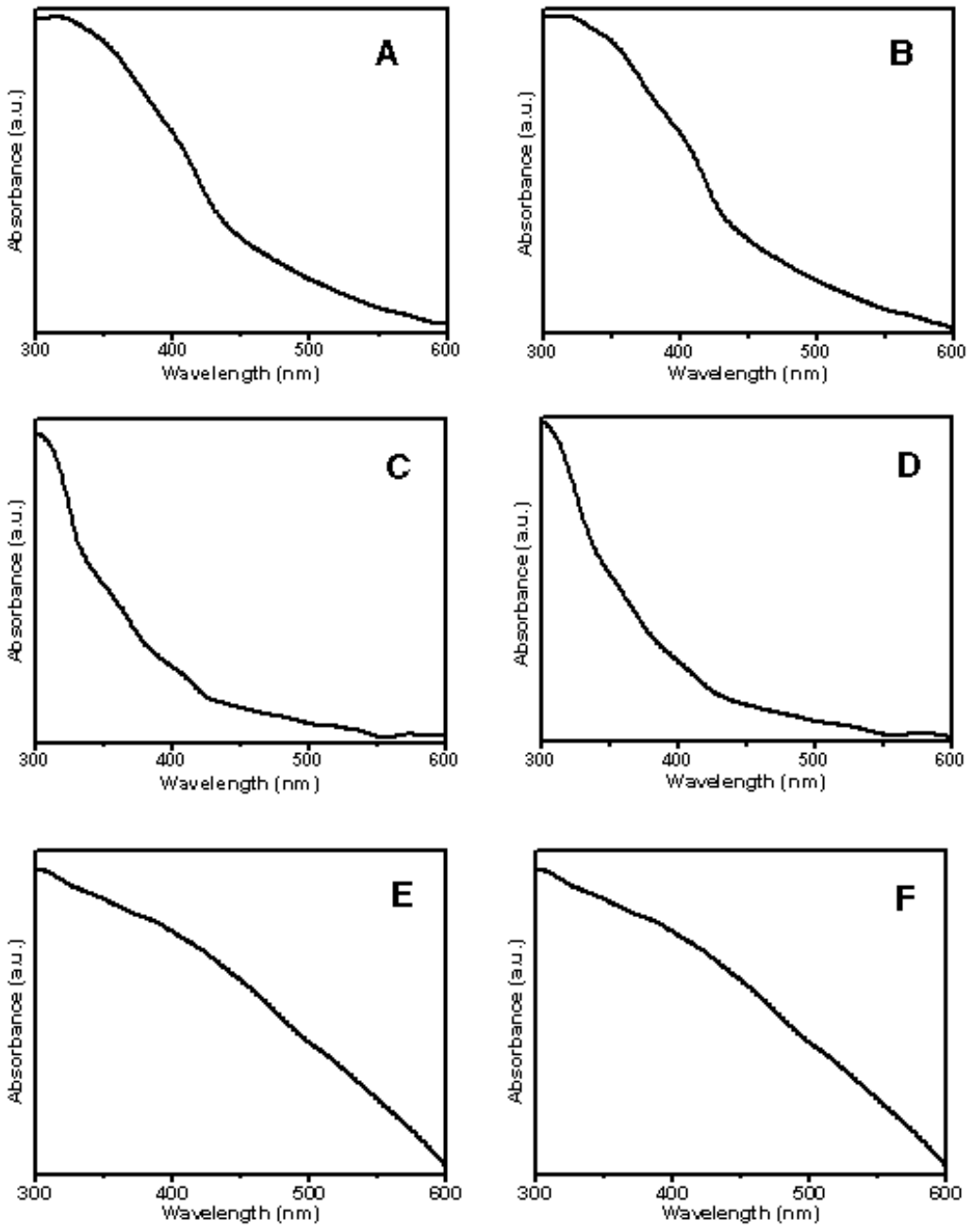

Figure 4.9 UV-visible spectra of (A) $CaWO_4$; (B) a physical mixture of $CaWO_4$ and $MnWO_4$; (C) $SrWO_4$; (D) a physical mixture of $SrWO_4$ and $MnWO_4$; (E) $BaWO_4$; (F) a physical mixture of $BaWO_4$ and $MnWO_4$.

The photoluminescent behavior of these as-prepared doped tungstate nanorod samples was also probed in Figure 4.10. For all of the Mn-doped tungstate samples, all of the emission peak positions (centered at 502 nm) were not noticeably altered by the variation in chemical composition, implying that the energy gap related to the blue emission was not directly coupled to changes in either overall Ca, Sr, or Ba content.[47] To deal directly with the potential issue of the existence of discrete grains of $MnWO_4$, incorporated within $CaWO_4$, $SrWO_4$, and $BaWO_4$ nanorod systems, which might therefore have given rise to the observed optical properties, we obtained photoluminescence spectra not only for $MnWO_4$ itself but also for control samples consisting of physical mixtures of each of these various undoped tungstate systems, as shown in Figure 4.11. Specifically, the photoluminescent features associated with nanorod mixtures of $MnWO_4$ and $CaWO_4$, $MnWO_4$ and $SrWO_4$, as well as $MnWO_4$ and $BaWO_4$ were essentially indistinguishable from those of pristine $CaWO_4$, $SrWO_4$, and $BaWO_4$, respectively; moreover, the ratios of peak intensities measured at 502 nm for these control sample mixtures ranged from 0.94 to 1.15, which strongly suggested that the presence of $MnWO_4$ did not overly affect the observed spectral profiles. In fact, photoluminescent data associated with $MnWO_4$ alone were distinctive but did not yield any useful features in the 502 nm region of interest.

In general, for bulk tungstates, the dominant blue emission band can be attributed to charge transfer transitions within the $[WO_4^{2-}]$ group between the last fully occupied t_1 orbital and the first empty 2e orbital.[48] Excitation from the ground state ($^1A_1$) of $[WO_4^{2-}]$ gives rise to four excited states, that is, $^1T_2$, $^1T_1$, $^3T_2$, and $^3T_1$, from which only the transition between $^1A_1$ and $^1T_2$ is electric dipole allowed.[49] However, the WO_4^{2-} complexes in scheelite tungstates are slightly distorted from T_d to D_{2d} symmetry by the influence of the Jahn-Teller effect and electron-phonon interactions in general.[50, 51] Hence, the orbitally degenerate T state undergoes distortion and symmetry lowering to a D_{2d} symmetry state, which strongly enhances the number of transitions observed. Therefore, both $^1A_1$ to $^1T_2$, $^1T_1$ as well as $^1A_1$ to $^3T_2$, $^3T_1$ transitions become partially allowable, thereby rendering radiating transitions from low-lying triplet excited states to the $^1A_1$

ground-state as clearly detectable emission peaks in the blue luminescent spectra. As such, the resulting emission bands possess a "spread-eagle" shape.[52]

Figure 4.10A illustrates typical PL spectra of both pure $CaWO_4$ nanorods (red curve) as well as Mn-doped $CaWO_4$ nanorods (black curve). No significant shifts of PL emission were observed for these two systems. As we have discussed, it can be observed that both of the emission curves exhibit broad luminescence in the blue wavelength range centered at 502 nm and possess a classic spread-eagle structure, wherein a narrow central peak is surrounded by two shoulders. In addition, the presence of weak green and red emission bands could be ascribed to the presence of radiative transitions within defect centers, such as Frenkel defects, i.e., oxygen ions shifted to intersite positions with a simultaneous creation of a vacancy, on the surfaces of our samples as well as the possibility of Schottky defects, such as, WO_3.[48, 49, 53] Similar behavior was observed in the PL spectra of $SrWO_4$, Mn-doped $SrWO_4$, $BaWO_4$, and Mn-doped $BaWO_4$ nanorods, respectively (Figure 4.10B and C).

For the three Mn-doped alkaline-earth metal tungstate nanorod samples, in particular, all of the emission peak positions were also not affected by the incorporation of Mn ions, implying that the energy gap related to the blue emission within WO_4^{2-} complexes is similarly unaltered by the presence of Mn dopant. That is, although size is evidently a factor in determining nanoscale optical behavior, our result with tungstate nanorods herein is consistent with the lack of an observable shift in the emission peak position as a specific function of increasing Mn dopant concentration in either binary metal sulfide or oxide systems.[54, 55] Moreover, the existence of Mn did not noticeably induce either quenching or blinking.[56, 57] All of these observations are suggestive of weak Mn-Mn exchange interactions.[54, 58] However, the Mn-doped alkaline-earth metal tungstate nanorod samples clearly showed far greater and enhanced photoluminescent emission intensity as compared with their undoped counterparts, all normalized in terms of concentration. That is, as compared with pure $CaWO_4$ nanorods, Mn-doped $CaWO_4$ nanorods yielded 1.8 ± 0.2 times greater luminescence intensity (Figure 4.10A) at the major peak position located at 502 nm. In the case of Mn-doped $SrWO_4$ and Mn-doped $BaWO_4$ nanorods, the corresponding PL emission intensities at 502 nm were 1.3 ± 0.1

and 2.1 $\pm$ 0.2 times larger than those of the pure $SrWO_4$ and $BaWO_4$ nanorods, respectively.

There are a number of plausible factors that may account for the obvious improvement in observed emission intensities for Mn-doped alkaline-earth metal tungstate nanorods. For example, PL enhancement in the analogous case of Mn-doped ZnS nanocrystals has been primarily attributed to the passivation of surface defects on nanoparticles, thereby minimizing and suppressing nonradiative recombination.[59] Others have suggested that improved sample crystallinity and quality (i.e., with few defect states present) enhance luminescence properties.[60-62]

Although all of these prior factors are clearly critical and relevant, it is evident that the migration of Mn into the tungstate host is also important. That is, the efficiency of luminescence with Mn doping can be ascribed to the physical nature of the Mn^{2+} ions, surrounding the WO_4^{2-} groups. In fact, the majority of the dopant Mn^{2+} ions are thought to be substitutionally incorporated into cation sites with a tetrahedral crystal field. As compared with Ca^{2+}, Sr^{2+}, and Ba^{2+}, Mn^{2+} ions are smaller and can more readily and efficiently accommodate the expansion of WO_4^{2-} complexes upon excitation. As a result, there is a higher thermal quenching temperature of the blue luminescence and a correspondingly lower probability of nonradiative transitions.[47, 63] Thus, the observed increase in luminescence can be partially attributed to the intra-3d-shell transitions of WO_4^{2-} ions. In other words, because the states within the 3d shell are strongly affected by the local crystal field environment associated with the WO_4^{2-} ions, occupying specific lattice sites in the host tungstate matrix, the Mn^{2+} ions are able to luminescent quite effectively.[64]

Furthermore, it is known that an orange/yellow luminescence band, peaking at around 573 nm, is a characteristic emission of Mn^{2+} ions, which can be attributed to a transition from $^4T_1$ (first excited state) to $^6A_1$ (ground state).[42, 65] As compared with pure alkaline-earth metal tungstates, the peaks centered at ~573 nm for Mn-doped nanorods show 1.8 $\pm$ 0.1, 1.1 $\pm$ 0.2, and 2.3 $\pm$ 0.2 times greater luminescence intensity than their undoped counterparts, as shown in Figure 4.10, respectively. We reiterate the fact that quenching is not observed in our system even with Mn doping levels as high as 7%.

Concentration quenching in this doping scenario has been previously ascribed to the transfer of excitation energy from one Mn^{2+} ion to a neighboring Mn^{2+} via nonradiative transitions.[41] Thus, the existence of Mn^{2+} pairs and strong Mn-Mn exchange interactions would be detrimental to PL, but the fact that the actual Mn dopant concentration is relatively low (i.e., less than 10% but still higher than the few percent threshold required for quenching of ZnS nanocrystals[41, 54, 66]) suggests that the Mn^{2+} ions are sufficiently diluted and stably isolated within the tungstate matrix and can therefore act as effective luminescence centers. Overall, due to the lack of quenching, it is plausible that no Mn^{2+} pairs are formed in our system and that few if any Mn^{2+} ions are surface quenched.

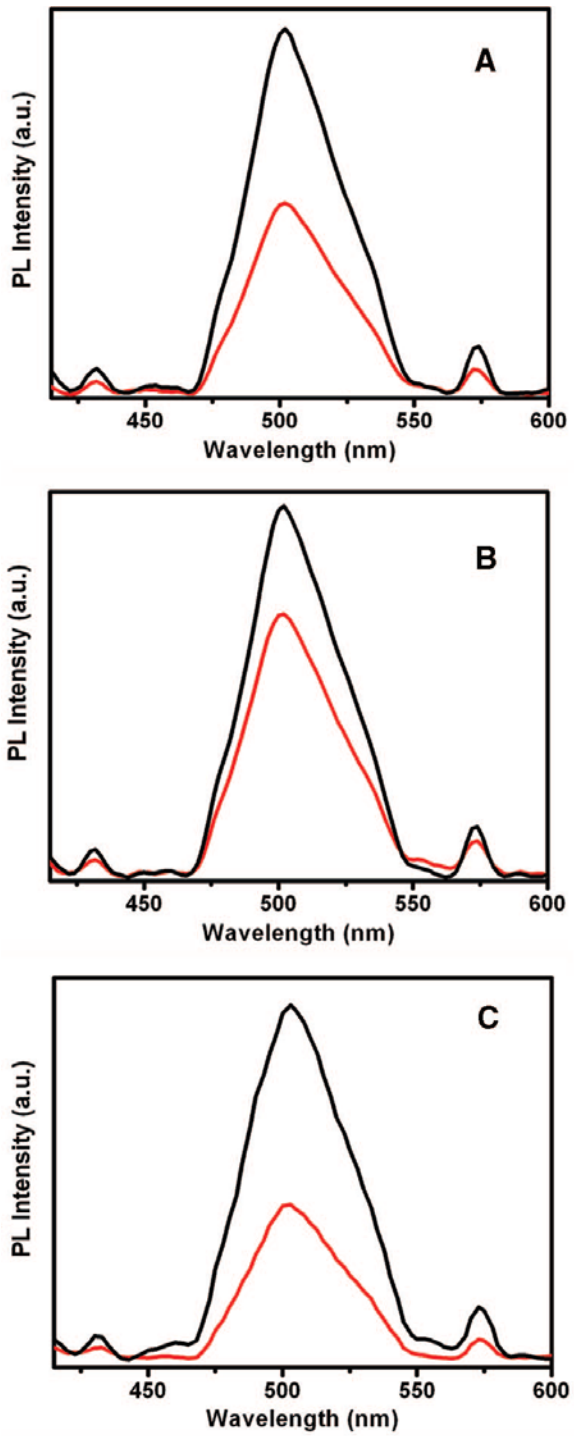

Figure 4.10 Photoluminescence spectra of as-prepared (A) Mn-doped $CaWO_4$ nanorods (top, black) as well as pure $CaWO_4$ nanorods (bottom, red); (B) Mn-doped $SrWO_4$ nanorods (top, black) as well as pure $SrWO_4$ nanorods (bottom, red); and (C) Mn-doped $BaWO_4$ nanorods (top, black) as well as pure $BaWO_4$ nanorods (bottom, red) at room temperature.

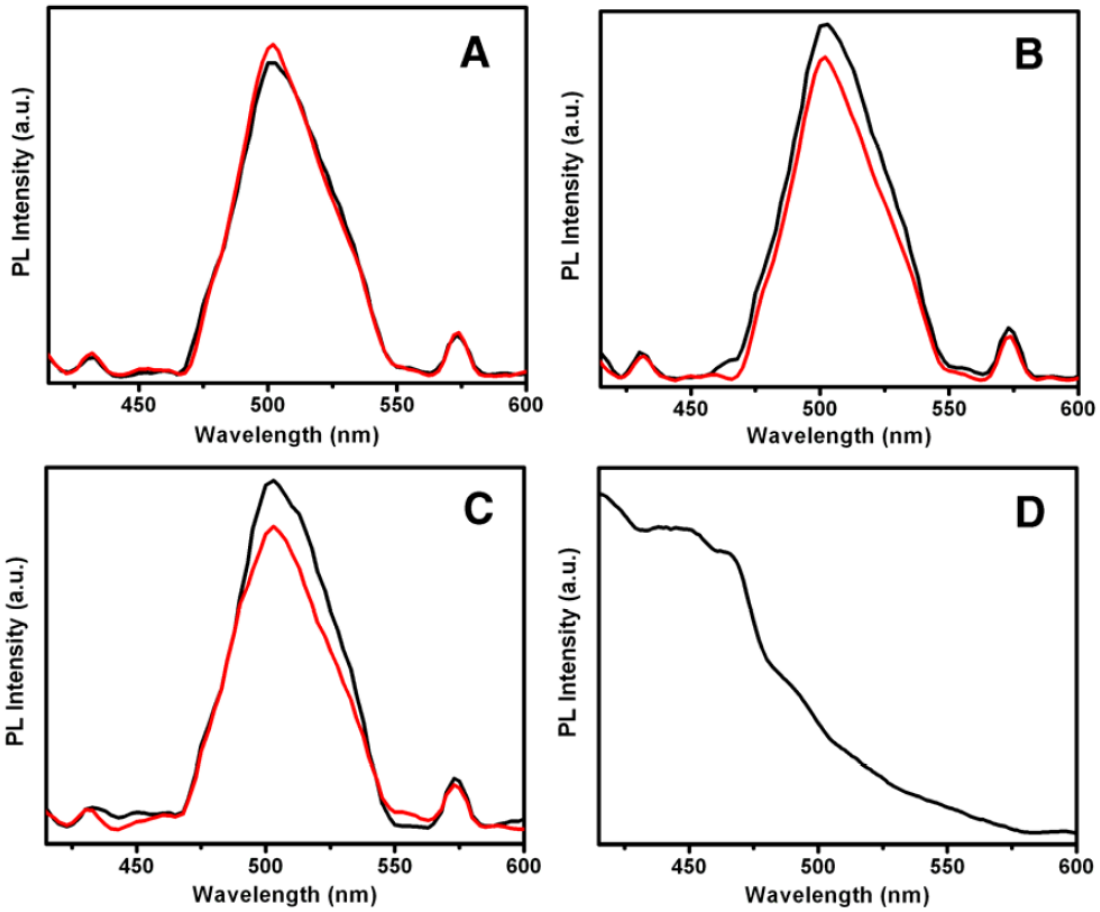

Figure 4.11 Photoluminescence spectra of (A) a physical mixture of $MnWO_4$ and $CaWO_4$ nanorods (black), as well as pure $CaWO_4$ nanorods (red); (B) a physical mixture of $MnWO_4$ and $SrWO_4$ nanorods (black), as well as pure $SrWO_4$ nanorods (red); (C) a physical mixture of $MnWO_4$ and $BaWO_4$ nanorods (black), as well as pure $BaWO_4$ nanorods (red); (D) pure $MnWO_4$ nanorods alone.

4.3.4 Magnetic Measurements

We have measured the magnetization of Mn-doped $CaWO_4$, $SrWO_4$, and $BaWO_4$ for temperatures from 1.8 to 300 K and in fields as large as 5 T using a Quantum Designs Magnetic Phenomena Measurement System. The field dependence of the magnetization, measured at 5 K, is presented in Figure 4.12. In each of the three systems, the magnetization is wholly linear in field, ruling out the possibility of ferromagnetic ordering at low temperature.

The temperature dependence of the magnetic susceptibility, $\chi(T) = M(T)/H$, normalized per gram of compound and measured in a fixed field H of 0.1 T, is shown in Figure 4.13A. As shown in Figure 4.13B, the inverse susceptibility of all three samples is linear in temperature above ~50 K, confirming that the Mn moments in each are paramagnetic and have equal moments. There is a modest variation in the Weiss temperatures for the three systems, being -21.8, -22.4, and -14.8 K for Mn-doped $CaWO_4$, $SrWO_4$, and $BaWO_4$, respectively. As may be noted by close examination of Figure 4.13B, there are small departures of the measured susceptibility from the Curie-Weiss expression at lower temperatures, suggestive of incipient magnetic order. Indeed, the inset to Figure 4.13A shows that the low temperature susceptibility in Mn-doped $CaWO_4$ and $BaWO_4$ has a broad maximum below 10 K, suggestive of a disorder broadened antiferromagnetic transition. Similar results were previously obtained on $MnWO_4$ in both bulk and nanoparticulate forms.

The susceptibility of Mn-doped $SrWO_4$ is distinctive in that it has a discontinuity in the slope of the temperature dependent susceptibility at 8.5 K, while becoming temperature independent at lower temperatures. This result indicates that Mn-doped $SrWO_4$ is antiferromagnetically ordered, and the relative lack of critical fluctuations may imply that the phase transition is at least weakly first order. We have observed no hysteresis in the susceptibility of Mn-doped $SrWO_4$ after cooling in zero field, or after cooling in a field of 0.1 T, as expected for a bulk antiferromagnet. This suggests that the magnetic order of Mn-doped $SrWO_4$ likely has no appreciable ferromagnetic component, as in a ferrimagnet, nor is there a role for uncompensated surface moments, as might be expected for nanometer sized particles. This last point is quite reasonable, since the

relatively large size of the nanorods implies that a relatively small fraction of the Mn atoms is actually at the surface, making the nanorods functionally bulk-like from the standpoint of the magnetic measurements. Indeed, we have previously failed to discern any difference in the magnetization of bulk versus nanoscale $MnWO_4$.[67]

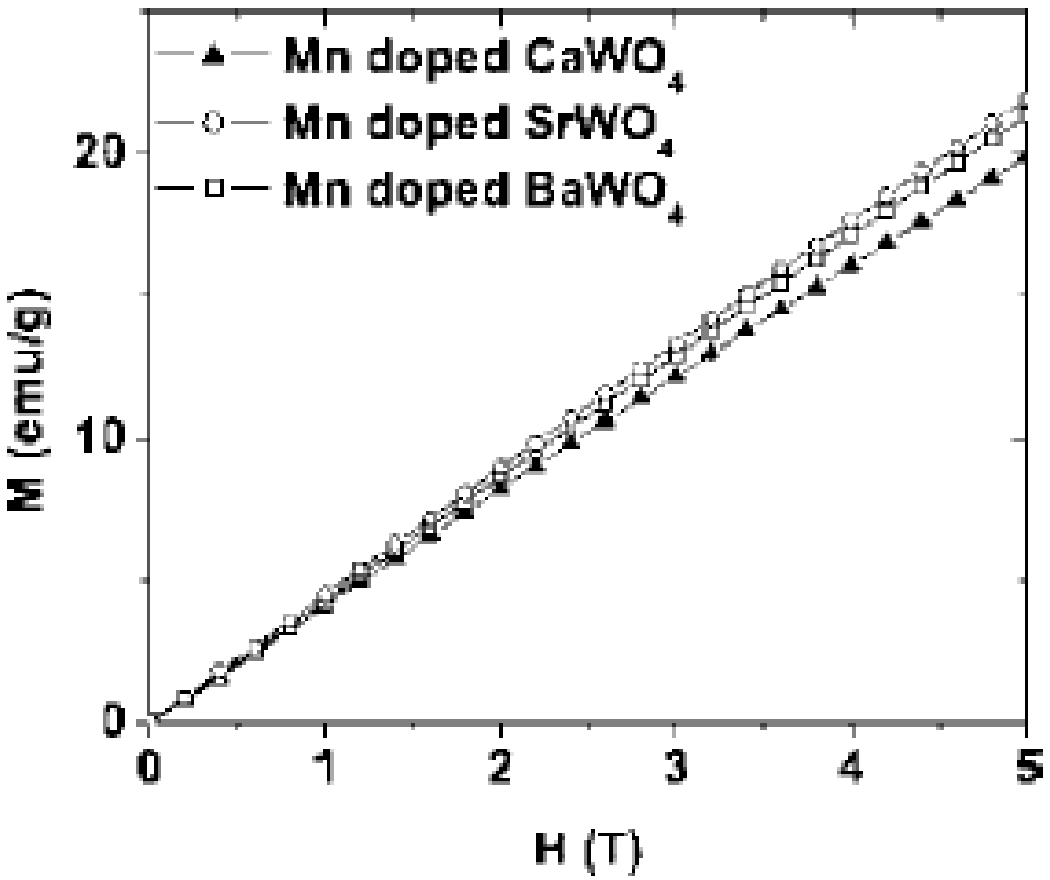

Figure 4.12 Field dependences of the magnetization (M), at 5 K for as-prepared Mn-doped $CaWO_4$ (filled triangles), $SrWO_4$ (open circles), and $BaWO_4$ (open squares) nanorods.

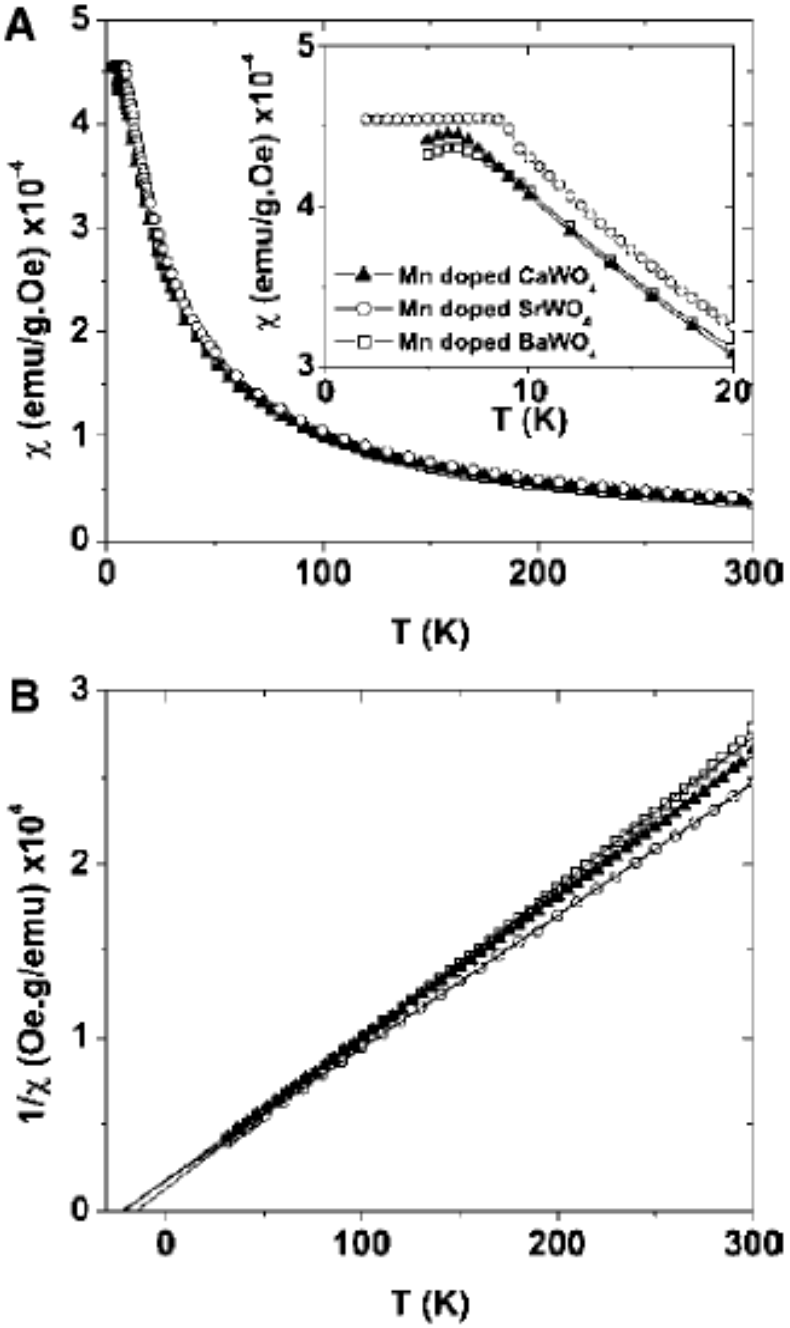

Figure 4.13 (A) Magnetic susceptibility χ of powder of 200 nm nanowires, measured in a field of 0.1 T. Inset shows an expanded view between 2 and 20 K of data for as-prepared Mn-doped $CaWO_4$ (filled triangles), $SrWO_4$ (open circles), and $BaWO_4$ (open squares) nanorods. (B) Corresponding temperature dependence of the inverse susceptibility χ^{-1} for as-prepared Mn-doped $CaWO_4$ (filled triangles), $SrWO_4$ (open circles), and $BaWO_4$ (open squares) nanorods. Linear behavior of data suggests the applicability of the Curie-Weiss law.

4.4 Conclusions

The current work demonstrates the synthesis of a family of Mn-doped alkaline-earth metal tungstate nanorods using a modified template-directed methodology under ambient, room-temperature conditions. Nanorod diameters were easily controlled by varying the pore sizes of the polycarbonate membranes, which provided confined spaces in order to direct the crystal growth. The resulting crystalline nanorods have been extensively characterized using a number of diffraction, electron microscopy, optical spectroscopy, and magnetic techniques. As-prepared Mn-doped alkaline-earth metal tungstate nanorods showed increased luminescence intensities, as compared with pure alkaline-earth metal tungstate counterparts. In addition, similar antiferromagnetic behavior to $MnWO_4$ was observed in these nanorods. The simplicity and versatility of the synthetic approach used highlight the possibility of incorporating multifunctions into individual 1D nanostructures, thereby suggesting their potential applications in a number of diverse fields.

4.5 References

1. Kim, J. S.; Rieter, W. J.; Taylor, K. M. L.; An, H.; Lin, W.; Lin, W., *J. Am. Chem. Soc.* **2007,** *129*, 8962.
2. Giri, S.; Trewyn, B. G.; Stellmaker, M. P.; Lin, V. S.-Y., *Angew. Chem. Int. Ed.* **2005,** *44*, 5038.
3. Lin, Y.-S.; Wu, S.-H.; Hung, Y.; Chou, Y.-H.; Chang, C.; Lin, M.-L.; Tsai, C.-P.; Mou, C.-Y., *Chem. Mater.* **2006,** *18*, 5170.
4. Santra, S.; Yang, H.; Holloway, P. H.; Stanley, J. T.; Mericle, R. A., *J. Am. Chem. Soc.* **2005,** *127*, 1656.
5. Nasongkla, N.; Bey, E.; Ren, J.; Ai, H.; Khemtong, C.; Guthi, J. S.; Chin, S.-F.; Sherry, A. D.; Boothman, D. A.; Gao, J., *Nano Lett.* **2006,** *6*, 2427.
6. Bao, J.; Chen, W.; Liu, T.; Zhu, Y.; Jin, P.; Wang, L.; Liu, J.; Wei, Y.; Li, Y., *ACS Nano* **2007,** *1*, 293.
7. Wei, C.; Dai, L.; Roy, A.; Tolle, T. B., *J. Am. Chem. Soc.* **2006,** *128*, 1412.

8. Sankapal, B. R.; Setyowati, K.; Chen, J.; Liu, H., *Appl. Phys. Lett.* **2007,** *91*, 173103.

9. Peng, H., *J. Am. Chem. Soc.* **2008,** *130*, 42.

10. Shim, B. S.; Tang, Z.; Morabito, M. P.; Agarwal, A.; Hong, H.; Kotov, N. A., *Chem. Mater.* **2007,** *19*, 5467.

11. Ohno, H., *Science* **1998,** *281*, 951.

12. Ando, K., *Science* **2006,** *312*, 1883.

13. Ohno, H.; Chiba, D.; Matsukura, F.; Omiya, T.; Abe, E.; Dietl, T.; Ohno, Y.; Ohtani, K., *Nature* **2000,** *408*, 944.

14. Ohno, Y.; Young, D. K.; Beschoten, B.; Matsukura, F.; Ohno, H.; Awschalom, D. D., *Nature* **1999,** *402*, 790.

15. Liao, H.-W.; Wang, Y.-F.; Liu, X.-M.; Li, Y.-D.; Qian, Y.-T., *Chem. Mater.* **2000,** *12*, 2819.

16. Wang, H.; Medina, F. D.; Zhou, Y. D.; Zhang, Q. N., *Phys. Rev. B* **1992,** *45*, 10356.

17. Li, L.; Su, Y.; Li, G., *Appl. Phys. Lett.* **2007,** *90*, 054105.

18. Yu, S.-H.; Liu, B.; Mo, M.-S.; Huang, J.-H.; Liu, X.-M.; Qian, Y.-T., *Adv. Funct. Mater.* **2003,** *13*, 639.

19. Yu, S.-H.; Antonietti, M.; Cölfen, H.; Giersig, M., *Angew. Chem. Int. Ed.* **2002,** *41*, 2356.

20. Liu, B.; Yu, S.-H.; Li, L.; Zhang, Q.; Zhang, F.; Jiang, K., *Angew. Chem. Int. Ed.* **2004,** *43*, 4745.

21. Kaminskii, A. A.; Eichler, H. J.; Ueda, K.-I.; Klassen, N. V.; Redkin, B. S.; Li, L. E.; Findeisen, J.; Jaque, D.; García-Sole, J.; Fernández, J.; Balda, R., *Appl. Optics* **1999,** *38*, 4533.

22. Zhang, Q.; Yao, W.-T.; Chen, X.; Zhu, L.; Fu, Y.; Zhang, G.; Sheng, L.; Yu, S.-H., *Crystal Growth & Design* **2007,** *7*, 1423.

23. Sun, L.; Guo, Q.; Wu, X.; Luo, S.; Pan, W.; Huang, K.; Lu, J.; Ren, L.; Cao, M.; Hu, C., *J. Phys. Chem. C* **2007,** *111*, 532.

24. Cho, W.-S.; Yashima, M.; Kakihana, M.; Kudo, A.; Sakata, T.; Yoshimura, M., *Appl. Phys. Lett.* **1995,** *66*, 1027.

25. Taniguchi, K.; Abe, N.; Takenobu, T.; Iwasa, Y.; Arima, T., *Phys. Rev. Lett.* **2006,** *97*, 097203.

26. Arkenbout, A. H.; Palstra, T. T. M.; Siegrist, T.; Kimura, T., *Phys. Rev. B* **2006,** *74*, 184431.

27. Lautenschläger, G.; Weitzel, H.; Vogt, T.; Hock, R.; Böhm, A.; Bonnet, M.; Fuess, H., *Phys. Rev. B* **1993,** *48*, 6087.

28. Ehrenberg, H.; Weitzel, H.; Heid, C.; Fuess, H.; Wltschek, G.; Kroener, T.; Tol, J. v.; Bonnet, M., *J. Phys.: Condens. Matter* **1997,** *9*, 3189.

29. Heyer, O.; Hollmann, N.; I. Klassen, I.; Jodlauk, S.; Bohatý, L.; Becker, P.; Mydosh, J. A.; Lorenz, T.; Khomskii, D., *J. Phys.: Condens. Matter* **2006,** *18*, L471.

30. Bode, M.; Vedmedenko, E. Y.; Von Bergmann, K.; Kubetza, A.; Ferriani, P.; Heinze, S.; Wiesendanger, R., *Nat. Mater.* **2006,** *5*, 477.

31. Meiklejohn, M. H.; Bean, C. P., *Phys. Rev.* **1956,** *102*, 1413.

32. Ramesh, R.; Spaldin, N. A., *Nat. Mater.* **2007,** *6*, 21.

33. Bleijenberg, K. C.; De Wit, H. G. M., *J. C. S. Faraday II* **1980,** *76*, 872.

34. Doroshenko, M. E.; Basiev, T. T.; Vassiliev, S. V.; Ivleva, L. I.; Komar, V. K.; Kosmyna, M. B.; Jelinkova, H.; Sulc, J., *Opt. Mater.* **2007,** *30*, 54.

35. Kuleshov, N. V.; Lagatsky, A. A.; Shcherbitsky, V. G.; Mikhailov, V. P.; Heumann, E.; Jensen, T.; Diening, A.; Huber, G., *Appl. Phys. B* **1997,** *64*, 409.

36. Treadaway, M. J.; Powell, R. C., *Phys. Rev. B* **1975,** *11*, 862.

37. Xia, Y.; Yang, P.; Sun, Y.; Wu, Y.; Mayers, B.; Gates, B.; Yin, Y.; Kim, F.; Yan, H., *Adv. Mater.* **2003,** *15*, 353.

38. Rutherglen, C.; Burke, P., *Nano Lett.* **2007,** *7*, 3296.

39. Ma, R.-M.; Dai, L.; Huo, H.-B.; Xu, W.-J.; Qin, G. G., *Nano Lett.* **2007,** *7*, 3300.

40. Puntes, V. F.; Krishnan, K. M.; Alivisatos, A. P., *Science* **2001,** *291*, 2115.

41. Peng, W. Q.; Qu, S. C.; Cong, G. W.; Wang, Z. G., *J. Cryst. Growth* **2005,** *279*, 454.

42. Na, C. W.; Han, D. S.; Kim, D. S.; Kang, Y. J.; Lee, J. Y.; Park, J.; Oh, D. K.; Kim, K. S.; Kim, D., *J. Phys. Chem. B* **2006,** *110*, 6699.

43. Wang, Y. S.; Thomas, P. J.; O'Brien, P., *J. Phys. Chem. B* **2006,** *110*, 21412.

44. Ejima, T.; Banse, T.; Takatsuka, H.; Kondo, Y.; Ishino, M.; Kimura, N.; Watanabe, M.; Matsubara, I., *J. Lumin.* **2006,** *119-120*, 59.

45. Huffman, D. R.; Wild, R. L.; Shinmei, M., *J. Chem. Phys.* **1969,** *50*, 4092.

46. Holmes, O. G.; McClure, D. S., *J. Chem. Phys.* **1957,** *26*, 1686.

47. Cho, W.-S.; Yashima, M.; Kakihana, M.; Kudo, A.; Sakata, T.; Yoshimura, M., *Appl. Phys. Lett.* **1996,** *68*, 137.

48. Grasser, R.; Scharmann, A., *J. Lumin.* **1976,** *12/13*, 473.

49. Grasser, R.; Scharmann, A.; Strack, K.-R., *J. Lumin.* **1982,** *27*, 263.

50. Polak, K.; Nikl, M.; Nitsch, K.; Kobayashi, M.; Ishii, M.; Usuki, Y.; Jarolimek, O., *J. Lumin.* **1997,** *72-74*, 781.

51. Nikl, M.; Bohacek, P.; Mihokova, E.; Ishii, M.; Usuki, Y.; Babin, V.; Stolovich, A.; Zazubovich, S.; Bacci, M., *J. Lumin.* **2000,** *87-89*, 1136.

52. Toyozawa, Y.; Inoue, M., *J. Phys. Soc. Jpn.* **1966,** *21*, 1663.

53. Ryu, J. H.; Yoon, J.-W.; Shim, K. B., *Electrochem. Solid-State Lett.* **2005,** *8*, D15.

54. Yang, H.; Holloway, P. H.; Ratna, B. B., *J. Appl. Phys.* **2003,** *93*, 586.

55. Roy, V. A. L.; Djurišić, A. B.; Liu, H.; Zhang, X. X.; Leung, Y. H.; Xie, M. H.; Gao, J.; Lui, H. F.; Surya, C., *Appl. Phys. Lett.* **2004,** *84*, 756.

56. Dabbousi, B. O.; Rodriguez-Viejo, J.; Mikulec, F. V.; Heine, J. R.; Mattoussi, H.; Ober, R.; Jensen, K. F.; Bawendi, M. G., *J. Phys. Chem. B* **1997,** *101*, 9463.

57. Larson, D. R.; Zipfel, W. R.; Williams, R. M.; Clark, S. W.; Bruchez, M. P.; Wise, F. W.; Webb, W. W., *Science* **2003,** *300*, 1434.

58. Chen, W.; Sammynaiken, R.; Huang, Y.; Malm, J.-O.; Wallenberg, R.; Bovin, J.-O.; Zwiller, V.; Kotov, N. A., *J. Appl. Phys.* **2001,** *89*, 1120.

59. Lu, S. W.; Lee, B. I.; Wang, Z. L.; Tong, W.; Wagner, B. K.; Park, W.; Summers, C. J., *J. Lumin.* **2001,** *92*, 73.

60. Xia, B.; Lenggoro, I. W.; Okuyama, K., *Chem. Mater.* **2002,** *14*, 4969.

61. Kim, J. S.; Kim, J. S.; Kim, T. W.; Kim, S. M.; Park, H. J., *Appl. Phys. Lett.* **2005,** *86*, 091912.

62. Son, D.; Jung, D.-R.; Kim, J.; Moon, T.; Kim, C.; Park, B., *Appl. Phys. Lett.* **2007,** *90*, 101910.

63. Cho, W.-S.; Yoshimura, M., *Jpn. J. Appl. Phys.* **1997,** *36*, 5658.

64. Gan, L. M.; Liu, B.; Chew, C. H.; Xu, S. J.; Chua, S. J.; Loy, G. L.; Xu, G. Q., *Langmuir* **1997,** *13*, 6427.

65. Counio, G.; Gacoin, T.; Boilot, J. P., *J. Phys. Chem. B* **1998,** *102*, 5257.

66. Biswas, S.; Kar, S.; Chaudhuri, S., *J. PHys. Chem. B* **2005,** *109*, 17526.

67. Zhou, H.; Yiu, Y.; Aronson, M. C.; Wong, S. S., *J. Solid State Chem.* **2008,** *181*, 1539.

Chapter V Semiconducting Metal Sulfide Nanowires and Their Photocatalytic Application

5.1 Introduction

Semiconducting metal sulfide nanoparticulates possess novel optical and electrical properties and are considered as building blocks for photovoltaic devices including dye-sensitized cells, all-inorganic nanoparticle solar cells, and hybrid nanocrystal-polymer composite solar cells in addition to lasers and waveguides.[1] It is well known that when the semiconductor nanocrystal diameter is comparable to or less than the bulk exciton diameter, size-dependent optoelectronic properties and ionization potentials result.[2, 3] Semiconductor nanoparticles exhibit lower ionization potentials as the particle diameter is decreased beyond the threshold for quantum confinement. Therefore, their optical properties are highly dependent upon size and morphology. For example, through particle size control, photocatalytic electron and hole redox potentials of size-quantized semiconductor nanocrystals can be tuned to achieve increased redox power for use in waste water decontamination, in solar cells, or for selective synthesis processes.[4-6]

Specifically, green covellite copper sulfide (CuS) possesses metal-like electrical conductivity and chemical sensing capabilities.[7-11] CuS films maintain transmittance in the infrared, low reflectance in the visible and relatively high reflectance in the near-infrared region, which are ideal characteristics for solar energy adsorption. Moreover, CuS transforms into a superconductor at 1.6 K[12, 13] and has recently been used as a cathode material in lithium rechargeable batteries.[14]

Cadmium sulfide (CdS) is a II-VI semiconductor with a direct band gap of 2.42 eV with potential applications in laser light-emitting diodes, displays, dye-sensitized solar cells, fluorescence probes, sensors, photoelectrocatalysts, waveguides, and optoelectronic devices, based on its nonlinear optical properties.[15-22] Very recently, in a manner analogous to ZnO, upon visible light illumination, CdS nanowires have been used to

convert mechanical energy into electricity by carefully coupling the piezoelectric, optoelectronic, and semiconducting properties of these materials.[23, 24]

As a narrow band gap semiconductor with a bulk band gap energy of 0.41 eV, lead sulfide (PbS) has a reasonably large exciton Bohr radius of 18 nm, which allows it to achieve stronger confinement effects, even at relatively larger dimensions.[25, 26] Hence, PbS is an extremely promising material for a large number of applications in mid- and near-infrared emission and detection,[27, 28] important for biology and sensing.[29] Moreover, it has found usage in optoelectronic devices, including light emitting diodes, flame monitors, photovoltaics, solar cells, and high-speed optical switches, due to its third order nonlinear optical properties.[30-33]

In recent years, semiconducting 1D nanostructures, such as nanowires and nanotubes, are drawing intense research interest due to their novel physical and chemical properties as determined by their size, shape, and crystallinity. Their inherent anisotropy and quantum confinement within the low dimensionality render them as model systems for the efficient transport of electrons and optical excitations. As such, semiconducting nanowires have been used as building blocks for nanoscale energy-conversion, photonic, and electro-optical devices, as well as for electronic circuits.[34, 35] Nevertheless, a lot of effort has been expended in overcoming numerous challenges associated with the controlled synthesis of semiconducting nanowires with reproducible morphology, crystallinity, chemical composition, and monodispersity, since Ijima's discovery of carbon nanotubes.

In particular, the synthesis of CuS nanorods and nanowire-like aggregates has been previously reported by methods such as reacting appropriate metal compounds with Na_2S in the presence of a tripodal cholamine-based hydrogel,[36] using the mediation of a microemulsion directed route,[37] carrying out an amine-assisted hydrothermal process with CuCl/$[Cu(NH_3)_4]^{2+}$ and thiourea at low temperature,[38, 39] mechanically grinding together either $Cu(NO_3)_2 \cdot 3H_2O$ or $CuCl_2 \cdot 2H_2O$ with $Na_2S \cdot 9H_2O$ in the presence of ethylenediamine tetraacetic acid disodium salt at ambient temperature,[40] as well as refluxing at 105 ºC in the presence of $CuCl_2$, CS_2, and ethylenediamine.[41] Thioglycerol has been found to catalyze the hydrolysis of $Na_2S_2O_3$ and the formation of CuS

nanorods.[42] Solvothermal reaction protocols have been recently devised involving the decomposition of $Cu(acac)_2$ precursors at 120 ºC to yield hexagonal phase CuS, occasionally mediated by the presence of ligands such as triethylenediamine and di-*n*butylamine.[38] Even sonoelectrochemical deposition and microwave irradiation have been tried.[43] Well-aligned arrays of CuS nanotubes have been successfully obtained through the gas-solid sulfurization reaction of CuCl precursors.[44]

With respect to CdS nanorods, the use of hydrothermal-related treatments has been common.[45, 46] Specifically, a surfactant-ligand co-assisted solvothermal method[47-49] at 160 ºC involving either $Cd(NO_3)_2$ and NH_2CSNH_2 in ethylenediamine at 80 to 160 ºC for 12-72 h, Cd acetate and ethylenediamine at 150 ºC for 5-7 h,[50] $CdSO_4$ and thiourea at 100-180 ºC for 12 h,[51] or Cd metal powder and sulfur at 120 to 200 ºC[52, 53] have all been tried, occasionally assisted by the presence of promoters such as L-cysteine and poly(vinyl alcohol).[54] The hot coordination solvent method frequently used to synthesize nanocrystals has also been utilized to produce CdS nanowires in the presence of either octadecylphosphonic acid,[55, 56] oleylamine,[57] or tetradecylphosphonic acid.[58] The decomposition of cadmium hexadecylxanthate in the presence of hexadecylamine has also been suggested as a means of producing CdS nanowires.[59] CdS nanorods have also been successfully fabricated in various microemulsion systems.[45] Moreover, a thermal evaporation of CdS powder itself[60] as well as the thermal decomposition of appropriate semicarbazide and diethyldithiocarbamate precursors[61] have also been reported. Single-source molecular precursors in a nanocluster-catalyzed VLS growth process, have also yielded single-crystalline CdS nanowire products in high yield.[16]

Finally, PbS nanorods have been synthesized via a novel biphasic solvothermal interface reaction at 120 to 160 ºC,[62, 63] a single-step low-temperature decomposition of lead hexadecylxanthane,[64, 65] the reaction of lead acetate and thiourea in the presence of oleic acid at 140 ºC for 0.5 h under nitrogen,[30] a gold nanoparticle-seeded growth at 200 ºC,[66] thermolysis of lead nitrate, surfactant, and ethylenediamine at 280 ºC,[67] and a surfactant-assisted decomposition of lead thiocyanate in boiling benzyl alcohol.[68] Even chemical vapor deposition of PbS using $PbCl_2$ and S as precursors under either hydrogen or argon flow as well as an interfacial reaction between $PbCl_2$ and H_2S gas have been

attempted.[69-71] Finally, a sonochemical synthesis in the presence of polyethylene glycol has been reported.[72]

It is obvious based on all of the prior work that it would be desirable to develop a protocol that allows for a green, cost-effective methodology of metal sulfide 1D nanoscale synthesis without the need to sacrifice on sample quality, crystallinity, monodispersity, and purity. That is, it would be a viable, complementary advance to develop a generalizable protocol aimed at CuS, CdS, and PbS nanowire/array formation. Such a methodology would overcome (i) the high-temperatures, (ii) the need for expensive, complicated equipment, (iii) the use of potentially toxic, gaseous precursors and byproducts, (iv) the utilization of costly catalysts and performance-altering capping agents (including surfactants), or (v) the polycrystallinity of the ultimate product, characteristic of a number of previous literature methods of sulfide nanoscale metal synthesis.

As a straightforward route, therefore, template synthesis enables a high degree of control over the dimensions of the resulting 1D nanostructures. Prior literature has suggested that the fabrication of PbS, CuS, and CdS nanorods can occur either by electrodeposition or injection of reactants within the channel pores of either anodic aluminum oxide[43, 73-77] or mesoporous silica[78, 79] templates. However, as drawbacks in terms of sample quality and reaction conditions, nanostructures synthesized using this traditional template method often either are polycrystalline or necessitate an additional annealing step at high temperature. We have successfully demonstrated the validity of the modified template-directed protocol through the production of 1D nanostructures of a number of classes of diverse materials. In this project, we describe the preparation and characterization of (a) discrete, individual motifs and (b) arrays of crystalline and pure semiconducting transition metal sulfide (CuS, PbS, and CdS) nanowires, via the inexpensive, generalizable, simplistic, and ambient template-directed technique. Nearly all band gap semiconductors can be effectively prepared at room-temperature through this simple template-directed method, including PbS, CuS, and CdS nanowires, with band gap energies for their bulk materials noted to be 0.41 eV, 1.55 eV, and 2.42 eV,

respectively. The method is generalizable and can be adapted to the production of other 1D nanostructures.

5.2 Experimental Section

5.2.1 Materials Preparation

The membrane was mounted between two half arms of a U-shaped tube. Precursors Na_2S (Alfa Aesar, 98%), $Cu(NO_3)_2$ (Alfa Aesar, 98%), $Pb(CH_3COO)_2$ (Aldrich, 99.99%), and $Cd(NO_3)_2$ (Alfa Aesar, 98.5%) were of analytical grade and were used without further purification. In a typical synthesis, one of the two half-cells was filled with freshly prepared 0.01 M Na_2S solution, which was adjusted to pH = 6 using HCl. The other half-cell contained a 0.01 M solution of $Cu(NO_3)_2$, $Pb(CH_3COO)_2$, or $Cd(NO_3)_2$, used to generate CuS, PbS, or CdS nanowires, respectively. The system was then left unperturbed for an incubation period of as little as 5 h and up to 12 h at temperatures ranging from ambient conditions to 80 ºC. In the specific cases of CuS and PbS, such temporal and thermal variations did not noticeably affect either the morphology or the composition of the resultant products (Figure 5.1). By contrast, as we will discuss, an increase in reaction temperature to 80 ºC resulted in the transformation of cubic zinc blende CdS nanowires into hexagonal würtzite cactus-like CdS nanostructures.

Subsequent to precursor solution immersion and product formation, either a black color (CuS and PbS) or a yellow hue (CdS) was observed, associated with the polycarbonate membrane, which was then detached, sonicated for ~2 min to remove unwanted particles on the surface, and thoroughly washed with distilled water, prior to dissolution and removal with methylene chloride. As-prepared sulfide nanowires were then collected and isolated from solution by centrifugation after washing.

5.2.2 Materials Characterization

X-ray Powder Diffraction See Section 1.7.1.

Electron Microscopy See Section 1.7.3.

Optical Spectroscopy See Section 1.7.5.

Photocatalytic Degradation Activity. In a typical experiment, the CdS powdered catalyst (with a resulting concentration of 0.5 g/L), suspended in an aqueous solution of

either 50 ppm Rhodamine B or methyl orange, was ultrasonicated for 10 min and magnetically stirred under dark, un-illuminated conditions for 30 min so as to establish an adsorption-desorption equilibrium with respect to the individual dye species. After given irradiation time intervals with UV light at 366 nm at a 5 cm separation distance, the photocatalytic performance of the various CdS nanoscale catalysts was subsequently gauged by measuring changes in the intensity of the optical absorbance peaks, localized at either 555 or 464 nm, of the aqueous supernatant aliquots containing either Rhodamine B or methyl orange dye species, respectively. Analogous control experiments were performed either without CdS (blank) or in the presence of a commercial bulk sample (CERAC Inc.; particle size corresponding to -325 mesh or < 64 μm), normalized for identical metal sulfide concentrations.

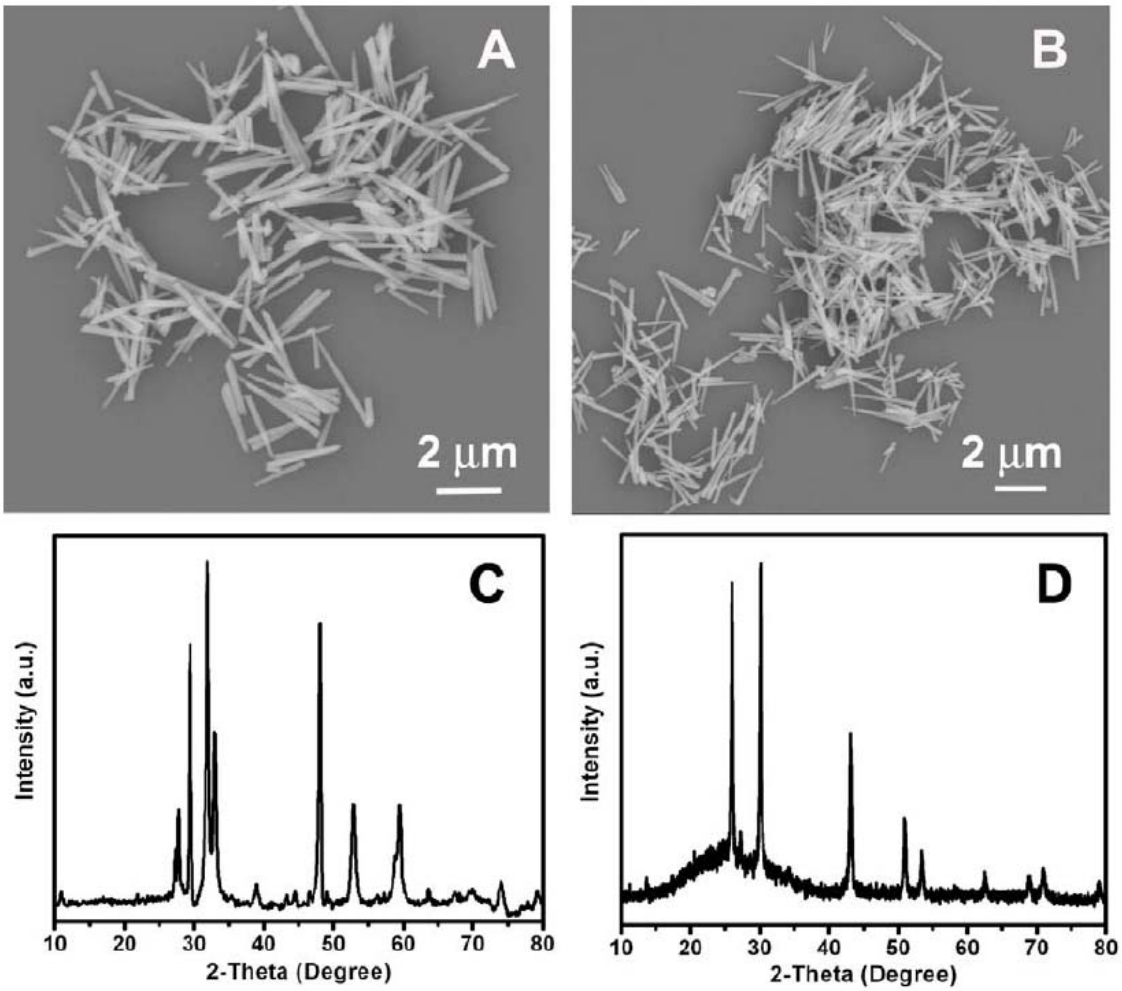

Figure 5.1 (A, B) Typical SEM images of as-prepared CuS and PbS nanowires, respectively, generated using polycarbonate membranes maintaining 200 nm pore diameters at 80 ºC. (C, D) Corresponding XRD patterns associated with CuS and PbS nanowires, respectively, prepared at 80 ºC.

5.3 Results and Discussion

5.3.1 X-ray Diffraction

The purity and crystallinity of as-prepared sulfide nanowire samples were initially characterized using powder XRD measurements. As shown in Figure 5.2 and summarized in Table 5.1, all of the diffraction peaks observed from each of the samples can be readily indexed and have been positively ascribed to pure phases of their bulk counterparts, with lattice constants comparable to the corresponding reported database values, associated with each of the target materials. Very little if any impurity peaks were present in any of the patterns, though it should be mentioned that two very weak peaks surrounding the (111) peak of cubic phase CdS (JCPDS No. 10-0454) in Figure 1C could be ascribed to the (100) and (101) peaks of hexagonal würtzite CdS (JCPDS No. 41-1049). Thus, overall, these results strongly suggest that reasonably pure, crystalline hexagonal-phase CuS, cubic-phase PbS, and cubic-phase CdS can be prepared under ambient, room-temperature conditions without the necessity of an additional annealing step at high temperature.

The CdS results are worthy of further discussion. CdS possesses three types of crystal structures, namely, hexagonal würtzite, cubic zinc blende, and high-pressure rocksalt phases. The hexagonal phase can be observed in both bulk and nanocrystalline structures, whereas the cubic and rocksalt phases are less commonly formed.[77] Among the three phases, hexagonal würtzite has been intensively investigated because it is the most thermodynamically stable form of CdS and has been extensively synthesized easily by a number of groups.[55, 80-82] By contrast, only a relatively few number of papers has ever claimed the synthesis of either spherical quantum dots or cylindrical nanowires of CdS possessing either the cubic zinc blende phase or even a mixture of both hexagonal and cubic phases.[17, 77, 83, 84] Hence, to the best of our knowledge, for the first time, we have demonstrated the ambient, room-temperature preparation of CdS nanowires associated with a metastable cubic phase with minimal hexagonal phase impurities.

Figure 5.3 shows the XRD patterns of CdS nanostructures prepared at 80 °C. In contrast with ambiently prepared cubic phase CdS nanowires, all of the diffraction peaks corresponding to the cactus-like nanostructures, formed at higher temperatures, can be

indexed to the pure hexagonal phase of CdS (JCPDS No. 41-1049). We note that the energy difference between the cubic and hexagonal CdS energy gap differs by less than 0.1 eV.[85] Hence, our observations are not surprising since it has been reported that, at low temperatures, the cubic phase can be more easily obtained whereas at higher temperatures, the hexagonal phase is more prevalent.[86-88] Moreover, the relative peak broadening observed can be attributed to the existence of crystalline faults, microstrains, crystalline domain sizes, and/or domain size distribution.[89]

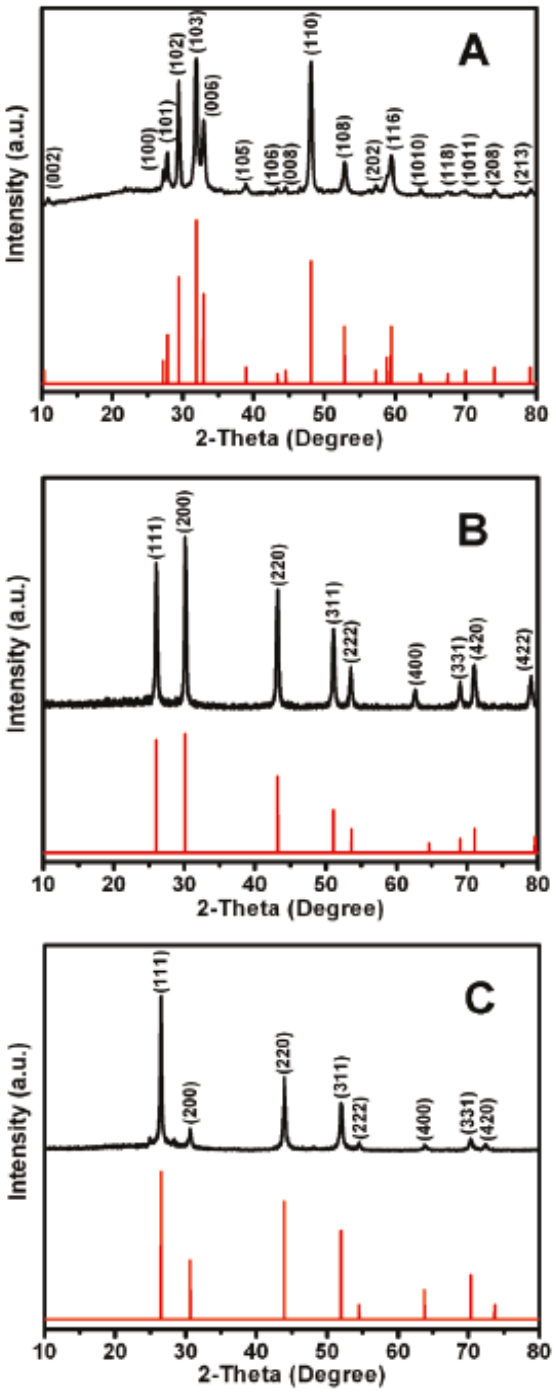

Figure 5.2 XRD patterns obtained from (A) as-prepared CuS nanowires (top, black) and corresponding JCPDS No. 06-0464 database standard for CuS (bottom, red); (B) as-prepared PbS nanowires (top, black) and corresponding JCPDS No. 78-1901 database standard for PbS (bottom, red); (C) as-prepared CdS nanowires (top, black) and corresponding JCPDS No. 10-0454 database standard for CdS (bottom, red).

Table 5.1 Crystallographic data of as-prepared sulfide nanowire samples and comparisons with reported literature values.

Nanowire Samples	JCPDS Database No.	Phase (Space Group)	Crystal Lattice	Calculated Constants (Å)	Literature Values (Å)
CuS	06-0464	Hexagonal ($P6_3/mmc$)	Primitive	$a = 3.815$ $c = 16.351$	$a = 3.792$ $c = 16.340$
PbS	78-1901	Cubic (Fm3m)	Face-centered	$a = 5.927$	$a = 5.931$
CdS	10-0454	Cubic (F43m)	Face-centered	$a = 5.826$	$a = 5.818$

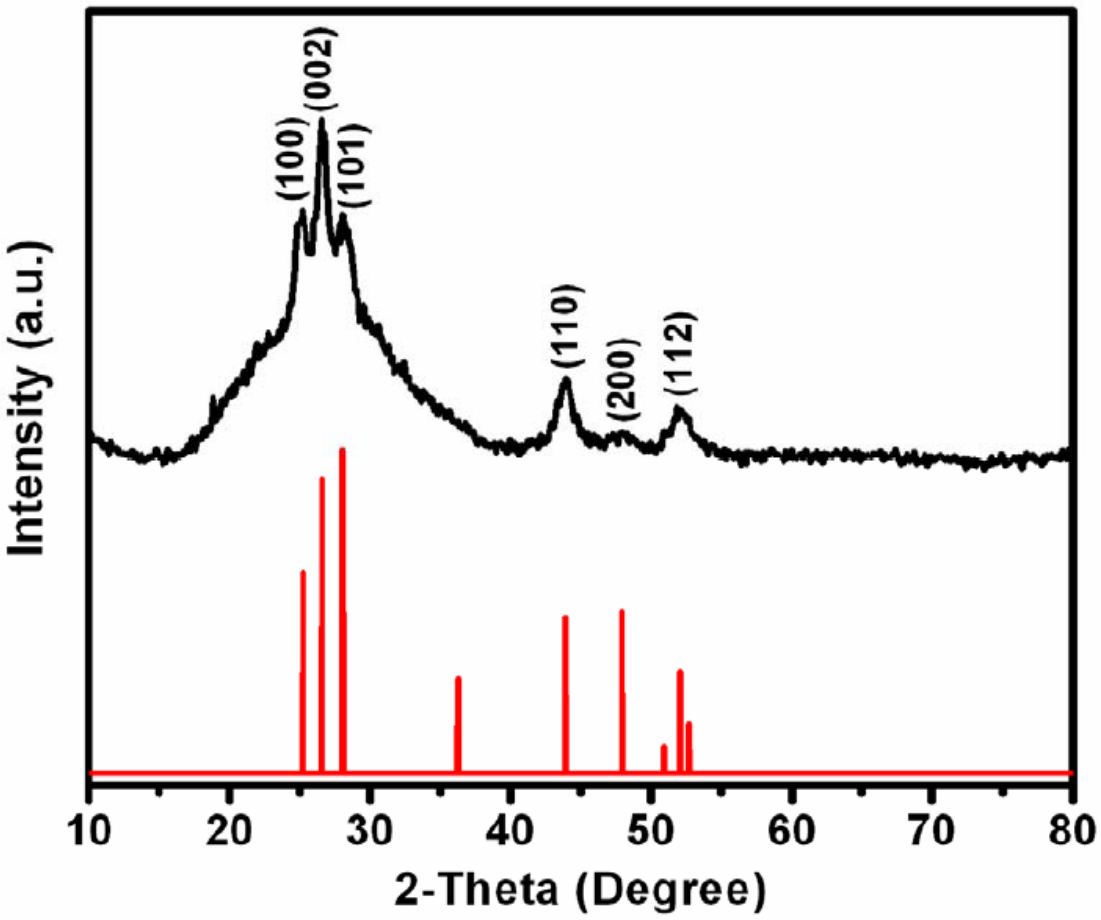

Figure 5.3 XRD patterns obtained from as-prepared CdS cactus-like nanostructures (top, black) and a JCPDS No. 41-1049 database standard for hexagonal CdS (bottom, red).

5.3.2 Electron Microscopy

5.3.2.1 CuS

The size and morphology of as-prepared metal sulfide 1D nanostructures have been studied using FE-SEM and TEM. Figure 5.4A and C, show typical SEM and TEM images of CuS nanowires, respectively, which had been fabricated using polycarbonate membranes with 100-nm diameter pore sizes. The presence of dispersed individual nanorods as well as of bundled, aggregated species clearly shows that straight, smooth, and crystalline wire-like CuS 1D nanostructures, with a relatively uniform diameter throughout their entire length, can be produced. Diameters of as-prepared CuS nanowires were 100 $\pm$ 13 nm, while measured lengths attained values of as much as several micrometers, comparable to the thickness (6 μm) of the PC membranes from whence these structures were derived. In addition, EDS elemental analysis data (Figure 5.4B) taken from SEM clearly indicate that the sample is only composed of Cu and S, as expected, with the presence of the Si peak attributable to the underlying silicon wafer.

To provide additional insight into the structure of the as-prepared sample, randomly chosen single nanowires, shown in Figure 5.4C, were analyzed by HRTEM and SAED. Figure 5.4D highlights the HRTEM image of a portion of an individual CuS nanowire, which is single-crystalline with a lattice fringe spacing of 0.191 nm, corresponding to the (110) plane of the hexagonal phase of a CuS crystal. The inset to Figure 5.4D shows the SAED pattern, consisting of sharp spots that can be indexed to the (110) and (100) diffraction planes, respectively, of primitive hexagonal CuS. These findings are consistent with observations from the XRD data shown in Figure 5.2A. Moreover, the HRTEM image and SAED patterns taken from different positions along the nanowires were found to be essentially identical within experimental accuracy, indicating the entire nanowire can be assumed to be single-crystalline, while a thin amorphous layer, visible in Figure 5.4D, likely coats at least part of the outer surface.

As a result of a high rate of occupancy of the interior of the membrane pores with the precursors associated with the CuS sample, the resulting nanowires tend to form arrays, after removal of the PC template by methylene chloride with modest sonication. As illustrated in Figure 5.5A, arrays of CuS nanowires appear to be structurally robust

and well preserved. The SEM image in Figure 5.5B under higher magnification clearly shows that the nanowires are individually separated from each other as opposed to forming mass aggregates and are roughly parallel to each other so as to generate a packed, vertically aligned array architecture upon template removal.

It is evident that these nanowires form a dense, continuous network, stretching over micrometer-sized areas. In particular, Figure 5.5C and D presents the tilt and top views of CuS nanowire arrays, respectively, grown within the pores of PC templates. The diameters of these nanowires are ~200 $\pm$ 18 nm, and their lengths measure in the micrometers, corresponding to the dimensions of the originating pore channels. We have not discounted the possibility that a remnant residue of the polycarbonate template, inter-dispersed within the nanowire framework, could be contributing to the mechanical support for these sulfide arrays. Such a scenario is not unusual considering that due to the random nature of the pore-production process in the track-etched membrane, a number of pores may have actually intersected within the membrane itself.[90] Moreover, while disulfide bond formation between dangling sulfur species is a plausible causal factor,[91] it is more likely that CuS growth "spilling" outside the pores themselves was a more important determinant, accounting for the additional reinforcing "glue" for these arrays.

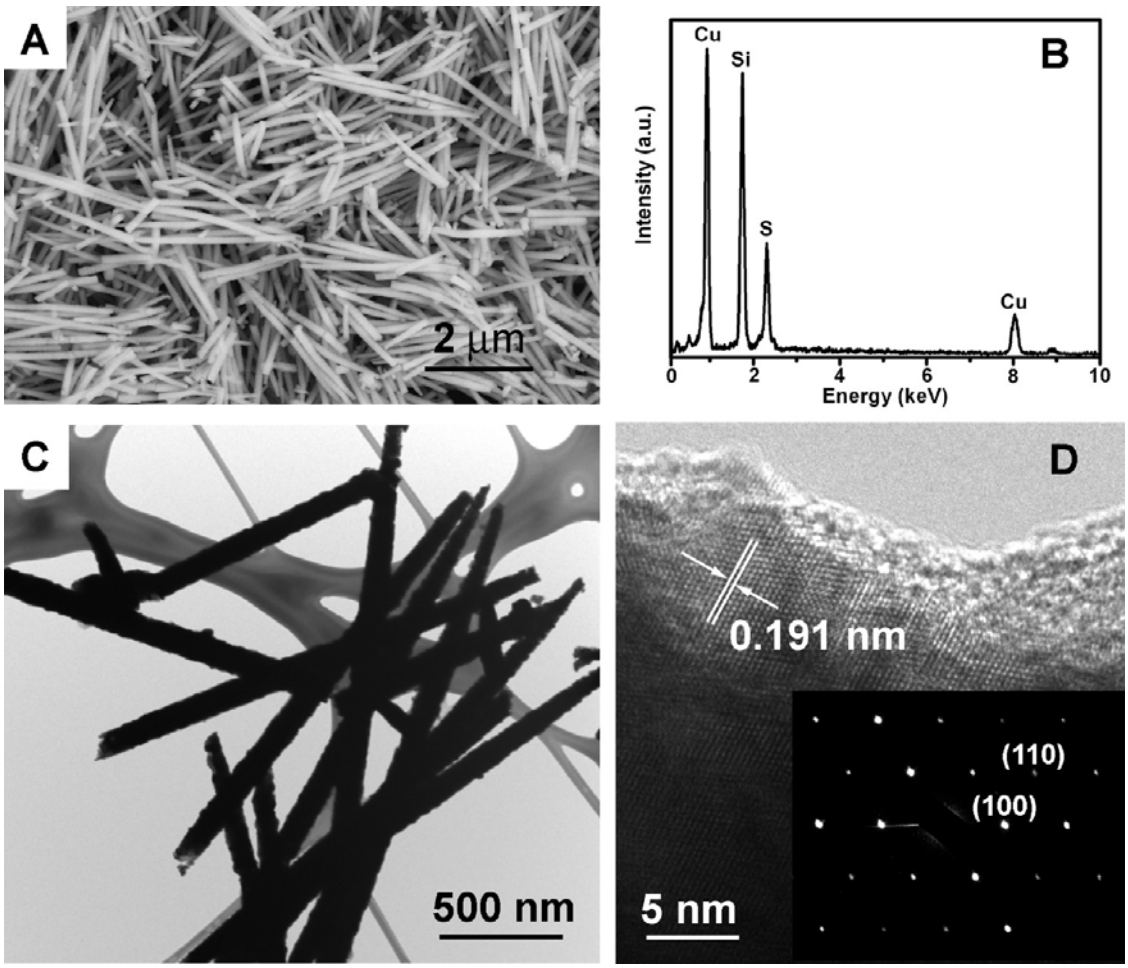

Figure 5.4 (A, C) Typical SEM and TEM images of as-prepared CuS nanowires, prepared using polycarbonate membranes with 100 nm pore diameters. (B) EDS spectrum of as-prepared CuS nanowires. The Si peak originates from the underlying silicon wafer. (D) HRTEM image of a representative portion of an individual CuS nanowire shown in (C). Corresponding SAED patterns are shown in the inset.

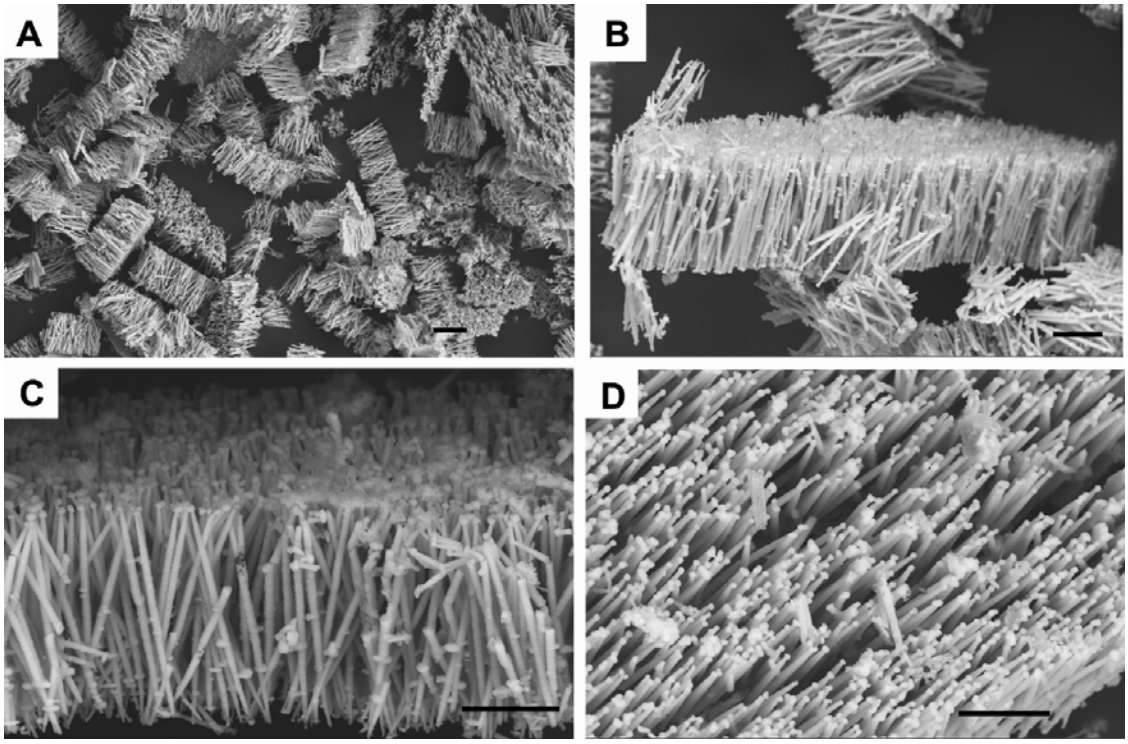

Figure 5.5 (A, B) Different magnification SEM images of CuS nanowire arrays, isolated from polycarbonate membranes containing 200 nm pore diameters. (C, D) Corresponding tilt-view and top-view SEM images of CuS nanowire arrays. Scale bars measure 2 μm.

5.3.2.2 PbS

Similarly, representative SEM and TEM images, as highlighted in Figure 5.6A and C, respectively, reveal that clusters of as-prepared PbS, isolated from PC membranes with 200 nm pore size diameters, primarily consist of one-dimensional structures possessing a straight, wire-like morphology with a relatively uniform diameter in the range of 200 $\pm$ 20 nm throughout their entire length of approximately 3.7-5.6 μm. The EDS spectrum (Figure 5.6B) shows signals associated with Pb and S, which overlap with each other in the energy scale at around 2.3-2.7 keV. The observed Si and C peaks likely originate from the silicon wafer and conductive carbon tape, respectively. The corresponding HRTEM image of a single PbS nanowire, shown in Figure 5.6D, suggests a lattice spacing of 0.298 nm, which can be indexed to the (200) plane of a face-centered cubic phase of a bulk PbS crystal (JCPDS File No. 78-1901), indicating that the nanowire likely grows in a [100] orientation. The somewhat distorted SAED pattern (inset to Figure 5.6D) suggests that the nanowires are not perfectly single-crystalline in nature. Indeed, the discrete but elongated bright spots can be indexed to the (200) planes of cubic PbS, unlike the usual broad, amorphous diffraction rings, characteristic of polycrystallinity. Moreover, the data indicate that the nanowire may consist of multiple single-crystalline domains composed of highly oriented nanocrystals growing along the [100] crystallographic axis.[92]

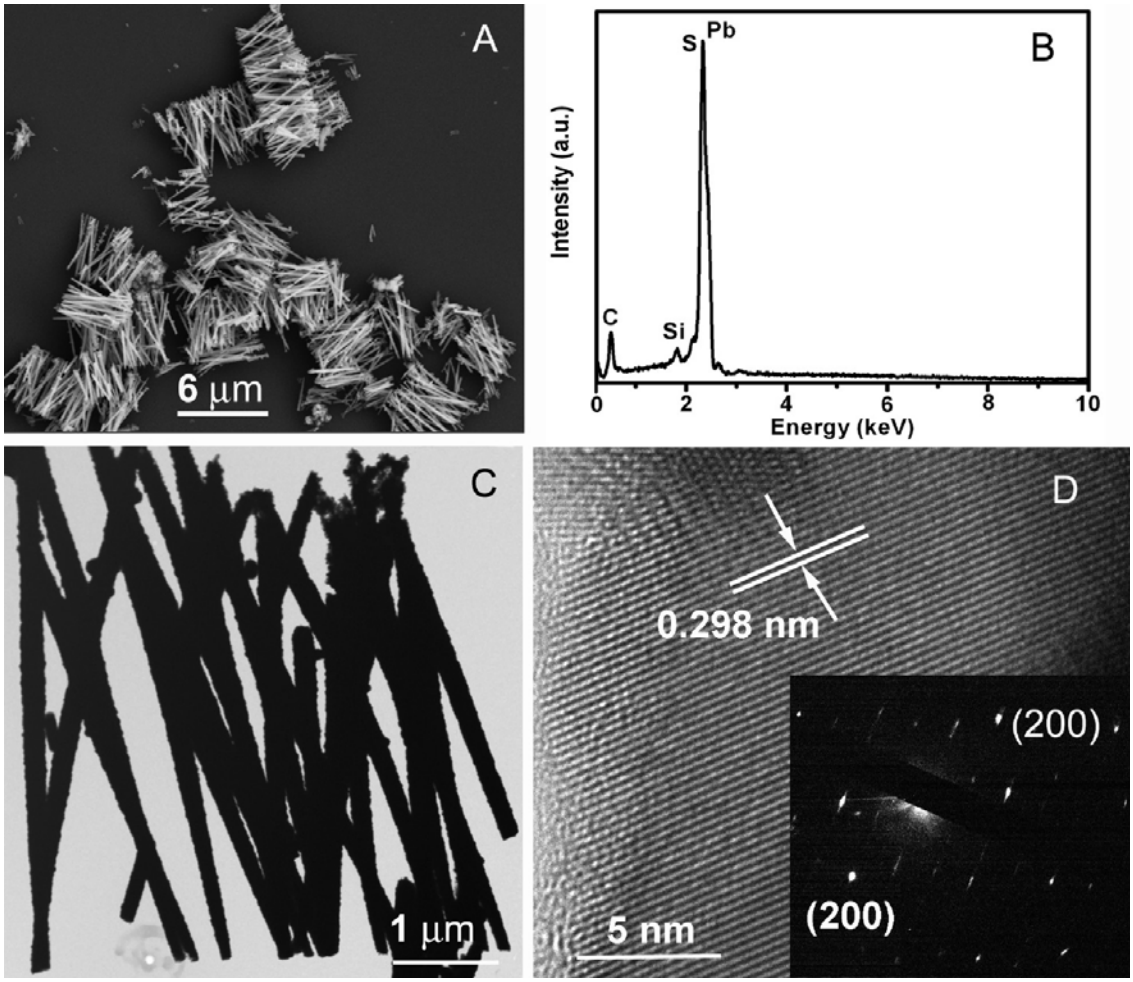

Figure 5.6 (A, C) Typical SEM and TEM images of as-prepared PbS nanowires, prepared using polycarbonate membranes containing 200 nm pore diameters. (B) EDS spectrum of as-prepared PbS nanowires. The C and Si peaks originate from the conductive carbon tape and silicon wafer, respectively. (D)HRTEM image of a representative portion of an individual PbS nanowire shown in (C). The corresponding SAED pattern is shown in the inset and is discussed in the text.

5.3.3.3 CdS

Figure 5.7A and C present typical SEM and TEM images of an as-prepared CdS sample, respectively, prepared under ambient conditions. It can be observed that straight and smooth nanowires with relatively uniform and homogeneous size can be routinely synthesized. Measured nanowires possess diameters spanning from 46 to 53 nm, based on the corresponding 50 nm pore sizes of the PC membranes used, and a length range of 2.1 to 4.6 μm. The resulting nanowires also tend to form reasonably robust arrays upon removal of the template. The chemical signatures obtained from the EDS spectra (Figure 5.7B) correspond to Cd and S elements, as expected. The Si signal arises from the underlying silicon wafer used for analysis. A representative HRTEM image, shown in Figure 5.7D, illustrates the single-crystalline nature of the CdS nanowires with an interplanar spacing of ~0.338 nm, corresponding to the (111) plane of pure face-centered cubic CdS, which agrees with the XRD results initially shown in Figure 5.2C. The sharp SAED pattern in the inset confirms that the entire nanowire is likely single-crystalline in nature, with two diffraction planes, that is, (111) and (220), that can be indexed to the cubic structure of CdS.

As we have previously noted, nanoscale CdS structures, prepared at 80 °C, evinced a different morphological motif and crystallographic structure. Specifically, SEM (Figure 5.8A) and TEM (Figure 5.8C) images were suggestive of the formation of visibly roughened CdS nanotubes, possessing an inner diameter of ~78-90 nm, a wall thickness of ~4 nm, and average lengths of up to several micrometers. As indicated in the higher magnification image (inset to Figure 5.8C), the roughness of these nanotubes could be attributed to the formation of needle-like, ultrathin structures measuring ~20 nm long, projecting out, like a multitude of tiny bristles, from the surface of the outer wall. Though it is not an uncommon structural archetype, this cactus-like nanostructure has never, to the best of our knowledge, been previously observed for CdS. As the Si signal could be ascribed to the underlying silicon wafer used for SEM imaging, EDS analysis (Figure 5.8B) showed that the hollow structures were essentially composed of Cd and S, without any extraneous chemical impurity. Figure 5.8D illustrates a representative SAED pattern taken from an individual cactus-like nanostructure highlighted in Figure 5.8C. The three

rings observed can be indexed to the (002), (110), and (112) diffraction planes, respectively, corresponding to the crystalline hexagonal phase of CdS.

Figure 5.9A highlights a portion of a typical cactus-like nanostructure (e.g., inset to Figure 5.8C), constructed from needle-like bristles projecting outward and branching off from the main CdS nanotube framework. In this magnified view, it is evident that the outer wall of the tubes is almost completely covered with these thin nanoscale needles.

Representative HRTEM images were taken from three different positions along the length of the hierarchical nanostructure shown in Figure 5.9A. Namely, these included the bristle-coated inner wall of the nanotube (Figure 5.9B), the intersection region between the central "trunk" and the secondary bristles (Figure 5.9C), and finally, the constituent needle-like bristles themselves in a different area of the sample (Figure 5.9D), respectively. While it is difficult to conclusively demonstrate that we were able to directly probe the nanotube wall motif itself by means of HRTEM, the diffuse nature of the SAED pattern suggests that the entire "trunk" may have been polycrystalline in nature, and therefore, it is plausible to hypothesize that the "trunk" may have consisted of a multitude of multioriented single-crystalline domains. Indeed, a lattice spacing of ~0.339 nm, obtained from one of these nanocrystals (Figure 5.9B), can be ascribed to the (002) plane of a hexagonal würtzite CdS structure. Some of these nanocrystals may therefore have served as seeds for the adjoining branching structures.[37] We also observed the presence of defects such as stacking faults within the confluence areas between the central "trunk" and its bristly "offshoots" (Figure 5.9C), similar to what has been previously described in analogous hierarchical systems.[93] Specifically, these stacking faults have been ascribed to the small energy difference between stacking sequences in the growth direction.[94] The bristles themselves maintain an obvious lattice spacing of ~0.341 nm, corresponding to the (002) planes of hexagonal CdS, an experimental result suggestive of the preferential [002] growth direction of these branched needle-like structures.

It is generally believed that, at room temperature, single crystals of cubic CdS nanorods were derived from isolated, disparate nucleation sites, which then grew by extension throughout the porous network until contact was made with the confining

membrane surface itself, acting as the ultimate barrier to growth. The hexagonal phase cactus-like nanostructure formation at 80 °C in the absence of surfactant is still a matter of study, but in the context of previous, analogous experiments by a multitude of groups, it can be explained as follows.

To account for the central nanotube "trunk", we have attributed tube-like formation to the fusion and coalescence of individual precursor particles preferentially localized along the surfaces of the template pore walls.[95] The observed formation of bristles or, alternatively, fractal dendritic structures in comparable systems has been previously ascribed to the non-equilibrium growth and the inherent molecular anisotropy of the hexagonal structure of CdS.[96] Diffusion-limited aggregation and nucleation-limited aggregation models have also been proposed to account for the formation of related complex hyper-branched structures.[94, 97-100] Hence, in an alternate but plausible mechanism, with increasing temperatures, multiple nuclei, pertaining to the thermodynamically stable hexagonal phase of CdS, can form in solution in an initial nucleation stage. In the next step, these will subsequently grow to produce thin, well-crystallized CdS nanorods in the presence of additional "monomers", which randomly move about and subsequently accumulate with each other to create kinetically roughened fractal structures.[101-104] The lack of any definite, preferential angles with which the different branches emerged from the central trunk supports this "fractal" hypothesis in our system[102] since there were no additives present to "direct" growth. Furthermore, the diffusion of smaller CdS nanostructures is known to be faster at higher temperatures, which is also conducive to their aggregation.[105]

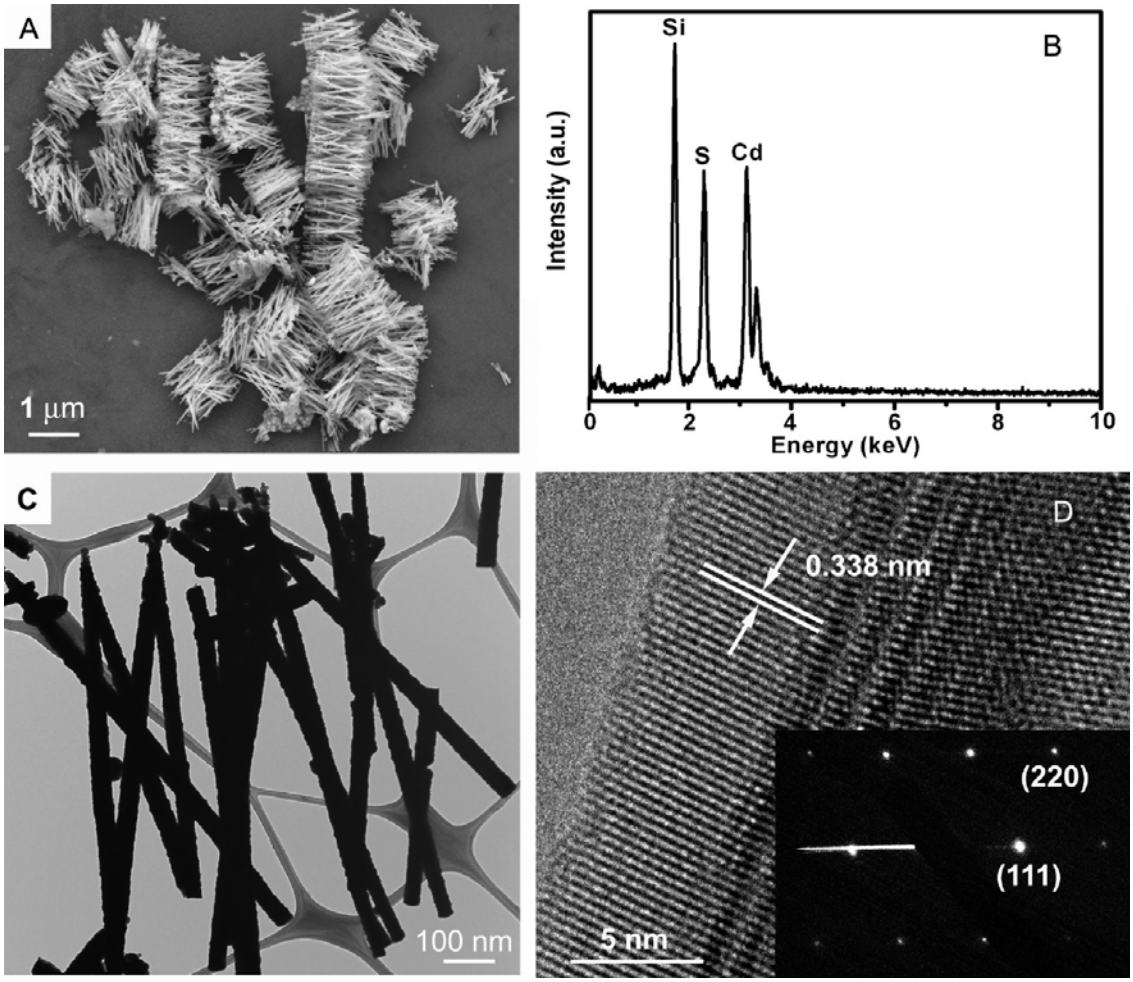

Figure 5.7 (A,C) Typical SEM and TEM images of as-prepared CdS nanowires, prepared using polycarbonate membranes with 50 nm pore diameters. (B) EDS spectrum of as-prepared CdS nanowires. The Si peak originates from the silicon wafer. (D) HRTEM image of a representative portion of an individual CdS nanowire shown in (C). The corresponding SAED pattern is shown in the inset.

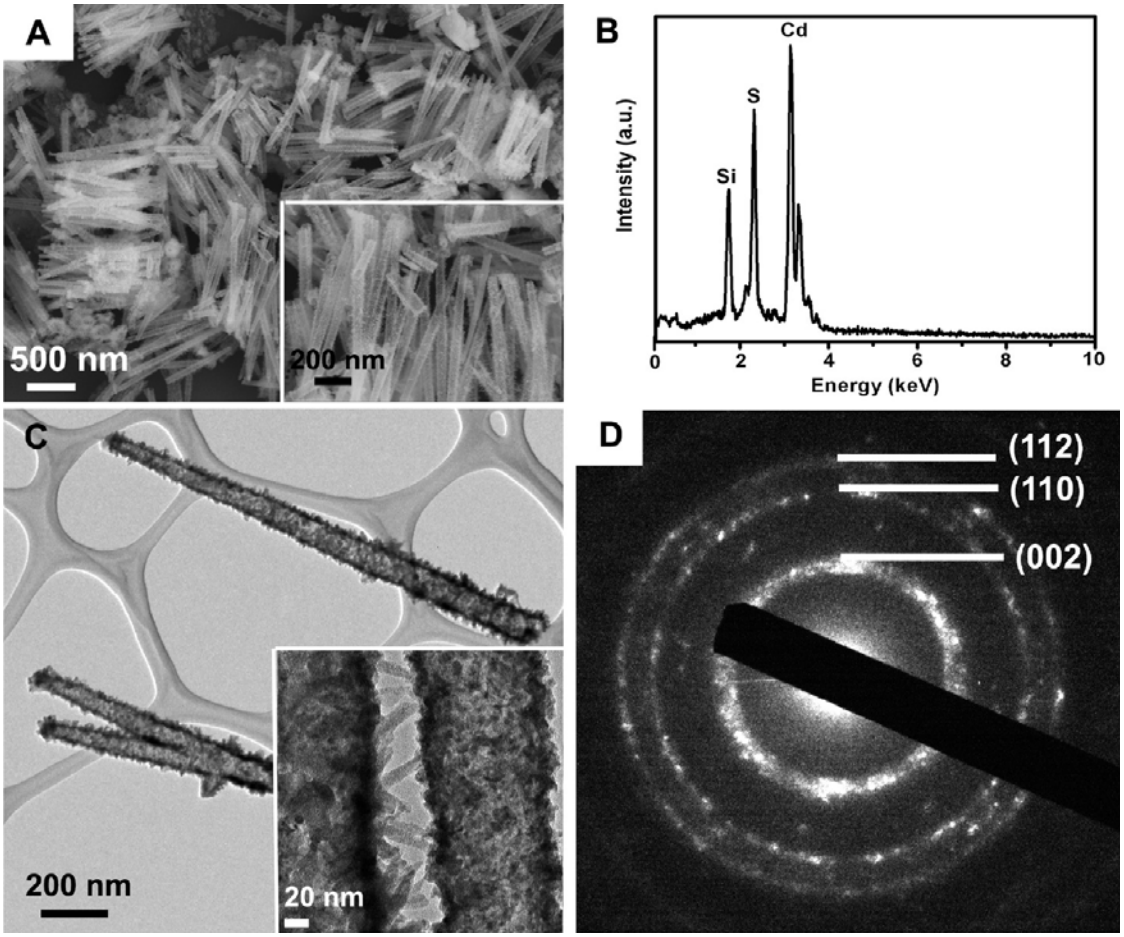

Figure 5.8 (A, C) Typical SEM and TEM images of as-prepared CdS cactus-like nanostructures, prepared using polycarbonate membranes with 100-nm pore diameters at 80 °C. Associated insets show a correspondingly magnified view of as-generated products. (B) EDS spectrum of as-prepared CdS cactus-like nanostructures. The Si peak originates from the underlying silicon wafer used for data collection. (D) SAED pattern of a representative portion of an individual CdS cactus-like nanostructure shown in (C).

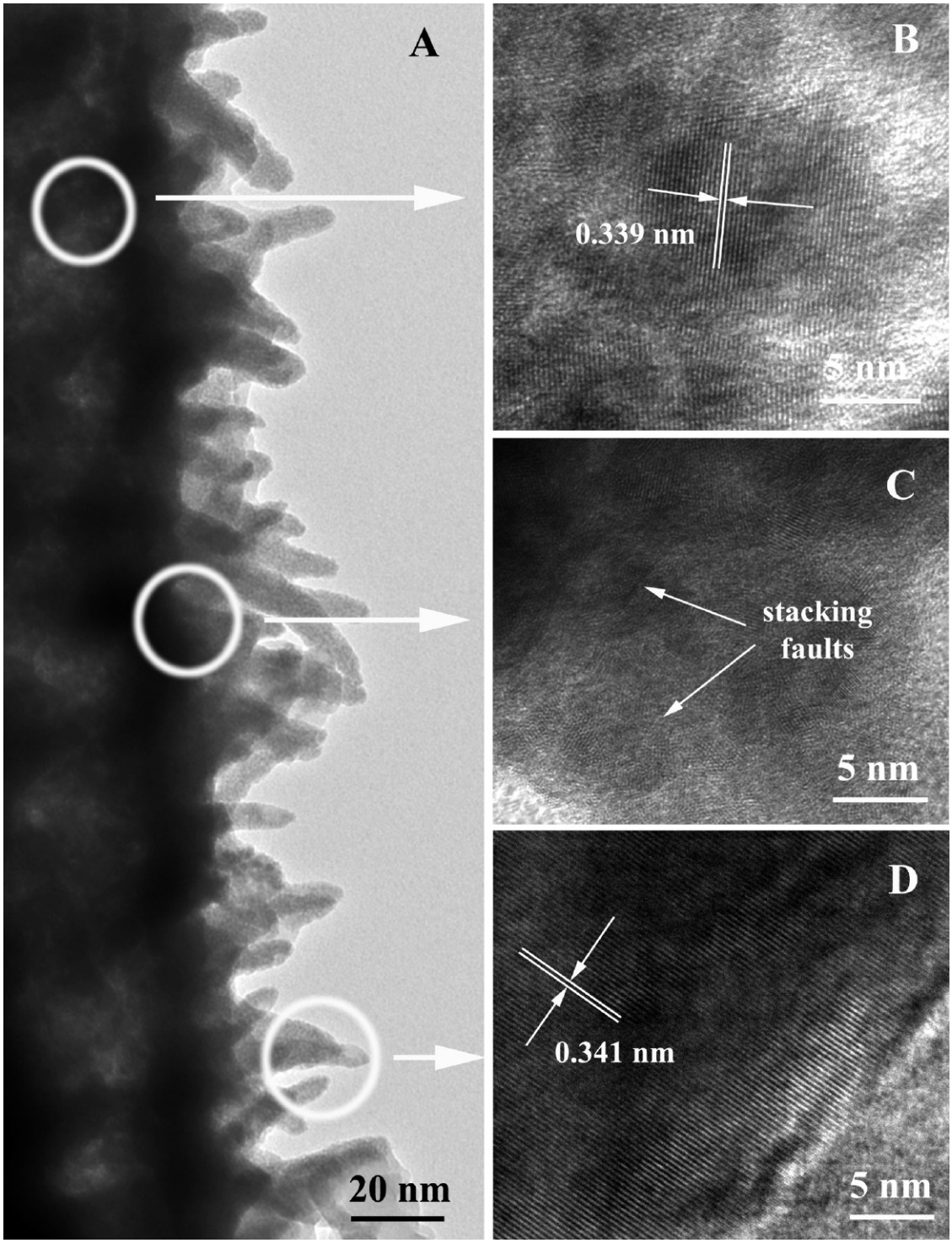

Figure 5.9 (A) TEM image of an individual CdS cactus-like nanostructure. (B-D)HRTEM images taken from various positions, delineated by white circles, respectively, along a portion of the cactus-like nanostructure in (A).

5.3.4 Optical Spectroscopy

5.3.4.1 Raman Spectroscopy

The optical properties of these sulfide 1D nanostructures were also investigated. It is well known that in a crystalline semiconductor, the observed Raman shifts are usually associated with the longitudinal optical phonons (LO), while in general, other modes, such as the transverse optical phonons (TO) and the surface phonons (SP), are not as observable because of symmetry restrictions and weaknesses in the observed intensities, respectively.[106-108] However, these other modes can become viable due to surface roughness and crystallite size considerations as well as the large surface-to-volume ratio intrinsic to nanostructured materials. Therefore, Raman scattering measurements have become a unique tool for probing nanoscale vibrational properties, especially the exciton-phonon coupling through the Fröhlich interaction of multiexcitonic materials such as PbSe.[69]

Figure 5.10 highlights the Raman spectra of as-prepared semiconducting nanowires, corroborating the chemical identity of our as-prepared nanostructures. Specifically, a strong, sharp peak appearing at 470 cm^{-1} is dominant in the spectrum of CuS nanowires (Figure 5.10A) and has been previously associated with the covellite (CuS) system,[109-111] though we cannot necessarily preclude potential contributions from S-S stretching vibrational modes as well.[112]

Figure 5.10B displays the Raman spectrum of PbS nanowires. PbS is an inherently weak Raman emitter, but increasing the intensity of the laser excitation might have led to sample photo-oxidation.[69] One strong peak at 143 cm^{-1} is clearly observed, which can be ascribed to the SP mode.[71, 113] According to earlier reports, the intensity of this peak greatly increases with decreasing crystal size.[114] We have found that this peak is so intense, though, that signals at 210 and 271 cm^{-1} resemble two small, secondary shoulders, corresponding to a 1 LO phonon mode and two-phonon mode process, respectively.[71, 108] Our observation also suggests that the nanowire may be composed of a substructure of small discrete nanocrystals. The weak intensity of these peaks has been previously assigned to decreasing crystallite size, which is also consistent with conclusions derived from our electron diffraction data. The Raman peak at 440 cm^{-1} can

be assigned to a 2 LO phonon mode, that is, a broad overtone whose intensity is strongly dependent on the excitation wavelength.[114] Finally, the peak at 602 cm^{-1} has been previously ascribed to a second overtone signal.[108]

Figure 5.10C shows the Raman spectrum of as-prepared CdS nanowires. Two features of CdS are clearly evident, illustrating characteristic Raman shifts analogous to those of pure crystalline CdS.[75] Specifically, the two peaks located at 301 and 602 cm^{-1} can be assigned to the first- and second-order TO phonon modes, respectively, though a number of groups have claimed that these peaks actually correspond to the fundamental LO band and its associated overtone.[47, 52, 74, 107] Nonetheless, the observed phonon peaks are shifted toward lower frequency than would be expected from bulk, likely due to effects of small size and high surface area. Moreover, the relatively sharp and symmetric profile of the peaks of our sample suggests that our nanorods are highly crystalline and relatively free of impurities,[80] which agrees with our electron microscopy data.

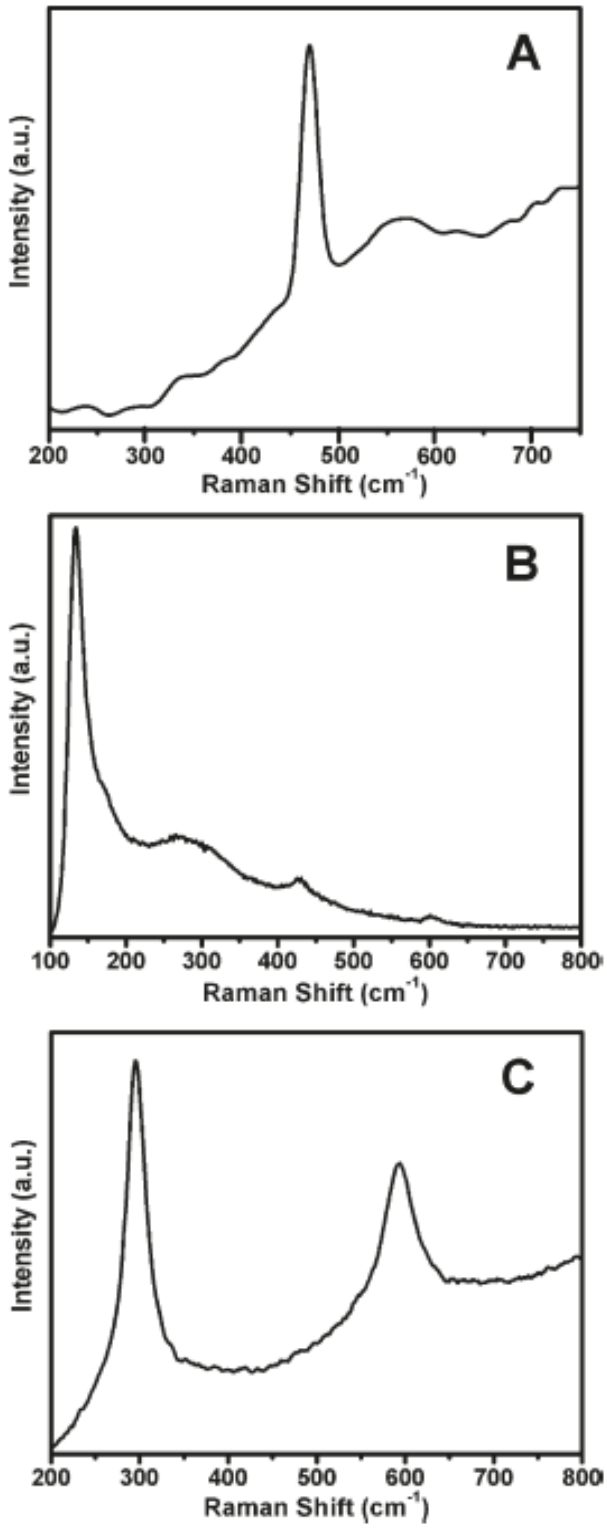

Figure 5.10 Raman spectra of as-prepared (A) CuS nanowires; (B) PbS nanowires; and (C) CdS nanowires.

5.3.4.2 UV-Visible Spectroscopy

Figure 5.11 highlights the UV-visible absorption spectra of as-prepared transition metal sulfide nanowires, collected at room temperature. The absorption spectrum (Figure 5.11A) of CuS nanowires, which has been attributed by one group to partial oxidation of the nanowire surface,[44] showed a broad spectral band in the region between 300 and 650 nm. This result is in agreement with prior reports,[39, 40, 110] with small peaks observed around 400 nm (i.e., 3.10 eV), potentially attributable to the nanorod morphology of the samples.[43] Previous studies have shown that covellite CuS also possesses a characteristically broad absorption band beyond 800 nm, which extends as a long absorption tail into the near-IR region and that can be ascribed to an electron-acceptor state lying within the bandgap.[36, 115, 116] We have also observed data consistent with this interpretation.

The absorption spectrum of as-prepared PbS nanowires is shown in Figure 5.11B. It has been reported that isotropic spheres of PbS with a size less than 18 nm showed regular red-shifted excitonic absorption peaks from the visible to the infrared region with increasing particle size.[117] A red shift in absorption corresponding to 60 nm as compared with 30 nm PbS nanowires has also been observed.[118] We have detected a similar behavioral trend here with our relatively large-diameter nanorods. Nonetheless, the position of the absorption peak itself at 783 nm (i.e., 1.58 eV) is in agreement with a previous report.[119] By comparison, the expected PbS bulk absorption edge occurs at 3024 nm.[70] One plausible hypothesis for this observation, which was supported by the HRTEM/SAED data, is that the nanowires may consist of multiple single, crystalline domains composed of highly oriented nanocrystals smaller than the representative Bohr exciton radius of PbS.[120] Another reasonable explanation put forward for the presence of the excitonic absorption peak is that there are little if any surface defect sites on the nanorods that can trap electron-hole pairs generated by light.[70] By contrast, it was noted that PbS nanowires measuring 16 and 35 nm in diameter did not show any distinctive maximum in the infrared region of their absorption spectrum. The absence of such a sharp, band-edge absorption feature has also been attributed to convolution of absorption

peaks from nanowires of different diameters as well as to the lack of confinement in the axial dimension of the wire.[66]

The UV-visible absorption spectrum of CdS nanowires is displayed in Figure 5.11C. The nanowires show a well-defined absorption feature at 498 nm (i.e., 2.49 eV), which can be ascribed to the first exciton peak of CdS.[121] This signal is considerably blue-shifted relative to the characteristic bulk band gap for hexagonal-phase CdS crystals (512 nm). In fact, the existence of a hexagonal CdS nanoscale impurity, the so-called minority phase, within the majority cubic phase was suggested by our XRD pattern (Figure 5.2C) and, thus, may have contributed to the observed UV absorption signal. These data are fully consistent with previous results.[50, 54, 61, 66, 121-123] It is worth noting that, as the cubic phase of CdS is not known in bulk form,[29] a direct band gap comparison could not be made.

While the origin of the observed blue shift, if real, as it is convoluted with the broadness of the measured spectra, in all of these sulfide systems is debatable, one general explanation that has been put forward is that, in semiconductors, even if the average radius of the nanostructures were larger than that of the exciton Bohr radius, the Coulombic energy component is dominant.[43] Hence, motion (e.g., translational degrees of freedom) of the exciton, which behaves as a quasi-particle, experiences size quantization, thereby accounting for the shift to the blue.[124]

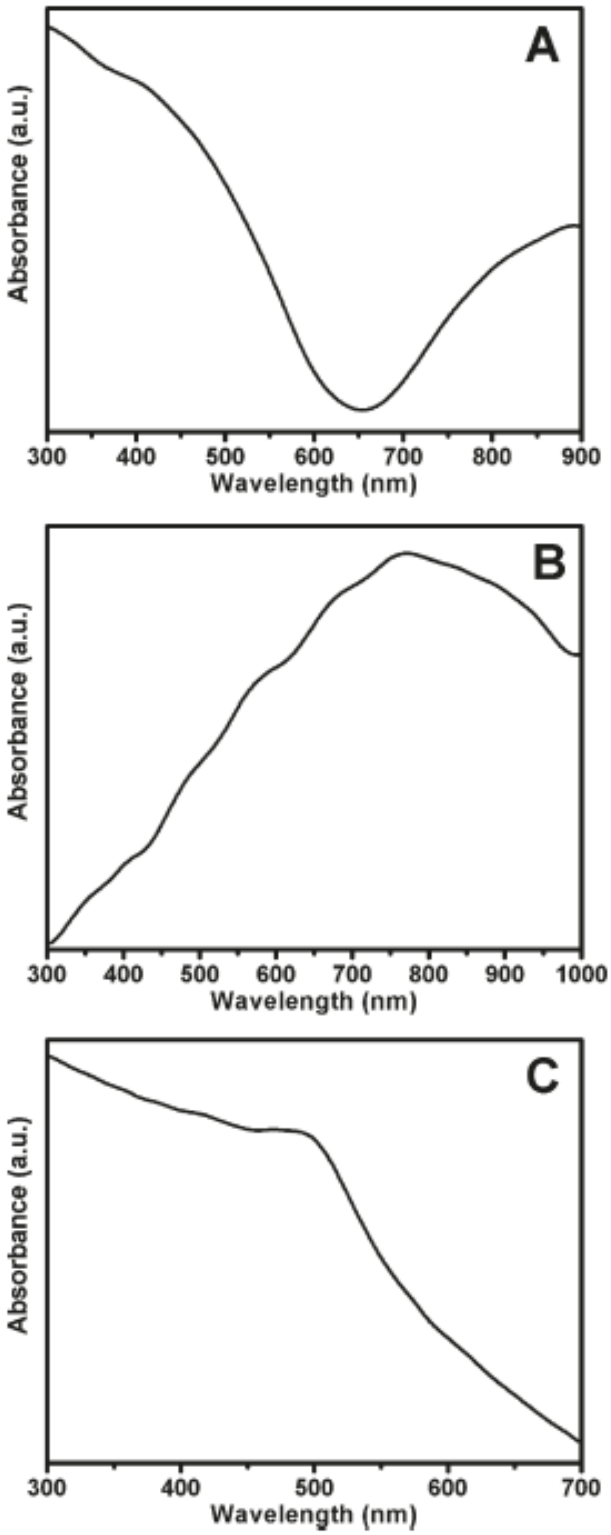

Figure 5.11 UV-visible spectra of as-prepared (A)CuS nanowires; (B) PbS nanowires; and (C) CdS nanowires.

5.3.4.3 Photoluminescence Spectroscopy

The photoluminescent activity of all of our as-prepared transition metal sulfide nanowires was also probed, as shown in Figure 5.12. In particular, Figure 5.12A illustrates the room-temperature PL spectrum of the CuS nanowire sample dispersed in water. Under an excitation wavelength of 370 nm, the sample evinced an emission peak at 423 nm. Although the exact mechanism for explaining the nature of PL emission for CuS nanostructures remains controversial, prior literature suggests that the nature of the emission spectrum depends on the morphology and inherent microstructure of the sample itself. For instance, CuS needle-like fibers did not appear to evince any PL signal in the range of 400-800 nm.[39] However, polycrystalline CuS nanorods have been found to possess two emission peaks at 414 and 437.5 nm, upon excitation at 371.5 nm,[124] while as-prepared CuS/C cables yielded a broad but weak emission peak at 465 nm upon excitation at 370 nm.[110] Moreover, hollow spheres composed of polycrystalline nm-sized CuS crystals were associated with a broad emission with a maximum at 526 nm upon excitation at 406 nm.[125] That result was explained by the presence of surface defects and an interface coupling effect between grain boundaries, thereby leading to an increase in wave function overlap and contributing to a narrower observable bandgap. Nonetheless, the sharp excitonic emission in our own results herein indicates that our as-prepared CuS nanowires are likely of high optical quality, since nanorods with stacking fault defects have been found to exhibit poor photoluminescence.[41]

The room-temperature PL spectrum of as-obtained PbS nanowires with an excitation wavelength of 495 nm is shown in Figure 5.12B. The fluorescence of PbS nanostructures is generally rather weak in intensity but detectable in the visible region.[126] A rather sharp PL band has been clearly observed at 794 nm (i.e., red fluorescence) and is blue-shifted as compared with bulk.[64, 119] Others have reported a PL peak for nanoscale PbS in the 655-665 nm range, which has been ascribed to a transition associated with the lowest energy exciton.[65] Our results are in agreement with and understandably red-shifted with respect to data obtained on < 10 nm PbS nanoparticles, wherein the strong emission response was assigned to band edge luminescence (BEL).[127, 128] Again, our observations

are consistent with the idea that our as-prepared nanowires may be plausibly composed of multiple single domains of PbS quantum dots.

Figure 5.12C denotes the PL spectrum of as-prepared CdS nanowires, obtained with an excitation wavelength of 400 nm at room temperature. Though the intensity of the peak has been previously attributed to the presence of surface defects,[77] a relatively sharp emission peak at 547 nm was detected, analogous to previously reported results.[77, 83, 129] This band has been ascribed to near-band-edge (NBE) emission, originating from the recombination of excitons and/or shallowly trapped electron hole pairs within surface states.[47, 60, 80, 82, 122, 130] We also note the relative narrowness of the PL peak, coupled with the lack of a strong emission near 600 nm from deep levels associated with defects (such as vacancies and interstitials) and impurities.[16, 131, 132] In fact, the lack of a broad, longer-wavelength, trap emission state, which would have resulted from an excess of either sulfur or cadmium at the interface and which is known to quench radiative recombination of electron hole-pairs,[133] strongly suggests the high degree of purity of our samples. Overall, our results intimate that our single-crystalline nanowires have high-quality optical properties, critical for photonic device applications, and also possess a reasonable size monodispersity in terms of diameter and length.

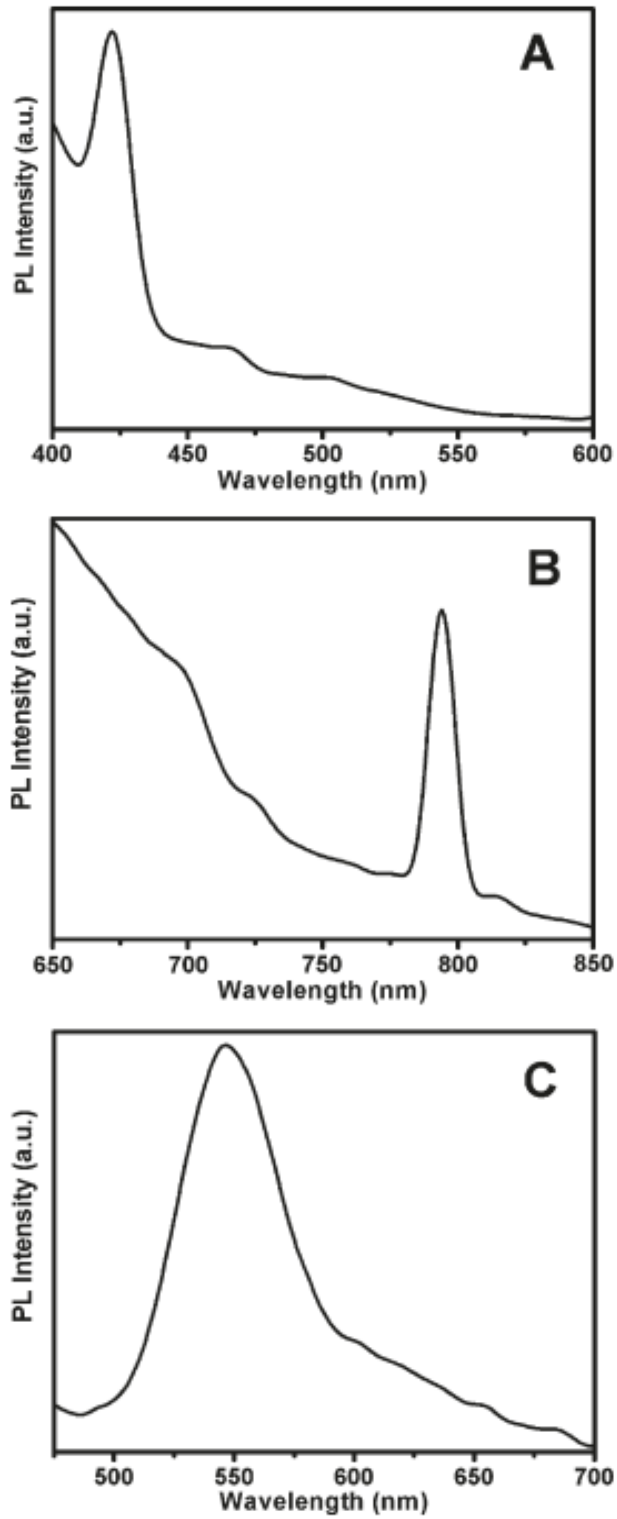

Figure 5.12 Photoluminescence spectra of as-prepared (A) CuS nanowires; (B) PbS nanowires; and (C) CdS nanowires.

5.3.5 Photocatalytic Activity

It is well known that illumination of semiconducting materials generates electrons and positive holes that rapidly move to the surface reducing or oxidizing solute or solvent molecules. Recombination of these charge carriers is often accompanied by emission of light.[134] In effect, semiconducting colloids often act as sensitizers and catalysts for photochemical reactions,[15, 135] including for solar-related applications.[136] For example, it has been reported that CdS nanocrystals serve as photocatalysts for nitrate reduction at neutral pH under conditions that mimic illumination by sunlight with overall product quantum yields of up to 4%, a figure that was strongly dependent on apparent particle size with the fastest rates measured for the smallest nanoparticles.[137]

CdS nanowires with higher crystallinity evinced a higher rate of photocatalytic hydrogen production from water containing Na_2S and Na_2SO_3 as sacrificial reagents under visible light irradiation; photocatalytic activity was clearly correlated with sample crystallinity.[138] Moreover, it has also been found that increased photocatalytic activity for hydrogen production from water under visible light was observed from a mixture of cubic and hexagonal CdS as compared with simply either pure cubic or hexagonal CdS nanocrystals; that reaction was noted to be dependent not only on the particles' surface area but also on the crystal phase, dispersity, average grain size, phase composition, crystallinity, and band gap of the analyzed CdS nanoparticle sample.[17] In addition, a different group claimed that Pt-loaded CdS powder having a hexagonal structure was more efficient as a photocatalyst for hydrogen production than its cubic counterpart.[139]

In terms of photoinduced degradation reactions, it is known that under UV light irradiation, in the presence of CdS nanocrystals, halogenated benzenes are often dehalogenated, yielding trichlorobenzene from hexachlorobenzene and tetrafluorobenzene isomers from hexafluorobenzene as the final products.[140] It is obvious though that the analogous roles of crystal phase, grain size, phase composition, and dimensionality have not been determined for photodegradation reactions of non-biodegradable organic dyes, which are model organic substrates, representative of organic pollutant systems.

Thus, in this work, we probed reasonably simple reactions involving the degradation of Rhodamine B and methyl orange under UV irradiation conditions in the presence of CdS.[141, 142] The photocatalytic potential of as-prepared CdS nanowires was evaluated by monitoring the optical behavior of Rhodamine B (RhB) and methyl orange (MO) at their peak absorbance upon photoexcitation with UV light at 366 nm. A continual fading of the coloration of both RhB and MO solutions has been noted as a function of reaction time, in the presence of CdS nanowires, cactus-like nanostructures, or commercial bulk samples, implying a steady, continuous degradation of the organic dyes.

As shown in Figure 5.13A, the photocatalytic performance of CdS was estimated by monitoring the intensity of RhB's characteristic absorption at 555 nm as a function of reaction time. The data clearly showed that nanowires, cactus-like nanostructures, and the bulk sample are active photocatalysts, as illustrated in Figure 5.13A, b-d. In addition, both CdS nanowires and cactus-like nanostructures exhibited a higher photocatalytic degradation activity as compared with the bulk sample. The photocatalytic activity of CdS was also evaluated by probing the analogous degradation of MO molecules in water, by measuring changes in absorption at 464 nm (Figure 5.13C, b-d) as a function of reaction time. Similar trends were observed in that the CdS nanowires and cactus-like nanostructures yielded an appreciably higher activity as compared with bulk behavior. As control experiments, we observed almost no dye degradation in solution, in the absence of CdS catalyst, similarly subjected to UV light irradiation.

The photocatalytic decolorization reaction of RhB can be modeled as a pseudo-first-order reaction with the kinetics expressed by the equation, $\ln (C_0/C_t) = kt$, where C_0 represents the initial concentration of aqueous RhB, C_t denotes the concentration of RhB at a given reaction time "t", and k is the reaction rate constant. From the linear extrapolations (Figure 5.13B), the computed reaction rate constants of the CdS cactus-like nanostructures, nanowires, and bulk sample are 1.2×10^{-2} min^{-1}, 9.5×10^{-3} min^{-1}, and 4.9×10^{-3} min^{-1}, respectively. For the corresponding degradation rates of MO in the presence of these various CdS morphologies, Figure 5.13D demonstrates calculated first-

order reaction rate constants of 7.6×10^{-3} min^{-1}, 5.5×10^{-3} min^{-1}, and 2.6×10^{-3} min^{-1} for CdS cactus-like nanostructures, nanowires, and bulk samples, respectively.

The potential photocatalytic mechanism in the degradation of RhB and MO has been previously described and may involve several steps: (1) photoabsorption of the CdS catalysts, (2) generation of photoinduced electrons and holes, (3) transfer of charge carriers to the surface, and (4) recombination of the available charge carriers with reactive, reagent dye molecules.[141] The observed enhancement of photocatalytic activity of our as-prepared nanowires and cactus-like nanostructures herein is most likely correlated with an increase in the purity, crystallinity, and availability of surface reactive sites of our samples as compared with the bulk. Moreover, in the case of cactus-like nanostructures, the hexagonal phase CdS is generally considered to be the more efficient phase for photocatalysis-related applications.[139]

A previous report on the photocatalytic degradation of RhB, under identical UV light irradiation conditions in the presence of cubic CdS nanocrystals measuring ~3 nm implanted in a metal hydroxide layer matrix, showed that the amount of observed dye decomposition was up to 95% after 100 min of UV light irradiation.[142] By contrast, our unbound samples necessitated about 135 min to achieve an identical degree of dye degradation. The superior photocatalytic performance of those nanocrystals was attributed to the more effective migration of photoinduced holes and electrons to the nanoparticle surface and their associated trapping at the interface between the nanoparticle and its solid layer matrix.

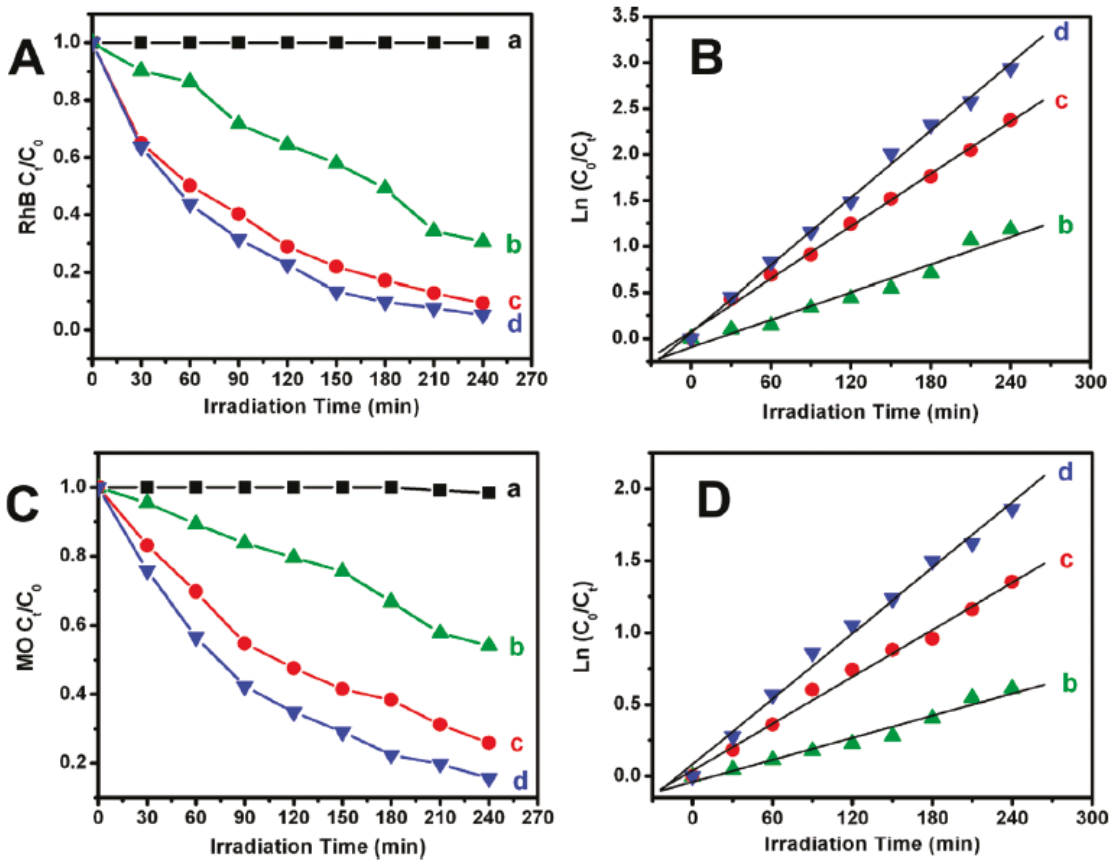

Figure 5.13 (A) Photodegradation of Rhodamine B (RhB) in the presence of (a, black) a blank control, (b, green) a commercial CdS bulk sample, (c, red) as-prepared CdS nanowires, and (d, blue) as-prepared CdS cactus nanostructures. (B) Plot of the logarithmic change in concentration of RhB as a function of irradiation in the presence of (b, green) a commercial CdS bulk sample, (c, red) as-prepared CdS nanowires, and (d, blue) as-prepared CdS cactus nanostructures. (C) Photodegradation of methyl orange (MO) in the presence of (a, black) a blank control, (b, green) a commercial CdS bulk sample, (c, red) as-prepared CdS nanowires, and (d, blue) as-prepared CdS cactus nanostructures. (D) Plot of the logarithmic change in concentration of MO as a function of irradiation in the presence of (b, green) a commercial CdS bulk sample, (c, red) as-prepared CdS nanowires, and (d, blue) as-prepared CdS cactus nanostructures.

5.4 Conclusions

The current report demonstrates room-temperature synthesis using a modified template-directed methodology of single-crystalline semiconductor metal sulfide (CuS, PbS, and CdS) nanowires, with various controllable sizes, including vertically aligned arrays and temperature-dependent cactus-like assemblies. The porous structures of our polycarbonate membranes not only enable the continuous flow of precursor solution but also provide for a spatially constrained environment in which to direct the growth of sulfide nanowires. The resulting 1D nanostructures have been extensively characterized using a variety of diffraction, electron microscopy, and optical spectroscopy techniques. Moreover, for the first time, we have demonstrated that as-prepared CdS nanowires, generated under ambient, room-temperature conditions, possessing a pure cubic phase, show potential applications in the photocatalytic degradation of organic dyes.

5.5 References

1. Xia, Y.; Yang, P.; Sun, Y.; Wu, Y.; Mayers, B.; Gates, B.; Yin, Y.; Kim, F.; Yan, H., *Adv. Mater.* **2003,** *15*, 353-389.
2. Brus, L. E., *J. Phys. Chem.* **1986,** *90*, 2555.
3. Alivisatos, A. P., *Science* **1996,** *271*, 933.
4. Fox, M. A.; Dulay, M. T., *Chem. Rev.* **1993,** *93*, 341.
5. Kamat, P. V., *Chem. Rev.* **1993,** *93*, 267.
6. Hoffman, M. R.; Martin, S. T.; Choi, W.; Bahnemann, D. W., *Chem. Rev.* **1995,** *95*, 69.
7. Wang, X.; Xu, C.; Zhang, Z., *Mater. Lett.* **2006,** *60*, 345-348.
8. Liang, W.; Whangbo, M.-H., *Solid State Commun.* **1993,** *85*, 405-408.
9. Mane, R. S.; Lokhande, C. D., *Mater. Chem. Phys.* **2000,** *65*, 1-31.
10. Janata, J.; Josowicz, M.; DeVaney, D. M., *Anal. Chem.* **1994,** *66*, 207-228.
11. Liao, X.-H.; Chen, N.-Y.; Xu, S.; Yang, S.-B.; Zhu, J.-J., *J. Cryst. Growth* **2003,** *252*, 593-598.
12. Blachnik, R.; Müller, A., *Thermochim. Acta* **2000,** *361*, 31-52.
13. Zhang, W.; Wen, X.; Yan, S., *Langmuir* **2003,** *19*, 4420-4426.

14. Chung, J.-S.; Sohn, H.-J., *J. Power Sources* **2002,** *108*, 226-231.

15. Henglein, A., *Chem. Rev.* **1989,** *89*, 1861-1873.

16. Barrelet, C. J.; Wu, Y.; Bell, D. C.; Lieber, C. M., *J. Am. Chem. Soc* **2003,** *125*, 11498-11499.

17. Bao, N.; Shen, L.; Takata, T.; Domen, K.; Gupta, A.; Yanagisawa, K.; Grimes, C. A., *J. Phys. Chem. C* **2007,** *111*, 17527-17534.

18. Britt, J.; Ferekides, C., *Appl. Phys. Lett.* **1993,** *62*, 2851-2852.

19. Morales, A. M.; Lieber, C. M., *Science* **1998,** *279*, 208-211.

20. Wang, Z. L., *Adv. Mater.* **2000,** *12*, 1295-1298.

21. Tsai, C. T.; S., C. D.; Chen, G. L.; Yang, S. L., *J. Appl. Phys.* **1996,** *79*, 9105-9109.

22. Berman, A.; Charych, D., *Adv. Mater.* **1999,** *11*, 296-300.

23. Lin, Y.-F.; Song, J.; Ding, Y.; Lu, S.-Y.; Wang, Z. L., *Adv. Mater.* **2008,** *20*, 3127-3130.

24. Lin, Y.-F.; Song, J.; Ding, Y.; Lu, S.-Y.; Wang, Z. L., *Appl. Phys. Lett.* **2008,** *92*, 022105-022107.

25. Peterson, J. J.; Krauss, T. D., *Nano Lett.* **2006,** *6*, 510-514.

26. Gadenne, P.; Yagil, Y.; Deutscher, G., *J. Appl. Phys.* **1989,** *66*, 3019-3025.

27. McDonald, S. A.; Konstantatos, G.; Zhang, S.; Cyr, P. W.; Klem, E. J. D.; Levina, L.; Sargent, E. H., *Nat. Mater.* **2005,** *4*, 138-142.

28. Bakueva, L.; Konstantatos, G.; Levina, L.; Musilkin, S.; Sargent, E. H., *Appl. Phys. Lett.* **2004,** *84*, 3459-3461.

29. Banerjee, R.; Jayakrishnan, R.; Ayyub, P., *J. Phys. -Condens. Mater.* **2000,** *12*, 10647-10654.

30. Wang, Z.; Zhao, B.; Zhang, F.; Mao, W.; Qian, G.; Fan, X., *Mater. Lett.* **2007,** *61*, 3733-3735.

31. Hirata, H.; Higashiayama, K., *Bull. Chem. Soc. Jpn.* **1971,** *44*, 2420-2423.

32. Plass, R.; Pelet, S.; Krueger, J.; Grätzel, M.; Bach, U., *J. Phys. Chem. B* **2002,** *106*, 7578-7580.

33. Warner, J. H.; R., W. A. A.; Tilley, R. D., *Nanotechnology* **2005,** *16* (2381-2384).

34. Sun, J.; Buhro, W. E., *Angew. Chem. Int. Ed.* **2008,** *47*, 3215-3218.

35. Wang, J.; Gudiksen, M. S.; Duan, X.; Cui, Y.; Lieber, C. M., *Science* **2001,** *293*, 1455-1457.

36. Kalyanikutty, K. P.; Nikhia, M.; Maitra, U.; Rao, C. N. R., *Chem. Phys. Lett.* **2006,** *432*, 190-194.

37. Gao, L.; Wang, E.; Lian, S.; Kang, Z.; Lan, Y.; Wu, D., *Solid State Commun.* **2004,** *130*, 309-312.

38. Lu, Q.; Gao, F.; Zhao, D., *Nanotechnology* **2002,** *13*, 741-745.

39. Jiang, X.; Xie, Y.; Lu, J.; He, W.; Zhu, L.; Qian, Y., *J. Mater. Chem.* **2000,** *10*, 2193-2196.

40. Wang, W.; Ao, L., *Mater. Chem. Phys.* **2008,** *109*, 77-81.

41. Roy, P.; Mondal, K.; Srivastava, S. K., *Cryst. Growth Des.* **2008,** *8*, 1530-1534.

42. Yang, Y. J.; Xiang, J. W., *Appl. Phys. A* **2005,** *81*, 1351-1353.

43. Singh, K. V.; Martinez-Morales, A. A.; Bozhilov, K. N.; Ozkan, M., *Chem. Mater.* **2007,** *19*, 2446-2454.

44. Wang, Q.; Li, J.-X.; Li, G.-D.; Cao, X.-J.; Wang, K.-J.; Chen, J.-S., *J. Cryst. Growth* **2007,** *299*, 386-392.

45. Zhang, P.; Gao, L., *Langmuir* **2003,** *19*, 208-210.

46. Zhao, Q.; Hou, L.; Huang, R.; Li, S., *Inorg. Chem. Commun.* **2003,** *6*, 1459-1462.

47. Kar, S.; Panda, S. K.; Satpati, B.; Satyam, P. V.; Chaudhuri, S., *J. Nanosci. Nanotech.* **2006,** *6*, 771-776.

48. Tang, K.-B.; Qian, Y.-T.; Zeng, J.-H.; Yang, X.-G., *Adv. Mater.* **2003,** *15*, 448-450.

49. Bao, C.; Jin, M.; Lu, R.; Xue, P.; Zhang, Q.; Wang, D.; Zhao, Y., *J. Solid State Chem.* **2003,** *175*, 322-327.

50. Maleki, M.; Mirdamadi, S.; Ghasemzadeh, R.; Sasani Ghamsari, M., *Mater. Lett.* **2008,** *62*, 1993-1995.

51. Yu, S.-H.; Yang, J.; Han, Z.-H.; Zhou, Y.; Yang, R.-Y.; Qian, Y.-T.; Zhang, Y.-H., *J. Mater. Chem.* **1999,** *9*, 1283-1287.

52. Li, Y.; Liao, H.; Ding, Y.; Fan, Y.; Zhang, Y.; Qian, Y., *Inorg. Chem. Commun.* **1999,** *38*, 1382-1387.

53. Li, Y.-D.; Liao, H.-W.; Ding, Y.; Qian, Y.-T.; Yang, L.; Zhou, G.-E., *Chem. Mater.* **1998,** *10* (2301-2303).

54. Wang, H.; Fang, P.; Chen, Z.; Wang, S., *J. Alloys Compd.* **2008,** *461*, 418-422.

55. Xi, L.; Tan, W. X. W.; Boothroyd, C.; Lam, Y. M., *Chem. Mater.* **2008,** *20*, 5444-5452.

56. Talapin, D. V.; Shevchenko, E. V.; Murray, C. B.; Kornowski, A.; Förster, S.; Weller, H., *J. Am. Chem. Soc* **2004,** *126*, 12984-12988.

57. Yong, K. T.; Sahoo, Y.; Swihart, M. T.; Prasad, P. N., *J. Phys. Chem. C* **2007,** *111*, 2447-2458.

58. Peng, Z. A.; Peng, X., *J. Am. Chem. Soc* **2002,** *124*, 3343-3353.

59. Acharya, S.; Patla, I.; Kost, J.; Efrima, S.; Golan, Y., *J. Am. Chem. Soc* **2006,** *128*, 9294-9295.

60. Kar, S.; Chaudhuri, S., *J. Phys. Chem. B* **2006,** *110*, 4542-4547.

61. Nair, P. S.; Scholes, G. D., *J. Mater. Chem.* **2006,** *16*, 467-473.

62. Mo, M.-s.; Shao, M.-w.; Hu, H.-m.; Yang, L.; Yu, W.-c.; Qian, Y.-t., *J. Cryst. Growth* **2002,** *244*, 364-368.

63. Xiang, J.; Yu, S.-H.; Liu, B.; Xu, Y.; Gen, X.; Ren, L., *Inorg. Chem. Commun.* **2004,** *7*, 572-575.

64. Acharya, S.; Gautam, U. K.; Sasaki, T.; Bando, Y.; Golan, Y.; Ariga, K., *J. Am. Chem. Soc* **2008,** *130*, 4594-4595.

65. Patla, I.; Acharya, S.; Zeiri, L.; Israelachvili, J.; Efrima, S.; Golan, Y., *Nano Lett.* **2007,** *7*, 1459-1462.

66. Yong, K.-T.; Sahoo, Y.; Choudhury, K. R.; Swihart, M. T.; Minter, J. R.; Prasad, P. N., *Chem. Mater.* **2006,** *18*, 5965-5972.

67. Chen, J.; Chen, L.; Wu, L.-M., *Inorg. Chem.* **2007,** *46*, 8038-8043.

68. Saraidarov, T.; Reisfeld, R.; Sashchiuk, A.; Lifshitz, E., *Phys. E* **2007,** *37*, 173-177.

69. Bierman, M. J.; Lau, Y. K. A.; Jin, S., *Nano Lett.* **2007,** *7*, 2907-2912.

70. Wang, C.-W.; Liu, H.-G.; Bai, X.-T.; Xue, Q.; Chen, X.; Lee, Y.-I.; Hao, J.; Jiang, J., *Cryst. Growth Des.* **2008,** *8*, 2660-2664.

71. Ge, J.-P.; Wang, J.; Zhang, H.-X.; Wang, X.; Peng, Q.; Li, Y.-D., *Chem. Eur. J.* **2005,** *11*, 1889-1894.

72. Xiu, Z.; Liu, S.; Yu, J.; Xu, F.; Yu, W.; Feng, G., *J. Alloys Compd.* **2008,** *457*, L9-L11.

73. Chen, J.-H.; Chao, C.-G.; Ou, J.-C.; Liu, T.-F., *Surf. Sci.* **2007,** *601*, 5142-5147.

74. Routkevitch, D.; Haslett, T. L.; Ryan, L.; Bigioni, T.; Douketis, C.; Moskovits, M., *Chem. Phys.* **1996,** *210*, 343-352.

75. Suh, J. S.; Lee, J. S., *Chem. Phys. Lett.* **1997,** *281*, 384-388.

76. Xu, D.; Xu, Y.; Chen, D.; Guo, G.; Gui, L.; Tang, Y., *Adv. Mater.* **2000,** *12*, 520-522.

77. Thiruvengadathan, R.; Regev, O., *Chem. Mater.* **2005,** *17*, 3281-3287.

78. Gao, F.; Lu, Q.; Liu, X.; Yan, Y.; Zhao, D., *Nano Lett.* **2001,** *1*, 743-748.

79. Gao, F.; Lu, Q.; Zhao, D., *Adv. Mater.* **2003,** *15*, 739-742.

80. Xiong, S.; Xi, B.; Wang, C.; Zou, G.; Fei, L.; Wang, W.; Qian, Y., *Chem. Eur. J.* **2007,** *13*, 3076-3081.

81. Zhang, J.; Jiang, F.; Zhang, L., *J. Phys. Chem. B* **2004,** *108*, 7002-7005.

82. Zhan, J. H.; Yang, X. G.; Wang, D. W.; Li, S. D.; Xie, Y.; Xia, Y.; Qian, Y. T., *Adv. Mater.* **2000,** *12*, 1348-1351.

83. Simmons, B. A.; Li, S.; John, V. T.; McPherson, G. L.; Bose, A.; Zhou, W.; He, J., *Nano Lett.* **2002,** *2*, 263-268.

84. Sathish, M.; Viswanath, R. P., *Catalysis Today* **2007,** *129*, 421-427.

85. Zelaya-Angel, O.; Alvarado-Gil, J.; Lozada-Morales, R.; Vargas, H.; Ferreira da Silva, A., *Appl. Phys. Lett.* **1994,** *64*, 291.

86. Chen, Q.; Bao, H.; Shen, X., *Phase Transitions* **2008,** *81*, 591.

87. Narayanan, K. L.; Vijayakumar, K. P.; Nair, K. G. M.; Thampi, N. S.; Krishan, K., *J. Mater. Sci.* **1997,** *32*, 4837.

88. Bandaranayake, R. J.; Wen, G. W.; Lin, J. Y.; Jiang, H. X.; Sorensen, C. M., *Appl. Phys. Lett.* **1995,** *67*, 831.

89. Shen, L.; Bao, N.; Yanagisawa, K.; Zheng, Y.; Domen, K.; Gupta, A.; Grimes, C. A., *J. Phys. Chem. C* **2007,** *111*, 7280-7287.

90. Hulteen, J. C.; Martin, C. R., *J. Mater. Chem.* **1997,** *7*, 1075.

91. Young, A. G.; Green, D. P.; McQuillan, A. J., *Langmuir* **2007,** *23*, 12923.

92. Tong, H.; Zhu, Y.-J.; Yang, L.-X.; Li, L.; Zhang, L., *Angew. Chem. Int. Ed.* **2006,** *45*, 7739-7742.

93. Manna, L.; Scher, E. C.; Alivisatos, A. P., *J. Am. Chem. Soc.* **2000,** *122*, 12700.

94. Yao, W.-T.; Yu, S.-H.; Liu, S.-J.; Chen, J.-P.; Liu, X.-M.; Li, F.-Q., *J. Phys. Chem. B* **2006,** *110*, 11704.

95. Zhou, H.; Wong, S. S., *ACS Nano* **2008,** *2*, 944-958.

96. Qing, W.; Gang, X.; Gao, H., *Cryst. Growth Des.* **2006,** *6*, 1776.

97. Halsey, T. C.; Duplantier, B.; Honda, K., *Phys. Rev. E* **1997,** *48*, 621.

98. Ming, N. B.; Wang, M.; Peng, R. W., *Phys. Rev. E* **1993,** *48*, 621.

99. Witten, T.; Sander, L. M., *Phys. Rev. Lett.* **1981,** *47*, 1400.

100. Meakin, P., *Phys. Rev. A* **1983,** *27*, 1495.

101. Dick, K. A.; Deppert, K.; Larson, M. W.; Martensson, T.; Seifert, W.; Wallenberg, L. R.; Samuelson, L., *Nat. Mater.* **2004,** *3*, 380.

102. Peng, Q.; Dong, Y.; Deng, Z.; Li, Y., *Inorg. Chem.* **2002,** *41*, 5249.

103. Qin, A.-M.; Fang, Y.-P.; Zhao, W.-X.; Liu, H.-Q.; Su, C.-Y., *J. Cryst. Growth* **2005,** *283*, 230.

104. Hou, H.; Yang, Q.; Tan, C.; Tian, X.; Xie, Y., *Mater. Lett.* **2005,** *59*, 3364.

105. Zhao, P.; Huang, K., *Cryst. Growth Des.* **2008,** *8*, 717.

106. Mlayah, A.; Brugman, A. M.; Carles, R.; Renucci, J. B.; Valakh, M. Y.; Pogorelov, A. V., *Solid State Commun.* **1994,** *90*, 567-570.

107. Nanda, K. K.; Sahu, S. N., *Appl. Surf. Sci.* **1997,** *119*, 50-54.

108. Wang, N.; Cao, X.; Guo, L.; Yang, S.; Wu, Z., *ACS Nano* **2008,** *2*, 184-190.

109. Rudigier, E.; Barcones, B.; Luck, I.; Jawhari-Colin, T.; Pérez-Rodríguez, A.; Scheer, R., *J. Appl. Phys.* **2004,** *95*, 5153-5158.

110. Chen, G.-Y.; Deng, B.; Cai, G.-B.; Dong, W.-F.; Zhang, W.-X.; Xu, A.-W., *Cryst. Growth Des.* **2008,** *8*, 2137-2143.

111. Minceva-Sukarova, B.; Najdoski, M.; Grozdanov, I.; Chunnilall, C. J., *J. Mol. Struct.* **1997,** *410-411*, 267-270.

112. Bastian, E. J.; Martin, R. B., *J. Phys. Chem.* **1973,** *77*, 1129.

113. Nanda, K. K.; Sahu, S. N.; Soni, R. K.; Tripathy, S., *Phys. Rev. B* **1998,** *58*, 15405-15407.

114. Krauss, T. D.; Wise, F. W., *Phys. Rev. B* **1997,** *55*, 9860-9865.

115. Xu, H.; Wang, W.; Zhu, W., *Mater. Lett.* **2006,** *60*, 2203-2206.

116. Gao, J.; Li, Q.; Zhao, H.; Li, L.; Liu, C.; Gong, Q.; Qi, L., *Chem. Mater.* **2008,** *20*, 6263-6269.

117. Watt, A.; Rubinsztein-Dunlop, H.; Meredith, P., *Mater. Lett.* **2005,** *59*, 3033-3036.

118. Wu, C.; Shi, J.-B.; Chen, C.-J.; Chen, Y.-C.; Wu, P.-F.; Lin, J.-Y., *Mater. Lett.* **2007,** *61*, 4659-4661.

119. Ye, S.; Ye, Y.; Ni, Y.; Wu, Z., *J. Cryst. Growth* **2005,** *284*, 172-175.

120. Wise, F. W., *Acc. Chem. Res.* **2000,** *33*, 773-780.

121. Xiong, Y.; Xie, Y.; Yang, J.; Zhang, R.; Wu, C.; Du, G., *J. Mater. Chem.* **2002,** *12*, 3712-3716.

122. Liu, W.; He, W.; Zhang, Z.; Zheng, C.; Li, J.; Jiang, H.; Ge, X.; Liu, H., *J. Cryst. Growth* **2006,** *290*, 592-596.

123. Spanhel, L.; Anderson, M. A., *J. Am. Chem. Soc* **1990,** *112*, 2278-2284.

124. Yoffe, A. D., *Adv. Phys.* **2002,** *51*, 799.

125. Yu, X.-L.; Cao, C.-B.; Zhu, H.-S.; Li, Q.-S.; Liu, C.-L.; Gong, Q.-H., *Adv. Funct. Mater.* **2007,** *17*, 1397-1401.

126. Machol, J. L.; Wise, F. W.; Patel, R.; Tanner, D. B., *Phys. A* **1994,** *207*, 427-434.

127. Chen, S.; Truax, L. A.; Sommers, J. M., *Chem. Mater.* **2000,** *12*, 3864-3870.

128. Kim, D.; Kuwabara, T.; Nakayama, M., *J. Lumin.* **2006,** *119-120*, 214-218.

129. Wang, W.; Germanenko, I.; S., E.-S. M., *Chem. Mater.* **2002,** *14*, 3028-3033.

130. Wang, W.; Germanenko, I.; El-Shall, M. S., *Chem. Mater.* **2002,** *14*, 3028.

131. Pike, R. D.; Cui, H.; Kershaw, R.; Dwight, K.; Wold, A.; Blanton, T. N.; Wernberg, A. A.; Gysling, H. J., *Thin Solid Films* **1993,** *224*, 221-226.

132. Mondal, S. P.; Dhar, A.; Ray, S. K., *Mater. Sci. Semicond. Proc.* **2007,** *10*, 185-193.

133. Hsu, Y.-J.; Lu, S.-Y., *Langmuir* **2004,** *20*, 23-26.

134. Henglein, A., *Pure Appl. Chem.* **1984,** *56*, 1215-1224.

135. Jing, D.; Guo, L., *J. Phys. Chem. B* **2006,** *110*, 11139-11145.

136. Shiragami, T.; Fukami, S.; Wada, Y.; Yanagida, S., *J. Phys. Chem.* **1993,** *97*, 12882-12887.

137. Korgel, B. A.; Monbouquette, H. G., *J. Phys. Chem. B* **1997,** *101*, 5010-5017.

138. Jang, J. S.; Joshi, U. A.; Lee, J. S., *j. Phys. Chem. C* **2007,** *111*, 13280-13287.

139. Matsumura, M.; Furukawa, S.; Saho, Y.; Tsubomura, H., *J. Phys. Chem.* **1985,** *89*, 1327-1329.

140. Yin, H.; Wada, Y.; Kitamura, T.; Yanagida, S., *Environ. Sci. Technol.* **2001,** *35*, 227-231.

141. Li, W.; Li, D.; Chen, Z.; Huang, H.; Sun, M.; He, Y.; Fu, X., *J. Phys. Chem. C* **2008,** *112*, 14943-14947.

142. Guo, Y.; Zhang, H.; Wang, Y.; Liao, Z.-L.; Li, G.-D.; Chen, J.-S., *J. Phys. Chem. B* **2005,** *109*, 21602-21607.

Chapter VI Large-Scale Growth of High Aspect Ratio Single-Crystalline Rare-Earth Phosphate Nanowires and Application for Bioimaging

6.1 Introduction

Nanoscale luminescent materials are increasingly being used for a number of significant biological applications including drug and gene delivery, biosensing, and bioimaging.[1] The unique optical properties of inorganic nanomaterials render them appealing as in vivo and in vitro fluorophores in a variety of biological investigations. For instance, 0D nanoparticles, including quantum dots (QDs), such as CdS, CdSe, and CdTe, have been demonstrated to be highly effective for cellular and animal imaging,[2-4] since as compared with conventional organic fluorophores (such as Rhodamine and FITC), QDs exhibit high photostability, possess size-dependent emission, maintain high quantum yields, as well as evince broad excitation spectra and narrow emission bands. Nevertheless, the widespread use of QDs is limited by issues associated with their low light-penetration depth, potential toxicity, surface ligand incompatibility, optical blinking, and the presence of strong background fluorescence in certain analyzed systems.

It is not surprising therefore that a number of other nanoscale systems, especially inorganic 1D probes such as striped metal nanowires[5] and functionalized carbon nanotubes,[6] have also initiated substantial interest in nanobiotechnology.[7-9] Compared to small nanospheres, there is a drastic reduction of the Plasmon dephasing rate in nanorods, which implies large local-field enhancement factors and relatively high light-scattering efficiencies, making them extremely interesting for optical applications. In addition, it has been reported that 1D nanostructures can be readily internalized into cells without in turn damaging them, which is an important issue for the development of nanowires-based probes of living cells.[10-12] Specifically, the internalization of fluorescent nanowires will allow us to directly observe the intracellular microenvironment by monitoring the fluorescence signal from nanowires.

As a complementary but relevant system, lanthanide-doped inorganic nanoparticles maintain a fluorescence, characterized by high photochemical stability, and long luorescence lifetimes (up to several microseconds).[13] In addition, as compared with conventional dyes, rare-earth lanthanide phosphate nanocrystals maintain comparatively higher quantum yields (up to 61%), lower photobleaching potential, expected low toxicity, and high chemical stability, all of which are excellent attributes for biological labeling applications. Moreover, these lanthanide probes also possess additional distinctive features, such as sharp emission bands, as determined by the nature of the lanthanide ions themselves. Furthermore, they maintain large Stokes shifts (as much as several hundred nm), such that the donor/acceptor emission signal can be detected far from the excitation wavelength with zero absorption, thereby improving overall sensitivity.[14-16]

The photoluminescence of rare-earth phosphates originates from transitions between *d* and *f* electron states, which are mainly affected local crystal symmetry and are independent of their size.[17, 18] The optical properties of these systems can also be tuned by the presence of rare-earth dopant ions, in that different emission colors can be achieved by judicious variation of the nature of the dopant ions (Ce, Tb, Eu, Dy).[19] In the specific case of Tb-doped $CePO_4$, upon UV excitation, efficient energy transfer from the broad (Ce^{3+}) to the narrow-line emitter (Tb^{3+}) can take place between nearest neighbors in the crystal lattice and when there is optimal spectral overlap, thereby resulting in an enhanced Tb^{3+} green emission.[20, 21] Therefore, bulk Tb-doped $CePO_4$ has been considered as an inexpensive lamp phosphor, i.e. the green emitter in fluorescent lamps, because it combines high luminescence efficiency with both chemical and thermal stability.[22] Moreover, Ca-doped $CePO_4$ has been developed as an environmentally friendly and nontoxic yellow-green pigment to replace chromium oxide.[23] Hence, increasing efforts have been focused on using (i) $CaPO_4$ nanoparticles doped with either fluorophores or lanthanides[13, 24] as well as (ii) microwave-synthesized Eu or Tb orthophosphate nanorods[7, 25] as novel fluorescent probes in cell biology.

However, to the best of our knowledge, the application of rare-earth ion-doped lanthanide phosphate nanostructures as biological labels for *in vivo* bioimaging purposes

has not as yet been demonstrated. Obvious reasons for doing so would be to enhance surface-to-volume ratios as well as to influence the electric/magnetic dipole fields in these 1D systems, as a result of their intrinsic shape anisotropy. There are a number of additional advantages of creating these rare-earth-ion-doped nanomaterials as compared with their non-doped analogues. First, Tb-doped $CePO_4$ systems are capable of a luminescent molecular switching behavior based on the reversible redox reaction of a Ce^{3+}/Ce^{4+} couple, rendering them sensitive to the localized redox environment within a biological context.[26, 27] Second, in the case of $EuPO_4$, doping can reduce the possibility of concentration quenching in which an excess of Eu, for instance, can increase the probability of non-radiative energy migration between Eu^{3+} ions, resulting in losing the excitation energy nonradiatively.[28-30] Third, in the case of $TbPO_4$, cerium doping can more specifically improve upon the inherently weak and narrow Tb^{3+} absorption by sensitization, thereby leading potentially to higher quantum yields.[31] Herein, we have systematically investigated, for the first time, the (a) production and (b) subsequent utilization of Tb-doped $CePO_4$ ultrathin nanowires as fluorescent labels in bioimaging.

In general, the rational synthesis of inorganic 1D nanotubes and nanowires with controlled size, shape, composition, and morphology has attracted intensive research interest, as they are potential building blocks for advanced materials as well as for functional devices with applicability in areas as diverse as electronics, optics and catalysis. Specifically, lanthanide phosphate ($LnPO_4$) nanorods, measuring 20-70 nm in length with aspect ratios from 2 to 7, have been synthesized by calcination of a sol-gel at 400ºC.[32] Electrospinning has been used in conjunction with the sol-gel process as well to yield polycrystalline nanowires ranging from 60 to 300 nm, after calcination at 650 to 750°C.[19] Generally, the hydrothermal methodology has been primarily used for the synthesis of 1D $LnPO_4$ nanostructures, measuring typically 20-60 nm in diameter with lengths from several hundred nm to several microns. The treatment usually involves reaction in a Teflon-lined stainless-steel autoclave often under anomalous pH conditions, at a relatively high temperature (in the range of 150-240ºC), and with reaction times ranging from a few hours up to several days, depending on the experimental circumstances.[27, 33-38] The synthesis of well-defined crystalline $CePO_4$ nanowires with a

diameter of 3.7 nm was reported by use of a microemulsion reaction medium, but could take as long as a month to produce,[39] while ultrasound irradiation of an inorganic salt aqueous solution has been reported for the synthesis of $CePO_4$:Tb and $CePO_4$:Tb/$LaPO_4$ core/shell nanorods.[40] Hence, one of the key motivators of this work was to develop a more facile, milder, less technically demanding, but more cost-effective approach towards the generation of 1D $LnPO_4$ nanostructures.

We have developed the modified template-directed technique, enabling us to prepare crystalline 1D nanostructure of a number of classes of diverse materials. In this chapter, we report the first demonstration of a facile, room-temperature template-directed synthetic route towards the production of 2 distinctive morphologies: (a) high-purity, high-aspect-ratio, single-crystalline ultrathin nanowires (external to the template), as well as (b) sheaf-like nanowire bundles (within the template pores) of Tb-doped $CePO_4$ at room temperature. Importantly, we can easily fabricate ultrathin nanowires on a reasonably large scale, i.e. >500 mg per lab run, which has been previously been difficult to achieve using a template-mediated synthesis. Moreover, we have also successfully demonstrated the use of these as-prepared Tb-doped $CePO_4$ ultrathin nanowires as fluorescent labels for in vivo bioimaging and furthermore, provided a series of data that relate to their relative non-toxicity.

6.2 Experimental Section

6.2.1 Materials Preparation

In a typical ambient synthesis, one of the two half cells was filled with a 0.01 M NaH_2PO_4 (Fisher Scientific; 99.1 %) solution, which was adjusted to acidic reaction conditions (e.g. pH values from 2 to 6) using HCl, and the other half cell contained a solution by mixing 0.05 M $CeCl_3$ (Aldrich, 99.9%) solution together with $Tb(NO_3)_3$ (Alfa Aesar, 99.9%) up to a final molar concentration of 10.0 %, so as to generate desired Tb-doped $CePO_4$ nanostructures. The system was then left unperturbed for an incubation period of only 2 h at room temperature.

Subsequent to immersion, the half cell containing both $CeCl_3$ and $Tb(NO_3)_3$ solutions became occluded in nature, and a white precipitate was obtained after

centrifugation. To isolate products within the template itself, the polycarbonate membrane was detached, sonicated for about 2 min to remove the unwanted particles on the surface, and thoroughly washed with distilled water, before being dissolved again with methylene chloride. As-prepared phosphate nanostructures were isolated from solution by centrifugation upon washing.

6.2.2 Materials Characterization

X-ray Powder Diffraction See Section 1.7.1.

Electron Microscopy See Section 1.7.3.

Optical Spectroscopy See Section 1.7.5.

Biological Experiments. We tested the viability of as-prepared Tb^{3+} doped cerium phosphate nanowires as fluorescent biological labels for *in vivo* bioimaging. Prior to processing, our Tb-doped $CePO_4$ nanowires were sonicated for about 1 hour in order to shorten their lengths so as to assist their biological incorporation.

Cell Culture. Human cervical cancer (HeLa) cells were initially propagated onto 100 mm-diameter tissue culture dishes in DMEM medium (Life Technologies, GIBCO), supplemented with 10% fetal bovine serum (FBS) at 37 °C in a humidified atmosphere containing 5% CO_2. At confluence, the cells were washed, trypsinized, and resuspended in culture medium.

Cellular Uptake. HeLa cells were seeded at a concentration of 104 cells/well on 12 mm-diameter glass cover slips in 24-well tissue culture plates, and allowed to grow for 24 h at 37 °C under 5% CO_2. Nanowires were subsequently added at different concentrations ranging from 0.1 to 0.5 mg/mL into the culture medium, and cells were grown for either an additional 2 h or 24 h at 37 °C under a 5% CO_2 atmosphere. Subsequently, the cell medium was removed, and cells on the coverslips were washed with phosphate buffered saline (PBS) three times so as to clear free nanowires from both the medium and the cell surface, prior to imaging.

Cell Cytotoxicity. A tetrazolium salt, 3-(4,5-dimethylthiazol-2-yl)-2,5-diphenyltetrazolium bromide (MTT), assay of HeLa cells was performed to test the cytotoxicity of as-prepared products. In this assay, cells were seeded in a 96-well microplate at a density of 5000 cells per well. After 24 h of incubation, the nanowires

were directly added to the culture medium at different concentrations ranging from 0.1 to 0.5 mg/mL, and the plate was incubated for another additional 2 h to 48 h at 37 °C. At the end of the cell culture incubation, MTT was added into each well. After processing for 4 h, all media were removed and acidic ethanol was added to each well before absorbance was measured by a microplate reader. The following formula was used to calculate the degree of inhibition of cell growth: cell viablility (%) = (mean of Absorbance value of treatment group / mean Absorbance value of control) * 100%.[41]

Confocal Microscopy (CFM) Imaging. Cells treated as described above were resuspended in 100 μL of PBS after each experiment, and dropped onto an uncoated bottom glass dish (MatTek Corp.). CFM experiments aimed at assessing cellular uptake, localization, and fluorescent signaling of the nanowires were subsequently performed using a Zeiss LSM 510 META NLO two-photon laser scanning confocal microscope system, operating at around a 380 nm excitation wavelength using a tunable Chameleon XR laser system and a 505 nm long-pass filter. Images were captured using either a C-Apochromat 63×/1.2 Water (corr.) objective or a Plan-Apochromat 100×/1.45 oil objective. Acquired data were analyzed using the LSM 510 META software. Orthogonal sectioning images were recorded within the cells by focusing on the *xy* plane along the *z* axis, the *yz* plane along the *x* axis, and the *xz* plane along the *y* axis, respectively.

6.3 Results and Discussion

6.3.1 X-ray Diffraction

In Figure 6.1, all of the diffraction peaks observed from the sample (top, black curve) can be readily indexed to a pure hexagonal phase formulation [space group: $P6_222$] of pristine $CePO_4$ (bottom, red curve), possessing lattice constants of a = 7.103 Å and c = 6.481 Å, which are comparable with reported database values of a = 7.055 Å and c = 6.439 Å for bulk $CePO_4$ (JCPDS File No. 34-1380). Moreover, the intensity of the (200) peak is much stronger than that of the other peaks, and is distinctly different from that of bulk hexagonal $CePO_4$. Nonetheless, our data indicate that the as-obtained nanowires should grow preferentially along the [001] direction (the *c*-axis), an assertion which is further demonstrated below by HRTEM and SAED analysis.

6.3.2 Electron Microscopy

Typical SEM and TEM images are shown in Figure 6.2A and B. A very large number of nanowires could be isolated, no matter what pore size dimension (50, 100, or 200 nm) of the polycarbonate membranes was used in our synthesis. In fact, for a typical reaction time of 2 h, we were able to collect as much as 600 mg per experimental run, corresponding to a reasonable 60 to 65% yield. The large quantities of nanowires synthesized are atypical of conventional template syntheses but were fully representative of the results associated with our modified protocol for this phosphate system.

Based on measurements of several tens of nanowires pertaining to each of our samples, our as-prepared nanowires measured 14 $\pm$ 5 nm in diameter with a length of up to 10 ± 2 micrometers. Curiously, these lengths were much longer than the reported thickness of the membrane (e.g. 6 μm), and measured diameters were much thinner than the smallest pore diameters used (e.g. 50 nm). Though these ultrathin nanowires tended to aggregate and cluster fairly easily, as can be observed from the SEM image (Figure 6.2A), sonication could readily resolve this problem, resulting in the isolation of individual nanostructures, as shown in the corresponding TEM image (Figure 6.2B).

The HRTEM image (Figure 2D) of a randomly chosen individual Tb-doped $CePO_4$ nanowire (Figure 6.2C) clearly shows resolvable planes corresponding to the (001) and (100) directions (Figure 6.2D). The (001) planes are oriented parallel to the nanowires' growth axis, suggesting that the growth direction of the single-crystalline nanowire occurs preferentially along the [001] direction (the *c*-axis). By contrast, the SAED pattern (Figure 6.2E) taken from single nanowires can be indexed to the (100) and (001) planes of a hexagonal $CePO_4$ single crystal phase, respectively. These findings are consistent with previous XRD analyses. EDS analysis (Figure 6.2F) confirms that the chemical signatures associated with the nanowires are composed of Tb, Ce, P, and O elements, while the Cu signal originates from the TEM grid.

The interesting nuances of our current template experiments herein are associated with two factors in particular. First, we were able to synthesize significantly thinner and shorter nanowires in the U-tubes (but not from the membrane pores themselves) than otherwise might have been expected based upon the pore diameter and membrane

thickness from whence these nanomaterials were derived. Second, we could easily generate hundreds of mg of product in a given experiment as opposed to merely synthesizing a few tens of mg at a given time, as was typical of template methods. We would have expected that the morphology of our Tb-doped $CePO_4$ nanorods should have faithfully mapped out the interior spatial profile, dimensionality, and localized contours of the internal pore channels of the polycarbonate membrane scaffolds from whence these 1D structures were produced. This simplistic mechanism did not obviously play out in the current study.

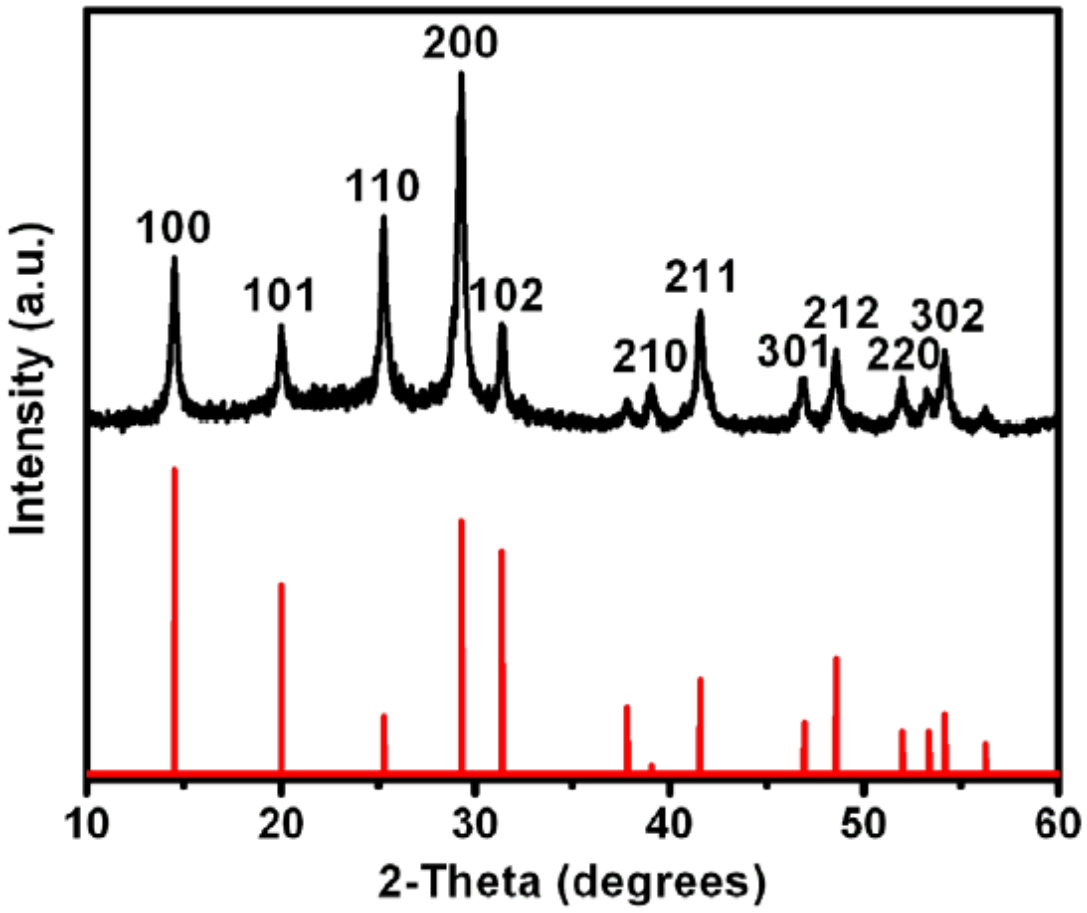

Figure 6.1 XRD patterns obtained from as-prepared Tb-doped $CePO_4$ nanowires (top, black) and corresponding JCPDS No. 34-1380 database standard for bulk $CePO_4$ (bottom, red).

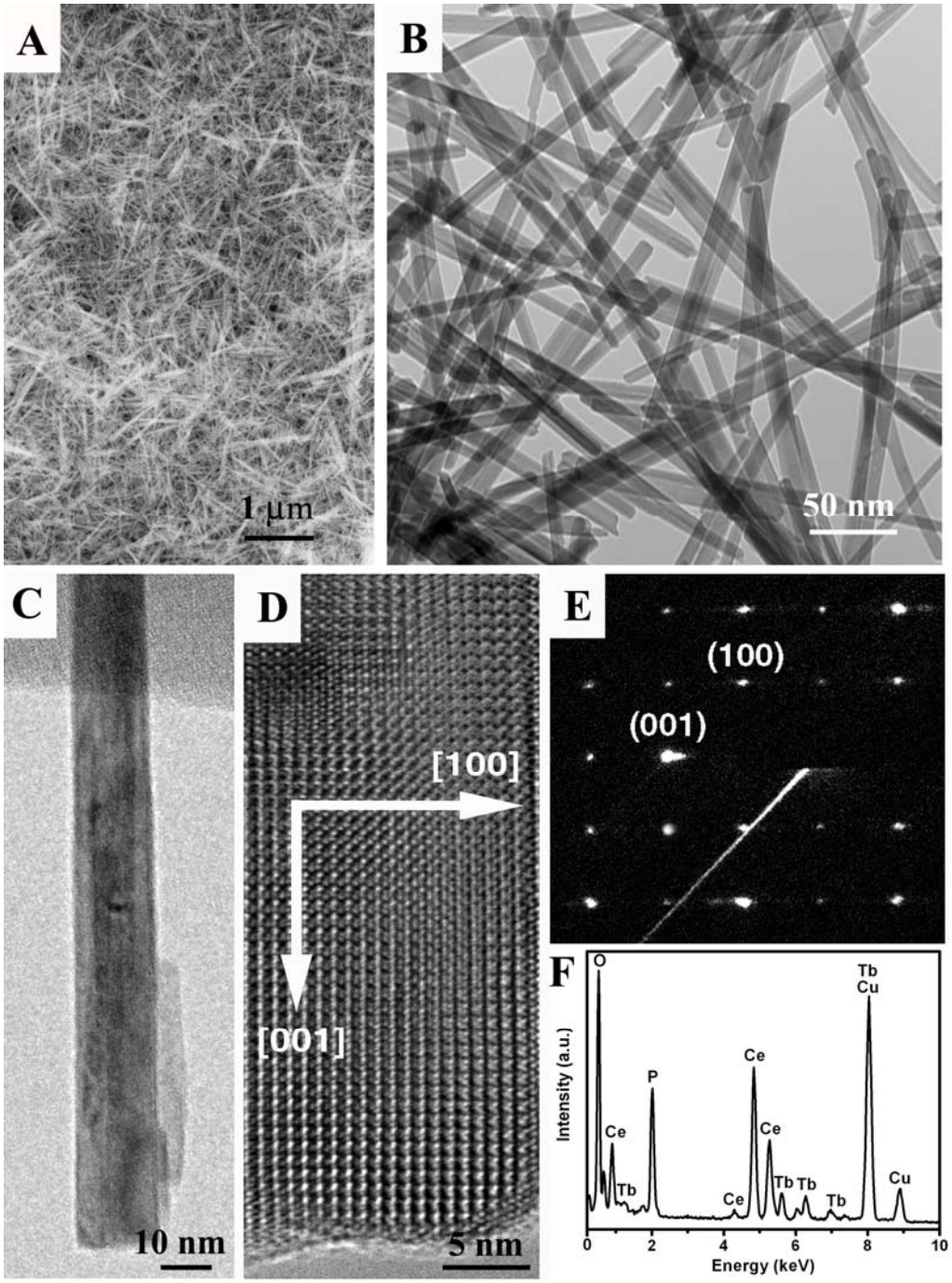

Figure 6.2 (A, B) Typical SEM and TEM images of as-prepared Tb-doped $CePO_4$ nanowires collected from aqueous solution. (C) TEM image of a representative single nanowire, randomly isolated from the sample. (D) HRTEM image of a representative portion of an individual nanowire. (E) Corresponding SAED pattern of these nanowires. (F) EDS spectrum of Tb-doped $CePO_4$ nanowires. The Cu peaks originate from the TEM grid.

Nonetheless, the observed nanorod formation is not surprising considering the crystal structure of hexagonal $CePO_4$, shown in Figure 6.3. From a structural point of view, hexagonal $CePO_4$ consists of infinite linear chains of alternating cerous and phosphate ions, extending along the *c* axis. From a thermodynamic perspective, the bonding between these chains is considerably weaker than that within the chains, such that the activation energy for the *c*-axis direction of growth of hexagonal $CePO_4$ is lower than that for a growth direction perpendicular to the *c*-axis itself.[42] Hence, these data imply a higher growth rate along the c-axis, suggesting that the nanorods end up growing preferentially along the [001] direction, consistent with what we have observed and with what others have also noted.[27, 33, 36] Thus, the intrinsic crystal structure of $CePO_4$ itself is inherently responsible for the observed 1D growth. Indeed, our results are consistent with the model put forward by Peng et al. in which one-dimensional growth only occurs if the chemical potential of monomers in solution is much higher than the highest attainable chemical potential of atoms on the surface of the nanocrystals.[43, 44] One other key point is that our synthesis is pH-dependent, which can help to define the localized chemical potential.[33] The pH parameter can sensitively influence the solute concentrations of both cerous and phosphate ions, which are around 0.05 M and 0.01 M, respectively. As with previous reports, we have found that a hexagonal-phase $CePO_4$ nanorod morphology was obtained when the pH value was acidic, presumably aided by enhanced dissolution of cerous and phosphate ions under these conditions, thereby allowing the ions sufficient time and opportunity to adopt correct positions within the developing crystal lattices.[45, 46]

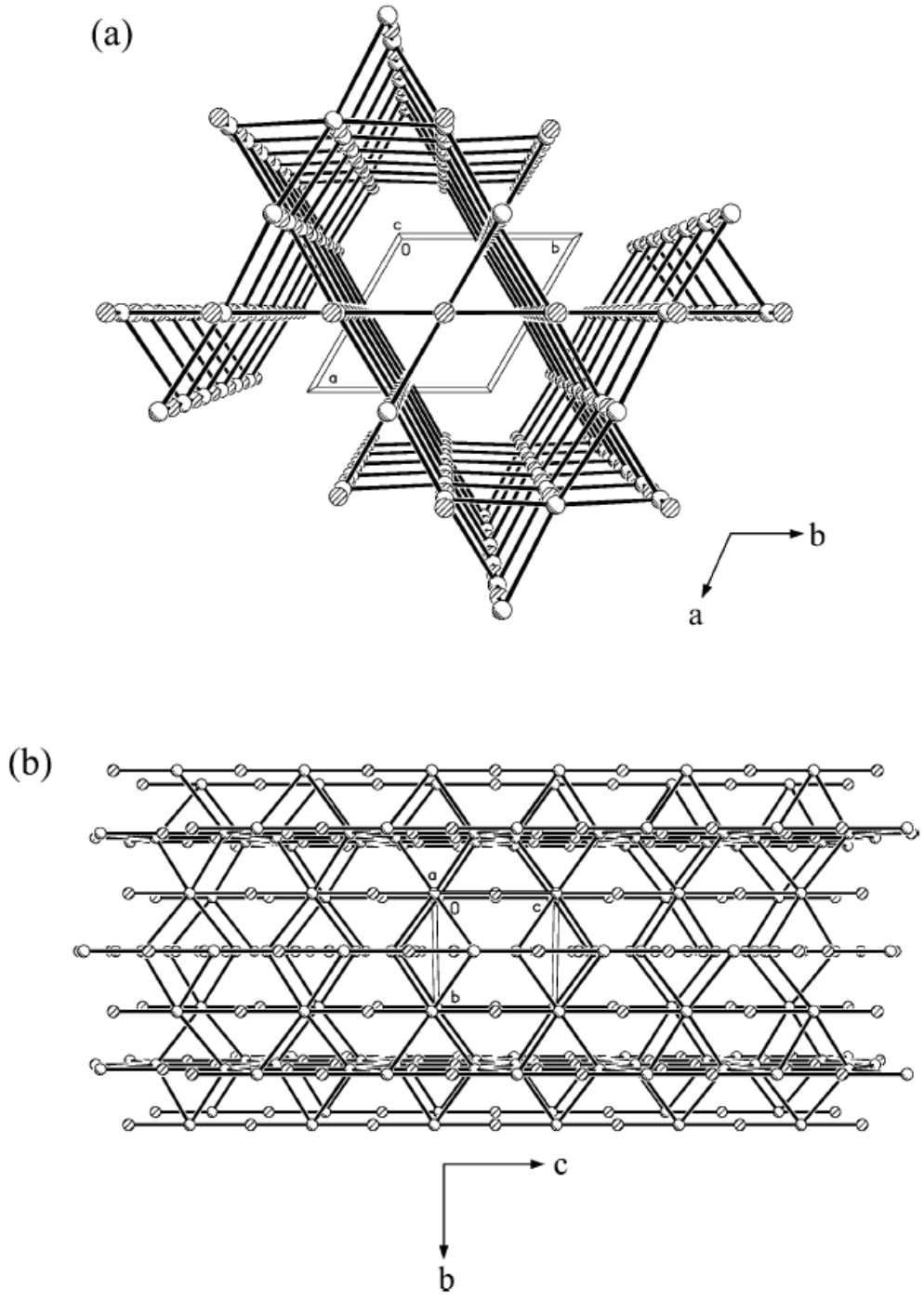

Figure 6.3 (a) Packing view of $CePO_4$ along the *c* axis. Each column is linked to four neighboring columns; open channels run though the structure along the hexagonal axis (the *c* axis). Oxygen atoms are omitted for clarity. (b) Packing view of $CePO_4$ along the *a* axis. Each column is built up of alternate cerous (shadow circles) and phosphate ions (open circles) and extends along the *c* axis. Oxygen atoms are omitted for clarity.[33]

We also were able to synthesize sheaf-like bundles of Tb-doped $CePO_4$ nanostructures to the tune of ~50 mg per run, corresponding to a ~5% yield, upon removal of the template membrane itself. Figure 6.4A and B are representative SEM and TEM images of these atypical morphologies. Specifically, each sheaf-like bundle measures ~100 nm in width, comparable to the pore width of the polycarbonate membrane. Individual constituent bristles of each bundle possess an average diameter of ~ 12 nm, comparable in dimension with that of the thin nanowires collected in the solution.

Although symmetric hay stack-like aggregates, composed of sheaf-like bundles projecting out at *both* ends, were often obtained, asymmetric, truncated structures consisting of sheaf-like bundles protruding from only *one* end formed the majority of as-prepared products isolated from within the template membrane pores. For example, Figure 6.4C shows a representative, asymmetric, truncated sheaf-like bundle. The associated SAED pattern is consistent with that of pure $CePO_4$ crystals pertaining to a hexagonal structure, as indexed in Figure 6.4D. The slightly diffuse, textured ring pattern is consistent with a sheaf-like bundle of nanoscale bristles partially aligned along the common axis. HRTEM analysis (Figure 6.4E) of the end of an individual sheaf-like bundle nanostructure indicates that each constituent bristle is single-crystalline without any visible defects and dislocations. The calculated interplanar distance is about 0.63 nm, corresponding to the (100) crystal plane of hexagonal $CePO_4$ crystals. This observation suggests that the nanoscale bristles are structurally uniform single crystals with a preferential growth direction of [001], e.g. identical to the *c*-axis of the ultrathin nanowires isolated from solution. The chemical signatures obtained from EDS spectra (Figure 6.4F) are identical within experimental accuracy, and only Tb, Ce, P and O elements were observed, as expected. The Cu signal arose from the TEM grid.

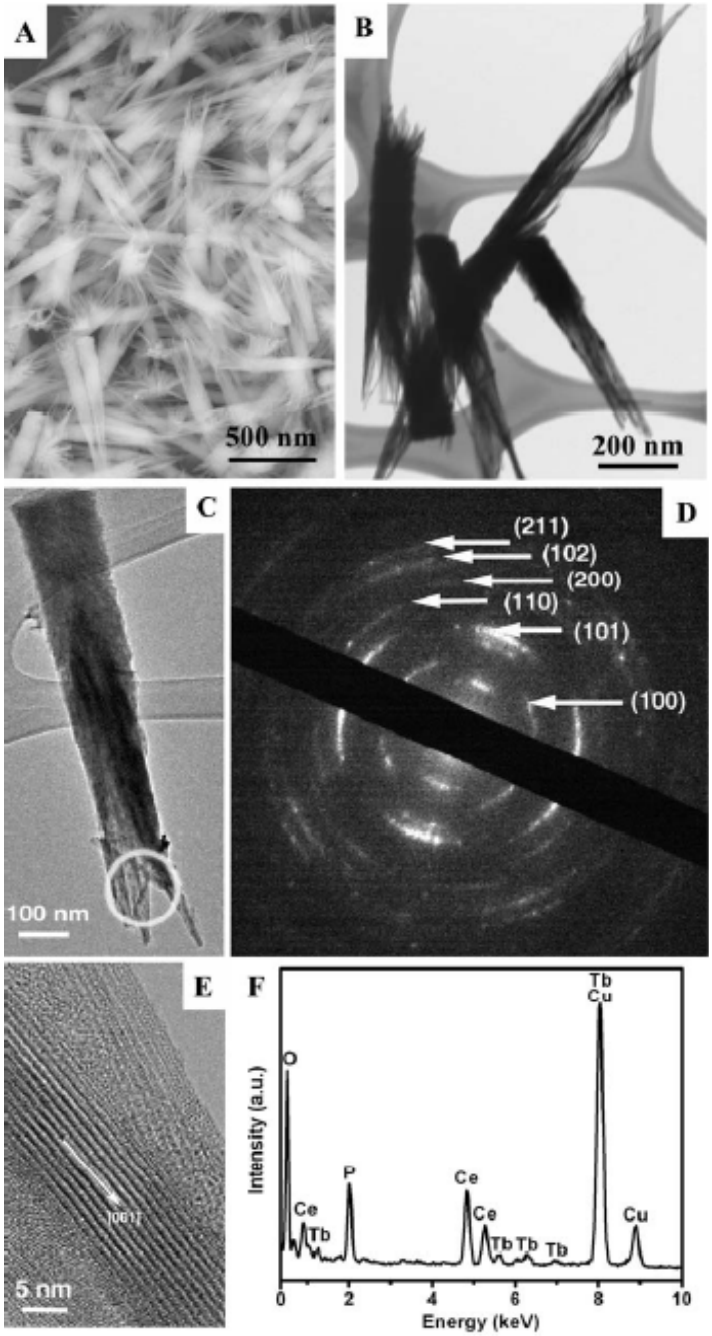

Figure 6.4 (A, B) Typical SEM and TEM images of sheaf-like bundles of as-prepared Tb-doped $CePO_4$ nanostructures grown the 100 nm pore channels of polycarbonate membranes. (C, D) TEM image and corresponding SAED pattern of a single half of a sheaf-like nanostructure bundle. (E) HRTEM image of a representative section at the tip of a sheaf-like bundle, highlighted by a white circle in (C). (F) EDS spectrum of as-prepared Tb-doped $CePO_4$ sheaf-like nanostructures. The Cu peaks originate from the TEM grid.

The coexistence of various novel morphological motifs, whose individual synthesis depends upon precise experimental conditions, has been commonly observed for a number of metal oxide systems.[47-50] In general, sheaf-like networks of nanostructures have been previously noted for β-FeO(OH),[51] iron phosphides,[52] Bi_2S_3,[53] lead selenides,[54] lanthanum orthovanadates,[55] CeO_2,[56] $BaWO_4$,[57] as well as Sb_2S_3 and Sb_2Se_3.[58] Moreover, the formation of ordered, oriented nanowire-based assemblies with bundle-like structures in the absence of copolymers and surfactants has also been observed for Eu^{3+}-doped $TbPO_4$ nanowires.[28] The exact growth mechanism associated with all of these nanomaterial motifs remains unclear. Though it has been proposed that these assemblies arise from the presence of intrinsic electric fields,[59-61] which direct the growth of dipole crystals, we believe that the splitting growth mechanism may more appropriately account for our observations.

In particular, crystal splitting is associated with fast crystal growth and depends strongly on the oversaturation of the solution.[54] It has been suggested that splitting is only possible if the oversaturation exceeds a certain critical level, unique to each material.[53] Factors known to cause crystal splitting include mechanical splitting (i.e. when extra molecules appear in some layers of its crystallographic network) and chemical splitting (i.e. when certain ions are present in the parent solution). According to this crystal splitting scenario, new surface area is created each time the crystal splits and the balance between bulk and surface energies determines the particular crystal size obtainable. Therefore, under the ambient, low-temperature conditions herein, there is an initial formation of only a few nuclei just after supersaturation followed by subsequent fast growth to a situation of metastability wherein crystals can grow beyond this size. It is then thermodynamically stable for the large crystal to split, partly because of the strong adhesion of an additive, such as the H^+ highly prevalent in an acidic environment, to the newly created surface.[53] Hence, by this mechanism, a single nanowire can essentially branch into a sheaf.[52]

In many ways, this process is akin to biomineralization, which defines the nature of the modified template growth process developed in our laboratory. In the current study, the growth mechanism involves a double-diffusion crystallization process, set in a U-tube

(Figure 6.5) which enables the continuous flow of precursor ions into spatially confined membrane pores. As previously mentioned, one of the two half cells was filled with a 0.01 M NaH_2PO_4 solution, and the other half cell contained a solution by mixing 0.05 M $CeCl_3$ solution together with $Tb(NO_3)_3$ up to a final molar concentration of 10.0 %, so as to generate desired Tb-doped $CePO_4$ nanostructures. In order to prevent overly rapid mixing, the solutions are separated by a polycarbonate membrane that slows down diffusion and the rate of crystallization. However, when the two solutions do meet, precipitation occurs, depleting the availability of ions in the local environment of the growing crystal within the template. The nucleation rate is primarily dictated by the supersaturation of the solution. Further growth of the nanostructures is limited by diffusion of ions in this localized region.

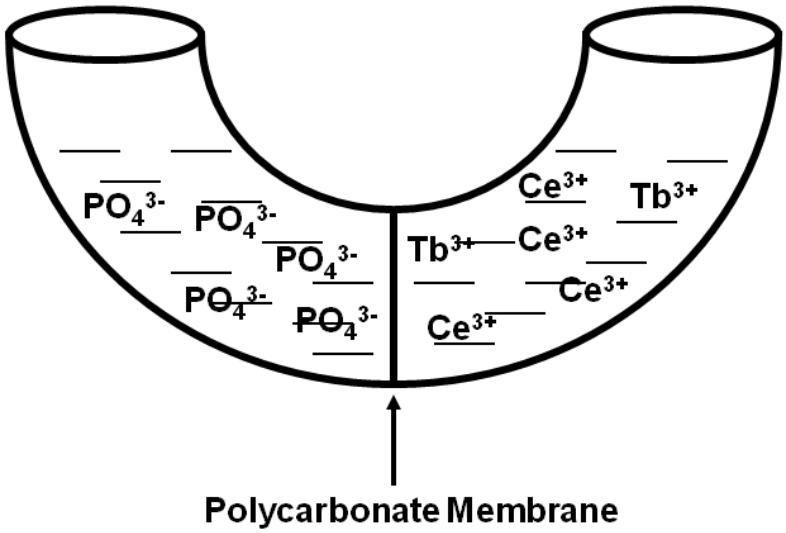

Figure 6.5 Schematic of the experimental setup used to synthesize Tb-doped $CePO_4$ nanostructures. The polycarbonate membranes used in this work had pore diameters of 50, 100 and 200 nm, respectively.

Herein, the initially formed ultrathin nanowires had a strong tendency to aggregate as larger ones and that the acidic medium was conducive to the self-assembly and subsequent crystal splitting of these as-formed bundles into sheaf-like patterns that propagate along the *c*-direction of elongation.[58, 62] This hypothesis is supported by the previously mentioned fact that the constituent bristles associated with the sheaf-like structure not only possess the same diameter range but also appear to grow along the [001] direction, precisely analogous to the ultrathin Tb-doped $CePO_4$ nanowires collected from the solution. The constituent bristles of the sheaths continually grow at a rate controlled by incident precursor ion diffusion, until they protrude externally from the template pores into solution. It has been previously observed for metals, that growing, elongating nanowires can attain sizes, that are significantly greater than the limited ~6 μm length of the template pore channels themselves.[63] Essentially, the nanowires then randomly break, perhaps due to mechanical fracturing[63] as a result of the presence of defects,[64] leading to the isolation of >10 microns long ultrathin nanowires in solution and remnant sheaf-like structures within the template pores themselves. A summary of our mechanism is highlighted in Figure 6.6.

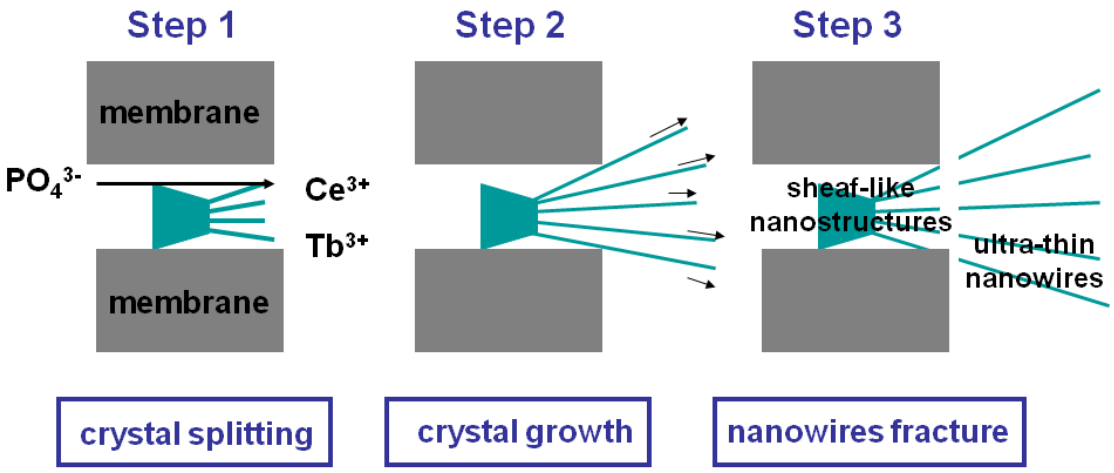

Figure 6.6 Schematic of crystal growth after initial nucleation and growth. Step 1: fast growth leads to a metastable situation, when thermodynamically favorable for a large crystal to split; Step 2: continuous growth of splitting nanowires along *c* axis at a rate controlled by precursor ion diffusion; Step 3: nanowires break into fragments once the protruding length becomes longer than a designated critical value determined by mechanical stability.

It is well known that complex morphologies of inorganic materials are usually difficult to be produce by simply directly mixing two aqueous solutions of metal salts due to a rapid decrease in supersaturation and further depletion of reaction nutrients within a short period of time.[65] To verify that the pores of the membrane are essential for the directed formation of Tb-doped $CePO_4$ nanostructures, reagent solutions were directly mixed in the absence of a polycarbonate membrane. Neither sheaf-like nanostructures nor ultrathin nanowires were evidently formed. In fact, direct mixing yielded a supersaturated medium and led to the formation of a large number of amorphous, irregularly-looking particles (Figure 6.7). As an experimental observation worthy of note, far fewer nanowires were isolated from the half-cell containing the NaH_2PO_4 solution, suggesting that the diffusion rate of PO_4^{3-} anionic groups was likely faster than that of either Ce^{3+} or Tb^{3+} cations under ambient, acidic reaction conditions. Moreover, after regular extraction of suspended ultrathin nanowires, we noted that a continuous addition of precursor solutions into the U-tube cells, still separated by a template membrane containing chemically active sheaf-like bundles of nanostructures, resulted in additional, unimpeded production of high-quality, single-crystalline ultrathin nanowires. Our data therefore strongly imply an ambient, green methodology for the large-scale and facile production of lanthanide-doped cerium phosphate nanowires.

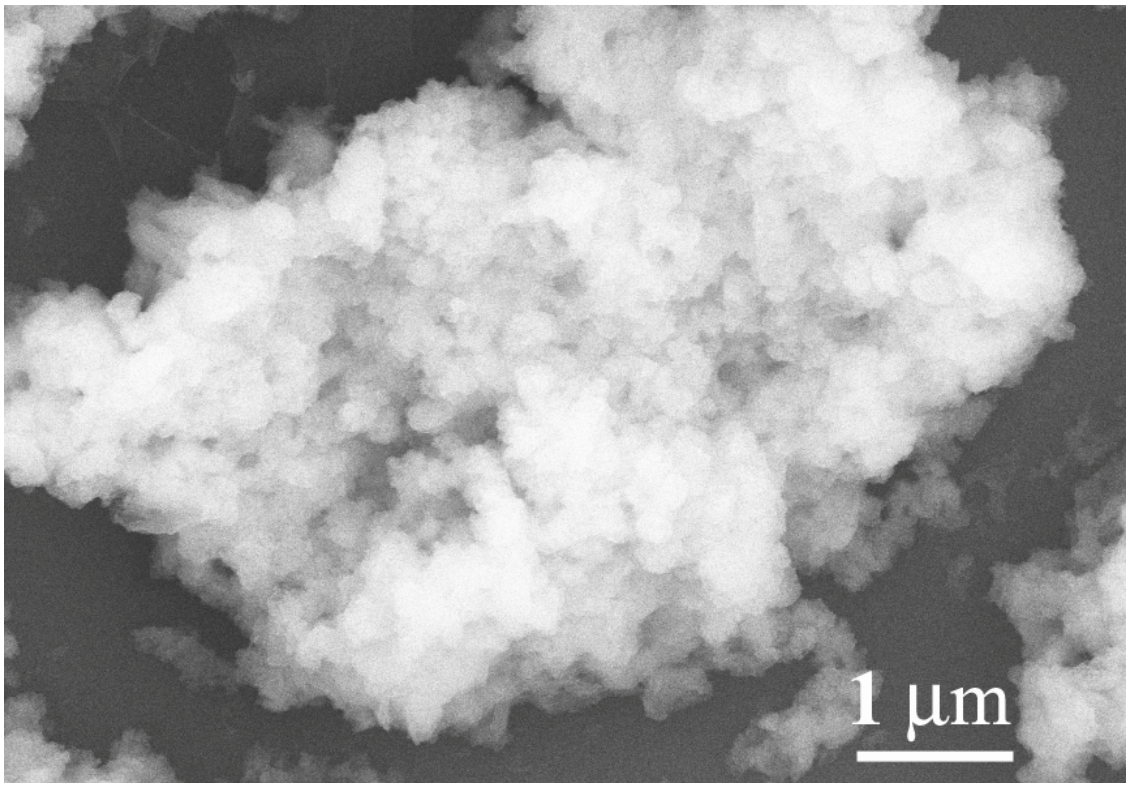

Figure 6.7 SEM image of Tb-doped $CePO_4$ particles prepared by directly mixing precursor solutions in the absence of templates.

6.3.3 UV-visible Spectroscopy and Photoluminescent Activity

Cerium-based compounds, such as CeO_2, CeP_2O_7 and $CePO_4$, are known to possess strong absorption for the ultraviolet and have been considered for applications such as tunable sunscreen materials.[23, 66] Figure 6.8 highlights the UV-visible absorption spectra of thin nanowires collected from solution. A magnified view of the region between 220 and 300 nm is shown as an inset, consisting of two major peaks located at 258 and 275 nm coupled with small shoulder-like substructure. These bands are overlapping as the excited state is strongly split by the crystal field.[26] Moreover, the results are consistent with reported data for transitions from the ground state $^2F_{5/2}$ ($4f^1$) of Ce^{3+} to the five crystal field split levels of the Ce^{3+} $^2D(5d^1)$ excited states (namely $^2D_{5/2}$ and $^2D_{3/2}$),[26, 33] suggesting that useful optical properties were retained in the nanostructured materials. Differences in the spectral behavior between the $CePO_4$ bulk and their nanoscale analogues have often been attributed to the presence of a higher degree of disorder and lattice distortion in the nanowires and the fact that there is a lower crystal field symmetry in these nanowires as compared with that of the bulk.[33]

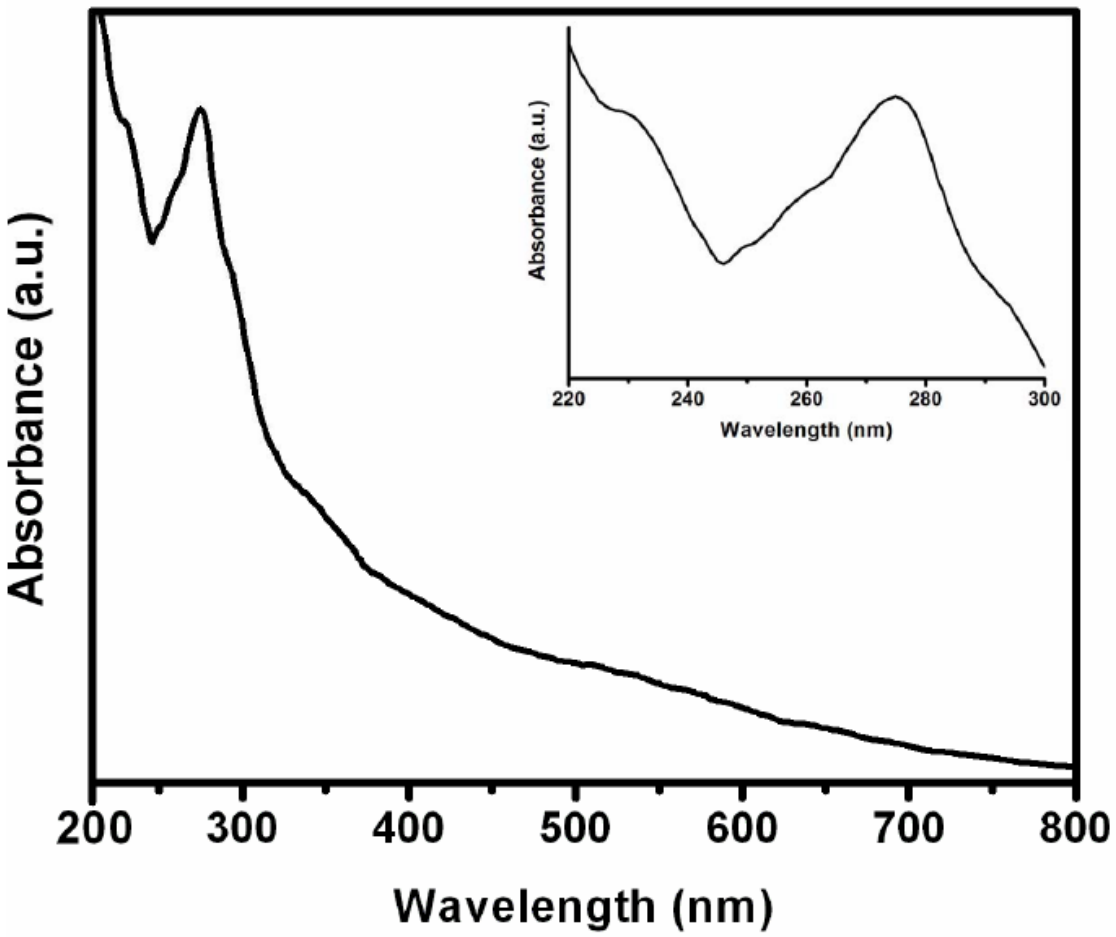

Figure 6.8 UV-visible spectrum of as-prepared Tb-doped $CePO_4$ nanowires. Expanded region between 220 and 300 nm is shown as an inset.

The black curve in Figure 6.9 highlights the room-temperature photoluminescent emission spectrum of Tb-doped $CePO_4$ nanowires in water upon excitation at 256 nm (where Tb^{3+} absorption is minimal) at room temperature. The actual doping concentration and inherent density of lanthanide ions are optically significant in terms of governing measured emission intensities.[27, 67] However, corresponding effects due to particle sizes on the emission signal are expected to be weak, since transitions of the well-shielded f electrons are mainly affected by the local symmetry of the crystal site.[17] Indeed, our data consists of four well-resolved peaks between 450 and 650 nm, corresponding to the $^5D_4$ - ^7F_J (J = 6, 5, 4, 3) transitions of Tb^{3+} ions. Specifically, these four peaks positioned at 488, 542, 586, and 620 nm can be ascribed to Tb^{3+} emission resulting from $^5D_4$ - $^7F_6$, $^5D_4$ - $^7F_5$, $^5D_4$ - $^7F_4$, and $^5D_4$ - $^7F_3$ relaxations, respectively. The relative intensity of each peak illustrates various numbers of photons according to different energy states.[68-70] The most intensive peak is located at 542 nm, consistent with the observed bright green luminescence of these samples, as shown in Figure 6.10.

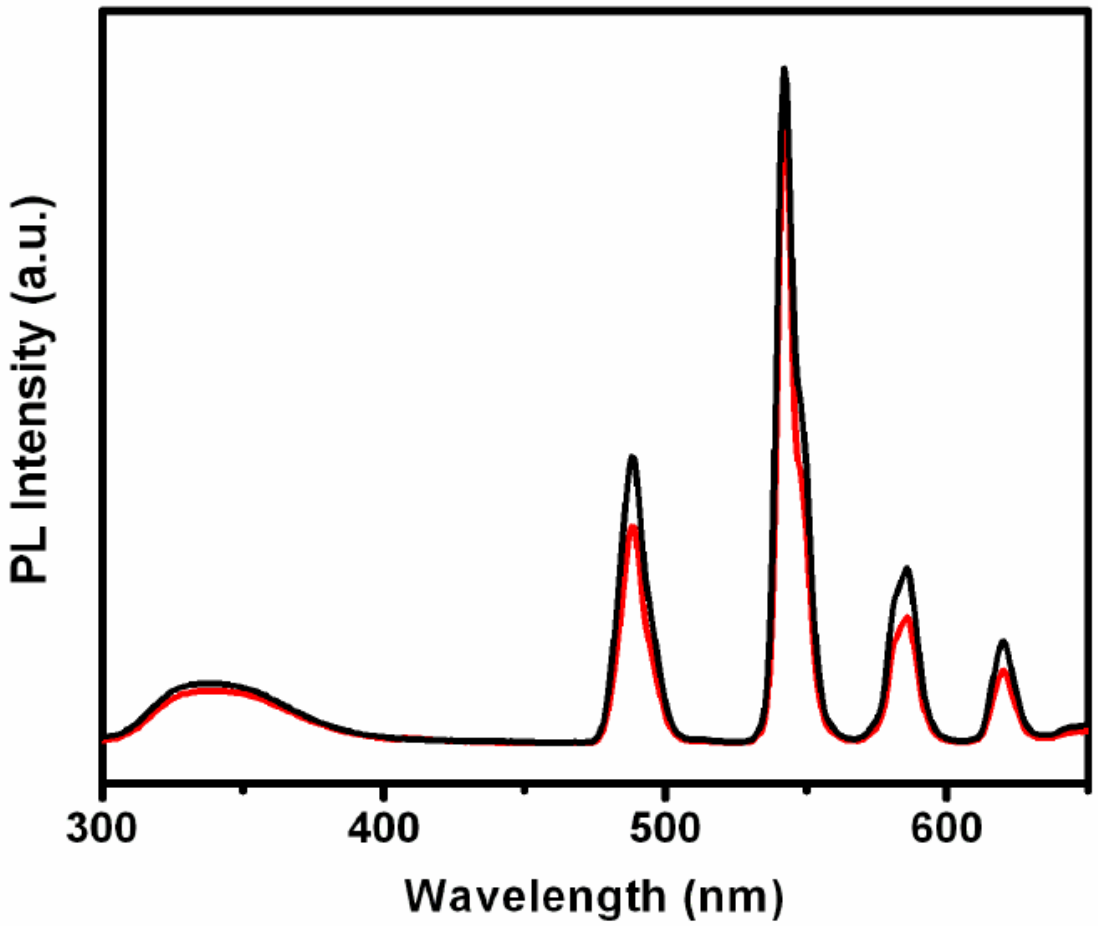

Figure 6.9 Photoluminescence emission spectra, obtained upon excitation at 256 nm at room temperature, of as-prepared Tb-doped $CePO_4$ nanowires before (black curve) and after (red curve) five successive redox cycles.

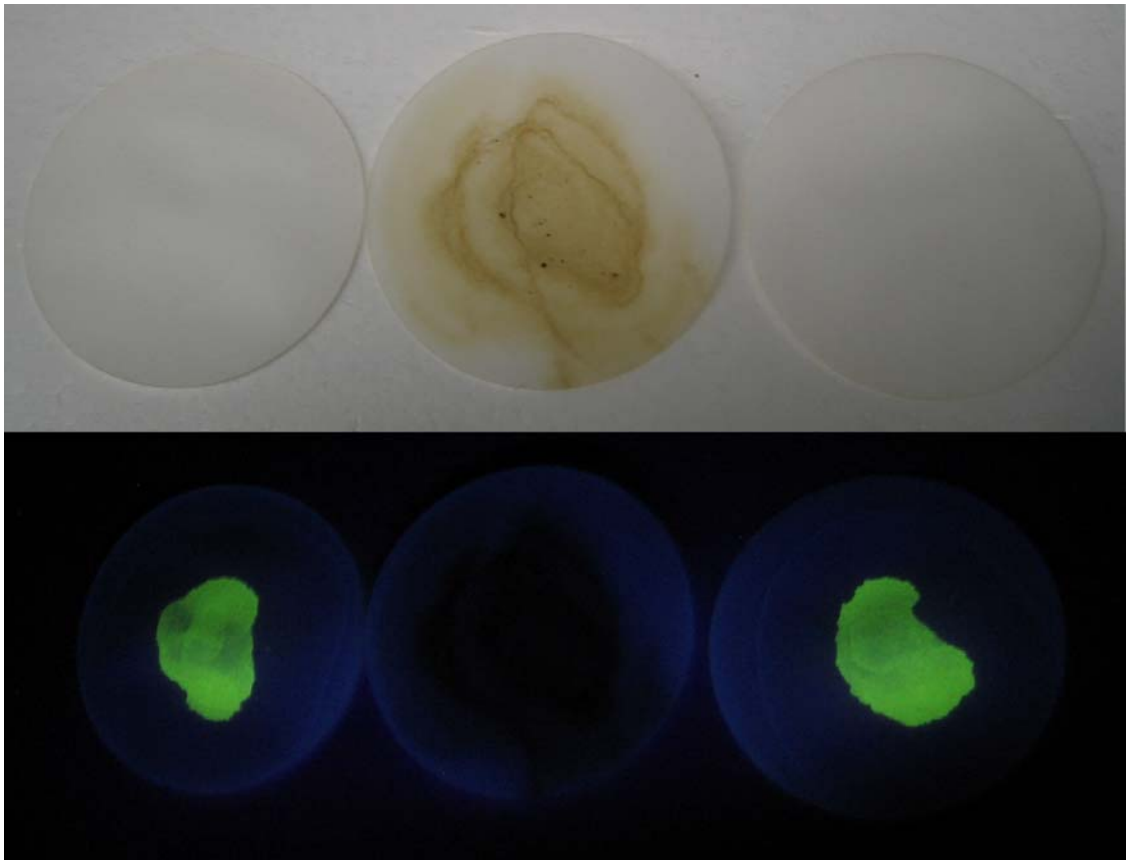

Figure 6.10 Optical photographs of nanowire suspensions on filter papers: as-prepared Tb-doped $CePO_4$ (left), Tb-doped $CePO_4$ + $KMnO_4$ (middle), and Tb-doped $CePO_4$ + $KMnO_4$ + ascorbic acid (right) under white light (top) and UV irradiation (bottom).

While the excitation spectra (Figure 6.11) exhibit a broad band between 250 and 320 nm, which can be attributed to the transition from $^2F_{5/2}$ to $^2D_{3/2}$ of Ce^{3+},[71] the broad band in the emission spectra (Figure 6.10) between 300 and 400 nm has been previously ascribed to 5d-4f transitions of Ce^{3+}. Owing to the high concentration of Ce^{3+} in the nanowires, the excited state of Ce^{3+} is not completely quenched by energy transfer to Tb^{3+}.[27] In fact, the nature of the observed photoluminescence depends on the probability of energy transfer through the host cerium lattice (governed by factors such as electric dipole-dipole interaction and reabsorption of emission) as well as the probability of energy transfer from the lattice to the Tb^{3+}.[72, 73] The intrinsic emission of Ce^{3+}, associated with two transitions from the lowest component of the ^2D state to the spin-orbit components of the ground state, $^2F_{7/2}$ and $^2F_{5/2}$, is a broad band.[17] By contrast, the absorption of Tb^{3+} consists of narrow lines.[31] The expected energy transfer process between Ce^{3+} and Tb^{3+} is schematically depicted in Figure 6.12, wherein energy transfer takes place from the $^5D_{3/2}$ state of Ce^{3+} to the acceptor states of Tb^{3+}, which decay non-radiatively to the $^5D_4$ and $^5D_3$ states followed by a radiative decay process to lower levels of ^7F_J (J = 0-6).[26]

However, efficient energy transfer between cerium and terbium is possible only between nearest neighbors in the crystal lattice and when there is optimal spectral overlap.[20] Therefore, if there is radiative transfer, some narrow dips at the location of Tb^{3+} absorption lines would appear to be associated with an emission intensity decrease but depression of the entire cerium emission spectrum would not occur.[31] This incomplete energy transfer from Ce^{3+} to Tb^{3+} has been observed for bulk analogues as well as for other Ce-based matrices.[72, 74]

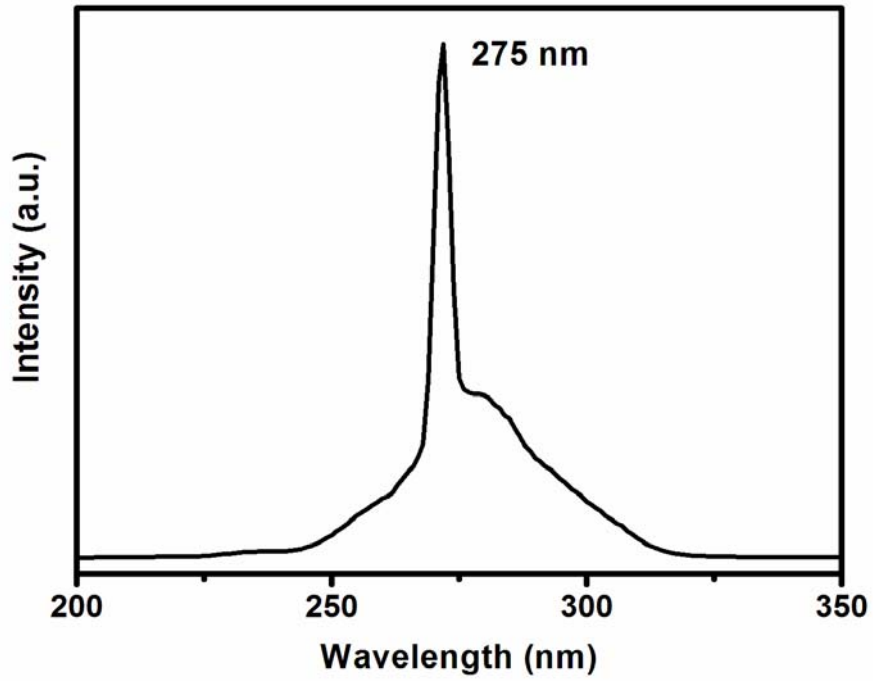

Figure 6.11 Photoluminescence excitation spectra, obtained upon emission at 542 nm.

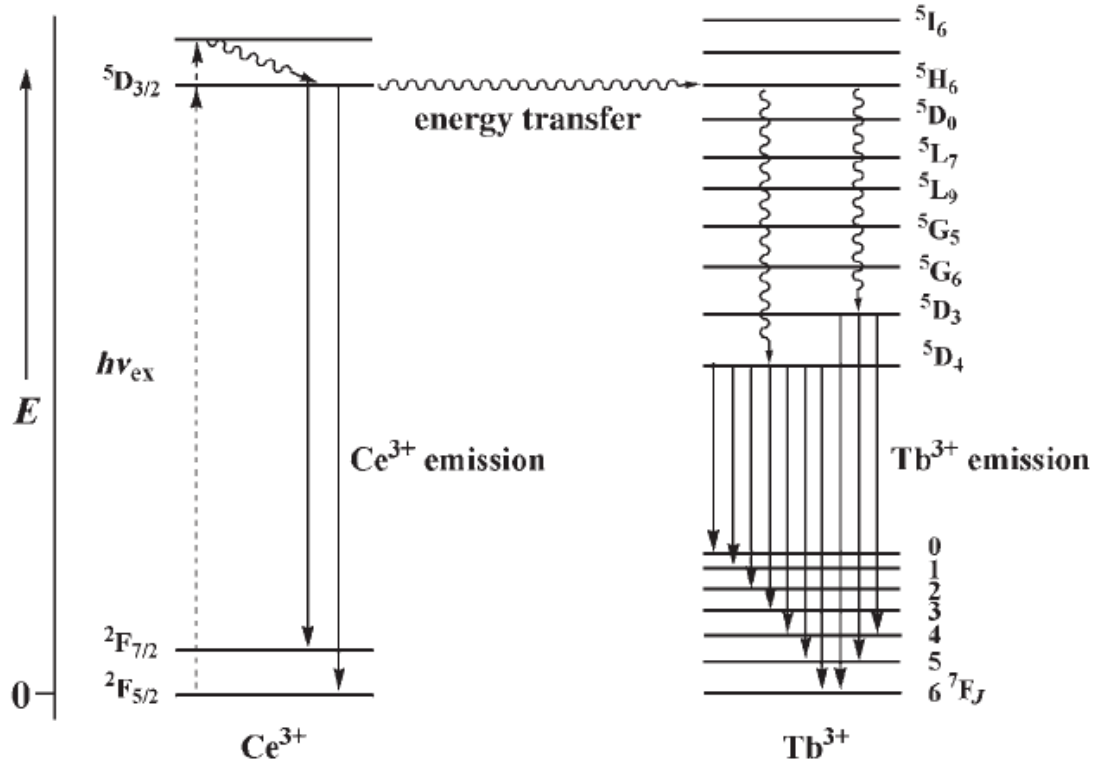

Figure 6.12 Energy-level diagram of Tb-doped $CePO_4$ with radiative transitions and energy transfer processes. Dashed arrows: excitation; wavy arrows: nonradiative decay; solid arrows: radiative decay.[26]

Photoluminescence switching behavior (Figure 6.10) has been previously observed in these systems,[26, 27, 74] related to dramatic changes in the emission intensity of Tb^{3+}, upon oxidation and reduction processes. Specifically, upon addition of $KMnO_4$ to the as-prepared colloidal dispersion of Tb-doped $CePO_4$ nanowires, Ce^{3+} was oxidized to Ce^{4+}, essentially suppressing the observed emission entirely. Subsequent reduction of Ce^{4+} to Ce^{3+} through the addition of ascorbic acid ($C_6H_8O_6$) to the oxidized nanowire solution effectively restored the observed luminescence to its original profile.

As shown in Figure 6.9 and Figure 6.10, the switching process is reversible. That is, the photoluminescence spectra of as-prepared Tb-doped $CePO_4$ nanowires (black curve) and of samples taken after five successive redox cycles (red curve) are shown in which the luminescence of these nanostructures was repeatedly quenched (off) by oxidation with $KMnO_4$ followed by its recovery (on) by reduction with ascorbic acid. The emission profiles are essentially identical with only a slight degradation in luminescence intensity with no apparent change in nanowire morphology (Figure 6.13). In fact, the ratio of luminescence intensities taken of the nanowire samples before and immediately after five successive $KMnO_4$/ascorbic acid redox cycles was as much as 95% at the 542 nm emission peak. These results demonstrate that our as-prepared ultrathin Tb-doped $CePO_4$ nanowires are robust and the reproducible change in luminescence signal can theoretically be used to as a sensitive and rapid indicator of the redox behavior of their surrounding environments. Moreover, owing to their reported low toxicity[26] and reasonable dispersibility in cell culture medium (up to as much as 0.5 mg/mL for a period of 2 days), these nanostructures are potentially viable candidates for biological labels and probes.

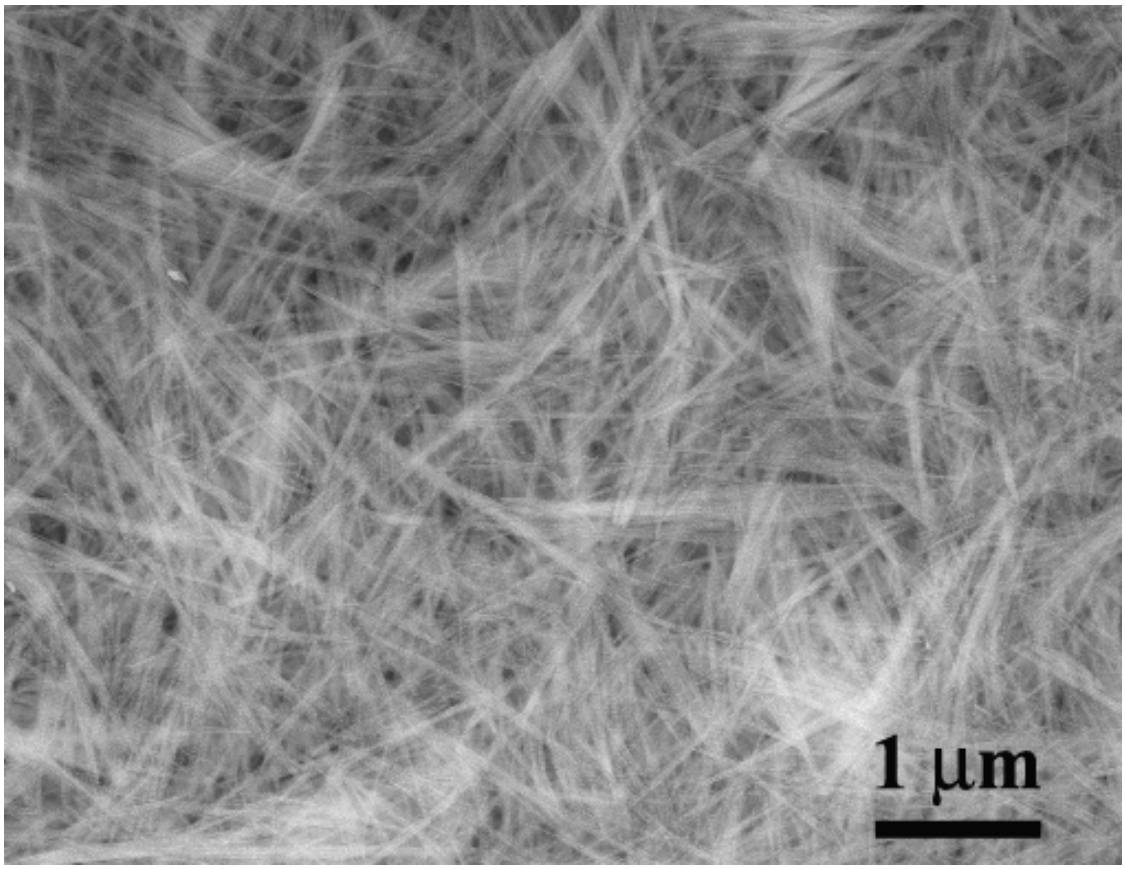

Figure 6.13 SEM images of Tb-doped $CePO_4$ nanowires after five successive redox cycles.

6.3.4 Biocompatibility and Bioimaging

In general, the cellular permeability and cytotoxicity characteristics of fluorescent nanomaterials are critical to their applicability as luminescent biological labels. It has already been established that inorganic fluorescent lanthanide (europium and terbium) orthophosphate (e.g. $EuPO_4 \cdot H_2O$ and $TbPO_4 \cdot H_2O$) nanorods, synthesized by a microwave technique, can behave as biolabels and can be internalized into either human umbilical vein endothelial cells, 786-O cells, or renal carcinoma cells, though the exact mechanism for their internalization remained unclear.[7, 25] Hence, to confirm the potential applicability of our ultrathin green luminescent Tb-doped $CePO_4$ nanowires in a biological system, we conducted analogous experiments using HeLa cells measuring 12 to 20 μm in diameter. To facilitate processing, prior to cellular incubation, our as-prepared thin, long nanowires were sonicated for ~1 hour in order to generate noticeably shorter structures (Figure 6.14), measuring 3.2 ± 2 μm in length.

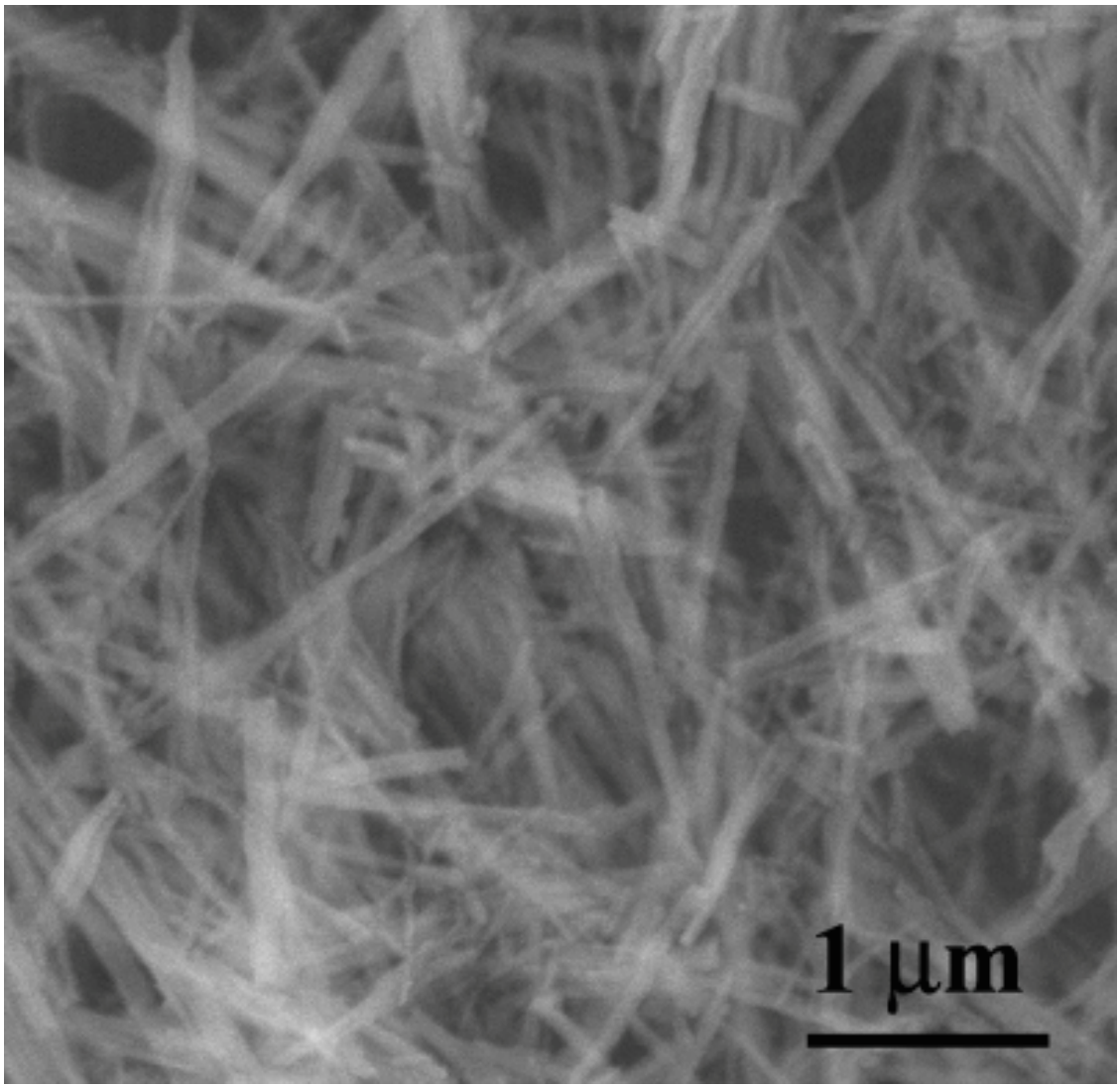

Figure 6.14 SEM image of Tb-doped $CePO_4$ nanowires after sonication for about 1 hour.

As a control experiment, HeLa cells alone showed negligible background fluorescence under two-photon excitation. Nonetheless, upon incubation, incorporation of cut, as-prepared Tb-doped $CePO_4$ nanowires into HeLa cells was confirmed by confocal fluorescence microscopy. Specifically, after incubation with 2 mg/mL of Tb-doped $CePO_4$ nanowires for 2 h at 37 °C, an intense intracellular luminescence was observed, as shown in Figure 6.15A. These inorganic phosphate nanowires clearly retained their intrinsic fluorescent properties upon cellular internalization. Moreover, the corresponding bright-field measurements taken after treatment with the nanowires confirmed that the cells were viable throughout the imaging experiments (Figure 6.15B) and that there were no evident regions of cell death. As indicated in Figure 6.15C, overlays of both confocal luminescence and bright-field images further demonstrated that the observed luminescence was noticeable throughout the entire intracellular region, thereby strongly suggesting that the nanowires were internalized into the interior of the cells themselves as opposed to merely staining the external membrane surface.[41]

To confirm the spatial localization of nanowires within a typical cell, we obtained a series of Z-stack images of the cell (e.g. top to bottom) at 1 μm 'slice' intervals of an individual HeLa cell stained with Tb-doped $CePO_4$ nanowires. Data associated with the middle, central slice (Figure 6.16), corresponding to orthogonal *xy*, *yz*, and *xz* planes, respectively, are shown. Because these three planes share a common focal center within the cell itself and moreover, as these intimately interconnected planes evidently all demonstrate green fluorescence simultaneously, we can reasonably conclude that the fluorescently doped lanthanide nanowires are localized within the interior environment of the HeLa cells themselves.

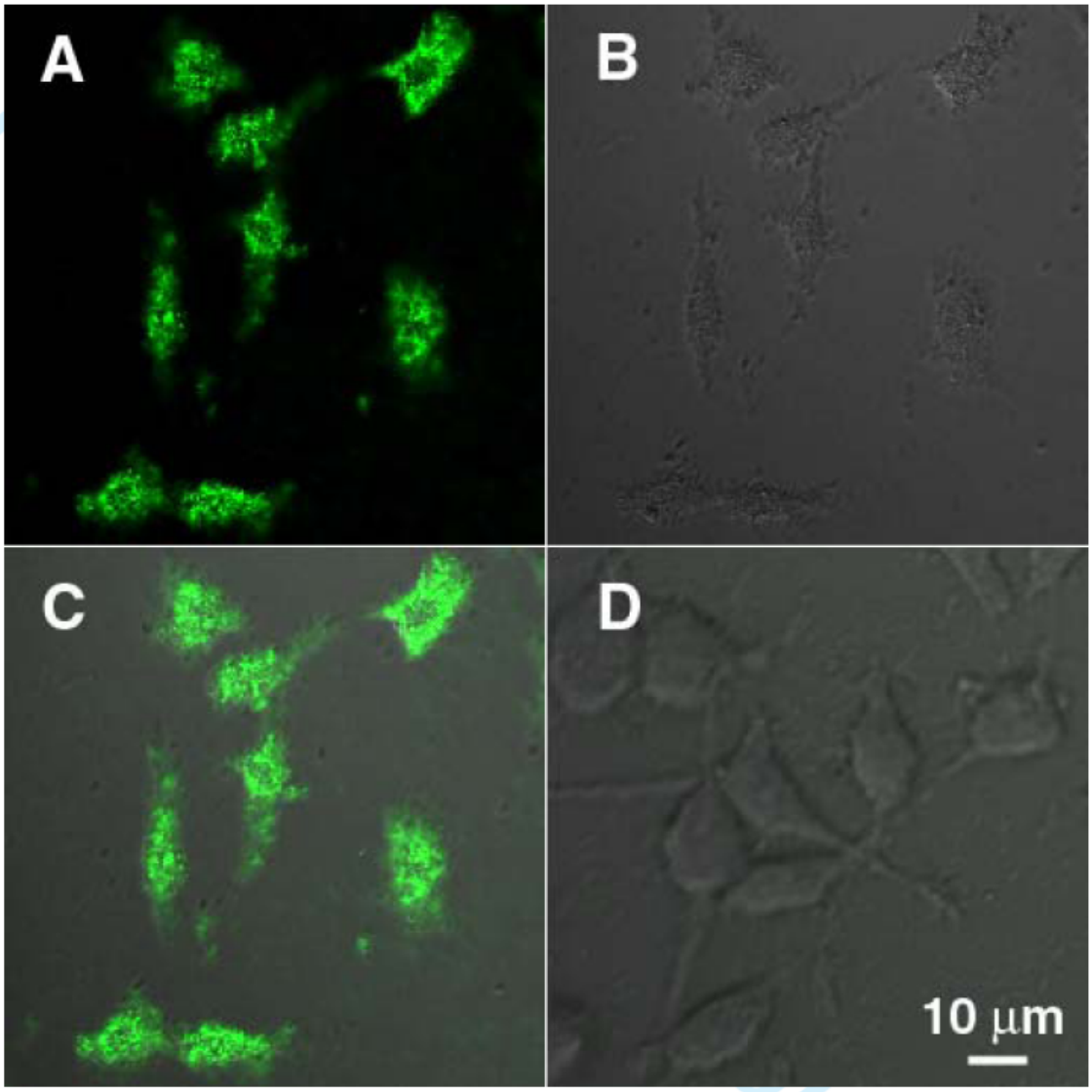

Figure 6.15 Confocal fluorescence microscopy images of HeLa cells. (A) Confocal luminescence images of cells taken after incubation with 0.2 mg/mL of Tb-doped $CePO_4$ nanowires for 2 h at 37°C. (B) Bright-field optical image of cells shown in (A). (C) Overlay image of both (A) and (B). (D) Corresponding overlay image of cells obtained after incubation with 0.2 mg/mL of Tb-doped $CePO_4$ nanowires for 2 h at 4°C.

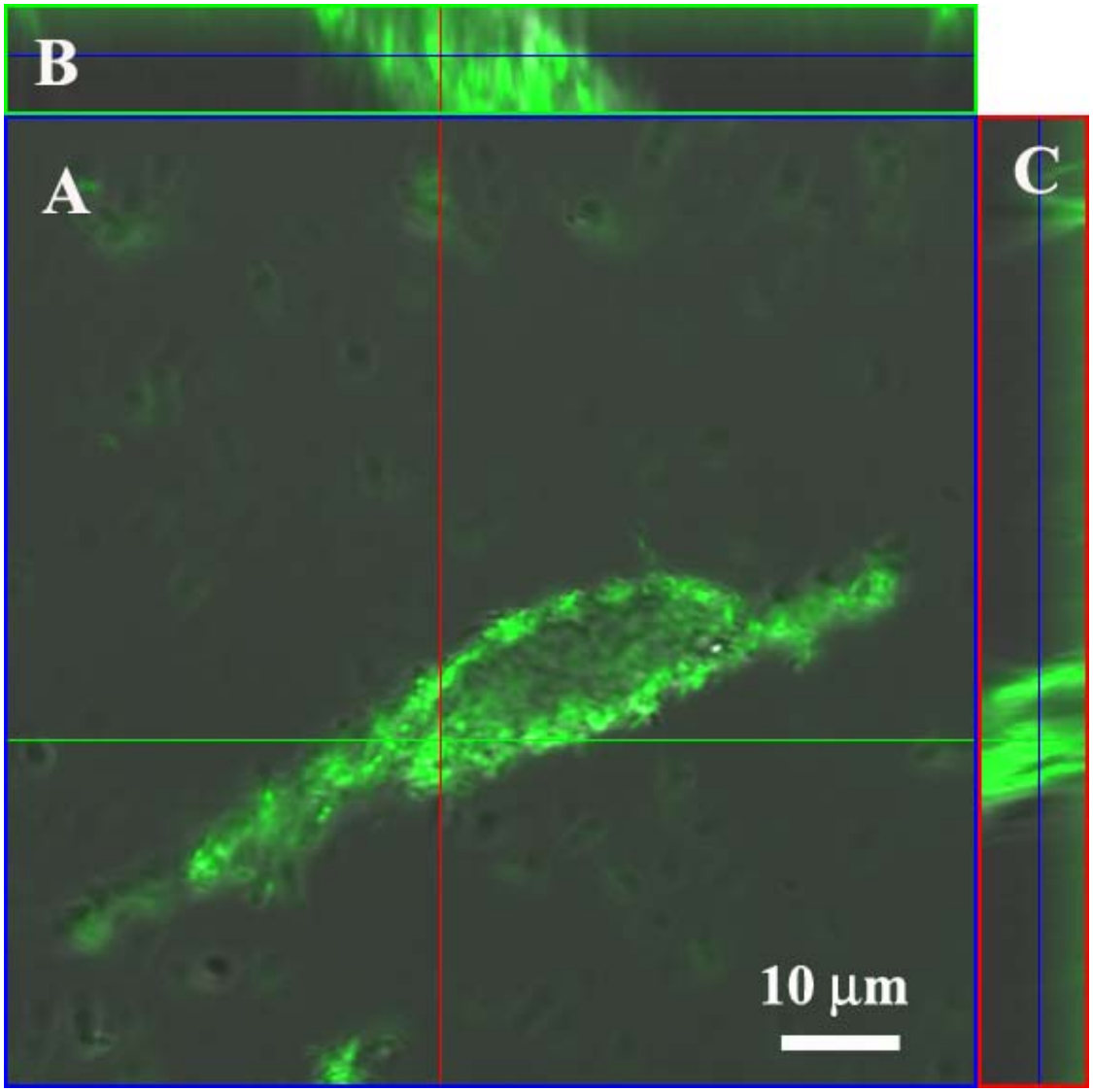

Figure 6.16 CFM images of orthogonal sections of an individual Hela cell stained with Tb-doped $CePO_4$ nanowires. (A) *xy* plane. (B) *yz* plane. (C) *xz* plane.

We noted a dramatic decrease in the fluorescence intensity in data taken after identical cellular incubation with our as-prepared Tb-doped $CePO_4$ nanowires at the same concentrations, but at a noticeably lower temperature (i.e. 4°C), as compared with that observed in cells treated with nanowires at 37°C. The overlap image (Figure 6.15D) suggests that there was little if any nanowire incorporation. Though the pathway for the nonspecific cellular uptake of the as-prepared phosphate nanowires has not been well-defined, the internalization mechanism has been suggested as being due to receptor-mediated endocytosis arising from cellular recognition of proteins from the media, due to the adsorption of serum proteins onto the nanostructure surface.[75]

Endocytosis is a conserved process in eukaryotes whereby extracellular substances are taken up into the cells usually by the invagination of plasma membrane forming vesicles. In addition to the classical receptor-mediated pathway, other endocytic mechanisms have been identified, namely phagocytosis, caveolae-mediated endocytosis, macropinocytosis, as well as clathrin- and caveolae-independent endocytosis.[76-79] The size and shape of nanomaterials contribute significantly to their interaction with cells. However, surface properties play a primary role in the internalization process.[80] Though our lanthanide nanowires were not specifically functionalized with biologically-relevant surface functional groups, regardless of the initial nanowire surface charge, serum proteins from the cell growth media, most likely bovine serum albumin, were found to self-assemble as monolayers onto gold nanorods, leading to all nanostructures bearing the same effective charge.[81] It has also been reported that these proteins possess the ability to adsorb onto many other surfaces because of the presence of different domains with different charge density.[82] Cells have receptors that can recognize proteins present in the serum-containing media. Incubation of the resulting phosphate nanowires with cells in media can lead to adsorption of serum proteins on their surface. Therefore, the mechanism of cellular uptake for biomolecules in the size range of nanorods has been suggested to involve receptor-mediated endocytosis.[83]

Nonetheless, our results confirm that as-prepared Tb-doped $CePO_4$ nanowires can viably be used as fluorescent labels for biological imaging. We also incubated our HeLa cells with different concentrations (ranging from 0.1 to 0.5 mg/mL) of as-prepared Tb-

doped $CePO_4$ nanowires in order to test their inherent sensitivity as luminescent probes. Representative CFM images are shown in Figure 6.17A-C. An analysis of the corresponding CFM intensities, proportional to the number of doped phosphate nanowires internalized by the HeLa cells, in Figure 6.18A demonstrates an increase in the measured fluorescence, with increasing nanowire concentrations and cellular incubation periods, as expected. Our data show that even nanowire concentrations as low as 0.1 mg/mL and incubation times as short as 2 h can yield sufficient nanowire integration into HeLa cells so as to generate sufficiently strong fluorescence for bioimaging purposes.

Furthermore, Tb-doped $CePO_4$ nanowires, subjected to repeated redox cycles, were also incubated with HeLa cells. The degree of cellular uptake was analogously confirmed by CFM data. Specifically, oxidized nanowires did not show any fluorescence within cells, whereas cells treated with reduced nanowires demonstrated a measurable degree of fluorescence (Figure 6.17D). Quantitatively, as compared with as-prepared nanowires, there was a small decrease (7% to 13%) in the fluorescence intensity measured in cells. This value was comparable in magnitude to the decrease observed in pure nanowire suspensions, as measured by PL spectroscopy (Figure 6.9).

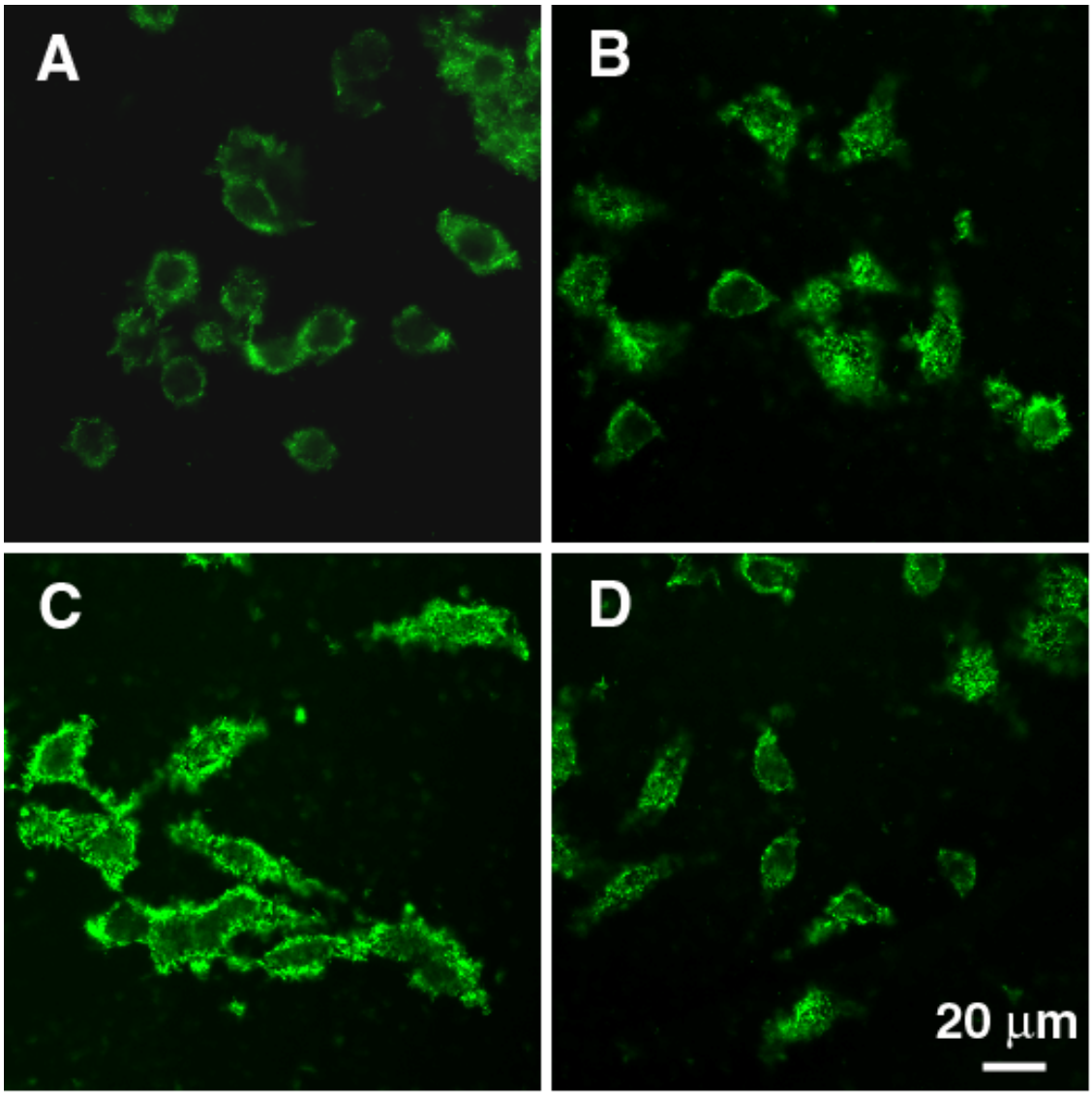

Figure 6.17 CFM images of Hela cells after incubation with Tb-doped $CePO_4$ nanowires at various concentrations for different time periods at 37 °C. (A) 0.1 mg mL^{-1} of as-prepared nanowires for 2 h. (B) 0.2 mg mL^{-1} of as-prepared nanowires for 24 h. (C) 0.5 mg mL^{-1} of as-prepared nanowires for 2 h. (D) 0.2 mg mL^{-1} of nanowires after five successive redox cycles for 24 h.

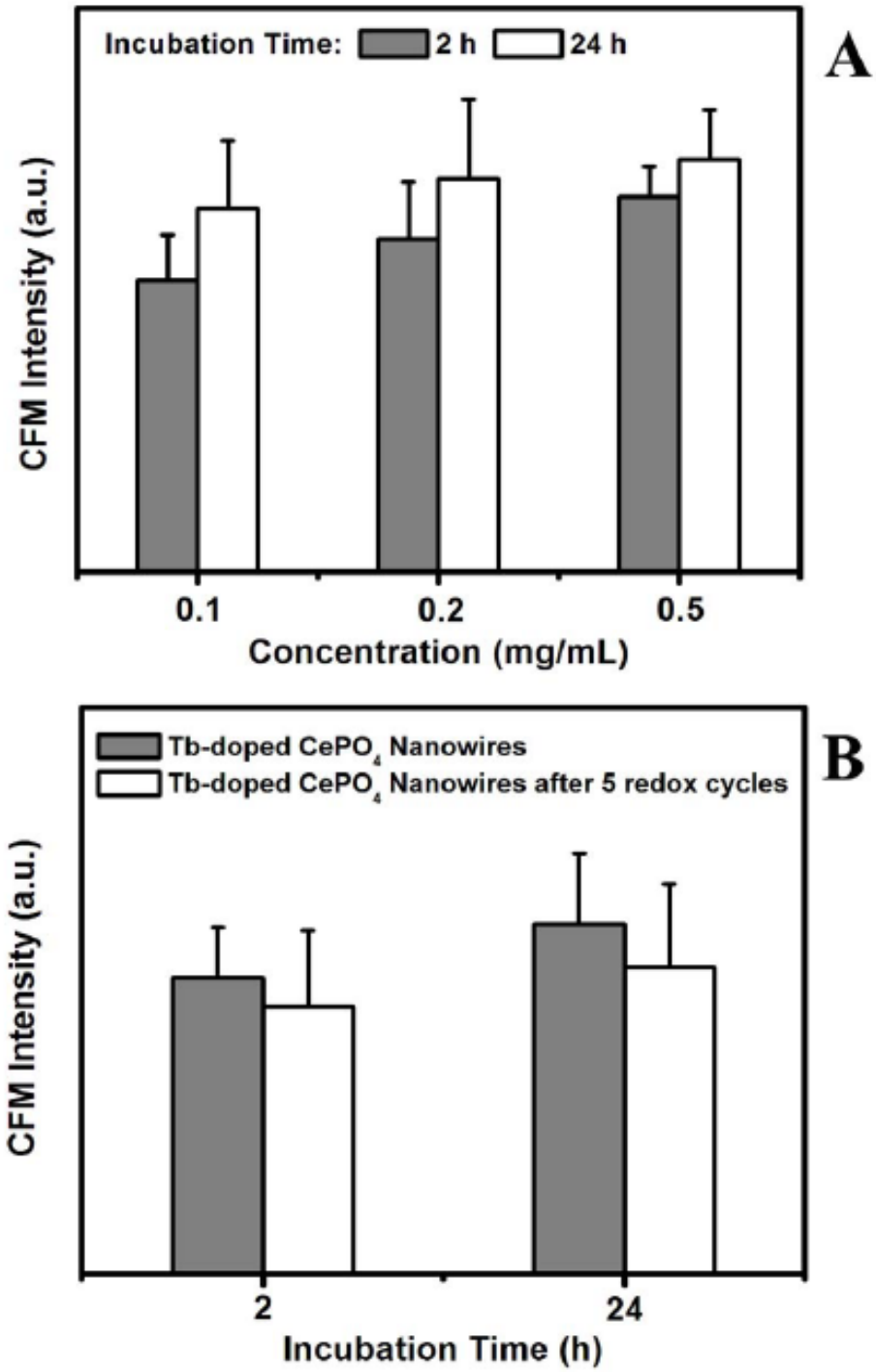

Figure 6.18 Statistical analysis pertaining to CFM intensity of HeLa cells after incubation with (A) as-prepared Tb-doped $CePO_4$ nanowires at different concentrations for periods of 2 and 24 h, respectively; and (B) 0.2 mg/mL as-prepared Tb-doped $CePO_4$ nanowires for 2 and 24 h, respectively, before and after redox cycles.

Moreover, to verify whether these ultrathin Tb-doped $CePO_4$ nanowires are biologically nontoxic and biocompatible, cytotoxicity studies of HeLa cells were performed, based on the reduction activity of methyl thiazolyl tetrazolium (MTT), and are shown in Figure 6.19, based on previous analogous work.[41] The viability of untreated cells was assumed to be 100%. Upon incubation of HeLa cells with a 0.1 mg/mL solution of Tb-doped $CePO_4$ nanowires, we noted that fewer than 15% of the cells died after a 48 h exposure. When the concentration of nanowires was increased to 0.5 mg/mL, the observed cell viability still remained above 80%, again after 48 h of exposure. Therefore, these data strongly suggested that ultrathin Tb-doped $CePO_4$ nanowires can be considered to possess reasonably low cytotoxicity, which is in agreement with previous reports that rare-earth-based nanophosphors maintain reasonable chemical stability and generally low toxicity, which are essential for legitimate bioimaging applications.[84]

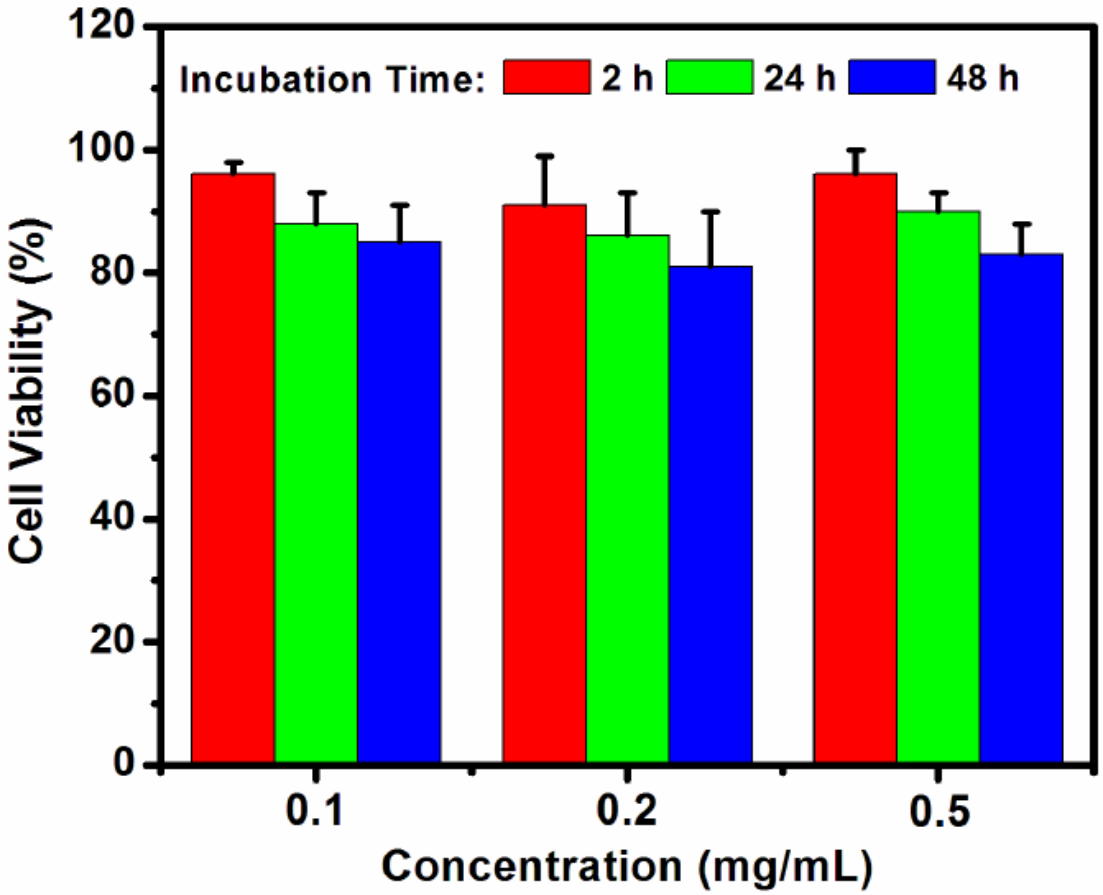

Figure 6.19 In vitro cell viability of HeLa cells incubated with Tb-doped $CePO_4$ nanowires at different concentrations for periods ranging from 2 to 48 h.

6.4 Conclusions

In summary, a simple, effective, and versatile template-directed method has been developed for the successful large-scale preparation of Tb-doped $CePO_4$ nanowires possessing very high aspect ratio, under ambient room temperature conditions. Sheaf-like bundles of ultrathin 1D nanostructures may initially form through a crystal splitting growth mechanism, followed by continuous growth out of template membrane pore channels, until they finally fracture in solution. This new synthetic approach is important not only because it involves a number of intriguing fundamental steps, but also because this environmentally benign route can be readily extended to the synthesis of other kinds of rare-earth phosphate nanomaterials either with or without dopants. The resulting Tb-doped $CePO_4$ nanowires displayed a redox-switchable green photoluminescence that was subsequently exploited for biological labeling purposes. Moreover, we noted that our nanostructures not only were biocompatible with cells but also were relatively nontoxic over reasonable time periods and concentrations, which is of significance for applications in biomedical diagnostics and analyses.

6.5 References

1. De, M.; Ghosh, P. S.; Rotello, V. M., *Adv. Mater.* 2008, *20*, 4225-4241.
2. Chan, W. C. W.; Nie, S., *Science* 1998, *281*, 2016.
3. Bruchez, M.; Moronne, M.; Gin, P.; Weiss, S.; Alivisatos, A. P., *Science* 1998, *281*, 2013.
4. Larson, D. R.; Zipfel, W. R.; Williams, R. M.; Clark, S. W.; Bruchez, M. P.; Wise, F. W.; Webb, W. W., *Science* 2003, *300*, 1434.
5. Cederquist, K. B.; Stoermer Golightly, R.; Clark, S. W., *Langmuir* 2008, *24*, 9162.
6. Wong Shi Kam, N.; Liu, Z.; Dai, H., *Angew. Chem. Int. Ed.* 2006, *45*, 577.
7. Patra, C. R.; Bhattacharya, R.; Patra, S.; Basu, S.; Mukherjee, P.; Mukhopadhyay, D., *J. Nanobiotech.* 2006, *4*, 11.
8. Li, Z.; Yang, R.; Yu, M.; Bai, F.; Li, C.; Wang, Z. L., *J. Phys. Chem. C* 2008, *112*, 20114.
9. Kuo, C.-W.; Lai, J.-J.; Wei, K. H.; Chen, P., *Adv. Funct. Mater.* 2007, *17*, 3707.

10. Salem, A. K.; Searson, P. C.; Leong, K. W., *Nat. Mater.* 2003, *2*, 668.

11. Keating, C. D.; Natan, M. J., *Adv. Mater.* 2003, *15*, 451.

12. Hultgren, A.; Tanase, M.; Chen, C. S.; Meyer, G. J.; Reich, D. H., *J. Appl. Phys.* 2003, *93*, 7554.

13. Mondejar, S. P.; Kovtun, A.; Epple, M., *J. Mater. Chem. 17*, 4153.

14. Meiser, F.; Cortez, C.; Caruso, F., *Angew. Chem. Int. Ed.* 2004, *43*, 5954.

15. Wang, L.; Qian, B.; Chen, H.; Liu, Y.; Liang, A., *Chem. Lett.* 2008, *37*, 402.

16. Zhang, Y.-W.; Sun, X.; Si, R.; You, L.-P.; Yan, C.-H., *J. Am. Chem. Soc.* 2005, *127*, 3260.

17. Riwotzki, K.; Meyssamy, H.; Schnablegger, H.; Kornowski, A.; Haase, M., *Angew. Chem. Int. Ed.* 2001, *40*, 573.

18. Meyssamy, H.; Riwotzki, K.; Kornowski, A.; Naused, S.; Haase, M., *Adv. Mater.* 1999, *11*, 840.

19. Hou, Z.; Yang, P.; Li, C.; Wang, L.; Lian, H.; Quan, Z.; Lin, J., *Chem. Mater.* 2008, *20*, 6686.

20. Jose, M. T.; Lakshmanan, A. R., *Opt. Mater.* 2004, *24*, 651.

21. Erdei, S.; Ainger, F. W.; Ravichandran, D.; White, W. B.; Cross, L. E., *Mater. Lett.* 1997, *30*, 389.

22. Hashimoto, N.; Takada, Y.; Sato, K.; Ibuki, S., *J. Lumin.* 1991, *48&49*, 893.

23. Imanaka, N.; Masui, T.; Hirai, H.; Adachi, G. Y., *Chem. Mater.* 2003, *15*, 2289.

24. Altinoglu, E. I.; Russin, T. J.; Kaiser, J. M.; Barth, B. M.; Eklund, P. C.; Kester, M.; Adair, J. H., *ACS Nano* 2008, *2*, 2075.

25. Patra, C. R.; Bhattacharya, R.; Patra, S.; Basu, S.; Mukherjee, P.; Mukhopadhyay, D., *Clin. Chem.* 2007, *53*, 2029.

26. Li, Q.; Yam, V. W., *Angew. Chem. Int. Ed.* 2007, *46*, 3486.

27. Chen, G.; Sun, S.; Zhao, W.; Xu, S.; You, T., *J. Phys. Chem. C* 2008, *112*, 20217.

28. Di, W.; Wang, X.; Zhu, P.; Chen, B., *J. Solid State Chem.* 2007, *180*, 467.

29. Huignard, A.; Gacoin, T.; Boilot, J.-P., *Chem. Mater.* 2000, *12*, 1090.

30. Di, W.; Zhao, X.; Lu, S.; Wang, X.; Zhao, H., *J. Solid State Chem.* 2007, *180*, 2478.

31. Shionoya, S.; Nakazawa, E., *Appl. Phys. Lett.* 1965, *6*, 118.

32. Yin, Y.; Alivisatos, A. P., *Nature* 2005, *437*, 664.

33. Fang, Y.-P.; Xu, A.-W.; Song, R.-Q.; Zhang, H.-X.; You, L.-P.; Yu, J. C.; Liu, H.-Q., *J. Am. Chem. Soc.* 2003, *125*, 16025.

34. Cao, M.; Hu, C.; Wu, Q.; Guo, C.; Qi, Y.; Wang, E., *Nanotechnology* 2005, *16*, 282.

35. Yu, L.; Li, D.; Yue, M., *Mater. Lett.* 2007, *61*, 4374.

36. Yan, R.; Sun, X.; Wang, X.; Peng, Q.; Li, Y., *Chem. Eur. J.* 2005, *11*, 2183.

37. Zheng, Y.; Cheng, Y.; Wang, Y.; Yu, Y.; Chen, D.; Bao, F., *J. Cryst. Growth* 2005, *280*, 569.

38. Yu, L.; Song, H.; Lu, S.; Liu, Z.; Yang, L.; Kong, X., *J. Phys. Chem. B* 2004, *108*, 16697.

39. Xing, Y.; Li, M.; Davis, S. A.; Mann, S., *J. Phys. Chem. B* 2006, *110*, 1111.

40. Zhu, L.; Liu, X.; Li, Q.; Li, J.; Zhang, S.; Meng, J.; Cao, X., *Nanotechnology* 2006, *17*, 4217.

41. Hu, H.; Yu, M.; Li, F.; Chen, Z.; Gao, X.; Xiong, L.; Huang, C., *Chem. Mater.* 2008, *20*, 7003.

42. Murphy, K. E.; Altman, M. B.; Wunderlich, B., *J. Appl. Phys.* 1977, *48*, 4122.

43. Peng, Z. A.; Peng, X. G., *J. Am. Chem. Soc.* 2001, *123*, 1389.

44. Peng, Z. A.; Peng, X. G., *J. Am. Chem. Soc.* 2002, *124*, 3343.

45. Zhang, Y.; Guan, H., *J. Cryst. Growth* 2003, *256*, 156.

46. Yan, Z.-G.; Zhang, Y.-W.; You, L.-P.; Si, R.; Yan, C.-H., *Solid State Commun.* 2004, *130*, 125.

47. Hu, W.; Zhao, Y.; Liu, Z.; Dunnill, C. W.; Gregory, D. H.; Zhu, Y., *Chem. Mater.* 2008, *20*, 5657.

48. Okada, A.; Yoshimura, M.; Ueda, K., *Appl. Phys. Lett.* 2007, *90*, 203102.

49. Dai, Q.; Xiao, N.; Ning, J.; Li, C.; Li, D.; Zou, B.; Yu, W. W.; Kan, S.; Chen, H.; Liu, B.; Zou, G., *J. Phys. Chem. C* 2008, *112*, 7567.

50. Zitoun, D.; Pinna, N.; Frolet, N.; Belin, C., *J. Am. Chem. Soc.* 2005, *127*, 15034.

51. Hu, Y.; Chen, K., *J. Cryst. Growth* 2007, *308*, 185.

52. Kelly, A. T.; Rusakova, I.; Ould-Ely, T.; Hofmann, C.; Luttge, A.; Whitmire, K. H., *Nano Lett.* 2007, *7*, 2920.

53. Tang, J.; Alivisatos, A. P., *Nano Lett.* 2006, *6*, 2701.

54. Shen, X.-F.; Yan, X.-P., *Angew. Chem. Int. Ed.* 2007, *46*, 7659.

55. Deng, H.; Liu, C.; Yang, S.; Xiao, S.; Zhou, Z.-K.; Wang, Q.-Q., *Cryst. Growth Des.* 2008, *8*, 4432.

56. Kim, S.; Lee, J. S.; Mitterbauer, C.; Ramasse, Q. M.; Sarahan, M. C.; Browning, N. D.; Park, H. J., *Chem. Mater.* 2009, *21*, 1182.

57. He, J.; Han, M.; Shen, X.; Xu, Z., *J. Cryst. Growth* 2008, *310*, 4581.

58. Chen, G.-Y.; Deng, B.; Cai, G.-B.; Zhang, T.-K.; Dong, W.-F.; Zhang, W.-X.; Xu, A.-W., *J. Phys. Chem. C* 2008, *112*, 672.

59. Busch, S.; Dolhaine, H.; Dechesne, A.; Hinez, S.; Hochrein, O.; Laeri, F.; Podebrad, O.; Vietze, U.; Weiland, T.; Kniep, R., *Eur. J. Inorg. Chem.* 1999, (1643).

60. Colfen, H.; Qi, L., *Progr. Colloid Polym. Sci.* 2001, *117*, 200.

61. Wang, T.; Colfen, H.; Antonietti, M., *J. Am. Chem. Soc.* 2005, *127*, 3246.

62. Dong, L.; Chu, Y.; Zhang, W., *Mater. Lett.* 2008, *62*, 4269.

63. Sharabani, R.; Reuveni, S.; Noy, G.; Shapira, E.; Sadeh, S.; Selzer, Y., *Nano Lett.* 2008, *8*, 1169.

64. Brambilla, G.; Payne, D. N., *Nano Lett.* 2009, *9*, 831.

65. Zhang, Z.; Shao, X.; Yu, H.; Wang, Y.; Han, M., *Chem. Mater.* 2005, *17*, 332.

66. Imanaka, N.; Masui, T.; Itaya, M., *Chem. Lett.* 2003, *32*, 400.

67. Yu, L.; Song, H.; Liu, Z.; Yang, L.; Lu, S.; Zheng, Z., *Solid State Commun.* 2005, *134*, 753.

68. Rambabu, U.; Munirathnam, N. R.; Prakash, T. L.; Buddhudu, S., *Mater. Chem. Phys.* 2003, *78*, 160.

69. Fu, Z.; Bu, W., *Solid State Sci.* 2008, *10*, 1062.

70. Kompe, K.; Borchert, H.; Storz, J.; Lobo, A.; Adam, S.; Moller, T.; Haase, M., *Angew. Chem. Int. Ed.* 2003, *42*, 5513.

71. Buchold, D. H. M.; Feldmann, C., *Adv. Funct. Mater.* 2008, *18*, 1002.

72. Blasse, G.; Bril, A., *J. Chem. Phys.* 1969, *51*, 3252.

73. Bourcet, J. C.; Fong, F. K., *J. Chem. Phys.* 1974, *60*, 34.

74. Zhang, C.; Chen, J.; Zhou, Y.; Li, D., *J. Phys. Chem. C* 2008, *112*, 10083.

75. Alkilany, A. M.; Nagaria, P. K.; Hexel, C. R.; Shaw, T. J.; Murphy, C. J.; Wyatt, M. D., *Small* 2009, *5*, 701.

76. Khalil, I. A.; Kogure, K.; Akita, H.; Harashima, H., *Pharmacol. Rev.* 2006, *58*, 32.

77. Conner, S. D.; Schmid, S. L., *Nature* 2003, *422*, 37.

78. Lamaze, C.; Schmid, S. L., *Curr. Opin. Cell Biol.* 1995, *7*, 573.

79. Nam, H. Y.; Kwon, S. M.; Chung, H.; Lee, S.-Y.; Kwon, S.-H.; Jeon, H.; Kim, Y.; Park, J. H.; Kim, J.; Her, S.; Oh, Y.-K.; Kwon, I. C.; Kim, K.; Jeong, S. Y., *J. Controlled Release* 2009, *135*, 259.

80. Chavanpatil, A. K. M. D.; Panyam, J., *J. Nanosci. Nanotechnol.* 2006, *6*, 2651.

81. Silin, V.; Weetall, H.; Vanderah, D. J., *J. Colloid Interface Sci.* 1997, *185*, 94.

82. Rezwan, K.; Meier, L. P.; Rezwan, M.; Voros, J.; Textor, M.; Gauckler, L. J., *Langmuir* 2004, *20*, 10055.

83. Dobrovolskaia, M. A.; McNeil, D. E., *Nature Nanotech.* 2007, *2*, 469.

84. Palmer, R. J.; Butenhoff, J. L.; Stevens, J. B., *Environ. Res.* 1987, *43*, 142.

Chapter VII Conclusions

Nanomaterials are fundamentally different from their bulk counterparts because of their unique size and shape-dependent properties, as well as their potential applications as building blocks in nanoscale devices. As a structure decreases in size to the nanoscale, a greater surface-to-volume ratio results in a significant change with respect to the properties due to predominant contributions from more active surface atoms as compared with core atoms. Thus they cannot solely be considered as miniaturized versions of bulk materials. In particular, the intrinsic anisotropy inherent in 1D nanomaterials renders them as the smallest dimension structures which are highly promising for applications in catalysis, electronics, condensed matter physics, materials science and biology fields.

The ability to synthesize, manipulate, and assemble matter in a controllable manner as well as to predict and understand the properties of resulting structures are of fundamental interest, and holds the promise of a completely new generation of advanced materials. However, nanoscience and nanotechnology is still in its infancy as compared with other science fields. There are many challenges and obstacles that need to be overcome, including (1) the development of an environmentally-friendly synthetic method, (2) a deep understanding of the relationship between size, composition, and physical properties in 1D nanostructures, (3) the design of 1D nanomaterials with novel properties, and (4) the application of 1D nanostructures in various fields, such as energy, catalysis, and biotechnology.

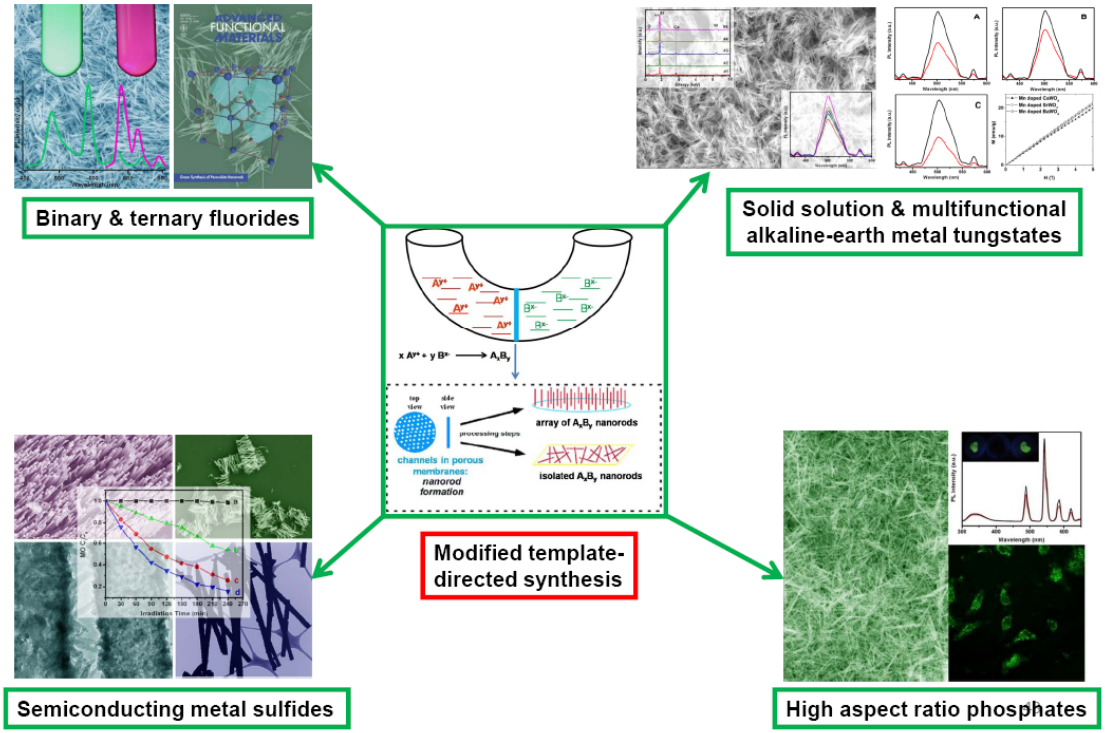

Figure 7.1 Representative electron microscopy images and property measurements of a variety of 1D nanostructures prepared via the modified template-directed method.

The rational synthesis of nanomaterials is critical in fundamental studies of crystal growth, the investigation of shape and structural dependence of properties, and the exploration of applications of associated nanomaterials. The conventional synthetic methodology has usually involved either toxic solvents, unstable precursors, or high energy input. The focus of my graduate research has been the development of a relatively environmentally friendly and energy effective technique to rationally prepare 1D nanomaterials with controllable size and composition, as well as the extensive characterization of these structures and the exploration of their novel properties and applications.

In this dissertation, as illustrated in Figure 7.1, we have developed a modified template-directed technique, using a double-diffusion setup via a biomimetic crystallization process, which has enabled the successful preparation of various 1D nanomaterials, including fluorides, tungstates, sulfides, and phosphates, under ambient, room-temperature conditions, without using either very harmful precursors or solvents, and without generating particularly toxic byproducts. The key to this technique has been the placement of membranes within a double-diffusion setup. In order for the generation of single-crystalline 1D nanostructures, we have proposed that single crystals originate from isolated single nucleation sites, which subsequently grow by extension through the porous network, until the crystals impinge on the template surface or block the pores. Crystal growth within the membrane is typically slow, limited by the availability of ions from the two precursor solutions, separated by the membrane. Therefore, the membranes not only enable a continuous flow of precursor ions through the pores, but also slow down ion diffusion and mixing as well as crystallization rates. In addition, the diameters of the resulting nanomaterials can be controlled by choosing membranes with predictable pore sizes.

In Chapter II, a family of single-crystalline alkaline-earth metal binary fluoride nanowires and perovskite ternary fluoride nanorods, in addition to their rare-earth ion-doped analogues, has been successfully synthesized using this method, implying that the synthetic approach is quite general and versatile. It is anticipated that it can be generalized to the preparation of other 1D nanostructures. Chapter III and IV have

highlighted the generalization of this technique for the formation of oxide nanostructures. Specially, the fabrication of single-crystalline alkaline-earth-metal tungstates AWO_4 (A = Ca, Sr, Ba) nanorods as well as the corresponding series of their crystalline solid-solution analogues, $Sr_{1-x}Ca_xWO_4$ and $Ba_{1-x}Sr_xWO_4$ ($0 < x < 1$), with varying controllable compositions has been reported in Chapter III. The composition-modulated luminescence properties provide the fundamental basis for a more thorough understanding of structure-property correlations in these systems. In Chapter IV, a family of multifunctional nanorods has been created by merging favorable luminescent and magnetic properties by incorporating Mn ions into the tungstate matrix. Metal sulfides have also been synthesized and then this synthetic method has been adapted to the fabrication of semiconducting nanowires in Chapter V. In particular, the resulting CdS nanostructures have shown higher photocatalytic degradation activity as compared with their bulk counterparts. In Chapter VI, we have generalized this approach into the large-scale synthesis of high aspect-ratio, single-crystalline Tb-doped $CePO_4$ nanowires, possessing a novel redox luminescence switch behavior and applications as fluorescent labels in bioimaging.

The major advantage associated with template-directed techniques is that both the dimensions and compositions of the resulting nanomaterials can be easily controlled by varying experimental conditions. Conventional templating methods often generate polycrystalline products as a result of additional annealing steps at high temperature, with more complicated techniques, such as sol-gel and electrodeposition, are usually needed in order to generate single-crystalline nanostructures. Our modified technique, by contrast, has enabled the preparation of a variety of single-crystalline 1D nanomaterials under ambient, room-temperature conditions using a relatively simple, straightforward experimental setup. In fact, the growth of our nanowires within the confinement of membrane pores is analogous to the biominetic crystallization of single crystals of calcium carbonate and calcium phosphate within micelles, chitin scaffolds, and collagen matrices in nature.

Besides 1D nanostructures, we have also synthesized unusual hierarchical cactus-like CdS and sheaf-like Tb-doped $CePO_4$ nanostructures. Different growth mechanisms

have been proposed to be associated with their varying crystal structures. These results have inspired the potential of generating various nanostructures using this approach by varying reaction conditions, such as temperature, pressure, solvent and precursor, or by simply using membranes containing different pore structures, since the morphology of the resulting nanomaterials is complementary to that of the template.

In addition to the as-prepared 1D nanomaterials possessing either luminescent or magnetic properties or even both coexisting within one structure, it is expected that our modified template-directed technique can be applied to the synthesis of other materials with versatile properties, including, but not limited, to metals, metal oxides, hydroxides, and carbonates, which can precipitate from soluble precursor solutions and stabilize under ambient conditions.

Since it is sometimes desirable for single nanomaterials to perform multiple functions simultaneously, we have demonstrated the formation of multifunctional nanorods using this templating approach. Another way single structures can be manipulated to perform multiple functions is if they are synthesized such that they consist of more than one component. The ability of this method in preparing multicomponent nanomaterials, such as core-shell and multisegmented striped structures, is quite promising as a low cost, high throughput, and easy synthetic methodology as compared with the traditional processes of epitaxial growth, vapor-solid-liquid (VLS), high-temperature catalytic growth, and chemical vapor deposition (CVD). It is anticipated that by varying precursor solutions and accordingly changing the reaction time within one run, multisegmented nanorods can be synthesized, and the interface between multiple components can also be controlled. In addition, by carefully selecting starting materials, we might be able to generate hollow nanotubes as shell structures. Subsequent filling of the center with another component will result in radial core-shell 1D nanostructures.

Because of the simplicity and versatility of our modified template-directed approach, it is expected that this particular technique can be generalized to the preparation of various nanomaterials with controllable size, shape, and component. However, as a major drawback, the quantity of nanostructures that can be produced using any template-directed methods in each run is relatively limited, and removal of the

templates requires chemical steps that could damage the resulting nanomaterials. It would be highly beneficial if the product yield associated with our template strategy, can be improved while eliminating any possible damage by template removal. Our phosphate nanowire work has provided a hint of the ability to grow nanowires protruding out of the pores, where they tend to break into fragments in solution. It is therefore proposed that the remaining fragments within the membranes can serve as seeds for continuous growth so as to generate 1D nanostructures on a reasonably large scale.

Future work in nanoscience and nanotechnology will continue to focus on the development of rational synthetic strategies and fundamental property investigations associated with 1D nanostructures. In particular, our modified template-directed method can be explored to the extension of fabricating either different morphologies, forming more complicated structures, and improving both the quantity and quality of the resulting products, as discussed. There are almost unlimited research opportunities that are being and will be explored in this general area of 1D nanostructures. A deeper understanding of structure-property relationships will open up new opportunities in this area.

References

Chapter I

1. Iijima, S., *Nature* **1991,** *354*, 56.
2. Lieber, C. M., *MRS Bulletin* **2003,** *28*, 486.
3. http://www.science.doe.gov/bes/scale_of_things.html.
4. *Nanoscience, and Nanotechnology: Opportunities and Uncertainties. The Royal Society* **2004**.
5. *A special issue on nanoscale materials, Acc. Chem. Res.* **1999,** *32*.
6. Wang, Z. L., *Adv. Mater.* **2000,** *12*, 1295.
7. Huczko, A., *Appl. Phys. A* **2000,** *70*, 365.
8. Erhardt, D., *Nat. Mater.* **2003,** *2*, 509.
9. *Future Trends in Microelectronics: The Nano Millennium* **2002**.
10. Binning, G.; Rohrer, H.; Gerber, C.; Weibel, E., *Phys. Rev. Lett.* **1982,** *49*, 57.
11. Whitesides, G. M., *Nat. Biotech.* **2003,** *21*, 1161.
12. Rao, C. N. R.; Cheetham, A. K., *J. Mater. Chem.* **2001,** *11*, 2887.
13. Nirmal, M.; Brus, L., *Acc. Chem. Res.* **1999,** *32*, 407.
14. Colvin, V. L.; Schlamp, M. C.; Alivisatos, A. P., *Nature* **1994,** *370*, 354.
15. Klein, D. L.; Roth, R.; Lim, A. K. L.; Alivisatos, A. P.; McEuen, P. L., *Nature* **1997,** *389*, 699.
16. Phillips, J., *J. Appl. Phys.* **2002,** *91*, 4590.
17. Shipway, A. N.; Katz, E.; Willner, I., *ChemPhysChem* **2000,** *1*, 18.
18. Klimov, V. I.; Mikhailovsky, A. A.; Xu, S.; Malko, A.; Hollingsworth, J. A.; Leatherdale, C. A.; Eisler, H. J.; Bawendi, M. G., *Science* **2000,** *314*, 290.
19. Gates, S. M., *Chem. Rev.* **1996,** *96*, 1519.
20. Kaiser, N., *Appl. Optics* **2002,** *41*, 3053.
21. Poortmans, J.; Arkhipov, V., *Thin film solar cells: fabrication, characterization and applications. Wiley* **2006**.

22. Xia, Y.; Yang, P.; Sun, Y.; Wu, Y.; Mayers, B.; Gates, B.; Yin, Y.; Kim, F.; Yan, H., *Adv. Mater*. **2003,** *15*, 353.

23. Ghosh, S.; Sood, A. K.; Kumar, N., *Science* **2003,** *299*, 1042.

24. Chen, J.; Chen, S.; Zhao, X.; Kuznetsova, L. V.; Wong, S. S.; Ojima, I., *J. Am. Chem. Soc.* **2008,** *130*, 16778.

25. Collins, P. G.; Zettl, A.; Bando, H.; Thess, A.; Smalley, R. E., *Science* **1997,** *278*, 100.

26. Gadd, G. E., *Science* **1997,** *277*, 933.

27. Dillon, A. C., *Nature* **1997,** *386*, 377.

28. Hu, J.; Odom, T. W.; Lieber, C. M., *Acc. Chem. Res.* **1999,** *32*, 435.

29. Wang, J.; Gudiksen, M. S.; Duan, X.; Cui, Y.; Lieber, C. M., *Science* **2001,** *293*, 1455.

30. Hurst, S. J.; Payne, E. K.; Qin, L.; Mirkin, C. A., *Angew. Chem. Int. Ed.* **2006,** *45*, 2672.

31. Nutzenadel, C.; Zuttel, A.; Chartouni, D.; Schmid, G.; Schlapbach, L., *Eur. Phys. J. D* **2000,** *8*, 245.

32. Schwarz, J. A.; Contescu, C.; Contescu, A., *Chem. Rev.* **1995,** *95*, 477.

33. Rossetti, R.; Nakahara, S.; Brus, L., *J. Chem. Phys.* **1983,** *79*, 1086.

34. Alivisatos, A. P., *Science* **1996,** *271*, 933.

35. Robertson, D. H.; Brenner, D. W.; Mintmire, J. W., *Phys. Rev. B* **1992,** *45*, 12592.

36. Menon, V. P.; Matin, C. R., *Anal. Chem.* **1995,** *67*, 1920.

37. Buffat, P.; Borel, J.-P., *Phys. Rev.* **1976,** *13*, 2287.

38. Wu, Y.; Yang, P., *Adv. Mater.* **2001,** *13*, 520.

39. Quere, D.; Meglio, J.-M. D.; Brochard-Wyart, F., *Science* **1990,** *249*, 1256.

40. Postma, H. W. C.; Peepen, T.; Yao, Z.; Grifoni, M.; Dekker, C., *Science* **2001,** *293*, 76.

41. Kong, J.; Franklin, N. R.; Zhou, C.; Chapline, M. G.; Peng, S.; Cho, K.; Dai, H., *Science* **2000,** *287*, 622.

42. Liu, X.; Lee, C.; Zhou, C.; Han, J., *Appl. Phys. Lett.* **2001,** *79*, 3329.

43. Collins, P. G.; Arnold, M. S.; Avouris, P., *Science* **2001,** *292*, 706.

44. Zhang, Z.; Sun, X.; Dresselhaus, M. S.; Ying, J. Y., *Phys. Rev. B* **2000,** *61*, 4850.

45. Huang, Y.; Duan, X.; Wei, Q.; Lieber, C. M., *Science* **2001,** *291*, 630.

46. Lu, X.; Hanrath, T.; Johnston, K. P.; Korgel, B. A., *Nano Lett.* **2003,** *3*, 93.

47. Wang, J. F.; Gudiksen, M. S.; Duan, X.; Cui, Y.; Lieber, C. M., *Science* **2001,** *293*, 1455.

48. Huynh, W. U.; Dittmer, J. J.; Alivisatos, A. P., *Science* **2002,** *295*, 2425.

49. El-Sayed, M. A., *Acc. Chem. Res.* **2001,** *34*, 257.

50. Zhou, X. T.; Lai, H. L.; Peng, H. Y.; Au, F. C. K.; Liao, L. S.; Wang, N.; Bello, I.; Lee, C. S.; Lee, S. T., *Chem. Phys. Lett.* **2000,** *318*, 58.

51. Lee, C. J.; Lee, T. J.; Lyu, S. C.; Zhang, Y.; Ruh, H.; Lee, H. J., *Appl. Phys. Lett.* **2002,** *81*, 3648.

52. Cui, Y.; Wei, Q.; Park, H.; Lieber, C. M., *Science* **2001,** *293*, 1289.

53. Wong, E. W.; Sheehan, P. E.; Lieber, C. M., *Science* **1997,** *277*, 1971.

54. Burda, C.; X., C.; Narayanan, R.; El-Sayed, M. A., *Chem. Rev.* **2005,** *105*, 1025.

55. Hashmi, A. S. K.; Hutchings, G. J., *Angew. Chem. Int. Ed.* **2006,** *45*, 7896.

56. Xia, Y.; Rogers, J. A.; Paul, K. E.; Whitesides, G. M., *Chem. Rev.* **1999,** *99*, 1823.

57. Haruta, M.; Delmon, B., *J. Chim. Phys. Phys.-Chim. Biol.* **1986,** *83*, 859.

58. Givargizov, E. I., *Highly Anisotropic Crystals. Reidel, Dordrecht, The Netherlands* **1987**.

59. Song, J. H.; Messer, B.; Wu, Y.; Kind, H.; Yang, P., *J. Am. Chem. Soc.* **2001,** *123*, 9714.

60. Tong, H.; Zhu, Y.-J.; Yang, L.-X.; Li, L.; Zhang, L., *Angew. Chem. Int. Ed.* **2006,** *45*, 7739.

61. Pan, Z. W.; Dai, Z. R.; Wang, Z. L., *Science* **2001,** *291*, 1947.

62. Parthasarathy, R. V.; Martin, C. R., *Nature* **1992,** *369*, 298.

63. Zhang, G.; Lu, X.; Zhang, T.; Qu, J.; Wang, W.; Li, X.; Yu, S., *Nanotech.* **2006,** *17*, 4252.

64. Puntes, V. F.; Krishnan, K. M.; Alivisatos, A. P., *Science* **2001,** *291*, 2115.

65. Park, K. H.; Jang, K.; Kim, S.; Son, S. U., *J. Am. Chem. Soc.* **2006,** *128*, 14780.

66. Wang, X.; Li, Y., *J. Am. Chem. Soc.* **2002,** *124*, 2880.

67. Heath, J. R.; Legoues, F. K., *Chem. Phys. Lett.* **1993,** *208*, 263.

68. Hench, L. L.; West, J. K., *Chem. Rev.* **1990,** *90*, 33.

69. Schwuger, M.; Stickdom, K.; Schomacker, R., *Chem. Rev.* **1995,** *95*, 849.

70. Yu, S.-H., *Handbook of nanostructured biomaterials and thier applications in nanobiotechnology* **2005**.

71. Kovtyukhova, N. I.; Kelly, B. K.; Mallouk, T. E., *J. Am. Chem. Soc.* **2004,** *126*, 12738.

72. Kovtyukhova, N. I.; Mallouk, T. E.; Mayer, T. S., *Adv. Mater.* **2003,** *15*, 780.

73. Mallouk, T. E., *Science* **2001,** *291*, 443.

74. Hulteen, J. C.; Martin, C. R., *J. Mater. Chem.* **1997,** *7*, 1075.

75. Schmid, G., *J. Mater. Chem.* **2002,** *12*, 1231.

76. Becker, A.; Becker, W.; Marxen, J. C.; Epple, M., *Z. Anorg. Allg. Chem.* **2003,** *629*, 2305.

77. Schwarz, K.; Epple, M., *Chem. Eur. J.* **1998,** *4*, 1898.

78. Grassmann, O.; Lobmann, P., *Biomaterials* **2004,** *25*, 277.

79. Lu, Q.; Gao, F.; Komarneni, S.; Mallouk, T. E., *J. Am. Chem. Soc.* **2004,** *126*, 8650.

80. Martin, C. R., *Science* **1994,** *266*, 1961.

81. Martin, C. R., *Chem. Mater.* **1996,** *8*, 1739.

82. Fleisher, R. L.; Price, P. B.; Walker, R. M., *Nuclear tracks in solids. University of California Press, Berkeley, CA* **1975**.

83. Cao, H.; Xu, Y.; Hong, J.; Liu, H.; Yin, G.; Li, B.; Tie, C.; Xu, Z., *Adv. Mater.* **2001,** *13*, 1393.

84. Gao, T.; Meng, G.; Zhang, J.; Sun, S.; Zhang, L., *Appl. Phys. A* **2002,** *74*, 403.

85. Lei, Y.; Zhang, L. D.; Meng, G. W.; Li, G. H.; Zhang, X. Y.; Liang, C. H.; Chen, W.; Wang, S. X., *Appl. Phys. Lett.* **2001,** *78*, 1125.

86. Sapp, S. A.; Mitchell, D. T.; Martin, C. R., *Chem. Mater.* **1999,** *26*, 3264.

87. Martin, C. R., *Acc. Chem. Res.* **1995,** *28*, 61.

88. Lakshmi, B. B.; Dorhout, P. K.; Martin, C. R., *Chem. Mater.* **1997,** *9*, 857.

89. Limmer, S. J.; Seraji, S.; Wu, Y.; Chou, T. P.; Nguyen, C.; Cao, G. Z., *Adv. Funct. Mater.* **2002,** *12*, 59.

Chapter II

1. Gao, P.; Xie, Y.; Li, Z., *eur. J. Inorg. Chem.* **2006**, 3261.

2. Bender, C. M.; Burlitch, J. M.; Barber, D.; Pollock, C., *Chem. Mater.* **2000,** *12*, 1969.

3. Lian, H.; Liu, J.; Ye, Z.; Shi, C., *Chem. Phys. Lett.* **2004,** *386*, 291.

4. Singh, R.; Sinha, S.; Chou, P.; Hsu, N. J.; Radpour, F., *J. Appl. Phys.* **1989,** *66*, 6179.

5. Hua, R.; Zang, C.; Shao, C.; Xie, D.; Shi, C., *Nanotechnology* **2003,** *14*, 588.

6. Johnson, L. F.; Guggenheim, H. J., *Appl. Phys. Lett.* **1971,** *19*, 44.

7. Zhang, X. X.; Hong, P.; Bass, M.; Chai, B. H. T., *Phys. Rev. B* **1995,** *51*, 9298.

8. Xie, P.; Rand, S. C., *Opt. Lett.* **1992,** *17*, 1198.

9. Cao, M.; Hu, C.; Wang, E., *J. Am. Chem. Soc.* **2003,** *125*, 11196.

10. Cao, M.; Wang, Y.; Qi, Y.; Guo, C.; Hu, C., *J. Solid State Chem.* **2004,** *177*, 2205.

11. De, G.; Qin, W.; Zhang, J.; Zhao, D.; Zhang, J., *Chem. Lett.* **2005,** *34*, 914.

12. Xia, Y.; Yang, P.; Sun, Y.; Wu, Y.; Mayers, B.; Gates, B.; Yin, Y.; Kim, F.; Yan, H., *Adv. Mater.* **2003,** *15*, 353.

13. Sun, X.; Li, Y., *Chem. Commun.* **2003**, 1768.

14. Grass, R. N.; Stark, W. J., *Chem. Commun.* **2005**, 1767.

15. Wang, F.; Fan, X.; Pi, D.; Wang, M., *Solid State Commun* **2005,** *133*, 775.

16. Laguna, M. A.; Sanuan, M. L.; Orera, V. M.; Rubin, J.; Palacios, E.; Pique, M. C.; Bartolome, J.; Berar, J. F., *J. Phys.: Condens. Matter.* **1993,** *5*, 283.

17. Pilla, O.; Freire, P. T. C.; Lemos, V., *Phys. Rev. B* **1995,** *52*, 177.

18. Zhao, C.; Feng, S.; Xu, R.; Shi, C.; Ni, J., *Chem. Commun.* **1997**, 945.

19. Bartolome, J.; Burriel, R.; Palacio, F.; Gonzalez, D.; Navarro, R.; Rojo, J. A.; De Jongh, J., *Physica B* **1983,** *115*, 190.

20. Roth, M.; Hempelmann, R., *Chem. Mater.* **1998,** *10*, 78.

21. Lu, L.; Wang, H.; Zhang, H.; Xi, S., *Chem. Commun.* **2001**, 1342.

22. Agnoli, F.; Zhou, W. L.; O'Connor, C. J., *Adv. Mater.* **2001,** *13*, 1697.

23. Tang, Q.; Shen, J.; Zhou, W.; Liu, J.; Liu, Z.; Qian, Y., *Inorg. Chem. Commun.* **2004,** *7*, 283.

24. Kumar, A.; Whitesides, G. M., *Appl. Phys. Lett.* **1993,** *63*, 2002.

25. Pi, D.; Wang, F.; Fan, X.; Wang, M.; Zhang, Y., *Spectrochim. Acta Part A* **2005,** *61*, 2455.

26. Cannas, C.; Casu, M.; Mainas, M.; Musinu, A.; Piccaluga, G.; Polizzi, S.; Speghini, A.; Bettinelli, M., *J. Mater. Chem.* **2003,** *13*, 3079.

27. Pivin, J. C.; Gaponenko, N. V.; Molchan, I.; Kudrawiec, R.; Misiewicz, J.; Bryja, L.; Thompson, G. E.; Skeldon, P., *J. Alloys Compd.* **2002,** *341*, 272.

28. Liu, P.; Liang, D.; Tong, Z.; Liu, X., *Macromolecules* **2002,** *35*, 1487.

29. O'Connor, C. J.; Kolesnichenko, V.; Carpenter, E.; Sangregorio, C.; Zhou, W.; Kumbhar, A.; Sims, J.; Agnoli, F., *Synth. Met.* **2001,** *122*, 547.

30. Hirakawa, K.; Hashimoto, T., *J. Phys. Soc. Jpn.* **1960,** *15*, 2063.

31. Heeger, A. J.; Beckman, O.; Portis, A. M., *Phys. Rev.* **1961,** *123*, 1652.

32. Pickart, S. J.; Alperin, H. A.; Nathans, R., *J. Phys.* **1964,** *25*, 565.

33. Shionoya, S.; Hirano, M., *Phys. Lett.* **1968,** *26A*, 533.

34. Martin, C. R.; Van Dyke, L. S.; Cai, Z.; Liang, W., *J. Am. Chem. Soc.* **1990,** *112*, 8976.

Chapter III

1. Saito, N.; Sonoyama, N.; Sakata, T., *Bull. Chem. Soc. Japan* **1996,** *69*, 2191.

2. Liao, H.-W.; Wang, Y.-F.; Liu, X.-M.; Li, Y.-D.; Qian, Y.-T., *Chem. Mater.* **2000,** *12*, 2819.

3. Kloprogge, J. T.; Weier, M. L.; Duong, L. V.; Frost, R. L., *Mater. Chem. Phys.* **2004,** *88*, 438.

4. Wang, H.; Medina, F. D.; Zhou, Y. D.; Zhang, Q. N., *Phys. Rev. B* **1992,** *45*, 10356.

5. Nagirnyi, V.; Feldbach, E.; Jönsson, L.; Kirm, M.; Lushchik, A.; Lushchik, C.; Nagornaya, L. L.; Ryzhikov, V. D.; Savikhin, F.; Svensson, G.; Tupitsina, I. A., *Radiat. Mes.* **1998,** *29*, 247.

6. Park, I.-H.; Kim, B.-S.; Kim, K.-Y.; Kim, B.-H., *Jpn. J. Appl. Phys.* **2001,** *40*, 4956.

7. Li, L.; Su, Y.; Li, G., *Appl. Phys. Lett.* **2007,** *90*, 054105.

8. Zhang, Q.; Yao, W.-T.; Chen, X.; Zhu, L.; Fu, Y.; Zhang, G.; Sheng, L.; Yu, S.-H., *Crystal Growth & Design* **2007,** *7*, 1423.

9. Nitsch, K.; Nikl, M.; Ganschow, S.; Reiche, P.; Uecker, R., *J. Cryst. Growth* **1996,** *165*, 163.

10. Kaminskii, A. A.; Eichler, H. J.; Ueda, K.-I.; Klassen, N. V.; Redkin, B. S.; Li, L. E.; Findeisen, J.; Jaque, D.; García-Sole, J.; Fernández, J.; Balda, R., *Appl. Optics* **1999,** *38*, 4533.

11. Treadaway, M. J.; Powell, R. C., *Phys. Rev. B* **1975,** *11*, 862.

12. Martini, M.; Meinardi, F.; Spinolo, G.; Vedda, A.; M., N.; Usuki, Y., *Phys. Rev. B* **1999,** *60*, 4653.

13. Cho, W.-S.; Yashima, M.; Kakihana, M.; Kudo, A.; Sakata, T.; Yoshimura, M., *Appl. Phys. Lett.* **1995,** *66*, 1027.

14. Yu, S.-H.; Liu, B.; Mo, M.-S.; Huang, J.-H.; Liu, X.-M.; Qian, Y.-T., *Adv. Funct. Mater.* **2003,** *13*, 639.

15. Pode, R. B.; Dhoble, S. J., *Phys. Stat. Sol. B* **1997,** *203*, 571.

16. Kobayashi, M.; Usukib, Y.; Ishiic, M.; Yazawac, T.; Harad, K.; Tanakad, M.; Nikle, M.; Nitsch, K., *Nucl. Instrum. Methods Phys. Res. A* **1997,** *399*, 261.

17. Murk, V.; Nikl, M.; Mihokova, E.; Nitsch, K., *J. Phys.: Condens. Matter* **1997,** *9*, 249.

18. Errandonea, D.; Somayazulu, M.; Häusermann, D., *Phys. Stat. Sol. B* **2003,** *235*, 162.

19. Sun, L.; Guo, Q.; Wu, X.; Luo, S.; Pan, W.; Huang, K.; Lu, J.; Ren, L.; Cao, M.; Hu, C., *J. Phys. Chem. C* **2007,** *111*, 532.

20. Tarte, P.; Liegeois-Duyckaerts, N., *Spectrochim. Acta Part A* **1972,** *28*, 2029.

21. Liegeois-Duyckaerts, N.; Tarte, P., *Spectrochim. Acta Part A* **1972,** *28*, 2037.

22. Tsuji, I.; Kato, H.; Kobayashi, H.; Kudo, A., *J. Am. Chem. Soc.* **2004,** *126*, 13406.

23. Torimoto, T.; Adachi, T.; Okazaki, K.; Sakuraoka, M.; Shibayama, T.; Ohtani, B.; Kudo, A.; Kuwabata, S., *J. Am. Chem. Soc.* **2007,** *129*, 12388.

24. Tsuji, I.; Kato, H.; Kudo, A., *Chem. Mater.* **2006,** *18*, 1969.

25. Inumaru, K.; Koyama, K.; Miyaki, Y.; Tanaka, K.; Yamanaka, S., *Appl. Phys. Lett.* **2007,** *91*, 152501.

26. Muktha, B.; Simon, A.; Darriet, J.; Guru Row, T. N., *Chem. Mater.* **2006,** *18*, 1240.

27. McKinlay, A.; Connor, P.; Irvine, J. T. S.; Zhou, W., *J. Phys. Chem. C.* **2007,** *111*, 19120.

28. Kolen'ko, Y. V.; Kovnir, K. A.; Gavrilov, A. I.; Garshev, A. V.; Meskin, P. E.; Churagulov, B. R.; Bouchard, M.; Colbeau-Justin, C.; Lebedev, O. I.; Van Tendeloo, G.; Yoshimura, M., *J. Phys. Chem. B* **2005,** *109*, 20303.

29. Hu, Q. M.; Kádas, K.; Hogmark, S.; Yang, R.; Johansson, B.; Vitos, L., *Appl. Phys. Lett.* **2007,** *91*, 121918.

30. Varshney, D.; Kaurav, N.; Kinge, R.; Singh, R. K., *J. Phys.: Condens. Matter* **2007,** *19*, 346212.

31. Fernandez-Gonzalez, A.; Andara, A. P., M., *Crystal Growth & Design* **2007,** *7*, 545.

32. Cho, W.-S.; Yashima, M.; Kakihana, M.; Kudo, A.; Sakata, T.; Yoshimura, M., *Appl. Phys. Lett.* **1996,** *68*, 137.

33. Cho, W.-S.; Yoshimura, M., *Jpn. J. Appl. Phys.* **1997,** *36*, 5658.

34. Wang, Z. L.; Song, J., *Science* **2006,** *312*, 242.

35. Ge, J.; Hu, Y.; Yin, Y., *Angew. Chem. Int. Ed.* **2007,** *46*, 7428.

36. Kovalenko, M. V.; Bodnarchuk, M. I.; Lechner, R. T.; Hesser, G.; Schäffler, F.; Heiss, W., *J. Am. Chem. Soc.* **2007,** *129*, 6352.

37. Xia, Y.; Yang, P.; Sun, Y.; Wu, Y.; Mayers, B.; Gates, B.; Yin, Y.; Kim, F.; Yan, H., *Adv. Mater.* **2003,** *15*, 353.

38. Rutherglen, C.; Burke, P., *Nano. Lett.* **2007,** *7*, 3296.

39. Ma, R.-M.; Dai, L.; Huo, H.-B.; Xu, W.-J.; Qin, G. G., *Nano. Lett.* **2007,** *7*, 3300.

40. Su, Y.; Li, G.; Xue, Y.; Li, L., *J. Phys. Chem. C* **2007,** *111*, 6684.

41. Wang, Y.; Ma, J.; Tao, J.; Zhu, X.; Zhou, J.; Zhao, Z.; Xie, L.; Tian, H., *Mater. Lett.* **2006,** *60*, 291.

42. Li, D.; Wu, H.; Li, Z.; Cong, X.; Sun, J.; Ren, Z.; Liu, L.; Li, Y.; Fan, D.; Hao, J., *Colloids Surf., A* **2006,** *274*, 18.

43. Chen, S.-J.; Li, J.; Chen, X.-T.; Hong, J.-M.; Xue, Z.; You, X.-Z., *J. Cryst. Growth* **2003,** *253*, 361.

44. Sun, L.; Cao, M.; Wang, Y.; Sun, G.; Hu, C., *J. Cryst. Growth* **2006,** *289*, 231.

45. Kwan, S.; Kim, F.; Akana, J.; Yang, P., *Chem. Commun.* **2001**, 447.

46. Kim, F.; Kwan, S.; Akana, J.; Yang, P., *J. Am. Chem. Soc.* **2001,** *123*, 4360.

47. Shi, H.; Qi, L.; Ma, J.; Cheng, H., *Chem. Commun.* **2002**, 1704.

48. Shi, H.; Qi, L.; Ma, J.; Cheng, H.; Zhu, B., *Adv. Mater.* **2003,** *15*, 1647.

49. Zhang, C.; Shen, E.; Wang, E.; Kang, Z.; Gao, L.; Hu, C.; Xu, L., *Mater. Chem. Phys.* **2006,** *96*, 240.

50. Shi, H.; Qi, L.; Ma, J.; Cheng, H., *J. Am. Chem. Soc.* **2003,** *125*, 3450.

51. Cho, W.-S.; Yoshimura, M., *J. Am. Ceram. Soc.* **1996,** *79*, 2783.

52. Mao, Y.; Wong, S. S., *J. Am. Chem. Soc.* **2004,** *126*, 15245.

53. Atuchin, V. V.; Kesler, V. G.; Maklakova, N. Y.; Pokrovsky, L. D.; Sheglov, D. V., *Eur. Phys. J. B* **2006,** *51*, 293.

54. Itoh, M.; Fujita, N.; Inabe, Y., *J. Phys. Soc. Jpn.* **2006,** *75*, 084705.

55. Ling, Z. C.; Xia, H. R.; Ran, D. G.; Liu, F. Q.; Sun, S. Q.; Fan, J. D.; Zhang, H. J.; Wang, J. Y.; Yu, L. L., *Chem. Phys. Lett.* **2006,** *426*, 85.

56. Zhang, G.; Jia, R.; Wu, Q., *Mater. Sci. Eng. B* **2006,** *128*, 254.

57. Ryu, J. H.; Yoon, J.-W.; Shim, K. B., *Electrochem. Solid-State. Lett.* **2005,** *8*, D15.

58. Orhan, E.; Anicete-Santos, M.; Maurera, M. A. M. A.; Pontes, F. M.; Paiva-Santos, C. O.; Souza, A. G.; Varela, J. A.; Pizani, P. S.; Longo, E., *Chem. Phys.* **2005,** *312*, 1.

59. Oaki, Y.; Imai, H., *Adv. Mater.* **2006,** *18*, 1807.

60. Nikl, M.; Bohacek, P.; Mihokova, E.; Kobayashi, M.; Ishii, M.; Usuki, Y.; Babin, V.; Stolovich, A.; Zazubovich, S.; Bacci, M., *J. Lumin.* **2000,** *87-89*, 1136.

61. Al-Suleiman, M.; Che Mofor, A.; El-Shaer, A.; Bakin, A.; Wehmann, H.-H.; Waag, A., *Appl. Phys. Lett.* **2006,** *89*, 231911.

62. Cheng, B.; Guo, H.; Yu, J.; Zhao, X., *J. Alloys Compd.* **2007,** *431*, L4.

63. Willis, A. L.; Turro, N. J.; O'Brien, S., *Chem. Mater.* **2005,** *17*, 5970.

64. Zhang, T.; Ge, J.; Hu, Y.; Yin, Y., *Nano Lett.* **2007,** *7*, 3203.

65. Wang, L.; Li, Y., *Nano Lett.* **2006,** *6*, 1645.

66. Zhang, Q.; Russell, T. P.; Emrick, T., *Chem. Mater.* **2007,** *19*, 3712.

67. Zhang, Y.; Guo, J.; White, T.; Tan, T. T. Y.; Xu, R., *J. Phys. Chem. C* **2007,** *111*, 7893.

68. Lu, S. W.; Lee, B. I.; Wang, Z. L.; Tong, W.; Wagner, B. K.; Park, W.; Summers, C. J., *J. Lumin.* **2001,** *92*, 73.

69. Polak, K.; Nikl, M.; Nitsch, K.; Kobayashi, M.; Ishii, M.; Usuki, Y.; Jarolimek, O., *J. Lumin.* **1997,** *72-74*, 781.

70. Grasser, R.; Scharmann, A., *J. Lumin.* **1976,** *12/13*, 473.

71. Grasser, R.; Scharmann, A.; Strack, K.-R., *J. Lumin.* **1982,** *27*, 263.

72. Toyozawa, Y.; Inoue, M., *J. Phys. Soc. Jpn.* **1966,** *21*, 1663.

73. Cho, W.-S.; Yoshimura, M., *J. Appl. Phys.* **1998,** *83*, 518.

74. Siebentritt, S.; Schuler, S., *J. Phys. Chem. Solids* **2003,** *64*, 1621.

75. Xue, C.; Papadimitriou, D.; Esser, N., *J. Phys. D: Appl. Phys.* **2004,** *37*, 2267.

76. Kuno, M.; Higginson, K. A.; Qadri, S. B.; Yousuf, M.; Lee, S. H.; Davis, B. L.; Mattoussi, H., *J. Phys. Chem. B* **2003,** *107*, 5758.

77. Wang, Y.; Hou, Y.; Tang, A.; Feng, B.; Li, Y.; Liu, J.; Teng, F., *J. Cryst. Growth* **2007,** *308*, 19.

78. Zhao, K.; Li, J.; Wang, H.; Zhuang, J.; Yang, W., *J. Phys. Chem. C* **2007,** *111*, 5618.

79. Beard, G. B.; Kelly, W. H.; Mallory, M. L., *J. Appl. Phys.* **1962,** *33*, 144.

80. Born, G.; Hofstaetter, A.; Scharmann, A.; Schwarz, G., *J. Lumin.* **1970,** *1/2*, 641.

81. Mikhailik, V. B.; Kraus, H.; Wahl, D.; Itoh, M.; Koike, M.; Bailiff, I. K., *Phys. Rev. B* **2004,** *69*, 205110.

82. de Mello Donegá, C.; Hickey, S. G.; Wuister, S. F.; Vanmaekelbergh, D.; Meijerink, A., *J. Phys. Chem. B* **2003,** *107*, 489.

83. Lee, H.; Holloway, P. H.; Yang, H.; Hardison, L.; Kleiman, V. D., *J. Chem. Phys.* **2006,** *125*, 164711.

84. Wehrenberg, B. L.; Wang, C.; Guyot-Sionnest, P., *J. Phys. Chem. B* **2002,** *106*, 10634.

85. Zhang, X. L.; Qiao, R.; Qiu, R.; Li, Y.; Kang, Y. S., *J. Phys. Chem. A* **2007,** *111*, 4195.

86. Jun, Y.-W.; Jung, Y.-Y.; Cheon, J., *J. Am. Chem. Soc.* **2002,** *124*, 615.

87. Na, C. W.; Han, D. S.; Kim, D. S.; Kang, Y. J.; Lee, J. Y.; Park, J.; Oh, D. K.; Kim, K. S.; Kim, D., *J. Phys. Chem. B* **2006,** *110*, 6699.

88. Ando, K., *Science* **2006,** *312*, 1883.

Chapter IV

1. Kim, J. S.; Rieter, W. J.; Taylor, K. M. L.; An, H.; Lin, W.; Lin, W., *J. Am. Chem. Soc.* **2007,** *129*, 8962.

2. Giri, S.; Trewyn, B. G.; Stellmaker, M. P.; Lin, V. S.-Y., *Angew. Chem. Int. Ed.* **2005,** *44*, 5038.

3. Lin, Y.-S.; Wu, S.-H.; Hung, Y.; Chou, Y.-H.; Chang, C.; Lin, M.-L.; Tsai, C.-P.; Mou, C.-Y., *Chem. Mater.* **2006,** *18*, 5170.

4. Santra, S.; Yang, H.; Holloway, P. H.; Stanley, J. T.; Mericle, R. A., *J. Am. Chem. Soc.* **2005,** *127*, 1656.

5. Nasongkla, N.; Bey, E.; Ren, J.; Ai, H.; Khemtong, C.; Guthi, J. S.; Chin, S.-F.; Sherry, A. D.; Boothman, D. A.; Gao, J., *Nano Lett.* **2006,** *6*, 2427.

6. Bao, J.; Chen, W.; Liu, T.; Zhu, Y.; Jin, P.; Wang, L.; Liu, J.; Wei, Y.; Li, Y., *ACS Nano* **2007,** *1*, 293.

7. Wei, C.; Dai, L.; Roy, A.; Tolle, T. B., *J. Am. Chem. Soc.* **2006,** *128*, 1412.

8. Sankapal, B. R.; Setyowati, K.; Chen, J.; Liu, H., *Appl. Phys. Lett.* **2007,** *91*, 173103.

9. Peng, H., *J. Am. Chem. Soc.* **2008,** *130*, 42.

10. Shim, B. S.; Tang, Z.; Morabito, M. P.; Agarwal, A.; Hong, H.; Kotov, N. A., *Chem. Mater.* **2007,** *19*, 5467.

11. Ohno, H., *Science* **1998,** *281*, 951.

12. Ando, K., *Science* **2006,** *312*, 1883.

13. Ohno, H.; Chiba, D.; Matsukura, F.; Omiya, T.; Abe, E.; Dietl, T.; Ohno, Y.; Ohtani, K., *Nature* **2000,** *408*, 944.

14. Ohno, Y.; Young, D. K.; Beschoten, B.; Matsukura, F.; Ohno, H.; Awschalom, D. D., *Nature* **1999,** *402*, 790.

15. Liao, H.-W.; Wang, Y.-F.; Liu, X.-M.; Li, Y.-D.; Qian, Y.-T., *Chem. Mater.* **2000,** *12*, 2819.

16. Wang, H.; Medina, F. D.; Zhou, Y. D.; Zhang, Q. N., *Phys. Rev. B* **1992,** *45*, 10356.

17. Li, L.; Su, Y.; Li, G., *Appl. Phys. Lett.* **2007,** *90*, 054105.

18. Yu, S.-H.; Liu, B.; Mo, M.-S.; Huang, J.-H.; Liu, X.-M.; Qian, Y.-T., *Adv. Funct. Mater.* **2003,** *13*, 639.

19. Yu, S.-H.; Antonietti, M.; Cölfen, H.; Giersig, M., *Angew. Chem. Int. Ed.* **2002,** *41*, 2356.

20. Liu, B.; Yu, S.-H.; Li, L.; Zhang, Q.; Zhang, F.; Jiang, K., *Angew. Chem. Int. Ed.* **2004,** *43*, 4745.

21. Kaminskii, A. A.; Eichler, H. J.; Ueda, K.-I.; Klassen, N. V.; Redkin, B. S.; Li, L. E.; Findeisen, J.; Jaque, D.; García-Sole, J.; Fernández, J.; Balda, R., *Appl. Optics* **1999,** *38*, 4533.

22. Zhang, Q.; Yao, W.-T.; Chen, X.; Zhu, L.; Fu, Y.; Zhang, G.; Sheng, L.; Yu, S.-H., *Crystal Growth & Design* **2007,** *7*, 1423.

23. Sun, L.; Guo, Q.; Wu, X.; Luo, S.; Pan, W.; Huang, K.; Lu, J.; Ren, L.; Cao, M.; Hu, C., *J. Phys. Chem. C* **2007,** *111*, 532.

24. Cho, W.-S.; Yashima, M.; Kakihana, M.; Kudo, A.; Sakata, T.; Yoshimura, M., *Appl. Phys. Lett.* **1995,** *66*, 1027.

25. Taniguchi, K.; Abe, N.; Takenobu, T.; Iwasa, Y.; Arima, T., *Phys. Rev. Lett.* **2006,** *97*, 097203.

26. Arkenbout, A. H.; Palstra, T. T. M.; Siegrist, T.; Kimura, T., *Phys. Rev. B* **2006,** *74*, 184431.

27. Lautenschläger, G.; Weitzel, H.; Vogt, T.; Hock, R.; Böhm, A.; Bonnet, M.; Fuess, H., *Phys. Rev. B* **1993,** *48*, 6087.

28. Ehrenberg, H.; Weitzel, H.; Heid, C.; Fuess, H.; Wltschek, G.; Kroener, T.; Tol, J. v.; Bonnet, M., *J. Phys.: Condens. Matter* **1997,** *9*, 3189.

29. Heyer, O.; Hollmann, N.; I. Klassen, I.; Jodlauk, S.; Bohatý, L.; Becker, P.; Mydosh, J. A.; Lorenz, T.; Khomskii, D., *J. Phys.: Condens. Matter* **2006,** *18*, L471.

30. Bode, M.; Vedmedenko, E. Y.; Von Bergmann, K.; Kubetza, A.; Ferriani, P.; Heinze, S.; Wiesendanger, R., *Nat. Mater.* **2006,** *5*, 477.

31. Meiklejohn, M. H.; Bean, C. P., *Phys. Rev.* **1956,** *102*, 1413.

32. Ramesh, R.; Spaldin, N. A., *Nat. Mater.* **2007,** *6*, 21.

33. Bleijenberg, K. C.; De Wit, H. G. M., *J. C. S. Faraday II* **1980,** *76*, 872.

34. Doroshenko, M. E.; Basiev, T. T.; Vassiliev, S. V.; Ivleva, L. I.; Komar, V. K.; Kosmyna, M. B.; Jelinkova, H.; Sulc, J., *Opt. Mater.* **2007,** *30*, 54.

35. Kuleshov, N. V.; Lagatsky, A. A.; Shcherbitsky, V. G.; Mikhailov, V. P.; Heumann, E.; Jensen, T.; Diening, A.; Huber, G., *Appl. Phys. B* **1997,** *64*, 409.

36. Treadaway, M. J.; Powell, R. C., *Phys. Rev. B* **1975,** *11*, 862.

37. Xia, Y.; Yang, P.; Sun, Y.; Wu, Y.; Mayers, B.; Gates, B.; Yin, Y.; Kim, F.; Yan, H., *Adv. Mater.* **2003,** *15*, 353.

38. Rutherglen, C.; Burke, P., *Nano Lett.* **2007,** *7*, 3296.

39. Ma, R.-M.; Dai, L.; Huo, H.-B.; Xu, W.-J.; Qin, G. G., *Nano Lett.* **2007,** *7*, 3300.

40. Puntes, V. F.; Krishnan, K. M.; Alivisatos, A. P., *Science* **2001,** *291*, 2115.

41. Peng, W. Q.; Qu, S. C.; Cong, G. W.; Wang, Z. G., *J. Cryst. Growth* **2005,** *279*, 454.

42. Na, C. W.; Han, D. S.; Kim, D. S.; Kang, Y. J.; Lee, J. Y.; Park, J.; Oh, D. K.; Kim, K. S.; Kim, D., *J. Phys. Chem. B* **2006,** *110*, 6699.

43. Wang, Y. S.; Thomas, P. J.; O'Brien, P., *J. Phys. Chem. B* **2006,** *110*, 21412.

44. Ejima, T.; Banse, T.; Takatsuka, H.; Kondo, Y.; Ishino, M.; Kimura, N.; Watanabe, M.; Matsubara, I., *J. Lumin.* **2006,** *119-120*, 59.

45. Huffman, D. R.; Wild, R. L.; Shinmei, M., *J. Chem. Phys.* **1969,** *50*, 4092.

46. Holmes, O. G.; McClure, D. S., *J. Chem. Phys.* **1957,** *26*, 1686.

47. Cho, W.-S.; Yashima, M.; Kakihana, M.; Kudo, A.; Sakata, T.; Yoshimura, M., *Appl. Phys. Lett.* **1996,** *68*, 137.

48. Grasser, R.; Scharmann, A., *J. Lumin.* **1976,** *12/13*, 473.

49. Grasser, R.; Scharmann, A.; Strack, K.-R., *J. Lumin.* **1982,** *27*, 263.

50. Polak, K.; Nikl, M.; Nitsch, K.; Kobayashi, M.; Ishii, M.; Usuki, Y.; Jarolimek, O., *J. Lumin.* **1997,** *72-74*, 781.

51. Nikl, M.; Bohacek, P.; Mihokova, E.; Ishii, M.; Usuki, Y.; Babin, V.; Stolovich, A.; Zazubovich, S.; Bacci, M., *J. Lumin.* **2000,** *87-89*, 1136.

52. Toyozawa, Y.; Inoue, M., *J. Phys. Soc. Jpn.* **1966,** *21*, 1663.

53. Ryu, J. H.; Yoon, J.-W.; Shim, K. B., *Electrochem. Solid-State Lett.* **2005,** *8*, D15.

54. Yang, H.; Holloway, P. H.; Ratna, B. B., *J. Appl. Phys.* **2003,** *93*, 586.

55. Roy, V. A. L.; Djurišić, A. B.; Liu, H.; Zhang, X. X.; Leung, Y. H.; Xie, M. H.; Gao, J.; Lui, H. F.; Surya, C., *Appl. Phys. Lett.* **2004,** *84*, 756.

56. Dabbousi, B. O.; Rodriguez-Viejo, J.; Mikulec, F. V.; Heine, J. R.; Mattoussi, H.; Ober, R.; Jensen, K. F.; Bawendi, M. G., *J. Phys. Chem. B* **1997,** *101*, 9463.

57. Larson, D. R.; Zipfel, W. R.; Williams, R. M.; Clark, S. W.; Bruchez, M. P.; Wise, F. W.; Webb, W. W., *Science* **2003,** *300*, 1434.

58. Chen, W.; Sammynaiken, R.; Huang, Y.; Malm, J.-O.; Wallenberg, R.; Bovin, J.-O.; Zwiller, V.; Kotov, N. A., *J. Appl. Phys.* **2001,** *89*, 1120.

59. Lu, S. W.; Lee, B. I.; Wang, Z. L.; Tong, W.; Wagner, B. K.; Park, W.; Summers, C. J., *J. Lumin.* **2001,** *92*, 73.

60. Xia, B.; Lenggoro, I. W.; Okuyama, K., *Chem. Mater.* **2002,** *14*, 4969.

61. Kim, J. S.; Kim, J. S.; Kim, T. W.; Kim, S. M.; Park, H. J., *Appl. Phys. Lett.* **2005,** *86*, 091912.

62. Son, D.; Jung, D.-R.; Kim, J.; Moon, T.; Kim, C.; Park, B., *Appl. Phys. Lett.* **2007,** *90*, 101910.

63. Cho, W.-S.; Yoshimura, M., *Jpn. J. Appl. Phys.* **1997,** *36*, 5658.

64. Gan, L. M.; Liu, B.; Chew, C. H.; Xu, S. J.; Chua, S. J.; Loy, G. L.; Xu, G. Q., *Langmuir* **1997,** *13*, 6427.

65. Counio, G.; Gacoin, T.; Boilot, J. P., *J. Phys. Chem. B* **1998,** *102*, 5257.

66. Biswas, S.; Kar, S.; Chaudhuri, S., *J. PHys. Chem. B* **2005,** *109*, 17526.

67. Zhou, H.; Yiu, Y.; Aronson, M. C.; Wong, S. S., *J. Solid State Chem.* **2008,** *181*, 1539.

Chapter V

1. Xia, Y.; Yang, P.; Sun, Y.; Wu, Y.; Mayers, B.; Gates, B.; Yin, Y.; Kim, F.; Yan, H., *Adv. Mater.* **2003,** *15*, 353-389.

2. Brus, L. E., *J. Phys. Chem.* **1986,** *90*, 2555.

3. Alivisatos, A. P., *Science* **1996,** *271*, 933.

4. Fox, M. A.; Dulay, M. T., *Chem. Rev.* **1993,** *93*, 341.

5. Kamat, P. V., *Chem. Rev.* **1993,** *93*, 267.

6. Hoffman, M. R.; Martin, S. T.; Choi, W.; Bahnemann, D. W., *Chem. Rev.* **1995,** *95*, 69.

7. Wang, X.; Xu, C.; Zhang, Z., *Mater. Lett.* **2006,** *60*, 345-348.

8. Liang, W.; Whangbo, M.-H., *Solid State Commun.* **1993,** *85*, 405-408.

9. Mane, R. S.; Lokhande, C. D., *Mater. Chem. Phys.* **2000,** *65*, 1-31.

10. Janata, J.; Josowicz, M.; DeVaney, D. M., *Anal. Chem.* **1994,** *66*, 207-228.

11. Liao, X.-H.; Chen, N.-Y.; Xu, S.; Yang, S.-B.; Zhu, J.-J., *J. Cryst. Growth* **2003,** *252*, 593-598.

12. Blachnik, R.; Müller, A., *Thermochim. Acta* **2000,** *361*, 31-52.

13. Zhang, W.; Wen, X.; Yan, S., *Langmuir* **2003,** *19*, 4420-4426.

14. Chung, J.-S.; Sohn, H.-J., *J. Power Sources* **2002,** *108*, 226-231.

15. Henglein, A., *Chem. Rev.* **1989,** *89*, 1861-1873.

16. Barrelet, C. J.; Wu, Y.; Bell, D. C.; Lieber, C. M., *J. Am. Chem. Soc* **2003,** *125*, 11498-11499.

17. Bao, N.; Shen, L.; Takata, T.; Domen, K.; Gupta, A.; Yanagisawa, K.; Grimes, C. A., *J. Phys. Chem. C* **2007,** *111*, 17527-17534.

18. Britt, J.; Ferekides, C., *Appl. Phys. Lett.* **1993,** *62*, 2851-2852.

19. Morales, A. M.; Lieber, C. M., *Science* **1998,** *279*, 208-211.

20. Wang, Z. L., *Adv. Mater.* **2000,** *12*, 1295-1298.

21. Tsai, C. T.; S., C. D.; Chen, G. L.; Yang, S. L., *J. Appl. Phys.* **1996,** *79*, 9105-9109.

22. Berman, A.; Charych, D., *Adv. Mater.* **1999,** *11*, 296-300.

23. Lin, Y.-F.; Song, J.; Ding, Y.; Lu, S.-Y.; Wang, Z. L., *Adv. Mater.* **2008,** *20*, 3127-3130.

24. Lin, Y.-F.; Song, J.; Ding, Y.; Lu, S.-Y.; Wang, Z. L., *Appl. Phys. Lett.* **2008,** *92*, 022105-022107.

25. Peterson, J. J.; Krauss, T. D., *Nano Lett.* **2006,** *6*, 510-514.

26. Gadenne, P.; Yagil, Y.; Deutscher, G., *J. Appl. Phys.* **1989,** *66*, 3019-3025.

27. McDonald, S. A.; Konstantatos, G.; Zhang, S.; Cyr, P. W.; Klem, E. J. D.; Levina, L.; Sargent, E. H., *Nat. Mater.* **2005,** *4*, 138-142.

28. Bakueva, L.; Konstantatos, G.; Levina, L.; Musilkin, S.; Sargent, E. H., *Appl. Phys. Lett.* **2004,** *84*, 3459-3461.

29. Banerjee, R.; Jayakrishnan, R.; Ayyub, P., *J. Phys. -Condens. Mater.* **2000,** *12*, 10647-10654.

30. Wang, Z.; Zhao, B.; Zhang, F.; Mao, W.; Qian, G.; Fan, X., *Mater. Lett.* **2007,** *61*, 3733-3735.

31. Hirata, H.; Higashiayama, K., *Bull. Chem. Soc. Jpn.* **1971,** *44*, 2420-2423.

32. Plass, R.; Pelet, S.; Krueger, J.; Grätzel, M.; Bach, U., *J. Phys. Chem. B* **2002,** *106*, 7578-7580.

33. Warner, J. H.; R., W. A. A.; Tilley, R. D., *Nanotechnology* **2005,** *16* (2381-2384).

34. Sun, J.; Buhro, W. E., *Angew. Chem. Int. Ed.* **2008,** *47*, 3215-3218.

35. Wang, J.; Gudiksen, M. S.; Duan, X.; Cui, Y.; Lieber, C. M., *Science* **2001,** *293*, 1455-1457.

36. Kalyanikutty, K. P.; Nikhia, M.; Maitra, U.; Rao, C. N. R., *Chem. Phys. Lett.* **2006,** *432*, 190-194.

37. Gao, L.; Wang, E.; Lian, S.; Kang, Z.; Lan, Y.; Wu, D., *Solid State Commun.* **2004,** *130*, 309-312.

38. Lu, Q.; Gao, F.; Zhao, D., *Nanotechnology* **2002,** *13*, 741-745.

39. Jiang, X.; Xie, Y.; Lu, J.; He, W.; Zhu, L.; Qian, Y., *J. Mater. Chem.* **2000,** *10*, 2193-2196.

40. Wang, W.; Ao, L., *Mater. Chem. Phys.* **2008,** *109*, 77-81.

41. Roy, P.; Mondal, K.; Srivastava, S. K., *Cryst. Growth Des.* **2008,** *8*, 1530-1534.

42. Yang, Y. J.; Xiang, J. W., *Appl. Phys. A* **2005,** *81*, 1351-1353.

43. Singh, K. V.; Martinez-Morales, A. A.; Bozhilov, K. N.; Ozkan, M., *Chem. Mater.* **2007,** *19*, 2446-2454.

44. Wang, Q.; Li, J.-X.; Li, G.-D.; Cao, X.-J.; Wang, K.-J.; Chen, J.-S., *J. Cryst. Growth* **2007,** *299*, 386-392.

45. Zhang, P.; Gao, L., *Langmuir* **2003,** *19*, 208-210.

46. Zhao, Q.; Hou, L.; Huang, R.; Li, S., *Inorg. Chem. Commun.* **2003,** *6*, 1459-1462.

47. Kar, S.; Panda, S. K.; Satpati, B.; Satyam, P. V.; Chaudhuri, S., *J. Nanosci. Nanotech.* **2006,** *6*, 771-776.

48. Tang, K.-B.; Qian, Y.-T.; Zeng, J.-H.; Yang, X.-G., *Adv. Mater.* **2003,** *15*, 448-450.

49. Bao, C.; Jin, M.; Lu, R.; Xue, P.; Zhang, Q.; Wang, D.; Zhao, Y., *J. Solid State Chem.* **2003,** *175*, 322-327.

50. Maleki, M.; Mirdamadi, S.; Ghasemzadeh, R.; Sasani Ghamsari, M., *Mater. Lett.* **2008,** *62*, 1993-1995.

51. Yu, S.-H.; Yang, J.; Han, Z.-H.; Zhou, Y.; Yang, R.-Y.; Qian, Y.-T.; Zhang, Y.-H., *J. Mater. Chem.* **1999,** *9*, 1283-1287.

52. Li, Y.; Liao, H.; Ding, Y.; Fan, Y.; Zhang, Y.; Qian, Y., *Inorg. Chem. Commun.* **1999,** *38*, 1382-1387.

53. Li, Y.-D.; Liao, H.-W.; Ding, Y.; Qian, Y.-T.; Yang, L.; Zhou, G.-E., *Chem. Mater.* **1998,** *10* (2301-2303).

54. Wang, H.; Fang, P.; Chen, Z.; Wang, S., *J. Alloys Compd.* **2008,** *461*, 418-422.

55. Xi, L.; Tan, W. X. W.; Boothroyd, C.; Lam, Y. M., *Chem. Mater.* **2008,** *20*, 5444-5452.

56. Talapin, D. V.; Shevchenko, E. V.; Murray, C. B.; Kornowski, A.; Förster, S.; Weller, H., *J. Am. Chem. Soc* **2004,** *126*, 12984-12988.

57. Yong, K. T.; Sahoo, Y.; Swihart, M. T.; Prasad, P. N., *J. Phys. Chem. C* **2007,** *111*, 2447-2458.

58. Peng, Z. A.; Peng, X., *J. Am. Chem. Soc* **2002,** *124*, 3343-3353.

59. Acharya, S.; Patla, I.; Kost, J.; Efrima, S.; Golan, Y., *J. Am. Chem. Soc* **2006,** *128*, 9294-9295.

60. Kar, S.; Chaudhuri, S., *J. Phys. Chem. B* **2006,** *110*, 4542-4547.

61. Nair, P. S.; Scholes, G. D., *J. Mater. Chem.* **2006,** *16*, 467-473.

62. Mo, M.-s.; Shao, M.-w.; Hu, H.-m.; Yang, L.; Yu, W.-c.; Qian, Y.-t., *J. Cryst. Growth* **2002,** *244*, 364-368.

63. Xiang, J.; Yu, S.-H.; Liu, B.; Xu, Y.; Gen, X.; Ren, L., *Inorg. Chem. Commun.* **2004,** *7*, 572-575.

64. Acharya, S.; Gautam, U. K.; Sasaki, T.; Bando, Y.; Golan, Y.; Ariga, K., *J. Am. Chem. Soc* **2008,** *130*, 4594-4595.

65. Patla, I.; Acharya, S.; Zeiri, L.; Israelachvili, J.; Efrima, S.; Golan, Y., *Nano Lett.* **2007,** *7*, 1459-1462.

66. Yong, K.-T.; Sahoo, Y.; Choudhury, K. R.; Swihart, M. T.; Minter, J. R.; Prasad, P. N., *Chem. Mater.* **2006,** *18*, 5965-5972.

67. Chen, J.; Chen, L.; Wu, L.-M., *Inorg. Chem.* **2007,** *46*, 8038-8043.

68. Saraidarov, T.; Reisfeld, R.; Sashchiuk, A.; Lifshitz, E., *Phys. E* **2007,** *37*, 173-177.

69. Bierman, M. J.; Lau, Y. K. A.; Jin, S., *Nano Lett.* **2007,** *7*, 2907-2912.

70. Wang, C.-W.; Liu, H.-G.; Bai, X.-T.; Xue, Q.; Chen, X.; Lee, Y.-I.; Hao, J.; Jiang, J., *Cryst. Growth Des.* **2008,** *8*, 2660-2664.

71. Ge, J.-P.; Wang, J.; Zhang, H.-X.; Wang, X.; Peng, Q.; Li, Y.-D., *Chem. Eur. J.* **2005,** *11*, 1889-1894.

72. Xiu, Z.; Liu, S.; Yu, J.; Xu, F.; Yu, W.; Feng, G., *J. Alloys Compd.* **2008,** *457*, L9-L11.

73. Chen, J.-H.; Chao, C.-G.; Ou, J.-C.; Liu, T.-F., *Surf. Sci.* **2007,** *601*, 5142-5147.

74. Routkevitch, D.; Haslett, T. L.; Ryan, L.; Bigioni, T.; Douketis, C.; Moskovits, M., *Chem. Phys.* **1996,** *210*, 343-352.

75. Suh, J. S.; Lee, J. S., *Chem. Phys. Lett.* **1997,** *281*, 384-388.

76. Xu, D.; Xu, Y.; Chen, D.; Guo, G.; Gui, L.; Tang, Y., *Adv. Mater.* **2000,** *12*, 520-522.

77. Thiruvengadathan, R.; Regev, O., *Chem. Mater.* **2005,** *17*, 3281-3287.

78. Gao, F.; Lu, Q.; Liu, X.; Yan, Y.; Zhao, D., *Nano Lett.* **2001,** *1*, 743-748.

79. Gao, F.; Lu, Q.; Zhao, D., *Adv. Mater.* **2003,** *15*, 739-742.

80. Xiong, S.; Xi, B.; Wang, C.; Zou, G.; Fei, L.; Wang, W.; Qian, Y., *Chem. Eur. J.* **2007,** *13*, 3076-3081.

81. Zhang, J.; Jiang, F.; Zhang, L., *J. Phys. Chem. B* **2004,** *108*, 7002-7005.

82. Zhan, J. H.; Yang, X. G.; Wang, D. W.; Li, S. D.; Xie, Y.; Xia, Y.; Qian, Y. T., *Adv. Mater.* **2000,** *12*, 1348-1351.

83. Simmons, B. A.; Li, S.; John, V. T.; McPherson, G. L.; Bose, A.; Zhou, W.; He, J., *Nano Lett.* **2002,** *2*, 263-268.

84. Sathish, M.; Viswanath, R. P., *Catalysis Today* **2007,** *129*, 421-427.

85. Zelaya-Angel, O.; Alvarado-Gil, J.; Lozada-Morales, R.; Vargas, H.; Ferreira da Silva, A., *Appl. Phys. Lett.* **1994,** *64*, 291.

86. Chen, Q.; Bao, H.; Shen, X., *Phase Transitions* **2008,** *81*, 591.

87. Narayanan, K. L.; Vijayakumar, K. P.; Nair, K. G. M.; Thampi, N. S.; Krishan, K., *J. Mater. Sci.* **1997,** *32*, 4837.

88. Bandaranayake, R. J.; Wen, G. W.; Lin, J. Y.; Jiang, H. X.; Sorensen, C. M., *Appl. Phys. Lett.* **1995,** *67*, 831.

89. Shen, L.; Bao, N.; Yanagisawa, K.; Zheng, Y.; Domen, K.; Gupta, A.; Grimes, C. A., *J. Phys. Chem. C* **2007,** *111*, 7280-7287.

90. Hulteen, J. C.; Martin, C. R., *J. Mater. Chem.* **1997,** *7*, 1075.

91. Young, A. G.; Green, D. P.; McQuillan, A. J., *Langmuir* **2007,** *23*, 12923.

92. Tong, H.; Zhu, Y.-J.; Yang, L.-X.; Li, L.; Zhang, L., *Angew. Chem. Int. Ed.* **2006,** *45*, 7739-7742.

93. Manna, L.; Scher, E. C.; Alivisatos, A. P., *J. Am. Chem. Soc.* **2000,** *122*, 12700.

94. Yao, W.-T.; Yu, S.-H.; Liu, S.-J.; Chen, J.-P.; Liu, X.-M.; Li, F.-Q., *J. Phys. Chem. B* **2006,** *110*, 11704.

95. Zhou, H.; Wong, S. S., *ACS Nano* **2008,** *2*, 944-958.

96. Qing, W.; Gang, X.; Gao, H., *Cryst. Growth Des.* **2006,** *6*, 1776.

97. Halsey, T. C.; Duplantier, B.; Honda, K., *Phys. Rev. E* **1997,** *48*, 621.

98. Ming, N. B.; Wang, M.; Peng, R. W., *Phys. Rev. E* **1993,** *48*, 621.

99. Witten, T.; Sander, L. M., *Phys. Rev. Lett.* **1981,** *47*, 1400.

100. Meakin, P., *Phys. Rev. A* **1983,** *27*, 1495.

101. Dick, K. A.; Deppert, K.; Larson, M. W.; Martensson, T.; Seifert, W.; Wallenberg, L. R.; Samuelson, L., *Nat. Mater.* **2004,** *3*, 380.

102. Peng, Q.; Dong, Y.; Deng, Z.; Li, Y., *Inorg. Chem.* **2002,** *41*, 5249.

103. Qin, A.-M.; Fang, Y.-P.; Zhao, W.-X.; Liu, H.-Q.; Su, C.-Y., *J. Cryst. Growth* **2005,** *283*, 230.

104. Hou, H.; Yang, Q.; Tan, C.; Tian, X.; Xie, Y., *Mater. Lett.* **2005,** *59*, 3364.

105. Zhao, P.; Huang, K., *Cryst. Growth Des.* **2008,** *8*, 717.

106. Mlayah, A.; Brugman, A. M.; Carles, R.; Renucci, J. B.; Valakh, M. Y.; Pogorelov, A. V., *Solid State Commun.* **1994,** *90*, 567-570.

107. Nanda, K. K.; Sahu, S. N., *Appl. Surf. Sci.* **1997,** *119*, 50-54.

108. Wang, N.; Cao, X.; Guo, L.; Yang, S.; Wu, Z., *ACS Nano* **2008,** *2*, 184-190.

109. Rudigier, E.; Barcones, B.; Luck, I.; Jawhari-Colin, T.; Pérez-Rodríguez, A.; Scheer, R., *J. Appl. Phys.* **2004,** *95*, 5153-5158.

110. Chen, G.-Y.; Deng, B.; Cai, G.-B.; Dong, W.-F.; Zhang, W.-X.; Xu, A.-W., *Cryst. Growth Des.* **2008,** *8*, 2137-2143.

111. Minceva-Sukarova, B.; Najdoski, M.; Grozdanov, I.; Chunnilall, C. J., *J. Mol. Struct.* **1997,** *410-411*, 267-270.

112. Bastian, E. J.; Martin, R. B., *J. Phys. Chem.* **1973,** *77*, 1129.

113. Nanda, K. K.; Sahu, S. N.; Soni, R. K.; Tripathy, S., *Phys. Rev. B* **1998,** *58*, 15405-15407.

114. Krauss, T. D.; Wise, F. W., *Phys. Rev. B* **1997,** *55*, 9860-9865.

115. Xu, H.; Wang, W.; Zhu, W., *Mater. Lett.* **2006,** *60*, 2203-2206.

116. Gao, J.; Li, Q.; Zhao, H.; Li, L.; Liu, C.; Gong, Q.; Qi, L., *Chem. Mater.* **2008,** *20*, 6263-6269.

117. Watt, A.; Rubinsztein-Dunlop, H.; Meredith, P., *Mater. Lett.* **2005,** *59*, 3033-3036.

118. Wu, C.; Shi, J.-B.; Chen, C.-J.; Chen, Y.-C.; Wu, P.-F.; Lin, J.-Y., *Mater. Lett.* **2007,** *61*, 4659-4661.

119. Ye, S.; Ye, Y.; Ni, Y.; Wu, Z., *J. Cryst. Growth* **2005,** *284*, 172-175.

120. Wise, F. W., *Acc. Chem. Res.* **2000,** *33*, 773-780.

121. Xiong, Y.; Xie, Y.; Yang, J.; Zhang, R.; Wu, C.; Du, G., *J. Mater. Chem.* **2002,** *12*, 3712-3716.

122. Liu, W.; He, W.; Zhang, Z.; Zheng, C.; Li, J.; Jiang, H.; Ge, X.; Liu, H., *J. Cryst. Growth* **2006,** *290*, 592-596.

123. Spanhel, L.; Anderson, M. A., *J. Am. Chem. Soc* **1990,** *112*, 2278-2284.

124. Yoffe, A. D., *Adv. Phys.* **2002,** *51*, 799.

125. Yu, X.-L.; Cao, C.-B.; Zhu, H.-S.; Li, Q.-S.; Liu, C.-L.; Gong, Q.-H., *Adv. Funct. Mater.* **2007,** *17*, 1397-1401.

126. Machol, J. L.; Wise, F. W.; Patel, R.; Tanner, D. B., *Phys. A* **1994,** *207*, 427-434.

127. Chen, S.; Truax, L. A.; Sommers, J. M., *Chem. Mater.* **2000,** *12*, 3864-3870.

128. Kim, D.; Kuwabara, T.; Nakayama, M., *J. Lumin.* **2006,** *119-120*, 214-218.

129. Wang, W.; Germanenko, I.; S., E.-S. M., *Chem. Mater.* **2002,** *14*, 3028-3033.

130. Wang, W.; Germanenko, I.; El-Shall, M. S., *Chem. Mater.* **2002,** *14*, 3028.

131. Pike, R. D.; Cui, H.; Kershaw, R.; Dwight, K.; Wold, A.; Blanton, T. N.; Wernberg, A. A.; Gysling, H. J., *Thin Solid Films* **1993,** *224*, 221-226.

132. Mondal, S. P.; Dhar, A.; Ray, S. K., *Mater. Sci. Semicond. Proc.* **2007,** *10*, 185-193.

133. Hsu, Y.-J.; Lu, S.-Y., *Langmuir* **2004,** *20*, 23-26.

134. Henglein, A., *Pure Appl. Chem.* **1984,** *56*, 1215-1224.

135. Jing, D.; Guo, L., *J. Phys. Chem. B* **2006,** *110*, 11139-11145.

136. Shiragami, T.; Fukami, S.; Wada, Y.; Yanagida, S., *J. Phys. Chem.* **1993,** *97*, 12882-12887.

137. Korgel, B. A.; Monbouquette, H. G., *J. Phys. Chem. B* **1997,** *101*, 5010-5017.

138. Jang, J. S.; Joshi, U. A.; Lee, J. S., *j. Phys. Chem. C* **2007,** *111*, 13280-13287.

139. Matsumura, M.; Furukawa, S.; Saho, Y.; Tsubomura, H., *J. Phys. Chem.* **1985,** *89*, 1327-1329.

140. Yin, H.; Wada, Y.; Kitamura, T.; Yanagida, S., *Environ. Sci. Technol.* **2001,** *35*, 227-231.

141. Li, W.; Li, D.; Chen, Z.; Huang, H.; Sun, M.; He, Y.; Fu, X., *J. Phys. Chem. C* **2008,** *112*, 14943-14947.

142. Guo, Y.; Zhang, H.; Wang, Y.; Liao, Z.-L.; Li, G.-D.; Chen, J.-S., *J. Phys. Chem. B* **2005,** *109*, 21602-21607.

Chapter VI

1. De, M.; Ghosh, P. S.; Rotello, V. M., *Adv. Mater.* 2008, *20*, 4225-4241.

2. Chan, W. C. W.; Nie, S., *Science* 1998, *281*, 2016.

3. Bruchez, M.; Moronne, M.; Gin, P.; Weiss, S.; Alivisatos, A. P., *Science* 1998, *281*, 2013.

4. Larson, D. R.; Zipfel, W. R.; Williams, R. M.; Clark, S. W.; Bruchez, M. P.; Wise, F. W.; Webb, W. W., *Science* 2003, *300*, 1434.

5. Cederquist, K. B.; Stoermer Golightly, R.; Clark, S. W., *Langmuir* 2008, *24*, 9162.

6. Wong Shi Kam, N.; Liu, Z.; Dai, H., *Angew. Chem. Int. Ed.* 2006, *45*, 577.

7. Patra, C. R.; Bhattacharya, R.; Patra, S.; Basu, S.; Mukherjee, P.; Mukhopadhyay, D., *J. Nanobiotech.* 2006, *4*, 11.

8. Li, Z.; Yang, R.; Yu, M.; Bai, F.; Li, C.; Wang, Z. L., *J. Phys. Chem. C* 2008, *112*, 20114.

9. Kuo, C.-W.; Lai, J.-J.; Wei, K. H.; Chen, P., *Adv. Funct. Mater.* 2007, *17*, 3707.

10. Salem, A. K.; Searson, P. C.; Leong, K. W., *Nat. Mater.* 2003, *2*, 668.

11. Keating, C. D.; Natan, M. J., *Adv. Mater.* 2003, *15*, 451.

12. Hultgren, A.; Tanase, M.; Chen, C. S.; Meyer, G. J.; Reich, D. H., *J. Appl. Phys.* 2003, *93*, 7554.

13. Mondejar, S. P.; Kovtun, A.; Epple, M., *J. Mater. Chem. 17*, 4153.

14. Meiser, F.; Cortez, C.; Caruso, F., *Angew. Chem. Int. Ed.* 2004, *43*, 5954.

15. Wang, L.; Qian, B.; Chen, H.; Liu, Y.; Liang, A., *Chem. Lett.* 2008, *37*, 402.

16. Zhang, Y.-W.; Sun, X.; Si, R.; You, L.-P.; Yan, C.-H., *J. Am. Chem. Soc.* 2005, *127*, 3260.

17. Riwotzki, K.; Meyssamy, H.; Schnablegger, H.; Kornowski, A.; Haase, M., *Angew. Chem. Int. Ed.* 2001, *40*, 573.

18. Meyssamy, H.; Riwotzki, K.; Kornowski, A.; Naused, S.; Haase, M., *Adv. Mater.* 1999, *11*, 840.

19. Hou, Z.; Yang, P.; Li, C.; Wang, L.; Lian, H.; Quan, Z.; Lin, J., *Chem. Mater.* 2008, *20*, 6686.

20. Jose, M. T.; Lakshmanan, A. R., *Opt. Mater.* 2004, *24*, 651.

21. Erdei, S.; Ainger, F. W.; Ravichandran, D.; White, W. B.; Cross, L. E., *Mater. Lett.* 1997, *30*, 389.

22. Hashimoto, N.; Takada, Y.; Sato, K.; Ibuki, S., *J. Lumin.* 1991, *48&49*, 893.

23. Imanaka, N.; Masui, T.; Hirai, H.; Adachi, G. Y., *Chem. Mater.* 2003, *15*, 2289.

24. Altinoglu, E. I.; Russin, T. J.; Kaiser, J. M.; Barth, B. M.; Eklund, P. C.; Kester, M.; Adair, J. H., *ACS Nano* 2008, *2*, 2075.

25. Patra, C. R.; Bhattacharya, R.; Patra, S.; Basu, S.; Mukherjee, P.; Mukhopadhyay, D., *Clin. Chem.* 2007, *53*, 2029.

26. Li, Q.; Yam, V. W., *Angew. Chem. Int. Ed.* 2007, *46*, 3486.

27. Chen, G.; Sun, S.; Zhao, W.; Xu, S.; You, T., *J. Phys. Chem. C* 2008, *112*, 20217.

28. Di, W.; Wang, X.; Zhu, P.; Chen, B., *J. Solid State Chem.* 2007, *180*, 467.

29. Huignard, A.; Gacoin, T.; Boilot, J.-P., *Chem. Mater.* 2000, *12*, 1090.

30. Di, W.; Zhao, X.; Lu, S.; Wang, X.; Zhao, H., *J. Solid State Chem.* 2007, *180*, 2478.

31. Shionoya, S.; Nakazawa, E., *Appl. Phys. Lett.* 1965, *6*, 118.

32. Yin, Y.; Alivisatos, A. P., *Nature* 2005, *437*, 664.

33. Fang, Y.-P.; Xu, A.-W.; Song, R.-Q.; Zhang, H.-X.; You, L.-P.; Yu, J. C.; Liu, H.-Q., *J. Am. Chem. Soc.* 2003, *125*, 16025.

34. Cao, M.; Hu, C.; Wu, Q.; Guo, C.; Qi, Y.; Wang, E., *Nanotechnology* 2005, *16*, 282.

35. Yu, L.; Li, D.; Yue, M., *Mater. Lett.* 2007, *61*, 4374.

36. Yan, R.; Sun, X.; Wang, X.; Peng, Q.; Li, Y., *Chem. Eur. J.* 2005, *11*, 2183.

37. Zheng, Y.; Cheng, Y.; Wang, Y.; Yu, Y.; Chen, D.; Bao, F., *J. Cryst. Growth* 2005, *280*, 569.

38. Yu, L.; Song, H.; Lu, S.; Liu, Z.; Yang, L.; Kong, X., *J. Phys. Chem. B* 2004, *108*, 16697.

39. Xing, Y.; Li, M.; Davis, S. A.; Mann, S., *J. Phys. Chem. B* 2006, *110*, 1111.

40. Zhu, L.; Liu, X.; Li, Q.; Li, J.; Zhang, S.; Meng, J.; Cao, X., *Nanotechnology* 2006, *17*, 4217.

41. Hu, H.; Yu, M.; Li, F.; Chen, Z.; Gao, X.; Xiong, L.; Huang, C., *Chem. Mater.* 2008, *20*, 7003.

42. Murphy, K. E.; Altman, M. B.; Wunderlich, B., *J. Appl. Phys.* 1977, *48*, 4122.

43. Peng, Z. A.; Peng, X. G., *J. Am. Chem. Soc.* 2001, *123*, 1389.

44. Peng, Z. A.; Peng, X. G., *J. Am. Chem. Soc.* 2002, *124*, 3343.

45. Zhang, Y.; Guan, H., *J. Cryst. Growth* 2003, *256*, 156.

46. Yan, Z.-G.; Zhang, Y.-W.; You, L.-P.; Si, R.; Yan, C.-H., *Solid State Commun.* 2004, *130*, 125.

47. Hu, W.; Zhao, Y.; Liu, Z.; Dunnill, C. W.; Gregory, D. H.; Zhu, Y., *Chem. Mater.* 2008, *20*, 5657.

48. Okada, A.; Yoshimura, M.; Ueda, K., *Appl. Phys. Lett.* 2007, *90*, 203102.

49. Dai, Q.; Xiao, N.; Ning, J.; Li, C.; Li, D.; Zou, B.; Yu, W. W.; Kan, S.; Chen, H.; Liu, B.; Zou, G., *J. Phys. Chem. C* 2008, *112*, 7567.

50. Zitoun, D.; Pinna, N.; Frolet, N.; Belin, C., *J. Am. Chem. Soc.* 2005, *127*, 15034.

51. Hu, Y.; Chen, K., *J. Cryst. Growth* 2007, *308*, 185.

52. Kelly, A. T.; Rusakova, I.; Ould-Ely, T.; Hofmann, C.; Luttge, A.; Whitmire, K. H., *Nano Lett.* 2007, *7*, 2920.

53. Tang, J.; Alivisatos, A. P., *Nano Lett.* 2006, *6*, 2701.

54. Shen, X.-F.; Yan, X.-P., *Angew. Chem. Int. Ed.* 2007, *46*, 7659.

55. Deng, H.; Liu, C.; Yang, S.; Xiao, S.; Zhou, Z.-K.; Wang, Q.-Q., *Cryst. Growth Des.* 2008, *8*, 4432.

56. Kim, S.; Lee, J. S.; Mitterbauer, C.; Ramasse, Q. M.; Sarahan, M. C.; Browning, N. D.; Park, H. J., *Chem. Mater.* 2009, *21*, 1182.

57. He, J.; Han, M.; Shen, X.; Xu, Z., *J. Cryst. Growth* 2008, *310*, 4581.

58. Chen, G.-Y.; Deng, B.; Cai, G.-B.; Zhang, T.-K.; Dong, W.-F.; Zhang, W.-X.; Xu, A.-W., *J. Phys. Chem. C* 2008, *112*, 672.

59. Busch, S.; Dolhaine, H.; Dechesne, A.; Hinez, S.; Hochrein, O.; Laeri, F.; Podebrad, O.; Vietze, U.; Weiland, T.; Kniep, R., *Eur. J. Inorg. Chem.* 1999, (1643).

60. Colfen, H.; Qi, L., *Progr. Colloid Polym. Sci.* 2001, *117*, 200.

61. Wang, T.; Colfen, H.; Antonietti, M., *J. Am. Chem. Soc.* 2005, *127*, 3246.

62. Dong, L.; Chu, Y.; Zhang, W., *Mater. Lett.* 2008, *62*, 4269.

63. Sharabani, R.; Reuveni, S.; Noy, G.; Shapira, E.; Sadeh, S.; Selzer, Y., *Nano Lett.* 2008, *8*, 1169.

64. Brambilla, G.; Payne, D. N., *Nano Lett.* 2009, *9*, 831.

65. Zhang, Z.; Shao, X.; Yu, H.; Wang, Y.; Han, M., *Chem. Mater.* 2005, *17*, 332.

66. Imanaka, N.; Masui, T.; Itaya, M., *Chem. Lett.* 2003, *32*, 400.

67. Yu, L.; Song, H.; Liu, Z.; Yang, L.; Lu, S.; Zheng, Z., *Solid State Commun.* 2005, *134*, 753.

68. Rambabu, U.; Munirathnam, N. R.; Prakash, T. L.; Buddhudu, S., *Mater. Chem. Phys.* 2003, *78*, 160.